Creation of Ultracold RbCs Ground-State Molecules

DISSERTATION

by

Markus Debatin

submitted to the Faculty of Mathematics, Computer
Science and Physics of the University of Innsbruck

in partial fulfillment of the requirements
for the degree of doctor of science

advisor:
Univ.Prof. Dr. Hanns-Christoph Nägerl,
Institute of Experimental Physics, University of Innsbruck

Innsbruck, July 2013

Abstract

Control of external and internal degrees of freedom at the level of single quantum states is essential for a series of molecular physics experiments. Heteronuclear dimers feature a large electric dipole moment, which makes them particular interesting candidates for experiments with strongly interacting quantum gases. However efficient cooling schemes such as laser cooling are difficult to realize for molecules. Therefore we create ultracold molecules from already cooled ultracold gases.

This this work presents a series of experiments that has been carried out in order to create the molecules in their lowest internal quantum state. Techniques to create ultracold atoms are readily available. However, the creation of stable mixtures is still a challenge since inter-species scattering plays a role in addition to intra-species scattering physics. This requires us to cool two clouds of ^{87}Rb and ^{133}Cs separately and merge the clouds afterwards. After overlapping the BECs, we produce weakly bound RbCs molecules using the Feshbach-association technique. We transfer the molecules from the weakly bound state to the lowest vibrational and rotational level of the $X^1\Sigma^+$ electronic ground-state potential. For the transfer the initial and the final state are linked with lasers to an intermediate electronically excited state. The transfer is achieved by the Stimulated Raman Adiabatic Passage (STIRAP) technique.

In order to identify a suitable route for STIRAP a variety of electronically excited molecular levels is investigated by high resolution spectroscopy. Two-photon spectroscopy is used in order to determine the binding energy of the lowest ro-vibrational level of the $X^1\Sigma^+$ ground state to be $D_0^X = 3811.5755(16)\,\mathrm{cm}^{-1}$. The vibrational level 29 of the $b^3\Pi_1$ electronic excited potential is determined to feature suitable couplings to both the initial and the final state and the molecules are transfered to the ground state with an efficiency of 89%. In order to determine the hyperfine level of the molecular ground state, the hyperfine splitting is measured and STIRAP transfer to a different vibrational level is carried out. It is found that for RbCs the Feshbach molecules can be directly transferred to the lowest hyperfine level of the ro-vibrational ground state.

Zusammenfassung

Diese Doktorarbeit umfasst experimentelle Studien zur Erzeugung ultrakalter dipolarer RbCs Grundzustandsmoleküle. Für dipolare Quantengase wird aufgrund der langreichweitigen Dipol-Dipol Wechselwirkung eine Vielfalt neuartiger Quantenzustände in optischen Gittern vorhergesagt. Für den experimentellen Nachweis vieler dieser Quantenzustände ist die Erzeugung eines Quantengases aus stark wechelwirkenden Dipolen essentiell. Heteronukleare Dimere weisen ein ausgeprägtes elektrisches Dipolmoment auf, welches es ermöglicht, Systeme mit starker Dipol-Dipol Wechselwirkung zu realisieren.

Die derzeit einzige nachgewiesene Möglichkeit, ein molekulares Quantengas zu erzeugen, ist die Feshbach-Assoziation mit anschließendem Grundzustandstransfer durch einen stimulierten adiabatischen Raman-Übergang (STIRAP). Durch die Feshbachi-Assoziation werden zunächst freie Atome zu schwach gebundenen Molekülen (Feshbach Molekülen) verbunden, welche sich in einem hoch angeregten Vibrationszustand befinden. Der darauf folgende STIRAP transferiert die Moleüle vom angeregten Zustand in den molekularen Grundzustand. Der Transfer in den Grundzustand ist notwendig, um inelastische Streuprozesse zu verhindern. Zudem ist das Dipolmoment heternonuklearer Moleküle in niedrigen Vibrationszuständen besonders stark ausgeprägt.

Auf diese Weise wurde bereits erfolgreich ein Quantengas aus fermionischem KRb erzeugt. Im Rahmen unserer experimentellen Studien ist es gelungen, bosonische RbCs Moleküle durch Feshbach-Assoziation ultrakalter Rb und Cs Quantengase zu erzeugen und mittels STIRAP in ihren Grundzustand zu transferieren. Neben einem bosonischen Charakter und einem größeren Dipolmoment unterscheidet sich RbCs von KRb hinsichtlich der chemischen Stabilität. KRb kann bei einer Kollision zweier Moleküle zu K_2+Rb_2 reagieren. Für RbCs sind solche Reaktionen endotherm und in ultrakalten Gasen aufgrund der niedrigen kinetischen Energie nicht möglich. Daher ist RbCs im Grundzustand stabil. Dies kann einen entscheidenden Vorteil für viele Experimente darstellen.

Zur Erzeugung ultrakalter RbCs Moleküle werden zunächst zwei separate ultrakalte Atomwolken aus Rb und Cs generiert. Aus den gemischtem Atomwolken werden hernach schwach gebundene Feshbach-Molekülen assoziiert. Um die Moleküle mittels STIRAP in den Grundzustand zu transferieren, ist es nötig, geeignete elektronisch angeregte Vibrationsniveaus zu identifizieren. Daher wird eine Reihe von Vibrationsniveaus hinsichtlich ihrer Eignung für STIRAP spektroskopisch untersucht. Letzteres umfasst auch die Bestimmung ihrer Energie sowie ihrer Kopplung an die Feshbach-Moleküle und den Grundzustand. Im Rahmen der spektroskopischen Untersuchungen wird die Bindungsenergie des niedrigsten Vibrationsniveaus des $X^1\Sigma^+$ Grundzustandes zu $D_0^X = 3811.5755(16)\,\mathrm{cm}^{-1}$ bestimmt. Die hochauflösende Spektroskopie erlaubt es ferner, einzelne Hyperfeinzustände zu detektieren.

Ausgehend von den gewonnenen Daten wird ein geeignetes angeregtes Niveau ausgewählt, und die Moleküle werden mit einer Effizienz von 89% in den Grundzustand transferiert. Dabei gelingt es, die Moleükle in das niedrigste Hyperfeinniveau des molekularen Grundzustandes zu transferieren. Die Arbeit zeigt im Detail, daß ein effizienter Grundzustandstransfer selbst bei geringen Kopplungsstärken möglich ist und analysiert Faktoren, die die Effizienz limitieren.

Contents

Chapter 1

Introduction

The field of ultracold molecules has shown a rapid and intriguing development throughout the recent years. Numerous articles review the fast progress and testify an increasing interest in the creation and investigation of cold and ultracold molecular gases [Doy04, Dul06, Car09, Dul09, Fer09, Fri09, Jin12]. Chemical physicists are thrilled by the large amount of precision and control that is possible in ultracold molecular samples [Fri09] and quantum physicists are excited about the possibility explore a large variety of phenomena that are based on strong dipolar interactions, which are present in heteronuclear dimers [Bar12, Mic06, Büc07a, Bre07, Pup08, Pup09, CS10]. For precision measurements cold molecules provide an enhanced sensitivity due to longer observation times as compared to molecular beams [Chi09, DeM08].

Experiments that are proposed for ultracold molecules mostly rely on or benefit from high phase-space densities [Car09]. Some of the proposals are even calculated for zero temperature or well defined motional quantum states. Phase-space density is defined in free space as $D = n\lambda_{\mathrm{dB}}^3$, where n is the number density and λ_{dB} is the thermal de Broglie wavelength $\lambda_{\mathrm{dB}} = \sqrt{2\pi\hbar^2/(mk_{\mathrm{B}}T)}$, with k_{B} being Boltsmann's constant, m the mass of the particle and T the temperature of the sample. When the phase-space density increases, for bosons a phase transition to a Bose-Einstein condensate (BEC) can occur. In a BEC a single quantum state is occupied by a macroscopic number of particles. For a uniform Bose gas in a three-dimensional box potential, the transition from a thermal gas to a BEC takes place at a phase-space density of $D \approx 2.612$ [Ket99]. Such a transition has been observed for dilute atomic gases [And95, Bra95, Dav95] and marked the beginning of a fruitful and exciting era in atomic, molecular, and optical (AMO) physics. One of the highlights of this era was the loading of ultracold atoms into optical lattice potentials, which allowed the realization of model systems from condensed matter physics with astonishing experimental control over all degrees of freedom and perfect decoupling from the external environment [Mor06, Blo08]. Thrilled by the great succes of atoms in optical lattices, theorists extended their models to strongly interacting dipolar systems, which can be realized with polar molecules [Mic06, Pol10, Bar12]. The experimental realization of such models is awaited with curiosity. The creation of a BEC of stable dipolar molecules would pave the way for exploration of a large variety of interesting phenomena and can be expected to have a profound impact on physics.

The tremendous success of atomic quantum gases was only possible due to novel cooling schemes that were developed for atoms. Namely laser cooling of atoms is a key ingredient in almost every atomic quantum gas experiment. Laser cooling, which relies on closed cycling optical transitions, was first demonstrated for ions in 1978 [Win78, Neu78]. Soon later laser cooling of atoms [And81, Phi82] led to the first trapping of atomic vapors by magnetic fields [Mig85]. Molecules generally lack such closed electronic transitions. However, a variety of molecular species with quasi-cycling transitions has been identified [Wei98, Hun12, Gut99, Vit08, Bah96] and recently a 2D magneto optical trap (MOT) has been realized with transverse temperatures of 2 mK [Hum13]. Despite the recent progress, direct cooling of molecules remains challenging and molecular quantum gases have only been created by associating molecules from atomic quantum gases.

The creation of molecules at rest in 2000 [Wyn00] marked the beginning of a continuing series of milestone experiments targeting the creation of ultracold molecules from ultracold atomic samples. The creation of weakly bound Feshbach molecules from quantum degenerate atomic samples [Don02, Her03, Joc03b, Fer09] proved the highly efficient creation of a molecular BEC. Many experiments on bosonic dipolar molecules require deeply bound molecules in well controlled internal and external quantum states. In order to achieve stability against radiative decay and inelastic two-body collisions, it is desirable to create the molecules in the lowest energy ground state of each degree of freedom. Few years after the creation of BECs of Feshbach molecules, the next highlight of research was the creation of a quantum gas of homonuclear molecules in the ro-vibrational ground state [Dan08b, Lan08] and the creation of a high phase-space density gas of polar KRb molecules [Ni08]. With the creation of a high phase-space density gas of KRb molecules the way has been paved for the investigation of dipolar molecules in the quantum regime. Soon later, dipolar collisions of polar molecules in the quantum regime [Ni10] and quantum state controlled chemical reactions have been observed [Osp10b]. These reactions occur along the $\mathrm{KRb} + \mathrm{KRb} \rightarrow \mathrm{K}_2 + \mathrm{Rb}_2$ path way, which is the only possible reaction for ground-state alkali dimers. The control of these reactions requires the confinement in a 2D geometry and alignment of the dipoles. For the alkali combinations NaK, NaRb, NaCs, KCs, RbCs this reaction path is endothermic and thus energetically forbidden [Żuc10b]. Hence these molecules are expected to be intrinsically stable against dimer-dimer collisions and therefore the ensemble is stable without alignment in 3D. The creation of a bosonic RbCs quantum gas would complement the fruitful experiments with fermionic KRb and would constitute great step towards the exploration of strongly interacting bosonic dipoles. While RbCs has been successfully created in the ro-vibrational ground state in the group of DeMille [Sag05] no quantum gas of RbCs has been created yet.

Currently a broad variety of alkali mixtures and molecules [Dei08b, Voi09, Wil08, Rid11, Had02, Heo12, Sil05, Deh08, Hai09, Hai04, Wu12, Par12] has been investigated and ongoing experiments target the creation of quantum gases of molecular ground-state molecules. Not only alkali mixtures, but also mixtures and molecules involving non-alkali atoms like RbYb [Mün11, Nem09, Tas10], SrF [Shu10, Shu09], RbSr [Zuc10a] and LiYb [Zuc10a, Bru12, Han11] are currently being investigated and are promising candidates for the creation of dipolar quantum gases or interesting mixture experiments.

Collisions of ultracold particles were a main concern since the early investigations of ultracold gases [Ket99]. While elastic collisions (“good” collisions) lead to a thermalisation of the sample, inelastic collisions (“bad” collisions) mostly result in loss of particles or heating of the sample. In the pre-BEC era “many people considered BEC to be an elusive goal, made inaccessible by inelastic interactions at the densities required" [Ket08]. Inelastic, light-induced collisions [Wal94] and absorption of scattered laser light [Wal90] limited the number and density of atoms for the early attempts to create a BEC with laser cooling methods. If atoms are not trapped in their lowest hyperfine state, hyperfine changing collisions constitute a loss mechanism that was hampering the creation of alkali BECs of other atoms than rubidium and sodium [Ket99]. Even for atoms in their lowest spin state scattering resonances can lead to a many-body loss process. A crucial step was the discovery of Feshbach resonances [Ino98, Cou98, Chi10], which allowed to magnetically control the scattering properties of ultracold gases [Tim99, Tie93]. For the creation of a Cs BEC the magnetic control of the scattering properties was essential [Web03a]. For atomic mixtures scattering physics is more complex than for single species experiments since the scattering properties of both species as well as interspecies scattering properties have to be well controlled simultaneously. This creates a major challenge and can hinder the creation of dual species BECs for mixtures like RbCs [Ler10, Ler11] and currently limits the phase-space density of our ultracold molecular sample. An advanced strategy to overcome this limitation and to reach quantum degeneracy is based on the use of an optical lattice and is currently being investigated in our laboratory.

While the creation of a BEC of strongly interacting dipolar molecules still remains a challenge, a variety of effects based on weaker dipolar interactions [Bar02, Bar08, Lah09] has successfully been explored with magnetic quantum gases. An excellent and clear manifestation of dipolar forces was the experimental detection of a characteristic deformation of an expanding chromium BEC which soon after was followed by the detection of a d-wave collapse [Stu05, Gri05, Lah07, Lah08]. Growing interest in atomic dipolar quantum gases led to the creation of Bose-Einstein condensates and degenerate Fermi gases of a variety of species including Dysprosium [You10, Lu11, Lu12] and Erbium [Fri12, Aik12]. While a variety of phenomena can be explored with magnetic dipoles, many of the experiments that are explicitly proposed for dipolar molecules clearly benefit from the strong dipolar interactions and various means of tunability [Mic06] provided by ultracold dipolar molecules. A quantum gas of dipolar molecules would allow to explore phenomena that are difficult to investigate with quantum gases of magnetic dipoles. Especially the regime of strongly interacting dipoles, which is characterized by a dipole length that is larger than the interparticle distance, is difficult to reach with magnetic dipoles. Even at the highest achievable densities obtained so far the dipole length is more than 100-fold smaller than the mean interparticle distance [Ni09].

In this thesis the creation of RbCs ro-vibrational ground-state molecules in a well defined hyperfine state is reported. We follow a scheme similar to [Ni08] which is presently the most successful way to create a high phase-space density sample of dipolar ground-state molecules. Weakly bound Feshbach molecules are created from a mixture of ultracold quantum gases at temperatures around the onset of condensation. These molecules are subsequently transferred to the ground state by a coherent process termed stimulated Raman adiabatic passage (STIRAP) [Ber98].

An overview of the scheme used for creation of ultracold RbCs ground-state molecules is shown in Fig. 1.1. A two-color magneto-optical trap (MOT) [Raa87] is loaded with Rb and Cs. The loading of the MOTs is followed by a compressed MOT and subsequently the atoms are cooled down by Raman sideband cooling [Ker00, Tre01] to temperatures of 2 to 5 μK. Evaporational cooling is performed in two separate traps [Ler10], which are subsequently overlapped in order to form Feshbach molecules. Since condensates of Rb and Cs are immiscible [McC11, Pat13], the evaporation is stopped at the onset of condensation and the two thermal clouds are merged. This strategy does not allow for high efficient creation of Feshbach molecules because the phase-space densities are low [Chi04]. However, because of its simplicity it is used for all measurements presented in this thesis. A more advanced strategy that will allow for highly efficient creation of Feshbach molecules in optical lattices [Dam03, Moo03, Jak02, Fre10] is currently under experimental investigation.

We use STIRAP to convert the Feshbach molecules into ground-state molecules. STIRAP has been widely explored and used during the last decades by the group of K. Bergmann [Gau88, Gau90, Sho91, Cou92, Kuh92, Mar95, Sho95, Mar96, Ber98, Vit98a]. A high efficient scheme for creation of ultracold heteronuclear alkali dimers has been proposed by Stwalley [Stw04]. As opposed to the proposal by Stwalley [Stw04] that suggests the use of the $A^1\Sigma^+ - b^3\Pi_0$ potential, it turned out that the $\mathrm{b}^3\Pi_1$ potential yields higher efficiencies for ground-state transfer. The potential energy curves and the range of vibrational levels of the electronically excited state that can be addressed by our laser system are shown in Fig. 1.2. Starting from a Feshbach level, the molecules are transferred to

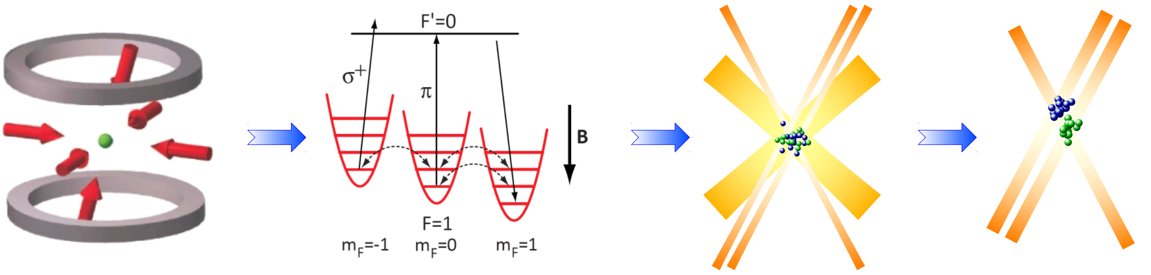

Two color MOT

Raman sideband cooling

loading of the small traps

separation of the traps

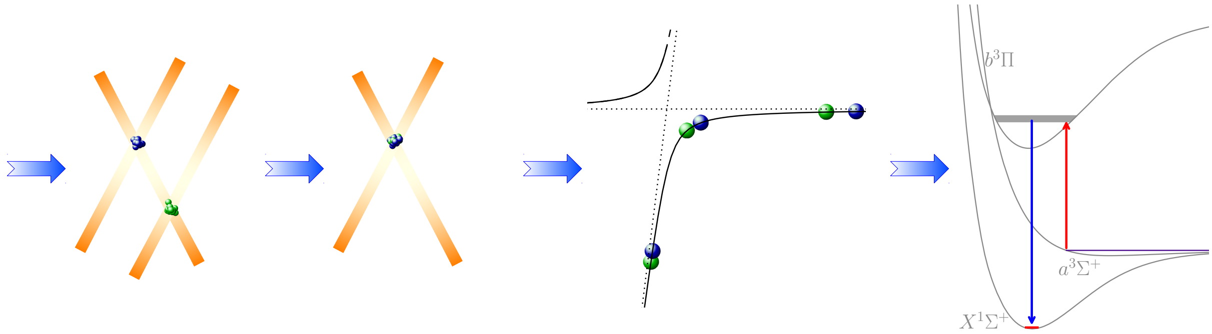

evaporational cooling

combination of the clouds

Feshbach association

STIRAP ground-state transfer

Figure 1.1: Overview of the scheme used for creation of RbCs ground-state molecules. As two colour MOT is loaded with Rb and Cs. In a next step, the atoms are cooled by a two species Raman sideband cooling to $2-5\,\mu$K. Subsequently the molecules are trapped by a large "reservoir trap" and by lowering the trap depth evaporative cooling leads to an accumulation in the two small traps. The two small traps are then separated from each other in order to avoid crosstalk. Further evaporation cooling steps allow for creation of BECs or partially condensed clouds, which are subsequently combined. Weakly bound molecules are created via Feshbach association and in a last step STIRAP is used to coherently transfer the molecules into the lowest hyperfine state of the rovibrational ground state.

the ground state using two-photon STIRAP.

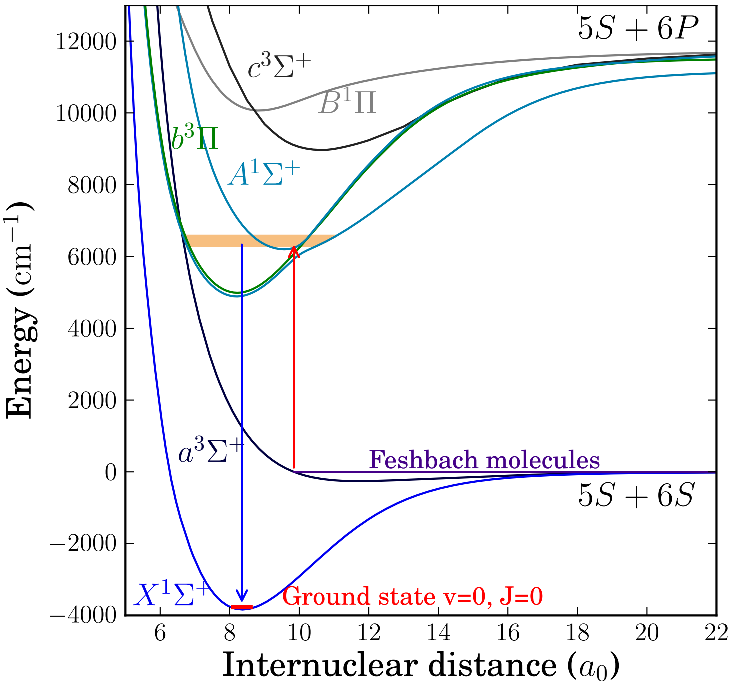

Figure 1.2: Potential energy curves of the electronic ground state and the lower electronic excited states of RbCs. The range of vibrational levels that can be addressed by our laser system is marked by a broad line in the excited potential. (Molecular BO-potential data from [Kot05, Doc10]).

Despite being a well established and robust technique for vibrational state transfer, STIRAP can be challenging if the energy distance between the initial and the final state is large and the Rabi frequencies are small. Under these circumstances the laser systems have to be well stabilized in order to maintain phase coherence [Yat02] throughout the whole transfer process. The time needed for the transfer depends on adiabaticity criteria [Kuh92, Ber98, Yat02] which read $\Omega_{\mathrm{eff}}^2\tau \gg \gamma\pi^2$ and $\Omega_{\mathrm{eff}}\tau \gg 10$, where Ω_{eff} is the effective Rabi frequency, τ is the timescale on which the transfer occurs and γ is the excited state decay rate. Small Rabi frequencies hence imply long transfer times and require lasers with low phase fluctuations [Yat02]. The effective Rabi frequency is determined by the transition strengths between the initial state and the excited state as well as the transition strength between the excited state and the ground state. Hence it is necessary to perform spectroscopic measurements in order to identify an excited state that has a good coupling strength for both transitions.

The dissertation is structured into two parts. The first part describes the physics of strongly interacting dipolar quantum gases (chapter 2) and the creation of ultracold molecules (chapter 3). Different approaches for creation of cold molecules are discussed with an emphasis on the scheme used in the RbCs experiment and the physics involved.

The second part describes the experimental setup and the measurements leading to the creation of ultracold ground-state RbCs molecules. In chapter 4 the experimental setup is summarized and the additional laser systems are described in detail. Chapter 5 discusses the Feshbach structure and explains the creation and characterisation of Feshbach molecules. The various one- and two-photon measurements used to characterize the excited states and the ground state are expounded in chapter 6. This forms the basis for successful STIRAP ground-state transfer, which is described in chapter 7 together with a detailed analysis of various factors that limit the efficiency. The thesis closes with an outlook on future experiments.

Part I

Physics and creation of ultracold dipolar molecules

Chapter 2

Dipolar quantum gases

Dipolar quantum gases have gained a lot of attraction attention and a tremendous progress was made during the last decade [Bar02, Bar08, Boh09]. The realization of atomic dipolar quantum gases [Lah09] has led to a vibrant activity in the field of dipolar quantum gases and a broad variety of interesting phenomena has been predicted. However, many of the phenomena predicted for strongly interacting dipolar quantum-gases [Bar12, Büc07a, Bre07, Pup08, Pup09, CS10] remain yet to be observed. A number of review articles [Bar02, Bar08, Lah09, Bar12] give an excellent overview over the field. Some of the fundamental principles and important physical phenomena are highlighted in the following. The basic parameters that are frequently used in literature to describe dipolar interactions are introduced. The scattering of dipolar particles, novel anticipated quantum phases and effects are outlined and some possible applications of dipolar quantum gases are sketched.

Scattering processes in the quantum regime

For a quantum gas the interaction of particles is formulated in terms of ingoing and outgoing waves, which are typically expanded into contributions from different angular momenta l via a partial wave expansion. Analogously to atomic states partial waves are named $S, P, D, F, \cdots$ according to their angular momentum $l = 1, 2, 3, 4, \cdots$ and the centrifugal potential $\hbar^2 l(l+1)/(mR^2)$ sets an energy dependent limit for the partial waves taking part in the scattering process. Usually quantum mechanical scattering is expressed in the center-of-mass frame, where m is the reduced mass, and R is the distance between the two particles. In the far field each of the partial waves experiences a different phase shift $\delta_l(k)$ between the incoming and the outgoing wave, where $\hbar k$ is the relative momentum of the colliding particles. The phase shift can have a complex contribution in the case of inelastic scattering [Bra06].

In the low energy limit when the de Broglie wavelengths of the particles are large compared to their range of interactions the centrifugal barrier prevents scattering other than s-wave scattering. In this limit the phase shift $\delta_0(k)$ can be written by the effective range expansion [Chi10] as

$$k \cot \delta_0(k) = -\frac{1}{a} + \frac{1}{2} r_0 k^2, \tag{2.1}$$

where a is the s-wave scattering length, which is a main parameter for the description of scattering phenomena in the ultracold regime. The effective range is directly related to the long-range behaviour of the van der Waals interaction [Chi10]. In the low energy limit $k \to 0$, the phase shift δ_0 converges to $k \cot \delta_0 = -1/a$. For low particle momenta on the order of $\hbar/r_0$ the large size of the de Broglie wavelength prevents the atoms from resolving the internal structure of the interaction potential. Therefore long-distance effect of the scattering is independent of the exact shape of the potential and does not distinguish between different potentials that yield the same value of a. Hence, the real inter-actomic potential can be replaced by a pseudopotential, which is short range, isotropic and characterized by a single parameter, the s-wave scattering length a. The inter-atomic contact interaction potential is given by

$$U_{\text{contact}} = \frac{4\pi\hbar^2 a}{m}\delta(\mathbf{r}) = g\delta(\mathbf{r}), \tag{2.2}$$

where m is the mass of the particles and $g = 4\pi\hbar^2 a/m$ is the coupling constant.

For identical bosons, the elastic cross section $\sigma(k)$ is connected to the scattering length via

$$\sigma(k) = \frac{8\pi a^2}{1+k^2a^2}\begin{cases} \xrightarrow{ka \ll 1} 8\pi a^2 \\ \xrightarrow{ka \gg 1} 8\pi/k^2 \end{cases} \tag{2.3}$$

For large positive values of a, a shallow bound state exists with the binding energy

$$E_b = \hbar^2/i(2\mu a^2), \tag{2.4}$$

where μ is the reduced mass of the atom pair and E_b is the binding energy of the last bound state.

The Gross-Pitaevskii equation

Bosons at temperatures T lower than the critical temperature of Bose-Einstein condensation $T \ll T_{\mathrm{c}}$ are frequently treated by a mean field theory [Pit03]. In particular a BEC can be described by a macroscopic wave function $\Psi(\mathbf{r}, t)$, for which the Gross-Pitaevskii equation [Gro61, Pit61] is valid:

$$i\hbar\frac{\partial}{\partial t}\Psi(\mathbf{r},t) = \left[-\frac{\hbar^2}{2m}\nabla^2 + g|\Psi(\mathbf{r},t)|^2 + V(\mathbf{r})\right]\Psi(\mathbf{r},t), \tag{2.5}$$

where $V(\mathbf{r})$ describes an external confining potential and the interaction between the particles is described by the coupling constant

$$g = \frac{4\pi\hbar^2 a}{m}. \tag{2.6}$$

Quantum gases are frequently described in terms of the scattering length a and the Gross-Pitaevskii equation is a very popular way to derive properties of bosonic quantum gases. For dipolar quantum gases the theoretical framework is modified through introduction of additional terms.

2.1 Dipole-dipole interactions

Dipolar quantum gases feature a long-range, anisotropic dipole-dipole interaction in addition to the sort-range and isotropic contact interaction usually present in ultracold gases. For two dipoles 1 and 2 in a three dimensional space at relative distance $\mathbf{r}$ and with dipole moments along the unit vectors $\mathbf{e}_1$ and $\mathbf{e}_2$ the energy due to the dipole-dipole interaction is given by

$$U_{\mathrm{dd}}(\mathbf{r}) = \frac{C_{\mathrm{dd}}}{4\pi} \frac{(\mathbf{e}_1 \cdot \mathbf{e}_2) r^2 - 3(\mathbf{e}_1 \cdot \mathbf{r})(\mathbf{e}_2 \cdot \mathbf{r})}{r^5}, \tag{2.7}$$

where $r = |\mathbf{r}|$. The dipolar coupling constant C_{dd} is $\mu_0 \mu^2$ for particles having a permanent magnetic dipole moment μ and d^2/ϵ_0 for electric dipoles with dipole moment d. The dipole-dipole interaction (2.7) features a $U_{\mathrm{dd}} \sim 1/r^3$ decay, which is also referred to as long-range character, contrary to the typical van der Waals potential that scales like $U_{\mathrm{vdW}} \sim -1/r^6$.

If all dipoles point into the same direction, the sample is polarized and the interaction reduces to

$$U_{\mathrm{dd}}(\mathbf{r}) = \frac{C_{\mathrm{dd}}}{4\pi} \frac{1 - 3\cos^2\theta}{r^3}. \tag{2.8}$$

Depending on the dimensionality of the system the dipole-dipole interaction can be treated as *long-range* or *short-range* and several differing definitions can be found. One definition is based on the behaviour of the energy in the thermodynamic limit [Lah09], which is intensive for interactions that decay faster than r^{-D}, where D is the dimensionality of the system. For 3D systems the energy becomes extensive, which reveals the

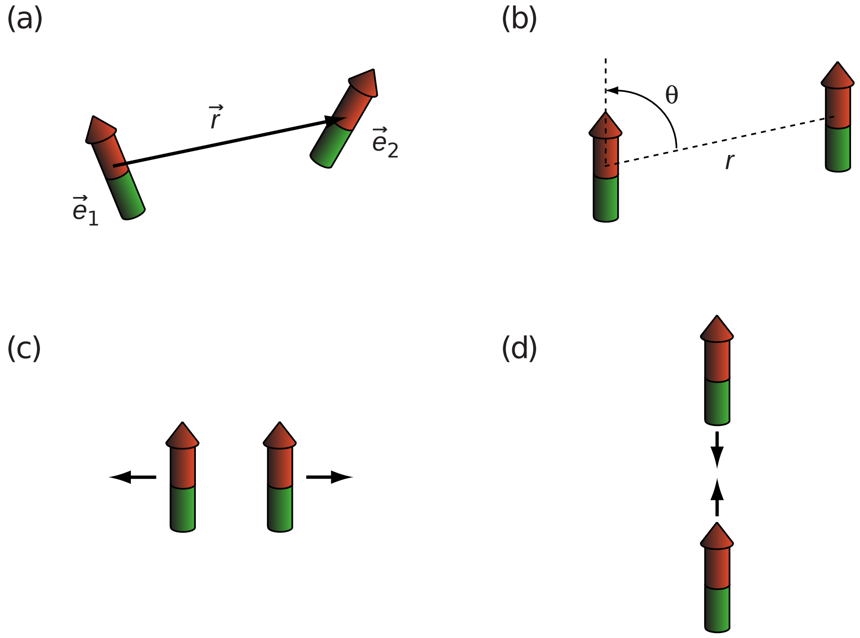

Figure 2.1: Schematic illustration of two dipoles. The distance $\mathbf{r}$ is the distance between the two dipoles, while θ is the angle between the direction in which the dipoles are oriented, and the vector describing the relative position. In configuration (c) dipoles repel each other while in configuration (d) the dipoles attract each other. Figure adapted from [Ler10].

long-range nature of dipole-dipole interactions, whereas in 1D and 2D these interactions are short range.

In the context of theoretical description of dipolar interactions as δ-interactions an alternative definition can be given that defines short-range potentials as potentials that can be described by an asymptotic phase shift. In [Ast08a] it is demonstrated that dipole-dipole interaction can be described by a short-range model in 2D, however not in 1D and 3D. Hence it depends on the investigated phenomenon whether dipolar interactions are long or short range.

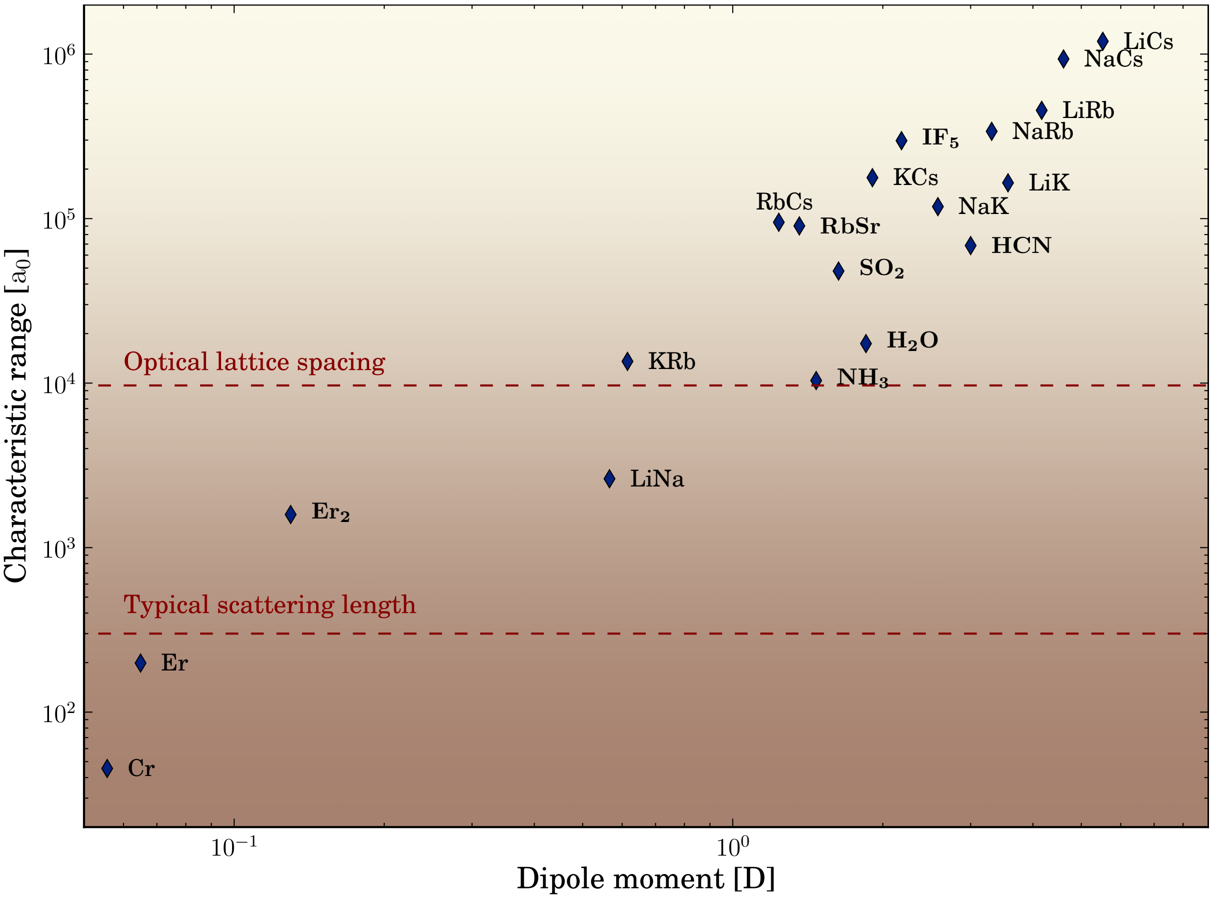

Figure 2.2: Characteristic dipole length of various dipolar species. The characteristic dipole length a_d is given in units of Bohr radii a_0 and the dipole moment is plotted in units of Debye. For magnetic dipoles equivalent electric dipole moment is plotted.

In dipolar systems not only the long distance behaviour of the interactions differs considerably from the standard atomic case, but also the size of the interaction itself. In an analog way to the atomic scattering length a dipolar length[1]

$$a_\mathrm{d} = \frac{m\mu^2}{4\pi\epsilon_0\hbar^2} \tag{2.9}$$

---

[1] Different definitions and a different nomenclature can be found for the dipolar length scale in literature. The definition in this dissertation follows the one in [Bar12]. In [Boh09] a similar definition of a dipole length $D = a_\mathrm{d}/2$ is given, which differs in the fact that it uses reduced masses (which for identical dipoles accounts for a factor of two). Yet another definition $a_\mathrm{dd} = a_\mathrm{d}/3$ differs by a factor of three and is motivated by the desire to account for the factor of three appearing in the definition of $\epsilon_\mathrm{dd} = a_\mathrm{dd}/a = a_\mathrm{d}/3a$[Lah09].

and a corresponding energy scale

$$E_{\mathrm{d}} = \frac{8\mu^2}{4\pi\epsilon_0 a_{\mathrm{d}}^3} = \frac{8\hbar^6(4\pi\epsilon_0)^2}{m^3\mu^4} \tag{2.10}$$

can be defined.[2] In the above definitions m is the mass of the molecule, μ is the dipole moment and ϵ_0 is the electric constant. In order to give an intuitive overview, the dipole length for different dipolar species is illustrated in Fig. 2.2.

In [Boh09] the definition of the dipole length $D = a_{\mathrm{d}}/2$ is motivated by a simplification of the Schrödinger equation for a pair of polarized dipoles with reduced mass M:

$$\left[\frac{\hbar^2}{2\,\mathrm{M}}\nabla^2 + \langle\mu_1\rangle\langle\mu_2\rangle\frac{1-3\cos^2\theta}{\mathrm{R}^3} + V_{\mathrm{SR}}\right]\psi = E\psi. \tag{2.11}$$

Here V_{SR} represents the short-range physics and is sometimes replaced by a boundary condition. By recasting $r = R/D$, $\epsilon = E/E_{\mathrm{d}}$ and ignoring short range physics Eq. (2.11) simplifies to

$$\left[\frac{1}{2}\nabla^2 + \frac{2C_{20}}{r^3}\right]\psi = \epsilon\psi, \tag{2.12}$$

where $C_{20}(\theta,\phi) = (3cos^2\theta + 1)/2$ is the standard reduced spherical harmonic. This makes the problem independent of the mass and the dipole moment.

The definition of the dipole length $a_{dd} = C_{\mathrm{dd}}m/12\pi\hbar^2 = a_{\mathrm{d}}/3$ given in [Lah09] is motivated by the description of inter-particle interactions in the ultracold regime, which govern most of the properties of quantum gases. Since a large theoretical framework exists for non-dipolar species, theories for dipolar systems are frequently adapted from and compared to theories for isotropic systems. In this context the parameter ϵ_{dd} is frequently used. This parameter describes the ratio of the dipole length and the scattering length

$$\epsilon_{\mathrm{dd}} = \frac{C_{\mathrm{dd}}}{3g} = \frac{1}{3}\frac{a_{\mathrm{d}}}{a} = \frac{a_{\mathrm{dd}}}{a}. \tag{2.13}$$

It measures the strength of the dipole-dipole interaction relative to the short-range repulsion described by the scattering length a. For the dipole lengh a_{dd} the parameter ϵ_{dd} becomes a simple ratio of the dipole length and the scattering length. The definition of the characteristic parameters for dipolar interactions allows to sketch how the dipolar interactions are included into the theoretical framework and to give a short example how dipolar interactions affect phenomena in ultracold quantum gases.

Gross-Pitaevskii equation for dipoles

For bosonic dipolar quantum gases the Gross-Pitaevskii equation is extended by an additional term $\Phi_{\mathrm{dd}}(\mathbf{r},t)$ that describes the dipolar interaction. It then reads [Yi00, Yi01]:

$$i\hbar\frac{\partial}{\partial t}\Psi(\mathbf{r},t) = \left[-\frac{\hbar^2}{2m}\nabla^2 + g|\Psi(\mathbf{r},t)|^2 + V(\mathbf{r}) + \Phi_{\mathrm{dd}}(\mathbf{r},t)\right]\Psi(\mathbf{r},t). \tag{2.14}$$

The dipolar contribution to the meanfield potential is given by

$$\Phi_{\mathrm{dd}}(\mathbf{r},t) = \int |\Psi(\mathbf{r}',t)|^2 V_{\mathrm{dd}}(\mathbf{r}-\mathbf{r}')d^3\mathbf{r}'. \tag{2.15}$$

---

[2] This definition follows the definition in [Boh09] but uses SI units and our dipole length a_{d}

The above equations set the framework for the description of the elementary effects in dipolar quantum gases. Similar to the non-dipolar gases, for interacting dipoles a generalized pseudo potential can be defined by

$$V_{\text{eff}}(\mathbf{r}) = g\delta(\mathbf{r}) + \frac{C_{\text{dd}}}{4\pi}\frac{1-3\cos^2\theta}{r^3}, \tag{2.16}$$

where

$$g = \frac{4\pi\hbar^2 a(d)}{m} \tag{2.17}$$

corresponds to the short range part of the interaction and is parametrized by the scattering length $a(d)$. Notably for this pseudopotential the scattering length $a(d)$ depends on the dipole moment [Bar08].

An example how dipolar interactions can alter phenomena present in quantum gases is the speed of sound, which for dipoles reads as [Lim10]

$$c(\theta) = c_\delta\sqrt{1+\epsilon_{\text{dd}}(3\cos^2\theta - 1)}, \tag{2.18}$$

with sound velocity in the case of pure contact interaction c_δ defined according to

$$c_\delta = \sqrt{\frac{gn_0}{m}}, \tag{2.19}$$

for particles with a density n_0.

At this example of the sound velocity one can see some dominant aspects of dipolar quantum gases. Firstly, the effects in the dipolar case can often be described in the existing framework by adding an additional term. Secondly, the additional term can be large, for dipolar molecules increasing the strength of some effects by orders of magnitude if the dipole length a_{d} is much larger than the scattering length a. For large values of ϵ_{dd} the system would probably have to be confined to two dimensions in order to prevent a collapse. Thirdly, the velocity of sound is anisotropic as a result of the dipolar interactions.

2.2 Scattering properties

It is not only the strength of interactions that can vary. As scattering processes are determined by the ratio of the inter-particle potential and other contributions like a rotational barrier, dipole interactions can change physics much more than just varying the magnitude of the scattering length. The scattering properties of ultracold polar molecules have been targeted by a variety of recent theoretical investigations [Tic07, Tic08, Boh09, Kot10, Que11, Tic11, Qu11].

In dipolar molecules higher partial waves are involved in scattering processes even at ultralow temperatures. This vastly differs from ultracold non-dipolar systems, where collisions are parametrized by a scattering length a_{s} and at ultralow temperatures only s-wave scattering is important[3].

For atoms at ultralow temperatures, scattering cross sections are either independent of energy or vanishing for fermions. In contrast for polarized molecules the near threshold

---

[3] apart from fermionic systems where s-wave scattering is forbidden

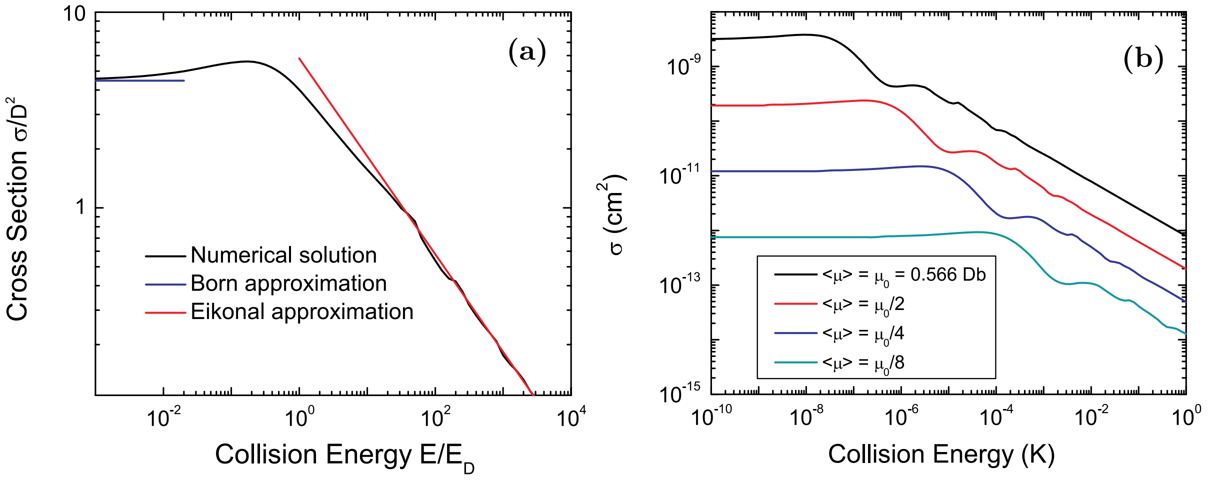

Figure 2.3: Graph (a) shows the total scattering cross section σ, averaged over all incident directions, for two distinguishable polarized dipoles. The units are scaled with the characteristic dipole length a_{dd} and the corresponding energy E_{D}. Graph (b) shows the elastic cross section of pairs of fermionic ${}^{40}\mathrm{K}^{87}\mathrm{Rb}$ molecules in identical internal states, averaged over incident directions for different values of the dipole moment μ. Figure adapted from [Boh09].

scattering is approximately determined by the dipole length a_{dd}. The threshold cross-section is set by the dipole length $\sigma \sim D^2$ and the scattering of two dipoles is nearly universal [Boh09]. The threshold below which higher partial waves only contribute perturbatively is given by $E_{\mathrm{D}} = \mu^2/(4\pi\epsilon_0 {\mathrm{a}_{\mathrm{dd}}}^3) = 16\pi^2\epsilon_0^2\hbar^6/(\mathrm{M}^3\mu^4)$ and can be extremely low.

In a cold regime, where the temperature is low enough for rotations to freeze out, but higher than E_{D}, the cross section scales as $\sigma \sim \mathrm{a}_{\mathrm{dd}}/\mathrm{K}$, where K is the wavenumber of the relative motion. In this region the deBroglie wavelength is smaller than the dipole length scale $2\pi/K < D$ or $E > \pi^2 E_{\mathrm{D}}$. For scattering many partial waves contribute and the scattering for aligned molecules can be treated semiclassically. An eikonal ansatz leads to a determination of the scattering cross section of $\sigma = 8\pi a_{\mathrm{dd}}/3K$.

For RbCs, having a large mass, E_{D} can be as low as $E_{\mathrm{D}}/k_{\mathrm{B}} = 0.7\,\mathrm{nK}$ for completely polarized molecules. Hence higher partial waves contribute to scattering even at ultralow temperatures. If the molecules are only polarized to 10% of their maximum value, the threshold temperature is at $E_{\mathrm{D}}/k_{\mathrm{B}} = 7\,\mu\mathrm{K}$. In this case the scattering cross section would be independent of the energy in the ultracold regime.

A graphical representation of the dependency of the cross section on the collision energy is given in Fig. 2.3. The curve on the left is universal as long as the scattering length is negligible. On the right hand side the behaviour of the cross section for different strengths of polarization is depicted.

2.3 Dipolar molecules in an electric field

In their ground state dipolar molecules do not show any dipole moment as the wave function is rotational symmetric. A net dipole moment can therefore only arise through an admixture of higher angular momentum states. For molecules in the ground state

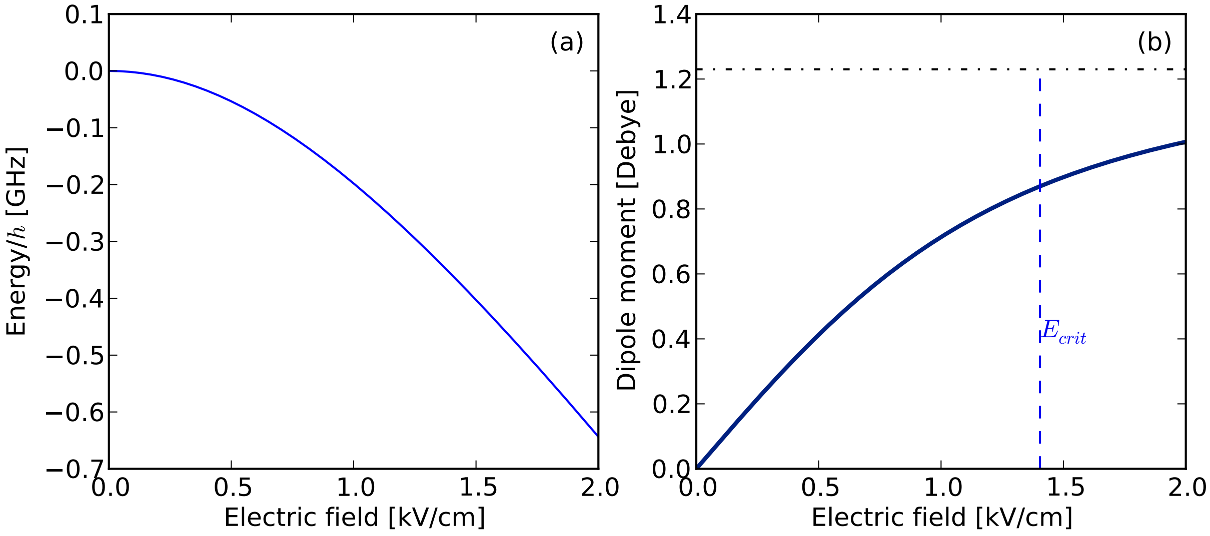

Figure 2.4: Stark shift (a) and dipole moment (b) of RbCs plotted against the electric field. The horizontal dashed line shows the dipole moment of RbCs when completely polarized. The vertical dashed line indicates the electric field E_{crit} at which the energy of the dipoles in the electric field equals the rotational energy splitting B_ν.

in small electrical fields, when the Stark shift is less than the rotational splitting, it is sufficient to consider only admixtures from the first rotational state. If the electronic state further is a Σ state, which is the case for the RbCs ground state, the Hamiltonian of the system can be expressed as:

$$H = \begin{pmatrix} -E_{\text{rot}}/2 & -\mu\mathcal{E} \\ -\mu\mathcal{E} & E_{\text{rot}}/2 \end{pmatrix}, \tag{2.20}$$

where μ is the dipole matrix element, $\mathcal{E}$ is the electric field and $E_{\text{rot}} = 2B_\nu$ is the rotational energy splitting [Boh09]. The energy eigenvalues are given by $E = \pm\sqrt{E_{\text{rot}}^2/4 + (\mu\mathcal{E})^2}$. From this model a quadratic behaviour of the stark shift for small fields and a linear behaviour for large fields can be deduced. Further a critical field

$$E_{\text{crit}} = E_{\text{rot}}/2\mu \tag{2.21}$$

can be defined at which the molecules are polarized to a factor of $\sqrt{1/2}$.

As can be seen in Fig. 2.4 the energy shift for molecules in an electrical field can be more than several hundreds of MHz. This implies that the shift could be easily measured by spectroscopic means. This has been done for dipolar molecules including LiCs and KRb [Ni08, Dei10].

In table 2.1 an overview the of properties relevant to dipolar physics is given for the alkali dimers. Notably, the characteristic dipolar energy for most of them lies below 100 nK when they are completely polarized. As the temperature of ultracold quantum gases is typically on the order of 100 nK this implies that a regime can be reached where higher partial waves contribute even in the ultracold regime.

	$B_\nu(\times 10^{-2}\text{cm}^{-1})$	d_ν(Debye)	E_{crit}(kV/cm)	$a_{\text{dd}}(\times 10^3 a_0)$	E_{dip}/k_B(nK)
RbCs	2.90	1.24	1.4	95	7.0×10^{-1}
KCs	3.10	1.91	1.0	177	2.5×10^{-1}
KRb	3.86	0.61	3.7	14	5.9×10^{1}
NaCs	5.93	4.61	0.8	934	1.0×10^{-2}
NaRb	7.11	3.31	1.3	339	1.1×10^{-1}
NaK	9.62	2.58	2.2	118	1.6×10^{0}
LiCs	19.40	5.52	2.1	1196	7.0×10^{-3}
LiRb	22.00	4.17	3.1	455	7.2×10^{-2}
LiK	26.10	3.56	4.4	165	1.1×10^{0}
LiNa	38.00	0.57	40.0	3	7.0×10^{3}

Table 2.1: Summary of ground-state properties of mixed alkali pairs for their orientation in electric field. B_ν is the rotational splitting, d_ν is the dipole moment when completely polarized, E_{crit} is the field needed to get about 70% orientation, a_{dd} is the dipole length given in units of Bohr radii and E_{dip} is the characteristic dipolar energy for complete orientation. (The data is taken from [Dei08a].)

2.4 Optical lattices

Optical lattices are a key element in many experiments and have played a major role in a variety of ground breaking discoveries [Blo08]. They allow the realization of model systems from condensed matter physics [Mor06]. Major highlights include the quantum phase transition from a superfluid to a Mott insulating phase for bosons [Gre02] and fermions [Sch08, Jör08] in three dimensional systems. In this Mott insulator phase strong on-site interactions inhibit tunneling processes and therefore transport through the lattice. The realization of the strongly correlated Tonks-Girardeau gas [Kin04, Par04], the observation of an excited, strongly correlated quantum gas phase [Hal09] and the measurement of a pinning quantum phase transition for a Luttinger liquid of strongly interacting bosons [Hal10] were major accomplishments. The creation of a quantum gas microscope that allows to detect single atoms in an optical lattice [Bak09] and the investigation of the transition from a superfluid to an insulating phase at the single atom level [Bak10] demonstrate the amount of control that can be achieved with optical lattices.

Optical lattices and systems with reduced dimensionality play a major role in most theoretical proposals for strongly interacting dipoles [Bar12, Lew07, Car09]. The suppression of losses in a two-dimensional dipolar system [Mir11] underlines the importance of optical lattices for dipolar systems. The simulation and implementation of quantum magnetism models [Bar06] is one of the major challenges in the near future. Systems with reduced dimensionality can be as well created by other means such as evanescent wave traps [Ham03, Ryc04]. However, optical lattices are preferred by many experimentalists due to the almost perfect decoupling from the environment and the well controlled optical potential [Orz01, Had06]. For the realization of model systems from condensed matter systems periodic potentials that are generated by optical lattices are essential. A broad variety of experiments and models relies on a combination of reduced dimensionality with an additional overlaid lattice along th non-confined directions [Spi07, Stö04, CS10, Bar12].

A standard way to create optical lattices is to use counter propagating light beams. Theses create a standing wave, which results in a periodical variation of the intensity. In optical traps the trapping potential is proportional to the intensity (see section 3.2.2). Hence the periodic variation of the intensity leads to a periodic trapping potential. If one standing light wave is used the lattice is called 1D optical lattice. The particles are confined in one dimension and can freely move in the other dimensions. The three dimensional space is split up in a series of pancake shaped traps. Accordingly, the physics that takes place at each site can be described by effective two dimensional models.

If two crossed standing waves are used a 2D lattice is created. Particles are confined to cigar-shaped effective one-dimensional tubes. Therefore in a 2D lattice 1D physics can be investigated. For strong 1D or 2D lattices, transfer of particles from one lattice site to an other is strongly suppressed. Hence, tunneling is frequently ignored in models describing 2D and 1D physics of ultracold quantum gases. If three orthogonal standing waves are used, the lattice is called a 3D optical lattice, and the particles in the lattice are ideally confined to single points in space. For a strong lattice, when the particles are well isolated and interaction with neighbouring traps is negligible, the situation of an isolated particle at a single point in space is trivial. Interesting physical phenomena occur mostly when particles in neighbouring lattice sites can interact for example through tunneling or dipolar interactions.

Theoretical models distinguish between physics in optical lattices in the narrow sense of the word and physics in reduced dimensions, where the lattice is only used to create low dimensional systems, which could also be created otherwise. The latter is frequently described by a formalism similar to the corresponding three-dimensional system. Physics in optical lattices depends on the periodicity of the potential. For shallow lattices it is frequently described in terms of delocalised Bloch functions [Blo29]. For deep lattices, Hubbard models [Hub63], which use so-called Wannier functions, provide a clear and concise description of the physics. Neighbouring lattice sites are coupled via a nonzero tunneling rate J, which allows the particles to tunnel from one site to another. Interactions with particles occur via an on site interaction U, which describes the energy shift that occurs when two particles are at the same lattice site. The Hamiltonian in a Hubbard model for bosons, the standard Bose-Hubbard model, is given by [Jak05]

$$\hat{H} = -J \sum_{\langle i,j \rangle} \hat{a}_i^\dagger \hat{a}_j + \sum_i \frac{U}{2} \hat{n}_i (\hat{n}_i - 1) + \sum_i \epsilon_i \hat{n}_i, \tag{2.22}$$

where ϵ_i describes a (typically weak) external potential; $\hat{a}_i$ and $\hat{a}_i^\dagger$ are bosonic creation and annihilation operators; $\hat{n}_i = \hat{a}_i^\dagger \hat{a}_i$ and $\langle i, j \rangle$ denotes the sum over nearest neighbours. For dipolar molecules the Hamiltonian is extended in order to include dipolar interactions. Many model systems for dipoles in optical lattices are maily based on the $1/r^3$ behaviour of the dipolar interactions and assume a two dimensional geometry with the dipoles aligned perpendicular to the plane. For this situation the Hamiltonian reads [CS10]

$$\hat{H} = -J \sum_{\langle i,j \rangle} \hat{a}_i^\dagger \hat{a}_j + \sum_i \frac{U}{2} \hat{n}_i (\hat{n}_i - 1) + V \sum_{i<j} \frac{\hat{n}_i \hat{n}_j}{r_{ij}^3} + \sum_i \epsilon_i \hat{n}_i, \tag{2.23}$$

where V describes the dipole-dipole interaction strength and $r_{i,j} = |i - j|$. For strongly interacting dipoles the onsite interaction can be so strong that doubly occupied sites do not exist. Hence for some models the onsite interaction is omitted. This Hamiltonian allows for the investigation of a variety of novel quantum phases. Namely the strong next neighbour interactions created by the dipole-dipole interaction clearly destinguishes physics with strongly interacting dipoles from physics with non-dipolar atoms.

Quantum phases in optical lattices

While for bosons, in the presence of a single species interacting via on-site interaction, the phase diagram presents only superfluid (SF) or Mott insulating (MI) phases, for long-range interaction or multiple species, a variety of novel exotic phases appear [Bar12]. Supersolidity (SS), which is a phase with coexistence of superfluidity and of a periodic spacial modulation of the density, different from the one of the lattice [Bru93], is a phenomenon that has long intrigued physicists [Pen56] and remains controversial in translationally invariant systems [Leg70]. In lattice models, theoretical studies confirm that SS ground states can exist [Bat95, Bat00, Héb01] and are thermodynamically stable [Sen05]. Depending on the relative values of the nearest neighbour and the next-nearest neighbour interaction the gas can order itself in a checkerboard (CB), a star (SR) or a striped solid (ST) pattern [Héb01].

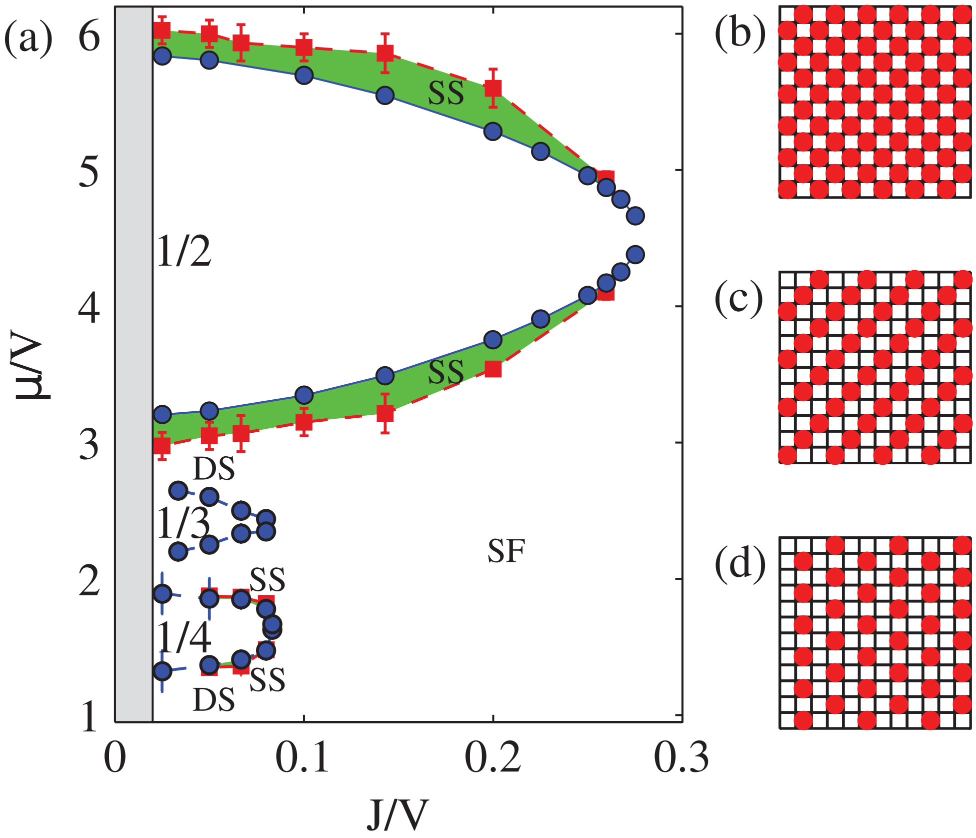

Figure 2.5: Typical phase diagram (a) for dipoles confined in a 2-dimensional lattice geometry. An orientation of the dipoles perpendicular to the plane leads to isotropic long range interactions in the 2D system. The chemical potential μ and the tunneling energy J are given in relation to the dipole-dipole interaction strength V. The calculations are based on Monte-Carlo methods. In contrast to conventional atomic phase diagrams a novel super-soild phase (SS) arises, which would be interesting to be observed. Graphs (b-d) show sketches of the ground state configuration for the Mott solids, which are the checkerboard, striped and star solid pattern, with fractional fillings of $\rho = 1/2$, $1/3$, and $1/4$. Figure taken from [CS10].

Due to their tunable long range interaction dipolar molecules form an ideal model system to observe these states. As recently predicted [CS10, Pol10], some of these phases should be observable in a temperature and density regime that could be reached with dipolar molecules. Especially super-solid phases have been intensively investigated by theoretical studies [Dan09a, Dan08a, CS10, Pol10, Yi07, Sen05, Kim04, Bat00, Bat95, Bru93]. On square lattices super-solid phases have been predicted for hard-core bosons (infinitely large U) with nearest-neighbor (NN) and next-nearest-neighbor (NNN) interactions for fractional fillings of $0.25 < \rho < 0.5$ and for soft-core bosons (finite value of $U > J$) with NN and $\rho > 0.5$.

A typical phase diagram for dipoles based on Monte-Carlo methods is shown in Fig. 2.5. While small parameter regions for some of the phases, as well as the necessary low temperatures constitute a challenge for experimentalists, the phases as such are manifest in distinct spacial density profiles, which can be observed directly in ultracold quantum gases. This allows an isolated observation of the distinct phenomena, which is not the case for experiments in solid He [Kim04], where the first observation of a supersolid was heavily debated. Furthermore the existence of supersolid without an underlying lattices structure is discussed controversially [Bar12] and could more clearly be investigated in systems without a crystalline structure.

2.5 Dipolar molecules in reduced dimensions

Strongly correlated dipolar quantum gases in reduced dimensions, namely in 2D, can be used to explore a variety of fundamental phenomena ranging from the formation of self-assembled dipolar crystals to exotic phases such like spin liquids [Bar12]. The regime of strong correlations between particles is reached when the strength of the inter-particle interactions becomes larger than the average kinetic energy. The relevant dimensionless parameter describing the strength of the interactions is

$$r_{\mathrm{d}} = \frac{E_{\mathrm{pot}}}{E_{\mathrm{kin}}} = \frac{d^2/a^3}{\hbar^2/ma^2} = \frac{a_{\mathrm{d}}}{a}, \tag{2.24}$$

which is the ratio of the interaction energy and the kinetic energy at the mean inter-particle distance a.

If the particles are confined in a 2D plane as depicted in Fig. 2.6, the dipole-dipole interaction is repulsive and a phase transition to the crystalline phase can occur [Mic07]. The phase-transition occurs at values of $r_{\mathrm{d}} = 20$, which means that in a dipolar crystal the inter-particle distance is at least a factor of 20 smaller than the dipole length a_{d}. For some dipolar molecules the dipole length is so large that the inter-particle distance in a crystal is larger than the typical inter-particle distance in an optical lattice. For these molecules a quantum-gas microscope that is capable of resolving individual lattice sites could also resolve individual particles in a self assembled cristal. Furthermore, the densities of a typical[5] ultra-cold molecular experiment would allow to observe the transition from a

---

[4] While in many theoretical treatments of weakly interacting dipolar particles a dipolar length scale is compared to the scattering length, the naming scheme varies for different authors. The signifier a is not connected in any way to the scattering length in this case.

[5] Typical densities are on the order of $8 \times 10^{12}\,\mathrm{cm}^{-3}$. This is particularly the case if a Mott insulator is involved in the strategy for pairing individual atoms to form molecules as is discussed below.

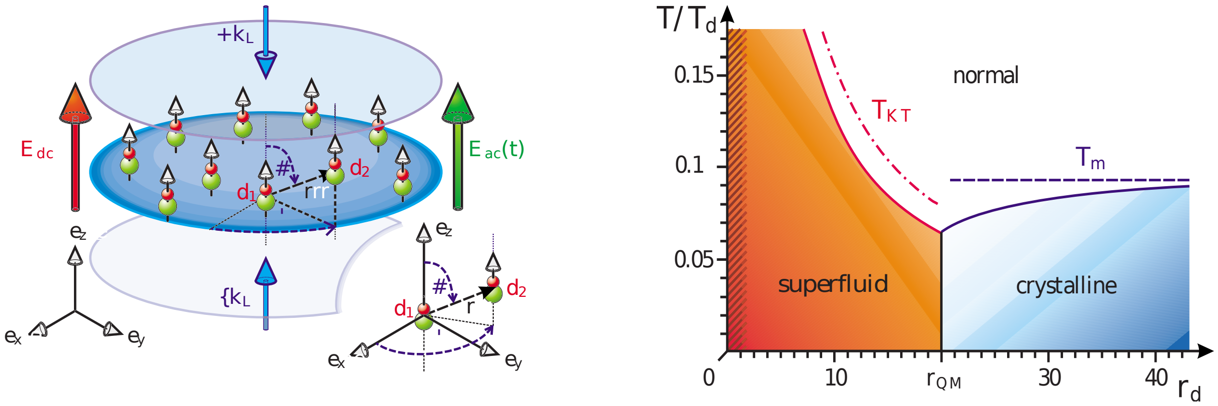

Figure 2.6: Cold polar molecules trapped in a plane by a 1D optical lattice (left). The dipoles are aligned by an electrical field E_{dc} and the dipole-dipole interaction can be tuned by a microwave field E_{ac} (for details see Refs. [Mic06, Mic07]). The angles θ and ϕ describe the orientation of the field with respect to the plane. The graph on the right hand side shows a phase diagram. A phase transition from a superfluid to a crystalline phase occurs when $r_{\mathrm{d}} = a_{\mathrm{d}}/a$ increased above a critical value. In this case a denotes the average inter-particle distance^4. T is the temperature in units of $T_{\mathrm{d}} = C_3/k_B a^3$, with $C_3 = \mu^2/4\pi\epsilon_0$ for electric dipoles. The melting temperature T_m has been calculated in [Büc07a]. Figure adapted from [Mic07].

superfluid to a crystalline state when the dipole length is increased from zero to its maximum value.

If the dipoles are not oriented orthogonal to the plane a crystalline stripe phase can occur [Mac12]. For a sufficiently large dipole length this crystalline stripe phase could be directly observed in the pair distribution function. Further studies in two dimensional (2D) systems include collective modes of a fermionic dipolar liquid [Li10], interlayer superfluidity [Pik10], self-assembled dipolar lattices [Pup08], and dimerisation [Pot10]. In one dimensional (1D) systems or quasi 1D systems the phase diagram for dipoles features novel states including linear, zigzag and multiple chain phases [Ast08b].

The vast range of interesting new phenomena that occur for dipolar molecular quantum gases is founded on the long-range character and the anisotropy of dipolar interactions. There are various novel effects and quantum states predicted, especially in the strongly interacting regime, which is difficult to be reached witch magnetic dipoles. Many of the novel phases rely on reduced dimensionality, periodic lattice structures, or both. Hence confinement of the dipolar quantum gas in an optical lattice is an essential ingredient in experiments with dipolar quantum gases.

2.6 Possible applications of dipolar quantum gases

The possibility to control polar molecules via electrical fields has triggered some interest in the use of ultracold polar molecules for quantum computing [DeM02, And06]. In the first scheme proposed by DeMille dipolar molecules are held in a standing optical wave. The individual qbits represented by the molecules are addressed spectroscopically and selected via an electric field gradient. Soon after, more elaborate schemes for quantum computing were proposed including the ones by Yelin *et al.* [Yel06]. In this schemes the individual qubits are selected by spacially constrained mechanisms as shown in Fig. 2.7. Furthermore the coupling of the dipolar qubits to other quantum devices could be achieved

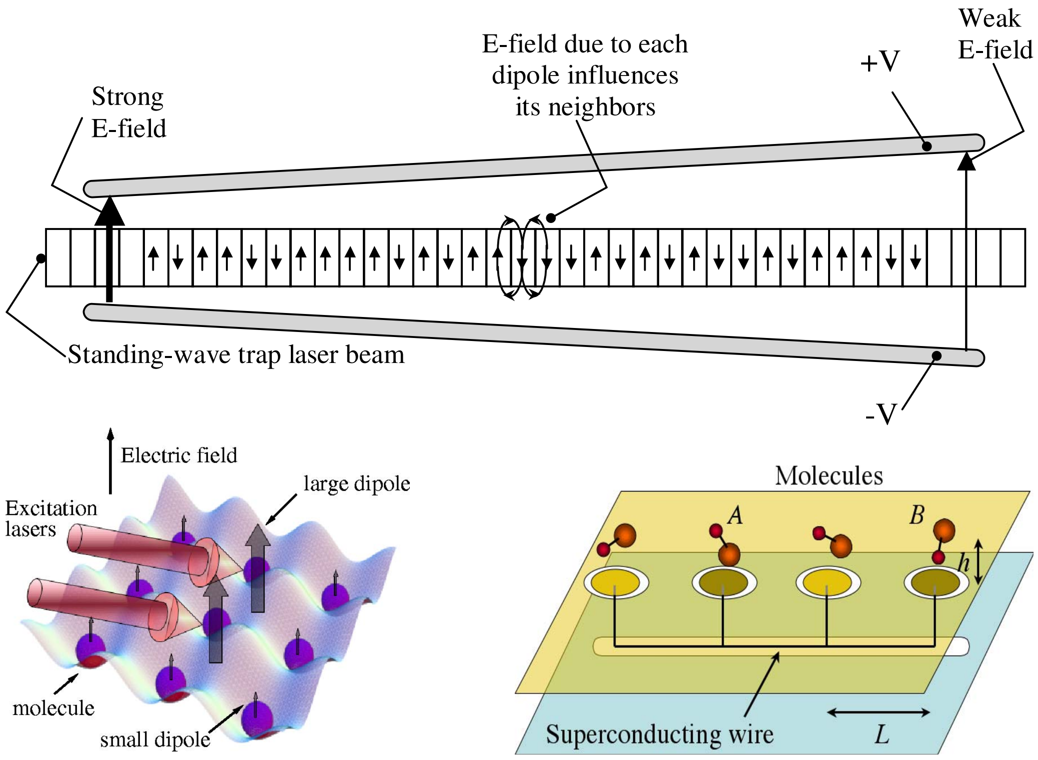

Figure 2.7: Different quantum computing schemes. In the scheme on top an electric field gradient allows the selection of single molecules. An extremely tight focussed laser beam would allow single site addressing in the scheme bottom left. The addressing in the scheme on the bottom right is done via a fine electric structure on a chip. Figures adapted from [DeM02, Yel06].

by trapping polar molecules at short distances from a superconducting transmission line. This greatly enhances the coupling of the molecular rotational transitions to microwave radiation [And06]. This can also be used for the creation of hybrid quantum computers [Rab06, Rab07]. While quantum computing certainly is not our prime goal, the proposals show, that the insight gained with dipolar molecules is also valuable for related fields.

Chapter 3

Ultracold molecules

Cold and ultracold molecules have captivated the interest of scientists for more than a decade [Bah00]. Outstanding achievements in the field such as the creation of a BEC of weakly bound molecules [Joc03a, Gre03, Zwi03] and the creation of a quantum gas of ground-state molecules [Dan08b, Ni08, Lan08] led to a vibrant activity in the field. The wide spectrum of the field and the various different approaches to generate cold molecules is covered by a broad variety of excellent review articles [Ulm12, Qué12, Nes12, Koc12, Jin12, Hut12, Dul06, Dul09, Car09, Fri09, Chi10].

An ensemble of cold molecules can either be created from hot molecules (direct methods) or by creation of molecules from an ensemble of already cold atoms (indirect methods). The direct methods can further be distinguished into slowing, selection and cooling methods. Slowing and selection methods [Sch09, Mee12, Nar12] do not increase the phase-space density of the samples as they do not include dissipation. Direct cooling methods such as laser cooling of molecules as well as buffer gas or sympathetic cooling [Hut12] and evaporative cooling can lead to an increase in phase-space density and are cooling methods in the proper sense. The indirect methods mainly use photoassociation [Koc12, Ulm12] or Feshbach association [Köh06], which is followed by a coherent STIRAP ground-state transfer. The indirect approach allows to draw on the methods well established for cooling of atomic species. Many experiments target heteronuclear molecules which involves the creation of an ultracold mixture of different species. By mixing two atomic species and associating pairs of atoms into a dipolar molecule the researcher enters an unknown territory hiding a lot of surprises and challenges.

The cooling method used depends on the molecules and temperatures needed for the particular investigation. Methods such as buffer gas cooling are applicable to cool a wide range of species to temperatures in the mK regime. This allows studying the properties of biologically or chemically relevant molecules. In contrast experiments associating molecules from ultracold samples of atoms are dedicated to a specific combination of species but yield much colder samples. In these kinds of experiments the number of species is limited to the ones that can be laser cooled and they rather target fundamental questions like properties of dipolar quantum gases [Bar08], quantum computing [DeM02] or the electron dipole moment [Tar09]. For the creation of dipolar quantum gases temperatures below $1\,\mu$K and densities on the order of $10^{13}\,\mathrm{cm}^{-3}$ have to be reached.

An overview of the methods (see table 3.1) shows the broad variety of species cooled by the various methods. The methods targeting the ultracold regime mainly focus on dimers since for dimers the molecular properties can be calculated up to a high precision and are considerably well understood. Alkali combinations are the main candidates for the indirect methods, since for these laser cooling schemes are well established. The temperatures reached with the indirect methods are far below the temperatures that are currently reached with direct methods. Due to the large variety of interesting phenomena predicted for dipolar molecules, heteronuclear dimers are currently at the centre stage.

The more general direct methods yielding higher temperatures target larger molecules as well as dimers. While the larger molecules are interesting for molecular reactions and investigation of their structure, dimers are often used in proof-of-principle experiments. The creation of a complicated source is avoided in the latter case by using molecules that are in the gas phase at room temperatures. For some fundamental physics tests methods yielding warmer molecules can outperform other cooling methods due to their higher flux rates. Yet another application is the possible use as a pre-cooling step, which is followed by sympathetic cooling, evaporational cooling, or even direct laser cooling.

Table 3.1: Overview of cold molecules, production methods, temperatures, and approximate numbers. If no reference is given, the data is from [Sch09].

Method	Molecule	T or v	N
photoassociation	Rb_2 , Cs_2 , He_2^* , Li_2 , Na_2 , K_2 , Ca_2 , KRb , RbCs , NaCs , LiCs , LiRb	30 μK	10^5
Feshbach association	Li_2 , Na_2 , K_2 , Rb_2 , Cs_2 , KRb , RbCs[1], NaK[2], LiK[3], LiNa[4]	$< 1\mu$k	10^5
STIRAP ground state	Rb_2[7], Cs_2[6], KRb[5], RbCs[1]	$< 1\mu$K	
optical deceleration	C_6H_6 , NO		
Stark deceleration and trapping	$^{14}NH_3$, $^{15}NH_3$, $^{14}ND_3$, CO* , OH , OD , NH* , SO_2 , YbF , H_2CO , C_7H_5N	5 mK	10^6
Zeeman deceleration	O_2	$50 ms^{-1}$	
velocity filters	H_2CO , ND_3 , S_2 , D_2O	1 K	10^9/s
buffer gas cooling	CaH , CaF , VO , PbO , NH , ND , CrH , MnH	400mK	$> 10^8$

[1] this work [2] [Wu12] [3] [Voi09, Spi10] [4] [Heo12] [5] [Ni08] [6] [Dan08b] [7] [Lan08]

In this chapter I will first outline the direct methods for creation of ultracold molecules. This is followed by a detailed description of our method of creating ultracold molecules from an ensemble of cold atoms. In our scheme the molecules are associated from ultracold mixtures. Therefore the physics and creation of mixtures is described in more detail in section 3.2. The next section describes methods to associate pairs of atoms into molecules and the chapter terminates with a short outline of the basic quantum numbers and properties of ultracold molecules.

3.1 Cooling methods

Slowing of supersonic beams

Starting from a supersonic expansion or a pulse of buffer-gas cooled molecules, molecules with an electric dipole moment can be decelerated using a Stark decelerator [Bet99]. Subsequent electrostatic trapping [Win80] yields a sample of cold molecules in the sub-K regime [Bet00], which can be a good starting point for further cooling and also increases measurement timescales for molecular spectroscopy or studies of reactional properties. The method relies on a permanent electric dipole moment of the particles that are trapped and slowed in a comoving electrostatic or quasi electrostatic trap. A variety of molecules has been slowed and trapped including NO, NH^3 NH and OH [Mee05, van08, Rie11].

Liouville's theorem ensures that the phase-space density is preserved under Hamiltonian evolution. As there is no dissipative force involved in Stark deceleration, the phase-space density is at best conserved and is determined by the properties of the source. Being applicable to a wide class of molecules this method complements supersonic expansion and transfers the cold cloud from moving at a high velocity to a cold cloud being at rest in the laboratory frame. Using the magnetic moment molecules can also be slowed by a moving magnetic trap [LO11] or with a series of pulsed magnetic coils [Nar08]. The topic of slowing supersonic beams by inhomogeneous fields is reviewed in [Hog11]. Furthermore

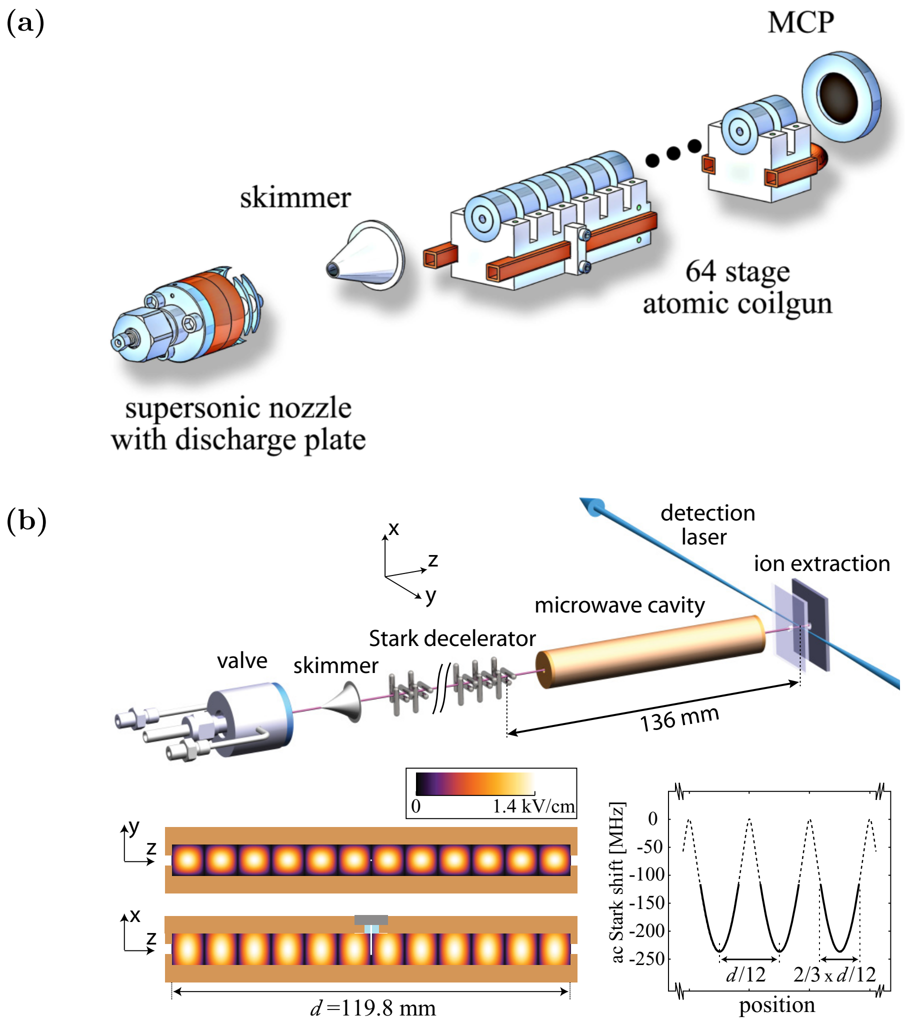

Figure 3.1: Schematic drawings of a magnetic slowing (a) and a Stark decelerator (b) apparatus. The picture bottom right shows the trapping potentials in a false color plot. (Pictures adapted from [Mer12, Nar08].)

the slowing approaches can be extended to microwave and optical fields [Mer12, R.06].

Billards like collisions

An internally cold but fast moving sample of molecules can be brought to rest by collision with a suitable colliding partner. This technique has been successfully applied to NO molecules colliding with Argon [Eli03]. This method is like other slowing methods limited by the velocity spread or internal temperature of the initial cloud. The temperatures and densities fall into the same cold region as most methods above.

Velocity selection

If molecules are available in a large amount, selection methods, which select the slowest molecules of a thermal distribution, can be a simple, effective and universal way to produce cold molecules. These can be loaded subsequently into e.g. an electrostatic trap [Win80, Rie05, Jun04b, Jun04a]. Velocity selection differs from evaporative cooling by the fact that no or little thermalisation occurs. Molecules are not cooled and the phase-space density is not increased. This method is applicable to a broad range of molecules and therefore it can be useful for investigation of molecular structure or controlled chemical reactions. However, the achievable densities and temperatures are up to now far from the range targeted in ultracold quantum gas experiments.

Buffer-gas and sympathetic cooling

Buffer-gas cooling is most closely related to our classical understanding of cooling. Similar to the cooling process in a fridge, the molecules to be cooled exchange energy with a coolant, which is cooled by other means. One example would be a buffer-gas loaded magnetic trap [deC99]. In this case the temperature is limited by the temperature of the coolant, which can reach down to the ultracold regime. One drawback is the possibility of inelastic collisions between the coolant and the particles to be cooled. Inelastic collisions can be reactive collisions in which the two colliding particles chemically react and different molecules are created. Another possibility of inelastic collisions are collisions that change the internal energy of the particle. In the case of magnetically trapped particles a change in the internal state of the particle usually leads to a change in the magnetic properties of the particle. As a result the particles are not trapped anymore and expelled from the trap. If the particles are initially prepared in a well-defined internal state with an energy higher than the thermal energy of the sample, an inelastic collision in which energy is released can lead to a heating of the sample. If the internal energy is higher than the depth of the confining potential, the energy released in an inelastic collision allows the particles to escape from the trap. For sympathetic cooling the rate of elastic to inelastic collisions is an important criterion.

Sympathetic cooling however, is observed down to the ultracold regime [Mya97, Mud02], and could be used as a cooling step at any stage. However, the coolants differ depending on the temperature regime. While in the Kelvin regime Helium is a favourite coolant, in the ultracold regime sympathetic cooling between different laser cooled atoms or isotopes is observed. In the case of RbCs, ground-state molecules could be cooled with ultracold Cs atoms, because endothermic reactions freeze out. However, reactions and the necessity to trap the molecules limit the temperature range in which this method can be applied.

Direct laser cooling

Direct laser cooling of molecules relies on the existence of cycling or quasi cycling transitions. In most molecules optical cooling by applying resonant light to an electronic transition fails due to optical pumping. This happens when an excited molecule spontaneously decays to an electronic ground state that is not resonant with the light. In some molecules however, there exists a dominant decay channel favoring one of the electronic molecular ground states over the others. The chance of decay into a specific level can be as high as 0.9999 [Wel11]. In this case one speaks of a quasi cycling transition and a large number of photons can be scattered before the molecule is pumped into another state. In this case optical cooling methods can be applied in a way similar to atoms. However, in contrast to the latter the number of lasers needed to completely close the absorption-emission cycle is typically on the order of a few dozen, but perfect efficiency is not necessary to reap the benefits of laser cooling.

It was shown by M. Di Rosa [Di 04] that monohydrides and monohalides have suitable Franck-Condon factors. Later Stuhl et al. [Stu08] showed that transitions to undesired rotational levels can be largely precluded by choosing molecular states where the ground-state rotational quantum number is higher than that of the excited states. To prevent pumping into a dark Zeeman sublevel they proposed an electrostatic remixing scheme and simulated an electrostatically remixed magneto-optical trap (ER-MOT) for the case of TiO molecules. In 2009 the group of DeMille demonstrated a scheme for an optical cycling transition in a molecular electronic transition of SrF [Shu09]. In their experiment vibrational branching is prevented to certain extent by favorable Franck-Condon factors. As the molecules are pumped from an N = 1 level to a N = 0 level they can only decay back to the initial level because the parity selection rule $\Delta P = \pm 1$ prevents decay to N $= 0, 2$ levels. Hence, most of the excited state population is decaying to the $(N = 1)$ vibrational ground state, which has four hyperfine states that are all populated. The energy splitting of these levels allows for simultaneous pumping of all levels using a single laser with sidebands created by an electro-optic modulator (EOM). This way they were able to observe cycling fluorescence and deflection of a molecular beam. The number of photons scattered from each molecule was ~ 150 in this first demonstration. It can be increased however, by adding a second repumping beam, which allowed for the demonstration of laser cooling of molecules in 1D [Shu10]. In this experiment it has been observed that Doppler and Sisyphus cooling lead to temperatures around or below 1mK in the transverse direction. As the loss rate of molecules is measured as being below the experimental reproducibility of 5% there is a good reason for assuming that, given the calculated Franck Condon factors, a large fraction of the molecules is able to scatter the ~ 40000 photons necessary to bring the molecules to rest.

Evaporative cooling

In order for evaporative cooling to work, the rate of elastic collisions should be a few orders of magnitude larger than the rate of inelastic ones. For NH Janssen *et al.* [Jan11] have shown that direct evaporative cooling of magnetically trapped molecules would be feasible since the calculated cross section for inelastic collisions is much smaller than for elastic ones. However, the inelastic cross section is increasing with decreasing temperatures and increasing magnetic fields. This makes NH a good candidate for direct evaporative cooling down to the ultracold regime. In the ultracold, however, the increasing inelastic collision rate might hinder further cooling for NH in a magnetic step. In combination with other cooling schemes evaporative cooling is certainly a viable approach to reach the ultracold regime.

Summary

Most of the methods above target a broad variety of molecules and are applied in the field of physical chemistry or chemical physics. The temperatures that can be reached, range from several mK to several K and some of the methods benefit from a high number of molecules that can be cooled. One of the key aspects is the possibility to cool different kinds of molecules with the same technique or even the same apparatus.

For ultracold quantum gas physics, the temperature range is in the sub μK regime and the phase-space density has to be on the order of unity. Further the focus of ultracold quantum physics is different. In physical chemistry focus is more on naturally occurring molecules and understanding of the structure and reactions. Therefore methods are preferred that can be used for a broad variety of molecules without major changes in the experimental apparatus. For the creation of a quantum gas of dipolar molecules the specific molecule is not important as such. Hence, it is sufficient to develop methods that can be used to cool a single type of molecule that fulfills the desired properties. Therefore, the techniques in the ultracold regime mostly are based on an apparatus dedicated to a specific molecule and frequently indirect methods are preferred since these currently yield samples with a higher phase-space density.

3.2 Creation of mixtures

Assembling dimers from mixtures of ultracold atomic quantum gases directly creates ultracold molecules and hence largely circumvents complex molecular cooling schemes. The creation of ultracold atomic quantum gases is based on established techniques. Typical cooling steps involve a MOT, which can be followed by an optical molasses, a compressed MOT, narrow line MOT, or Raman sideband cooling step before degeneracy is reached by some sort of evaporative cooling.

Most of the molecule experiments targeting the ultracold regime involve the creation of mixtures as an initial step and a large variety of mixtures has been created, including LiYb, KRb, LiCs, LiRb and LiK [Oka10, Roa02, Sim03, Kra06c, Mos01, Sil05, Wil08].

Despite the fact that all cooling steps are well understood in the single species case the generation of mixtures can be challenging due to interspecies interactions and the necessity to create a trap that features suitable conditions for both species. In the following I describe the creation of a RbCs mixture and some of the underlying physics.

3.2.1 Cooling of atoms

The creation of an ultracold atomic gas typically starts with hot atomic vapor that is cooled and loaded into a MOT by using standard techniques as described in [Met03]. For alkali atoms the melting points are typically low and heating the sample to a few hundreds of °C is typically enough to create a vapor pressure on the order of up to 10^{-4} mbar inside an oven.

	^{6}Li	^{23}Na	^{39}K	^{87}Rb	^{133}Cs
mass [u]	6.0	23.0	39.0	86.9	132.9
melting point [°C]	180.5	97.8	63.6	39.3	28.5
wavelength D_2 [nm]	671.0	589.2	766.7	780.2	852.3
natural linewidth [MHz]	5.9	9.8	6.0	6.1	5.2
saturation intensity $[\frac{\mathrm{mW}}{\mathrm{cm}^2}]$	2.5	6.3	1.8	1.7	1.1
Doppler temperature [μK]	141	235	145	146	126
recoil temperature [nK]	7072	2400	836	362	198
recoil velocity [mm/s]	99	29	13	6	4

Table 3.2: Properties of selected alkali elements. In general with increasing mass the melting point decreases and so do the temperatures required to have a certain vapor pressure. The wavelength of the cooling transitions of the alkali lie in the visible or near infrared region, accessible with diode lasers. The natural line widths and saturation intensities of the cooling transitions using circular polarized light are on the same order for all alkali elements, leading to cold atomic samples on the order of a hundred μK in a MOT. Different recoil temperatures lead to different challenges for imaging, cooling, and operating optical lattices. For the table atomic D-line data is used from the following publications [Geh03, Ste10, Tie10, Ste08a, Ste08b].

In current experiments the atoms leave the high pressure section as a collimated beam and are slowed down before they are loaded into a MOT that is situated in a low pressure environment. Slowing can be achieved either in the high pressure part of the experiment when a Pyramid MOT or a 2D-MOT is loaded directly from the background gas or by a Zeeman slower slowing the hot atoms coming out of the effusive oven. The atomic transition mostly used in MOT cooling of alkali atoms, the D_2 line, is from the $^2S_{1/2}$ state to the $^2P_{3/2}$ state. The latter state features a larger total angular momentum and for pumping into the largest magnetic sub-level creates a closed optical cycle.

In a classical MOT the photon recoil heating on one hand and the velocity dependent cooling force on the other hand balance at a certain energy distribution corresponding to the Doppler temperature,

$$T_{\mathrm{D}} = \frac{\hbar\Gamma}{2k_{\mathrm{B}}}. \tag{3.1}$$

This temperature depends on the linewidth of the transition and limits the cooling in optical molasses [Let88]. In order to overcome this limit sub-Doppler cooling strategies like polarization gradient cooling or Raman sideband cooling are applied. Therefore, another temperature, the recoil temperature T_{r}, has to be looked at corresponding to an ensemble with a root-mean-square (RMS) momentum of one photon recoil

$$T_{\mathrm{r}} = \frac{\hbar^2 k_{\mathrm{L}}^2}{m k_{\mathrm{B}}} = \frac{h^2}{m k_{\mathrm{B}} \lambda^2}. \tag{3.2}$$

The photon recoil limits some cooling schemes and also has to be considered in imaging processes. While for light atoms like Lithium the system is heated drastically after scattering a few photons, for heavier elements a convenient amount of photons can be scattered in imaging processes before the image blurs due to recoil heating. Further, recoil energy also plays a major role in the process of storing atoms in optical lattices, since lattice parameters, like the band structure, depend on the ratio between trap depth and recoil energy.

The strategies that are applied after the MOT vary throughout the field depending on collisional properties of the species involved and the aims of the experiments. The atoms can be either loaded directly into a conservative force trap for evaporative cooling or one of the afore mentioned techniques can be applied as an intermediate cooling step. Photoassociation experiments (see next section) are also frequently carried out with atoms cooled by a MOT without further steps. While the means of slowing the atoms and the procedures that are carried out after the MOT phase can vary, a MOT as such is the key ingredient for almost every experiment with ultracold gases.

3.2.2 Atoms in traps

Ultracold quantum gases are typically trapped in conservative force traps. Depending on the rates for inelastic two-body processes magnetic or optical dipole traps are used.

Magnetic traps have a larger trap depth and size than optical dipole traps, however, atoms can be trapped only in low-field seeking states. The lowest spin states however, are high-field seeking. Hence, atoms can be trapped in magnetic traps only in higher spin states, which allow for exothermic spin relaxation processes. In Cs the cross section of inelastic scattering in low field seeking states is too high to allow for creation of a BEC [Web03a]. Therefore magnetic traps (apart from the MOT) are not used in the RbCs experiment.

Optical dipole traps are widely used and well described in [Gri00]. Therefore, just the main aspects will be summarized. In optical dipole traps a trapping potential is created by the electric field of a far-off resonance light beam interacting with the particles through an induced dipole moment. In a quantum mechanical description of a two level atom the ac-polarisability of the atoms depends on the frequency of the laser ω, the decay rate Γ, and the frequency ω_0 of the transition involved. The dipole potential U_{dip} and the scattering rate is then given by

$$U_{\mathrm{dip}}(\mathbf{r}) = -\frac{3\pi c^2}{2\omega_0^3} \left(\frac{\Gamma}{\omega_0 - \omega} + \frac{\Gamma}{\omega_0 + \omega} \right) I(\mathbf{r}), \tag{3.3}$$

$$\Gamma_{\mathrm{sc}}(\mathbf{r}) = \frac{3\pi c^2}{2\hbar\omega_0^3} \left(\frac{\omega}{\omega_0} \right)^3 \left(\frac{\Gamma}{\omega_0 - \omega} + \frac{\Gamma}{\omega_0 + \omega} \right)^2 I(\mathbf{r}). \tag{3.4}$$

Usually the frequency of the trapping laser is close to a resonance so that the detuning $\Delta = \omega - \omega_0$ is much smaller than the frequency itself $|\Delta| \ll \omega_0$. In this case the rotating wave approximation can be applied and equation 3.4 can be written

$$U_{\mathrm{dip}}(\mathbf{r}) = -\frac{3\pi c^2}{2\omega_0^3}\frac{\Gamma}{\Delta}I(\mathbf{r}), \tag{3.5}$$

$$\Gamma_{\mathrm{sc}}(\mathbf{r}) = -\frac{3\pi c^2}{2\hbar\omega_0^3}\left(\frac{\Gamma}{\Delta}\right)^2 I(\mathbf{r}). \tag{3.6}$$

From this equation some notable consequences can be extracted. The strength of an optical dipole potential and the scattering rate depend differently on the detuning Δ. A larger detuning results in less scattering even if the same strength of the potential is reached by adjusting the intensity. Therefore the detuning has to be chosen appropriately depending on the desired trap depth, the tolerable scattering rate and the laser power available. High power lasers are available only for certain wavelengths whereof 1064 nm is one of the most common wavelengths for optical dipole traps.

In real atoms in principle more than one level can contribute and the optical potential, as the latter depends on the sum of all dipole matrix elements divided by the corresponding detunings. In alkali atoms however, mostly the D_1 and the D_2 lines are relevant. If the trapping laser is sufficiently far detuned the trapping potential can be described by

$$U_{\mathrm{dip}} = \frac{\pi c^2\Gamma_{\mathrm{eff}}}{2\omega_{\mathrm{eff}}^3}\left(\frac{2}{\omega_{\mathrm{D}_2}-\omega} - \frac{1}{\omega_{\mathrm{D}_1}-\omega}\right)I(\mathbf{r}), \tag{3.7}$$

with an effective linewidth $\Gamma_{\mathrm{eff}} = 2/3\Gamma_{\mathrm{D}_2} + 2/3\Gamma_{\mathrm{D}_1}$, and effective frequency $\omega_{\mathrm{eff}} = 2/3\omega_{\mathrm{D}_2} + 2/3\omega_{\mathrm{D}_1}$.

Typically dipole traps are created by a Gaussian beam. If desired however, other trap geometries can be created by using higher-order modes or a time averaged potential. In a Gaussian beam traveling along the z direction the intensity is given by

$$I(r,z) = \frac{|E(r,z)|^2}{2\eta} = I_0\left(\frac{w_0}{w(z)}\right)^2 \exp\left(\frac{-2r^2}{w^2(z)}\right), \tag{3.8}$$

where r is the radial distance, $w(z)$ is the waist, $w_0 = w(0)$ is the waist size and $I_0 = I(0,0) = \frac{2P}{\pi w_0^2}$ is the intensity at the center of the beam for a total power P. At the center of the beam when $r \ll w(z)$ the Gaussian profile can be approximated by a parabola. Hence it can be viewed as a harmonic trapping potential. Therefore instead of beam waist w and intensity I the quantities trap frequency $\omega_{\mathrm{trap}} = \sqrt{\frac{4U_{\mathrm{dip}}(0)}{w_0^2 m}}$ and trap depth $U_{\mathrm{dip}}(0)$ are frequently used to describe dipole traps. The trap depth is frequently often given in units of photon recoil E_{rec} or in temperature units.

The spatially dependent density of a thermal gas trapped in such a harmonic trap is described by

$$n(\mathbf{r}) = n_0 e^{-\frac{x^2}{2\sigma_x^2}-\frac{y^2}{2\sigma_y^2}-\frac{z^2}{2\sigma_z^2}}, \tag{3.9}$$

with $\sigma_i = \omega_i^{-1}\sqrt{k_{\mathrm{B}}T/m}$ and ω_i denotes the trap frequency in the direction $i = x, z, y$. The spatial extensions of the cloud size are thus related to the trap frequency, the temperature, and the mass. For two species thermalised in the same optical trap the dimensions σ_i scale with $1/\sqrt{U_{\mathrm{dip}}(0)}$. This effect can reduce the overlap of the clouds.

In Fig. 3.2 (b) the trap depth of different species is compared to the trap depth of Cs. The difference in trap depths is notable, yet the trap depths lie within the same order of magnitude. Hence, from this point of view, the overlap of the two species is not drastically reduced. In the ultracold regime however, especially in quantum degenerate Bose-Fermi mixtures the situation can be further complicated. In the ultracold regime the cloud sizes depend on the mean-field interactions and the Fermi pressure.

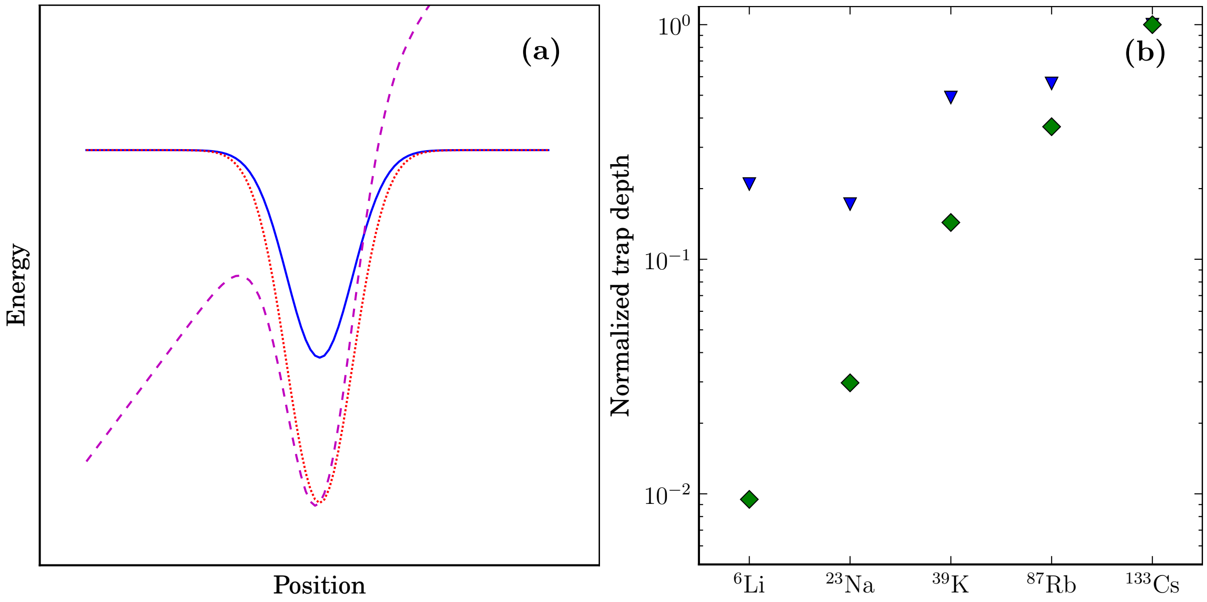

Figure 3.2: Part (a) illustrates different trapping potentials that are created by the same beam. Different species result in different trap depths (line and dotted). The dashed curve illustrates a situation when gravitational forces are only partially compensated. In (b) the trap depth for different species in a 1064 nm dipole trap is shown. While the triangles show the trap depths in energy units, the diamonds show the same data in units of the recoil energy E_{rec} of the respective species, which is important for lattice experiments. Both datasets are normalized to the value of Cs. For the plots atomic D-line data is used from [Geh03, Ste10, Tie10, Ste08a, Ste08b].

The overlap of the two species can be further reduced due to gravity as illustrated in part a) of Fig. 3.2. The gravitational potential tilts the trap and thereby creates a mass dependent shift in the trapping potential called gravitational sag.

Gravity can be compensated by a magnetic field gradient acting on the magnetic moment of the atoms. The compensation of gravity is also called levitation. The levitating force depends on the strength of the magnetic field gradient and on the ratio between the magnetic moment μ and the mass of the particle m. In mixtures however, the magnetic-moment-to-mass ratio μ/m can be different for the two species. Hence, in general, gravity can not be compensated for both species simultaneously. If the two species experience different net forces due to different masses or different levitation, the overlap of the clouds can be reduced.

In Fig. 3.3 the magnetic moment and the ratio of magnetic moment to mass is shown for different species in their lowest hyperfine states. As can be seen from the plot the magnetic-moment-to-mass ratio is almost equal for Rb and Cs. This allows for simultaneous levitation of Rb and Cs. For combinations of the species shown in the plot the only other mixture[1] that allows for simultaneous levitation is ^{23}Na^{40}K.

---

[1] Probably for other mixtures higher lying hyperfine states could be found for simultaneous levitation.

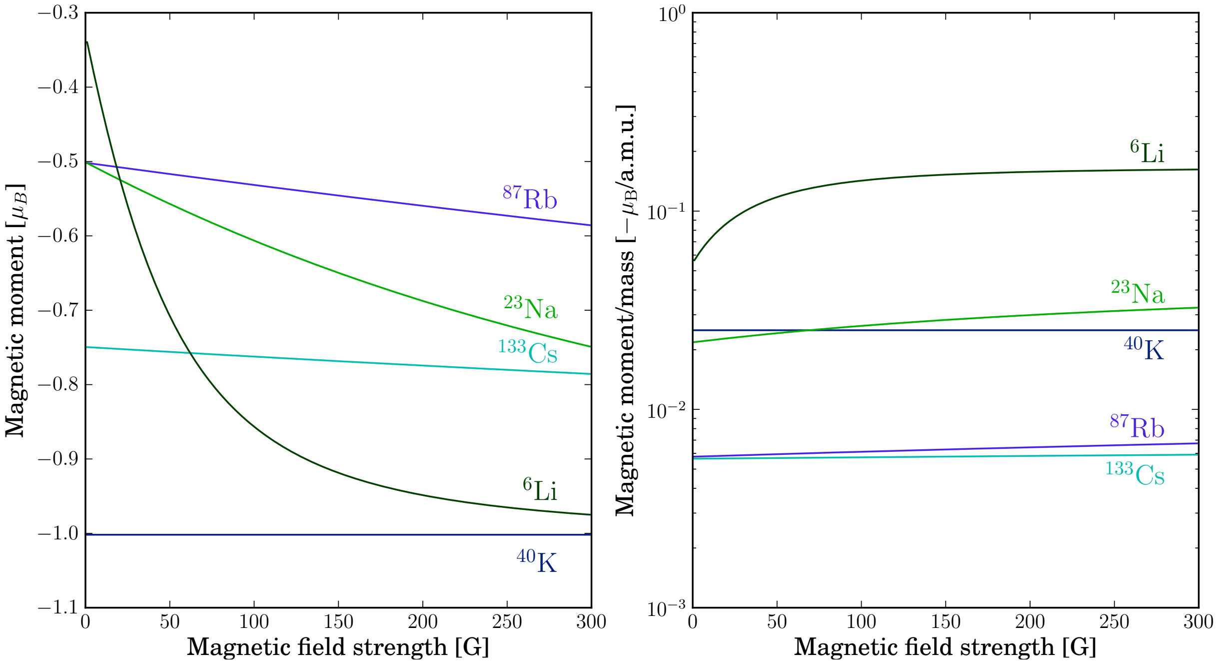

Figure 3.3: Magnetic moment and magnetic-moment-to-mass ratio for different alkali species in their lowest spin state. For the plots atomic D-line data is used from Refs. [Geh03, Ste10, Tie10, Ste08a, Ste08b].

3.2.3 Collisions and losses

In mixtures collisional properties determine which experimental strategies should be followed. Even though for single species the collisional properties are mostly known from previous experiments and well understood [Wei99], for mixtures the outcome can be completely different and is often unknown a priori. Effects of mixtures can already be seen in the first cooling step the MOT phase, when light assisted interspecies collisions add to the loss rate and can reduce the number of atoms in the MOT. In a mixed RbCs MOT the rate of light assisted collisions is much higher than the rate of light assisted collisions in a pure Rb or Cs MOT [Har08]. In consequence Rb and Cs are separated in order to achieve higher atom numbers.

Even when atoms are trapped in their lowest spin state in an optical trap inelastic collisions can happen due to formation of molecules in a process involving three particles. The binding energy of the molecules has to be transformed into an other kind of energy. In a non-radiating process the binding energy of the molecule that is created is transformed into kinetic energy. Momentum conservation requires the presence of a third particle. If the energy released exceeds the depth of the confining potential, the inelastic three-body collision can lead to losses. Through further elastic scattering the energy can also be transferred to other particles, which leads to a heating of the atomic sample. Because momentum conservation necessitates a third particle to be present this loss process is called three-body loss [Web03b].

Three-body loss processes play a major role in ultracold quantum gases and for species such as Cs a strategy to control these processes was a key ingredient to achieve a BEC [Web03a]. Three-body losses have been studied in detail for Rb and Cs [Smi07, Web03b,

---

This however, bears the problem of spin-changing collisions.

Kra06a]. For a single species losses can be described by the following rate equation for the particle number N in the trap

$$\dot{N}(t) = -\frac{N(t)}{\tau} - \int [L_2 n^2(\mathbf{r},t) + L_3 n^3(\mathbf{r},t)] d^3r, \tag{3.10}$$

where τ is the one-body lifetime, typically determined by background gas collisions, $n(\mathbf{r},t)$ is the atomic density distribution, and L_2 (L_3) is the thermally averaged two-body (three-body) loss coefficient. The loss equation can be further simplified if $n(\mathbf{R},t)/N(t)$ remains constant. In a harmonic trap for a thermal cloud at constant temperature T, neglecting mean-field interactions one finds

$$\dot{\bar{n}}(t) = -\frac{\bar{n}(t)}{\tau} - L_2\bar{n}(t)^2 - (4/3)^{3/2} L_3 \bar{n}(t)^3, \tag{3.11}$$

where $\bar{n} = N\bar{\omega}^3(4\pi k_\mathrm{B}T/m)^{-3/2}$ is the mean density; m is the atomic mass, and $\bar{\omega} = \sqrt[3]{\omega_x\omega_y\omega_z}$ is the geometric mean of the trap vibrational frequencies.

A connection between the three-body loss parameter and the scattering length is explained in Ref. [Web03b]

$$L_3 = n_l C(a)\frac{\hbar a^4}{m}, \tag{3.12}$$

where n_l refers to the particle lost in the process and $C(a)$ describes the non-trivial physics, such as Efimov physics [Efi79, Bra03, Kra06b, Bra07, N$\ddot{0}$6]. Typically, $n_l = 3$. This scaling behaviour played a fundamental role for further studies of the loss process, which led to the discovery of three-particle resonances predicted by Efimov [Kra06b]. For the RbCs experiment this connection is important because a control of the scattering length allows to control the three-body loss.

In the case of two different species a and b equation (3.10) generalizes to a set of two coupled differential equations

$$\begin{aligned}
\dot{N}(t)_a = \dot{N}_{a,\mathrm{single}} &- \int \Big[L_2^{ab} n_a(\mathbf{r},t) n_b(\mathbf{r},t)\Big] d^3r \\
&- \int \left[\frac{2}{3} L_3^{aab} n_a^2(\mathbf{r},t) n_b(\mathbf{r},t) + \frac{1}{3} L_3^{abb} n_a(\mathbf{r},t) n_b^2(\mathbf{r},t)\right] d^3r \\
\dot{N}(t)_b = \dot{N}_{b,\mathrm{single}} &- \int \Big[L_2^{ab} n_a(\mathbf{r},t) n_b(\mathbf{r},t)\Big] d^3r \\
&- \int \left[\frac{1}{3} L_3^{aab} n_a^2(\mathbf{r},t) n_b(\mathbf{r},t) + \frac{2}{3} L_3^{abb} n_a(\mathbf{r},t) n_b^2(\mathbf{r},t)\right] d^3r.
\end{aligned} \tag{3.13}$$

In addition to the intra-species losses $\dot{N}_{a,\mathrm{single}}, \dot{N}_{b,\mathrm{single}}$, which are described by equation (3.10), new 2-body and 3-body loss terms appear, which depend on the density distribution of both species. Along with the loss terms additional loss parameters are introduced, where L_2^{ab} is an interspecies two-body loss coefficient and L_3^{aab}, L_3^{abb} are three-body loss coefficients for loss processes involving the particles indicated as superscript.

For stationary density distributions the equations can be simplified similar to equation (3.11) yielding

$$\begin{aligned}
\dot{\bar{n}}_a &= \dot{\bar{n}}_{a,s} - \alpha_2\bar{n}_a\bar{n}_b - 2\alpha_3^{aab}L_3^{aab}\bar{n}_a^2\bar{n}_b - \alpha_3^{abb}L_3^{abb}\bar{n}_a\bar{n}_b^2 \\
\dot{\bar{n}}_b &= \dot{\bar{n}}_{b,s} - \alpha_2\bar{n}_a\bar{n}_b - \alpha_3^{aab}L_3^{aab}\bar{n}_a^2\bar{n}_b - 2\alpha_3^{abb}L_3^{abb}\bar{n}_a\bar{n}_b^2,
\end{aligned} \tag{3.14}$$

where $\dot{\bar{n}}_a, \dot{\bar{n}}_b$ is the single species loss, $\bar{n}_a, \bar{n}_b$ are averaged densities and α_2, α_3^{aab}, α_3^{abb} are pre-factors depending on the spatial distributions of the two species. In Fig. 3.4 a measurement is shown where the interspecies three-body losses are dominant. In RbCs the large three-body losses are hampering the simultaneous condensation of Rb and Cs when they are mixed. For a fast evaporation with a low efficiency, the creation small Rb and Cs BECs have been reported in Ref. [McC11]. In order to achieve large BECs, in our experiment the two species are Bose condensed in two different traps [Ler10].

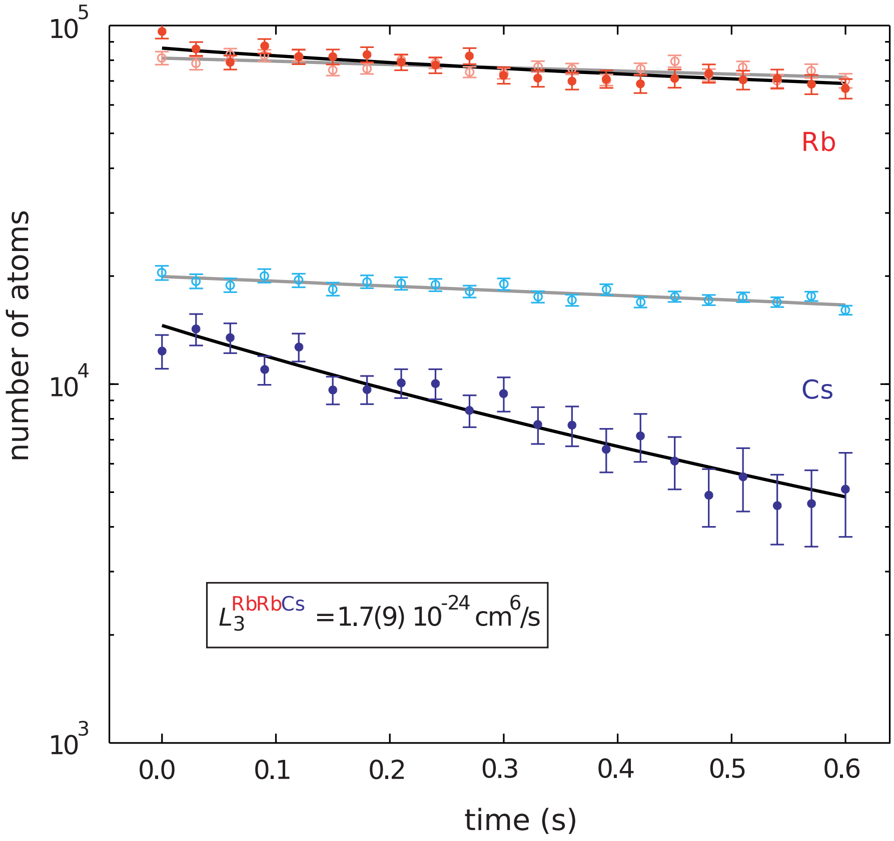

Figure 3.4: The graph shows three lifetime measurements of ^{87}Rb and ^{133}Cs at a magnetic field of 17 G. The open circles show data for Rb and Cs in a trap without the other species present. The filled circles show the behaviour of the system when both species are mixed in the same trap. The lines represent a numerical solution of the corresponding differential equations fitted to the data. [Ler10]

In addition to mere loss of particles the loss processes are a source of heating. As collisional losses depend on the density they mainly occur in the dense central regions of the trap where the coldest particles are located. Thereby preferentially the coldest particles are lost, which leads to a net heating of the sample. This so called “anti-evaporation” can be regarded as the opposite of evaporative cooling [Ket99], where the hottest particles are removed. Furthermore, if scattering cross sections are large, escaping particles can scatter with other particles in the trap and thereby deposit their energy, which leads to further heating of the sample.

During our first attempts to create a double-species BEC we observed strong losses when both species were kept in the same trap, which demanded for a detailed investigation

[Ler11]. Therefore, the loss rate of the mixture and the single species was measured. Fig. 3.4 shows the result of such a measurement. The species are both kept in their lowest spin state and hence spin changing collisions are ruled out as a possible cause. A fit of the rate equation 3.14 to our data yields a three-body loss coefficient of $L_3^{\mathrm{RbRbCs}} = 1.7(9) \times 10^{-24}\,\mathrm{cm}^6/\mathrm{s}$. Since the majority of atoms in the trap are Rb atoms, it is assumed that a three-body process involving two Rb atoms and one Cs atom is more likely than a process involving two Cs atoms and one Rb atom. In order to judge the effect of three-body losses it is useful to compare the obtained value to typical densities in a BEC. For our BECs [Ler10] we obtain maximum densities of $n_{\mathrm{Rb}} = 7.8 \times 10^{13}\,\mathrm{cm}^{-3}$ and $n_{\mathrm{Rb}} = 3.2 \times 10^{13}\,\mathrm{cm}^{-3}$. For the obtained loss coefficient a density of $3 \times 10^{13}\,\mathrm{cm}^{-3}$ leads to a lifetime of less than a ms and in order to obtain lifetimes longer than 10 s the densities have two be lower than $2 \times 10^{11}\mathrm{cm}^{-3}$. At these low densities not only three-three body losses but also elastic collisions are drastically reduced.

In contrast to the above discussed inelastic collisions, elastic inter-species collisions can be useful in experiments. In an intermediate range of collisional cross-sections sympathetic cooling, meaning cooling by thermalisation of one species with another, can help cooling down species that are difficult to cool by evaporation. Especially in the case of fermions, which do not interact at ultralow temperatures, sympathetic cooling is a major tool for reaching quantum degeneracy [Mud02, Mya97, Aub06, Fer06, Mic10b]. Also in sympathetic cooling effects occur [And05], which in our case help to enhance thermalisation as discussed later in section 4.1.4. For evaporative cooling [Hes87] elastic collisions are necessary for thermalisation.

The miscibility of two BECs [Rib02] is governed by the inter-species and intra-species scattering properties. Two species A and B are immiscible if $\Delta = g_{AB}/\sqrt{g_A g_B} > 1$, where $g_X = 2\pi\hbar^2 a_X/\mu_X$. The reduced mass is denoted by μ_X, a_X is the scattering length of the species and $X \in \{A, B, AB\}$. For RbCs at low magnetic fields the scattering length a_{RbCS} is much larger than a_{Rb} and a_{CS}. Therefore Rb and Cs are immiscible at low magnetic field values [McC11]. Therefore a mixed RbCs BEC can only be created when the inter-species scattering properties are tuned by a Feshbach resonance (see next section). Interspecies RbCs Feshbach resonances only exist at magnetic field values above 150 G [Tak12]. Therefore a creation of a RbCs BEC is not possible at low magnetic field values. For magnetic field values that are not close to a Cs Feshbach resonance, large Cs three-body losses drastically reduce the lifetime of a Cs BEC [Web03b]. This hampers the creation of a Cs BEC at magnetic field values in the region from 150 to 500 G. Hence the creation of a mixed RbCs BEC in the region below 500 G is extremely difficult. The magnetic field region above 700 G, which might be more suitable for the creation of a sufficiently stable atomic RbCs mixture [Tak12] can currently not be accessed with our magnetic coil system.

3.2.4 Feshbach resonances

Feshbach resonances are widely used in ultracold quantum gas experiments to tune scattering properties and to associate atoms into molecules [Joc02, The04, Joc03a, Her03, Joc03b]. As described in [Chi10] a scattering resonance occurs when the phase shift changes rapidly by $\approx \pi$ over a relatively narrow range of energy due to the coupling of a discrete quasi-bound level to the continuum (scattering states). The resonances can be caused by a specific shape of a single Born-Oppenheimer (BO) potential featuring quasi-bound levels behind a repulsive barrier or by an approximate bound state that has a different symmetry and potential from the colliding atoms. A discussion of the former, which is known as a shape resonance, is beyond the scope of this thesis. An discussion of the latter, called Feshbach resonance, is introducing the tuning of scattering length and Feshbach association discussed in this thesis.

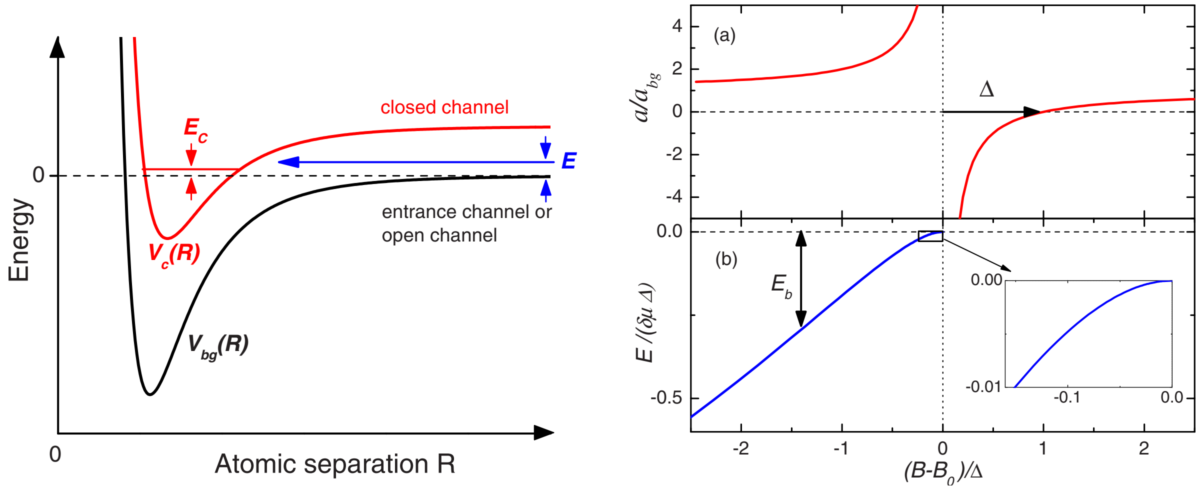

Figure 3.5: Schematic drawing of an atomic interaction potential. Depending on their quantum numbers scattering particles can be in different states and thus are subjected to different two-particle interaction potentials $V_c(R), V_{\mathrm{bg}}(R)$ drawn in black and red. If the energy of the scattering particles is higher than the value of the potential for $R \to \infty$ the state belongs to an open channel. In any other case the state is a bound state, which represents a closed channel for the scattering problem. Scattering particles enter at an open channel with an energy E, which can interact with a closed channel depending on coupling of the two states and their energy difference $E_C - E$.(picture from [Chi10])

Feshbach resonances were analyzed in theory by Feshbach and Fano independently. While Fano approached the phenomenon from the perspective of atomic physics [Fan35, Fan61], Feshbach described the problem in the context of nuclear reactions. However, as is concluded already in the original publication, *the formalism developed in this paper has a wide range of applicability extending beyond just nuclear reactions* [Fes62, Fes58]. A providence, which proved itself true when with the first observation in ultracold quantum gases [Ino98] Feshbach resonances became one of the most important techniques for tuning inter-atomic scattering properties.

In a simple picture, the scattering of particles with a kinetic energy E is governed by a Born-Oppenheimer potential $V_{\mathrm{bg}}(R)$ representing the energetically open channel. Depending on the internal states of the particles, different potentials exist with different energies for $R \to \infty$. The latter are called asymptotic energies. A state $V_c(R)$ with higher asymptotic energy represents a closed channel, and features bound states with energies larger or equal to the asymptotic energy of the open channel. If the energy of a bound molecular state in the closed channel approaches the scattering state of the open channel, even weak coupling can lead to a strong mixing of the two channels and a Feshbach resonance can occur.

Since the open channel and closed channel BO-potentials belong to different internal states they depend in different ways on external fields. Because of this the states of different potentials can be shifted with respect to each other. Feshbach resonances (FR) are called magnetic FR, electric field induced FR or optical FR depending on whether the shift is caused by a Zeeman effect, a Stark effect or an AC Stark shift. From an experimental point of view only magnetic Feshbach resonances are relevant for tuning of scattering properties.

In the RbCs experiment we use magnetically tuned FR in order to control the scattering lengths of the atoms and to associate molecules. The scattering length in the vicinity of a FR can be described by a simple expression

$$a(B) = a_{\mathrm{bg}} \left(1 - \frac{\Delta}{B - B_0}\right), \tag{3.15}$$

where a_{bg} is the background scattering length associated with $V_{\mathrm{bg}}(R)$, and Δ is the width of the resonance, which depends on the coupling strength [Chi10]. As shown in Fig. 3.5, the channel coupling mixes the closed and open channels near the center of the resonance, and the closed channel connects to the open channel.

This phenomenon, which can be also regarded as an avoided crossing, also leads to a quadratic dependence of the binding energy E_b (2.4) on the magnetic detuning $B - B_0$. Feshbach resonances can not only be used to alter the scattering length but also to create molecules as proposed by Timmermanns [Tim99]. In fact the creation of molecules using Feshbach resonances is one of the most efficient procedures for formation of molecules from ultracold mixtures as described further below.

In experiments the dependence of the three-body loss parameter L_3 on the scattering length (Eq. 3.12) facilitates the detection of Feshbach resonances by measuring the trap loss as a function of the magnetic field.

The variation of the scattering length and the three-body losses using Feshbach resonances has much more impact than just for the detection of resonances. It was only due to the use of Feshbach resonances that species with otherwise unfavorable scattering properties like ^{85}Rb and ^{133}Cs could be condensed [Cor00, Web03a].

Feshbach resonances are widely used in ultracold quantum gases and they have become the most prominent tool for tuning scattering properties. One could be tempted to conclude that once a sufficiently broad Feshbach resonance is discovered, all problems due to unfavorable scattering parameters seem to disappear. However, a trivial, subtle detail has to be taken into account concerning mixtures: there are three scattering parameters but there is only one magnetic field to tune them. If one of the species is only stable in a certain magnetic field range this can severely limit the ability to tune the scattering properties of the mixture. This is hindering the creation of a stable mixture of RbCs. A strategy to overcome such challenges is discussed in section 3.3.4.

More flexibility for tuning the scattering length of multicomponent quantum gases is added by radio-frequency (rf) dressing of Feshbach resonances [Kau09, Han10, Zha09]. According to [Han10] there are three ways to dress the atoms. Firstly, rf can couple a colliding pair and a bound state, which is similar to an optical Feshbach resonance and can shift the position of a broad resonance. Secondly, two molecular bound states can be coupled that then interact with the colliding pair. Lastly, a superposition of atomic states can be created by dressing the atom, which leads to a superposition of several entrance channels. The case of two different species is discussed in [Zha09] taking $^{40}\mathrm{K} - {}^{6}\mathrm{Li}$ as an example.

In principle optically-induced Feshbach resonances are a way to change scattering parameters independently of the magnetic field [Fed96, Tal05]. In an optical Feshbach resonance the free atom pair is coupled to an electronically excited state by light. If the excited state does not have a long lifetime this leads to decay and decoherence, furthermore a sufficient strong coupling from a free state to the excited state is necessary. In [Tal05] the decay of the excited state is circumvented by driving a two-photon transition to a state of the ground electronic potential. However, even two-photon optical Feshbach resonances lead to additional losses. This makes the method questionable if a change in scattering length is desired in order to control loss problems.

To conclude, for the creation of an ultracold atomic mixture most of the techniques developed for single species can be used. However, interspecies interactions can lead to additional losses at all stages ranging from light assisted collisions in the MOT to three-body losses in dense ultracold gases. There are much more different possible interactions but the number of means to control these interactions are the same as for a single species. Hence, it is not always possible to adjust all interactions in the optimum way. Often a compromise has to be found since both species are affected by the same fields. The fact, that there is only one magnetic field hinders the independent control of the different scattering lengths impossible. In RbCs, where the background scattering lengths for Cs and for the mixture are large this hinders the creation of a stable mixture. In mixtures different from RbCs the concept of levitation might be of limited use.

3.3 Association of molecules

3.3.1 Feshbach association

The association of cold molecules via magnetically tunable Feshbach resonances is highly efficient and coherent scheme to create ultracold molecules from ultracold gases. In 2002 Donley *et al.* studied atom-molecule coherences induced by time dependent magnetic-field variations in the vicinity of a Feshbach resonance [Don02]. Just a year later a refined technique involving sweeps across a Feshbach resonance was applied to create Feshbach molecules of Li,Na,K,Rb and Cs [Joc03b, Xu03, Reg03, Dür04, Her03].

The details of Feshbach association is described in detail in [Fer08, Köh06, Chi10]. Therefore I will only provide a brief summary that is relevant for the explanation of our measurements.

From practical point of view Feshbach association is achieved in ultracold gases by a magnetic field ramp from negative to positive scattering lengths across a Feshbach resonance. The conversion efficiency can be up to 80% in degenerate Fermi gases or up to unity in an optical lattice. In a thermal sample however, the conversion efficiency is reduced depending on the phase-space densities Φ_N, $\Phi_{\mathrm{N}'}$ of the atoms [Chi04], where N, N' denote the number of atoms for the two different species. The phase-space density of the molecules Φ_M is given by

$$\Phi_{\mathrm{M}} = \Phi_{\mathrm{N}}\Phi_{\mathrm{N}'}e^{E/k_{\mathrm{B}}T}, \tag{3.16}$$

where E is the binding energy of the molecular state and Φ_{N}, $\Phi_{\mathrm{N}'}$ denote the phase space densities of the two species. Since the scattering length diverges near a Feshbach resonance, losses are enhanced in the proximity of a Feshbach resonance. This implies that the conversion efficiency depends on the speed of the magnetic field ramp. As introduced in [Hod05] and further described in [Chi10] the conversion efficiency follows a Landau-Zener-like behaviour

$$\frac{P}{P_{\mathrm{max}}} = 1/\exp\left(-\alpha n \frac{\hbar}{m}\left|\frac{\Delta a_{\mathrm{bg}}}{\dot{B}}\right|\right), \tag{3.17}$$

where P_{max} is the maximum conversion efficiency solely determined by the phase-space density of the atomic cloud, Δ is the width of the Feshbach resonance, a_{bg} is the scattering length, n is the atomic number density and m is the mass of the atom.

Furthermore, collisions of the Feshbach molecules with free atoms can lead to additional losses reducing the number of detected Feshbach molecules. For mixtures of different species mismatch of the cloud size and shifts of the clouds due to a gravitational sag can reduce the overlap of the clouds and thereby the efficiency.

Since in bosonic mixtures density dependent heating and loss processes near a resonance limit the achievable phase space densities [Mar05], typical efficiencies on the order of $5-15\%$ are common in bosonic mixtures [Tak12, Heo12]. In fermionic systems scattering losses are prevented and high efficiencies of 50% can be achieved [Wil08, Spi10, Voi09]. The efficiencies can be increased however, if the atoms are paired up in an optical lattice.

A standard way to prove Feshbach association is the Stern-Gerlach separation. It makes use of the different magnetic moments of the molecular bound and the free atomic state. When a magnetic field gradient is applied, the two molecular clouds are split apart, and the two clouds can be imaged and analysed separately.

3.3.2 Radio-frequency association

Radio-frequency association (rf-association) could be alternative to Feshbach-association [Tho05]. The technique relies on resonant coupling of a free atom state to a weakly bound molecular state by an oscillating magnetic field. This implies that the two states have different magnetic momenta. Since typical binding energies are on the order of $h \times 1\,\mathrm{MHz}$, rf-association is typically performed near a Feshbach resonance. A detailed description of the process and a form of the lineshape can be found in [Chi05], a recipe for optimization depending on temperature and density is described by Hanna *et al.* [Han07] and further studies on association far from a Feshbach resonance have been performed by Beaufils *et al.* [Bea10].

Since typical time scales for association are longer than for Feshbach association the technique is less favorable in systems that suffer from collisional losses even far from a resonance. In stable mixtures, mixtures in lattices or single species BECs the conversion efficiency can be on the order of 30% and heating and losses in the remaining atomic samples can be reduced [Osp06, Tho05].

rf-association and dissociation can also be used for detection of molecular bound states and was also used for mapping out molecular bound state structure in RbCs [Bar05, Reg03, Lan09b]. In rf-spectroscopy losses of atoms are observed if the modulation frequency corresponds to the binding energy of the state investigated. For each magnetic field value investigated, the modulation frequency is varied in a series of measurement in order to find the binding energy. Since for each magnetic field value a series of data points with different rf frequency has to be measured, this technique is more time consuming than a simple loss scan. However, the precision is much higher.

3.3.3 Photoassociation

Photoassociation (PA) [Tho87, Fio98, Ulm12, Jon06] is widely used in alkali mixtures to create ultracold molecules in low vibrational states or even in the ground state [Aik10, Kra06c, Sag05]. Scattering atoms are transferred by absorption of a photon into a molecular bound state of an electronically excited Born-Oppenheimer potential. The excited molecule subsequently decays by spontaneous decay into one of several molecular ground states. Depending on the overlap of the excited state wave functions with the ground-state wave functions a considerable fraction can even reach the vibrational or ro-vibrational ground-state. Due to the incoherent nature of the process it is generally not possible to create a pure sample of ground-state molecules in a well defined state. However, to gain information on some ground-state properties the phase-space density is not important and therefore this simple technique, which has comparatively low requirements on laser frequency stability, is frequently used with mixtures and the first creation reported for many mixtures was achieved by photoassociation. In order to overcome low formation rates due to the limited overlap of the free atom wave function with the excited state, the process can be enhanced in the proximity of a Feshbach resonance [Pel08, Jun08]. In order to overcome the incoherent nature of the spontaneous decay, two-color photoassociation [Koc12] can be used. In two color PA the spontaneous decay is replaced by a stimulated emission, either in an adiabatic passage [Wyn00] or a nonadiabatic scheme [Val00]. This allows to select a target state. Free-to-bound adiabatic passage requires a good Franck-Condon overlap between the wave function of free atoms and a molecular bound state. For many molecules including RbCs the free to bound Franck-Condon overlap is not sufficient to yield a high efficiency.

3.3.4 Enhanced association from pairs of atoms

The production of molecules can be enhanced if pairs of atoms are confined at sites of an optical lattice [Jak02, Fre10]. This pairing can be reached by a coherent phase transition to a Mott-insulating state if the density is chosen such that the central region of the gas contains two atoms per lattice site. If U/J is slowly increased to values above a critical value $(U/J)_\mathrm{c}$ a transition to a Mott insulating phase takes place [Gre02] and for suitable densities the atoms are paired in the central region of the lattice. An association of the pairs to molecules leads to a Mott insulating state of molecules. A subsequent melting of the Mott insulator should lead to a BEC of molecules.

The critical value has been evaluated by a mean field calculation to be $(U/J)_\mathrm{c} = 5.8z$ where z denotes the number of nearest neighbours [Fis89]. For a typical 3D optical lattice $z = 6$ and $(U/J)_\mathrm{c} = 34.8z$. Later Monte-Carlo Calculations yielded in a critical value of $(U/J)_\mathrm{c} = 29.3z$ [CS07].

Association of molecules in a lattice was first realized for Rb Feshbach molecules [Vol06]. Soon after the scheme was used to enhance the efficiency for creation of ground-state molecules of Rb and Cs [Lan08, Dan09c, Dan09b]. Up to now the limited efficiencies for creation of ground-state molecules lead to defects in the Mott-insulating state. There-for the formation of a molecular BEC by melting of the Mott insulator has not yet been observed.

For mixtures the creation of a Mott-insulating state with one atom of each species has been proposed [Dam03, Moo03]. This allows the creation of heteronuclear molecules in an optical lattice. In the described scheme the power of the optical lattice beams is increased slowly. Since the trap depth in units of recoil is different for different species (see Fig. 3.2) the transition from superfluid to Mott insulator occurs at different lattice depths for different species. First experiments on creation of heteronuclear molecules in optical lattices have been carried out by C. Ospelkaus *et al.* [Osp06]. These first experiments however did not have a unity occupation of each lattice site.

While for stable mixtures this scheme can be directly applied, for RbCs we make use of an additional feature, which will allows us to avoid the collisional losses. For Cs high three-body losses occur if the magnetic field is tuned away from resonance. This prevents us from tuning the magnetic field to a RbCs resonance in order to avoid interspecies collisional losses. If Cs is frozen out in a Mott insulator the three-body losses are highly suppressed, even if the magnetic field is not tuned near a zero crossing of a Cs Feshbach resonance.

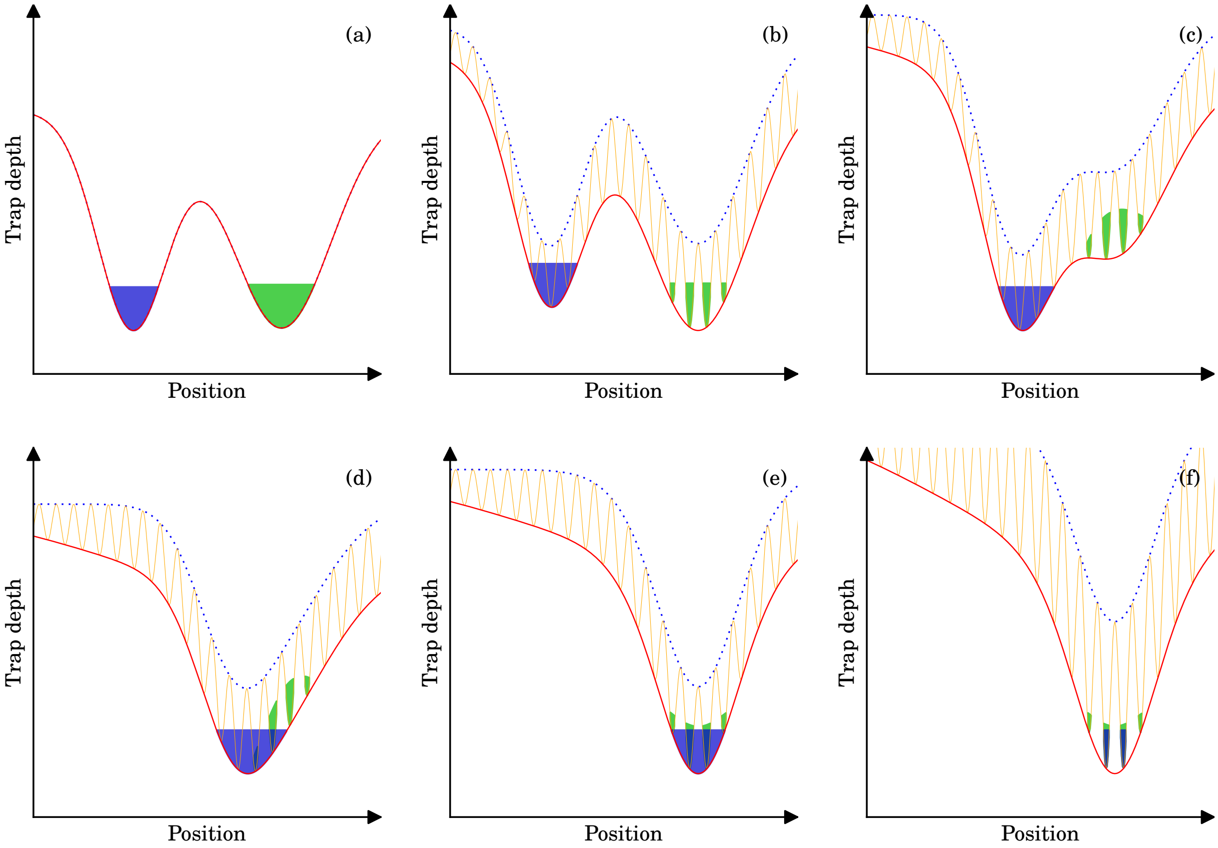

Figure 3.6: Schematic overview of our planned cloud combination and pairing scheme. Firstly Cs is loaded into an optical lattice (a) and a Mott insulator of Cs is created (b). Then the magnetic field is tuned onto a RbCs Feshbach resonance in order to avoid inelastic collisions and Rb is moved over the Cs Mott insulator (c,d,e). In a last step (f) the depth of the optical lattice is increased and a Mott insulator of Rb is created.

We therefore extend the method into a cloud combination and pairing scheme. As is shown in Fig. 3.6, Cs is kept in an optical lattice and transferred into a MI phase with one atom per site. During this time the magnetic field is tuned close to a Cs resonance in order to keep the Cs scattering length at low values. When Cs is frozen out in the lattice, the magnetic field is tuned to a RbCs Feshbach resonance in order to reduce the RbCs interspecies scattering length and losses. Subsequently the Rb cloud, which is still superfluid, is moved on top of the Cs cloud. In a last step the depth of the lattice is further increased and a MI of Rb is created. This should result in a two species MI with one atom of each species per lattice site.

The atoms will be subsequently associated to Feshbach molecules by rf- or Feshbach association and transferred to the ground-state via STIRAP. A subsequent melting of the Mott-insulator phase [Jak02] should allow for the creation of a high phase-space density sample of RbCs.

3.4 Quantum numbers and properties of ultracold molecules

In the most general form molecules are described by positively charged cores at positions $\{\mathbf{R}_i\}$ and negatively charged electrons at $\{\mathbf{r}_j\}$ interacting via Coulomb forces - a many-body problem that is unsolvable in most cases. The large difference between the nuclear and electronic mass facilitates the treatment of the problem with the Born-Oppenheimer (BO) approximation, which allows the separation of the molecular wave function

$$\Psi_{\mathrm{mol}} = \Phi(\mathbf{R}_i, \mathbf{r}_j) \cdot \Psi(\mathbf{R}_i) \tag{3.18}$$

into an electronic part $\Phi(\mathbf{R}_i, \mathbf{r}_j)$ and a wave function $\Psi(\mathbf{R}_i)$ of the nuclear core. In this picture the electrons create a potential energy surface $V(\mathbf{R}_i)$ governing the nuclear motion. In the case of diatomic molecules this potential energy surface is a one dimensional function $V(R)$ of the distance $R = |\mathbf{R}_1 - \mathbf{R}_2|$ and often called molecular (electronic) potential. If the electronic potentials are known with enough precision most molecular properties can be derived.

Type of angular momentum	**Operator**	**Quantum numbers**	
		total	**projection**
Electronic orbital	$\mathbf{L}$	L	$\Lambda = \|M_L\|$
Electronic spin	$\mathbf{S}$	S	Σ
Rotational	$\mathbf{R}$	R	$\ldots$
Total	$\mathbf{J} = \mathbf{R} + \mathbf{L} + \mathbf{S}$	J	$\Omega = \|\Lambda + \Sigma\|$
Total-Spin	$\mathbf{N} = \mathbf{R} + \mathbf{L}$	N	Λ
Total nuclear Spin	$\mathbf{I}$	I	M_I
Total incl. nuclear	$\mathbf{F} = \mathbf{J} + \mathbf{I}$	F	M_F

Table 3.3: Angular momentum operators and quantum numbers used in the description of diatomic molecules. The values of these quantum numbers are mostly given as numbers, an exception being Λ whose values are labeled $\Lambda = \Sigma, \Pi, \Delta, \Phi, \cdots$ The spin S is often given as $2S + 1$ and the two frequent values of $S = 0$ and $S = 1$ are called singlet and triplet accordingly.

Similar to atoms, there are many different quantum numbers describing the properties of the molecular state, which are summarized in 3.3. Compared to atoms, in molecular dimers the symmetry is reduced due the linear geometry, which leads to precession of the electronic angular momentum and spin around the molecular axis. The electronic angular momentum can couple as well to the electronic spin, which is called spin-orbit coupling. In order to get an intuitive understanding one tries to describe the system in a basis formed by eigenvalues of quantum mechanical operators. If a quantum number is an eigenvalue of the systems Hamiltonian it is called a *good* quantum number.

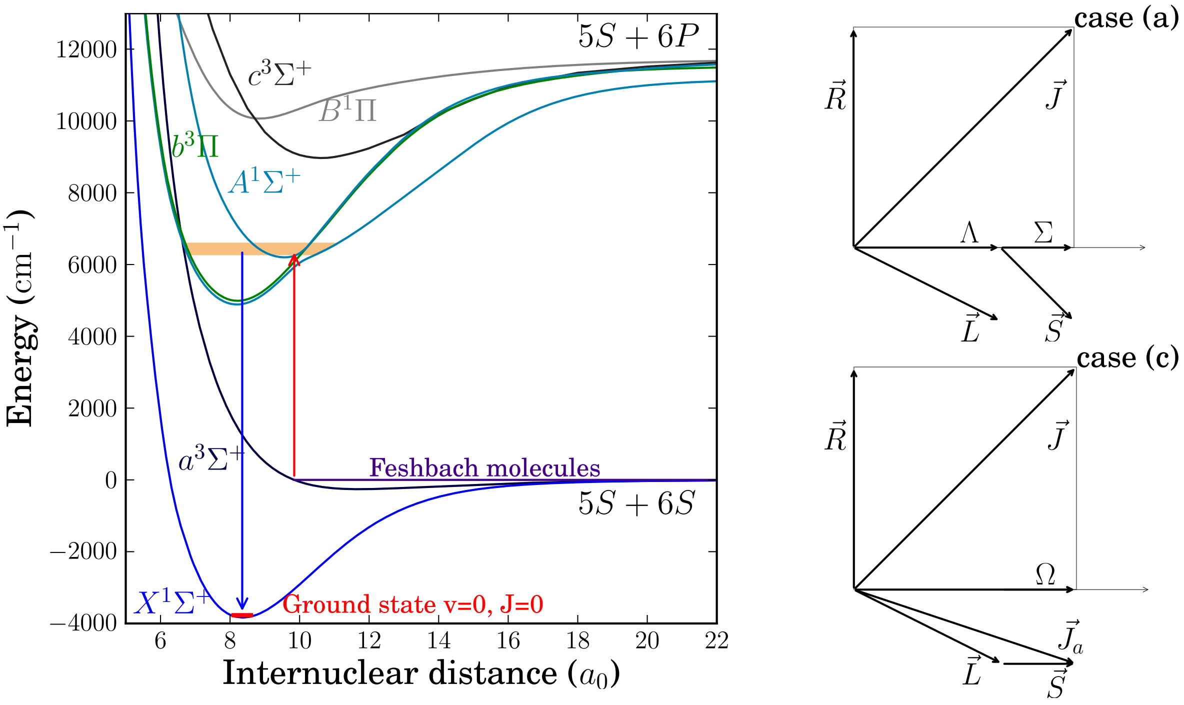

Figure 3.7: Potential energy curves of the electronic ground state and the lower electronic excited states of RbCs (left side). The range of vibrational levels that can be addressed by our laser system is marked orange. (Molecular BO-potential data from [Kot05, Doc10]). The graphs on the right show schematic drawings of the Hund's cases (a) and (c). In Hund's case (a) **L** and **S** are coupled to the molecular axis separately. In Hund's case (c) spin-orbit coupling dominates, **L** and **S** are coupled to each other and the resulting angular momentum vector precesses around the molecular axes.

If some weaker couplings are neglected, a system can be described by Hund's coupling cases where of the most important for RbCs are Hund's case a) and c).

In Hund's case a) spin-orbit coupling and the interaction of the nuclear rotation with the electronic motion are neglected. The electron spin and angular momentum couple separately to the molecular axis yielding the projections Λ, S, Ω and Σ as good quantum numbers. The electronic states are labelled by $^{2S+1}\Lambda_\Omega$ where the values of Λ are noted in Greek letters $\Sigma, \Pi, \Delta, \Phi, \cdots$ in analogy to the atomic angular momenta (s,p,d,f,g,...). In alkali dimers where mostly singlet and triplet states occur the states are additionally numbered by capital and small letters in alphabetic order respectively - with the exception of the ground state that is called X. For example the lower lying states of RbCs are called $X^1\Sigma^+$, $a^3\Sigma^+$, $A^3\Pi$, $b^1\Sigma^+$.

In Hund's case c) spin-orbit coupling dominates, therefore **L** couples to **S** yielding $\mathbf{J}_a = \mathbf{L} + \mathbf{S}$. This momentum $\mathbf{J}_a$ precesses around the internuclear axis leaving it's projection Ω as the only good quantum number in the non-rotating case. If there is nuclear rotation, this rotation R couples then to Ω giving **J**.

In Fig. 3.7 BO-potentials for RbCs are shown. The arrows denote the transitions that are used for STIRAP and spectroscopy in our experiment. The orange region in the excited state potential indicates the tuning range of the laser system.

Depending on the coupling case a variety of selection rules for electric dipole transitions exist that have to be taken into account for a transition from Feshbach molecules to the ground state [Her50]. In Hund's case a) these are:

$$\Delta J = 0, \pm 1, \text{ with the restriction } J = 0 \nrightarrow J = 0, \tag{3.19}$$

$$\Delta \Lambda = 0, \pm 1, \tag{3.20}$$

$$\Delta S = 0, \tag{3.21}$$

$$\Delta \Sigma = 0, \tag{3.22}$$

$$\Delta \Omega = 0, \pm 1, \tag{3.23}$$

$$\Delta J = 0 \text{ is forbidden for } \Omega = 0 \to \Omega = 0, \tag{3.24}$$

$$\Delta M_I = 0, \pm 1 \text{ for } \Delta M_J = 0, \tag{3.25}$$

$$\Delta M_I = 0 \text{ for } \Delta M_J = 0, \pm 1, \tag{3.26}$$

and

$$\Delta M_F = 0, +1, -1 \text{ for respective polarizations of the light field } \pi,\ \sigma^+ \text{ and } \sigma^- \tag{3.27}$$

If these rules were strictly obeyed, a transfer from triplet Feshbach molecules to singlet ground-state molecules would not be possible. In the excited state, namely in the $b^3\Pi$ and $A^1\Sigma^+$ potential strong spin-orbit coupling leads to a mixture of the states [Stw04] and hence some of the quantum numbers are not well defined anymore. For strong spin-orbit coupling the molecules are better described by Hund's case c) and "good" quantum numbers are J_a, J and Ω. Nuclear spin quantum numbers are not included in Hund's coupling cases. For the Feshbach molecules, which are more accurately described in a free atom basis, the full set of good quantum numbers if given by $|\nu, f_{\mathrm{Rb}}, m_{f_{\mathrm{Rb}}}, m_{\mathrm{Cs}}, m_{f_{\mathrm{Cs}}}, m_f, l, m_l, M_F\rangle$, where l is the quantum number for the mechanical rotation of the molecule and m_l is its projection on the laboratory axis. The quantum numbers f_{Rb} and f_{Cs} denote the total spin of the atoms, $m_{f_{\mathrm{Rb}}}$ and $m_{f_{\mathrm{Cs}}}$ are their projections on the laboratory axis and $m_f = m_{f_mathrmRb} + m_{f_{\mathrm{cs}}}$. The projection of the total angular momentum on the laboratory axis M_{F} is a good quantum number for the Feshbach, the excited, and the ground state. Selection rules for quantum numbers that are not well defined are not valid anymore. Therefore mixed states can couple to both singlet and triplet potentials and allow to drive a ground-state transfer from triplet Feshbach molecules to singlet ground-state molecules. For more details see Ref. [Her50].

3.4.1 Reactive collisions

Reactive collisions can be detrimental to the creation of a stable dipolar quantum gas. Żuchowski and Hutson have investigated possible reactions of all relevant ultracold alkali-metal dimers [Żuc10b] in dimer-dimer collisions. In the ultracold regime collision energies and trap depths are much lower than energies involved in chemical reactions. This leads to

Table 3.4: Energy changes for the reactions $2XY \rightarrow X_2 + Y_2$ (in cm^{-1}). The quantities in parentheses are uncertainties in the final digit(s). Unstable molecules are marked in red.(The table is adapted from [Żuc10b].)

	Na	K	Rb	Cs
Li	−328(2)	−533.9(3)	−618(200)	−415.38(2)
Na		74.3(3)	45.5(5)	236.75(20)
K			−8.7(9)	37.81(20)
Rb				29.10(15)

trap loss in the case of exothermic reactions and to the concept of energetically forbidden reactions if the reaction is endothermic.

It was found that reactions into a trimer plus a single atom $2XY \rightarrow X_2Y + Y$ or $XY_2 + X$ are endothermic for all alkali dimers. However, atom exchange reactions are only energetically forbidden for some combinations including RbCs (see table 3.4). In KRb and all combinations involving Li these reactions can lead to a major loss channel. For KRb these losses have been observed experimentally [Ni10].

Part II

The RbCs experiment

Chapter 4

Experimental setup

The description of the experimental apparatus is split into two sections. The first section describes the Rb-Cs machine, which simultaneously creates Bose-Einstein condensates of Rb and Cs. The second section describes the spectroscopy setup used for spectroscopy and highly efficient STIRAP ground-state transfer.

4.1 Setup for creation of an ultracold Rb-Cs mixture

Details of the existing Rb-Cs machine are described in the theses of A. Lercher [Ler10] and K. Pilch [Pil09a]. Here I will briefly discuss the methods we use for creating an ultracold gas of Rb and Cs atoms and describe the additions made since Lercher's theses. A summary of fundamental properties of Rb and Cs is followed by a short description of the vacuum apparatus and the scheme used to create cold Rb-Cs samples. Further, a sketch of the coil system used for generation of the magnetic fields is presented. The strategy of simultaneous condensation of the two species is discussed, which is followed by an outline of our scheme we use to combine the two ultracold clouds.

4.1.1 Rb and Cs atomic properties

Rubidium and Cesium, the two most heavy stable[1] alkali metal elements are both well known for their laser cooling properties. Rubidium features two stable isotopes ^{85}Rb and ^{87}Rb whereof the latter gained a lot of attention in the first BEC experiments [And95]. Its main cooling transition at 780 nm lies at a wavelength range that is also used in modern electronic devices like CD-players. Hence plenty of laser diodes are available. Already moderate heating to temperatures below 100 °C yields sufficient pressure to create an atomic beam source.

Cesium is most known for its hyperfine splitting defining the current SI second. It has a single stable Isotope the ^{133}Cs. Similar to Rb it features a low melting point of 28.5 °C. Diode lasers are available for the main cooling transition at 852 nm.

The Zeeman structure of Rb and Cs is shown in Fig. 4.1. For both species in the ground state the hyperfine splitting is comparatively large. Also in the excited state the

---

[1] Fr is even heavier then Cs but it does not have a stable isotope. The short half life time of its longest-lived isotope of 22 minutes makes it unpractical for use in experiments.

splittings are large enough to clearly resolve the spectral lines. Therefore, the cycling transitions in MOT cooling schemes are close to ideal and only a small amount of repumping power is needed for creation of a closed cycle.

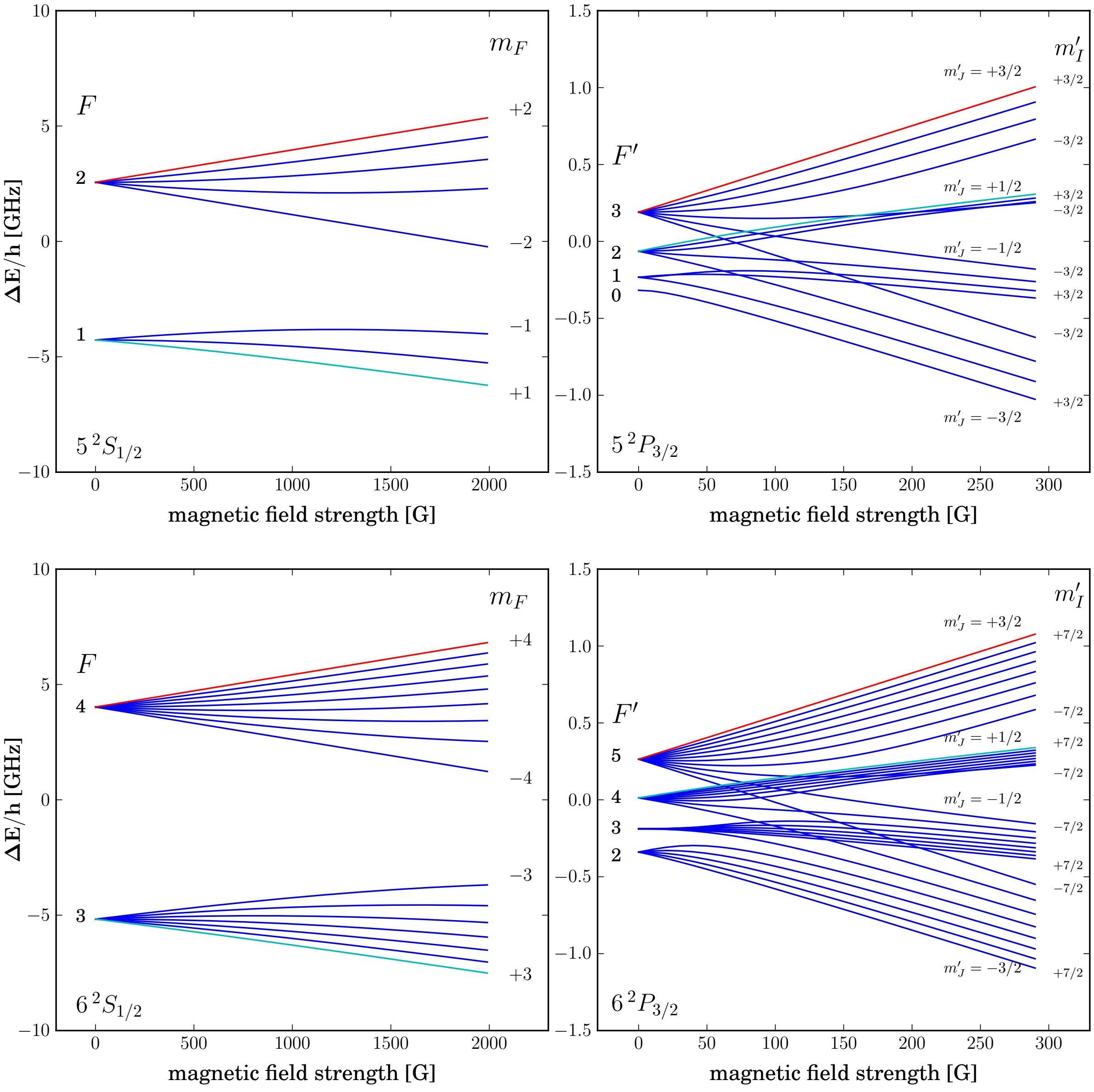

Figure 4.1: Zeeman structure of the Rb (top) and Cs (bottom pictures) states used in the experiment. The green line indicates the state of the atoms when kept in the dipole trap and the repumper transition. The red lines indicate the cycling transition used for cooling and imaging. The graphs are produced from data in [Ste08a, Ste08b].

4.1.2 Creation of cold atomic gases

We use a vacuum apparatus with a Zeeman slower [Phi82] and a glass cell. An atomic beam is created by a series of micro tubes that are connected to two ovens for the two species, each with a separate temperature control. The atomic beam enters the Zeeman slower and reaches the glass cell, where all the experiments take place. The glass cell features a prism, which was used in former times for evanescent wave trapping [Ham03, Ryc04] and now serves as an obstacle preventing the proper positioning of electrodes.

In a first step we simultaneously cool and trap Rb and Cs in a dual species magneto-optical trap (MOT). The MOT's are loaded from the slowed beam using the Zeeman-slowing technique [Phi82]. During the MOT loading phase, which takes about 7 s, the Cs MOT position is shifted with respect to the Rb MOT position in order to avoid light-induced collisional losses. This shift is achieved by radiation pressure of the Cs Zeeman slowing beam, which partially hits the Cs MOT. After the loading phase the mixture is compressed in a compressed MOT (CMOT) phase, in which the magnetic field gradient and the optical detuning from resonance is increased. This yields about 2×10^8 atoms for each species at temperatures of approximately $40\,\mu$K. A scheme of the transitions used is shown in Fig. 4.2.

We apply degenerate Raman-sideband cooling [Ker00, Vul98, Tre01] on both species to further decrease the temperature to about $2-5\,\mu$K and polarize the sample. The atoms are prepared in their lowest magnetic sublevels, which is for Cs the state $|F = 3, m_\mathrm{F} = 3\rangle$ and for Rb the state $|F = 1, m_\mathrm{F} = 1\rangle$. In these states the magnetic-moment-to-mass ratio, neglecting quadratic Zeeman effect, differs by less than 3% allowing for simultaneous levitation of the two species using a magnetic field gradient of $\approx 31\,\mathrm{G/\,cm}$ that is applied at the end of the Raman sequence.

In Cs the dipolar relaxation process induced by second-order spin-orbit interaction [Leo98] gives rise to spin relaxation rates several orders of magnitude higher than for other alkali atoms. Hence, the evaporation efficiency in magnetic traps decreases for phase-space densities above 10^{-3} and limits the maximum achieved phase-space density to a factor of four away from condensation [Tho02]. The inelastic two-body loss problem can be overcome by using Cs in its lowest magnetic state $|3, 3\rangle$, which is not magnetically trappable and hence necessitates an optical approach [Kra04, Web03a].

4.1.3 Magnetic and electric fields

A set of three coil pairs in approximate Helmholtz configuration can each be used to generate homogeneous fields or quadrupole fields depending on their connection as shown in Fig 4.3. The quadrupole coils create the necessary field for the MOT and allow for the levitation of atoms and molecules. The homogeneous fields are needed for tuning the scattering length and to control losses of Cs during the evaporative cooling process. Furthermore, the homogeneous fields are used for Feshbach association and spectroscopy. For the high-field spectroscopy the setup can reach up to 600 G if two sets of coils are used.

The coils are water cooled and protected by a thermal switch, which shuts down the power supplies if the coils reach 40 °C. In steady state operation fields up to 130 G can be created with a single coil pair. Higher fields necessitate the operation with a reduced duty cycle. The time constant for cooling down the coils is on the order of 10 s and operation

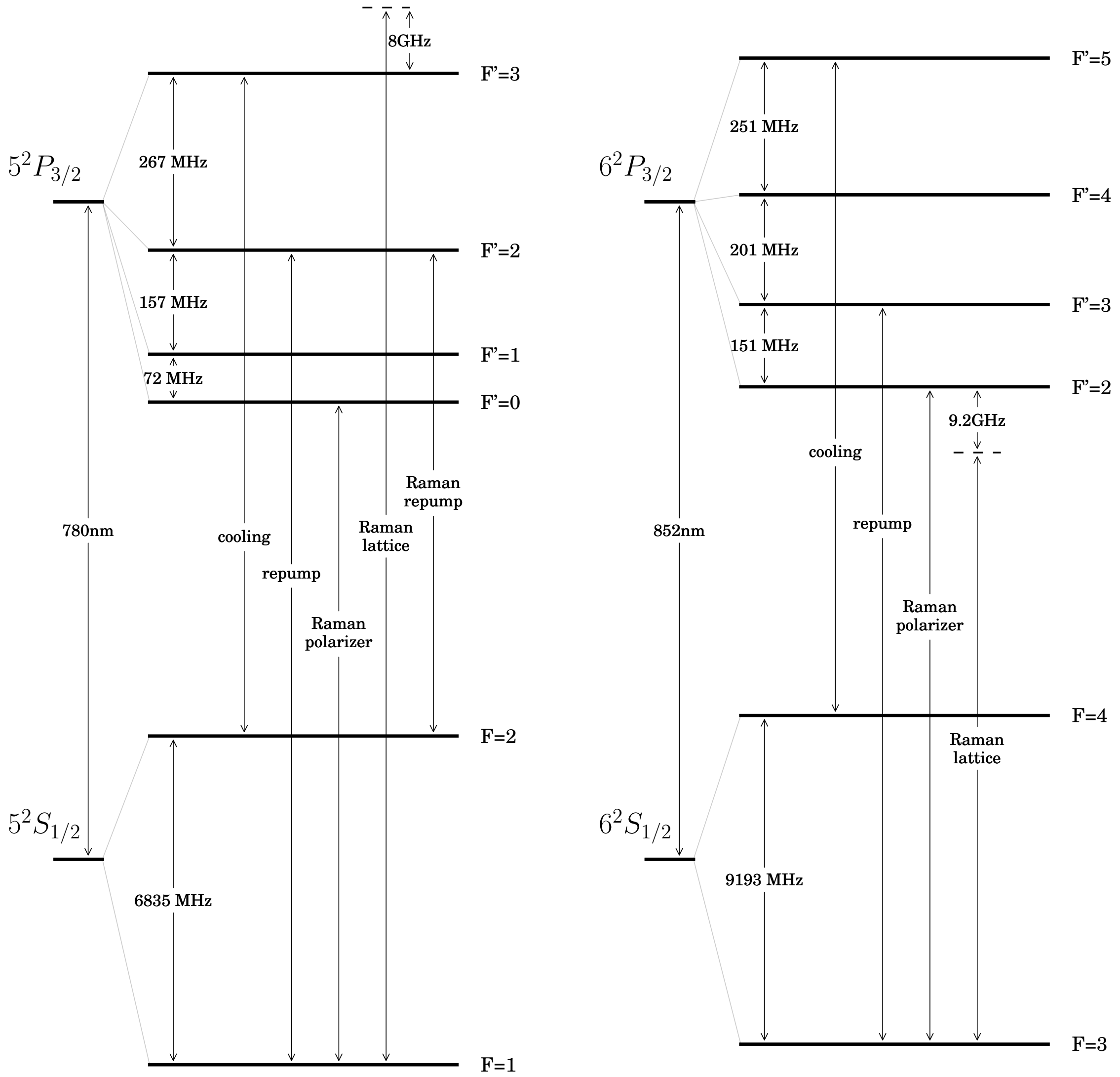

Figure 4.2: The atomic level scheme of Rb (left) and Cs (right) is shown. The arrows indicate the transitions used for the various cooling lasers. The cooling and the imaging laser use the closed cycle between the highest hyperfine states. The Raman laser of the Rb Raman lattice is used either in a red-detuned operation mode, or in a blue-detuned mode, since both operational modes are found to work equally well. (For the plots atomic D-line data is used from [Ste08a, Ste08b].)

at a typical experimental cycle with a total duration of 16 s off time and 2 s on time at 180 G leads to temperature oscillations of typically less than 10 °C.

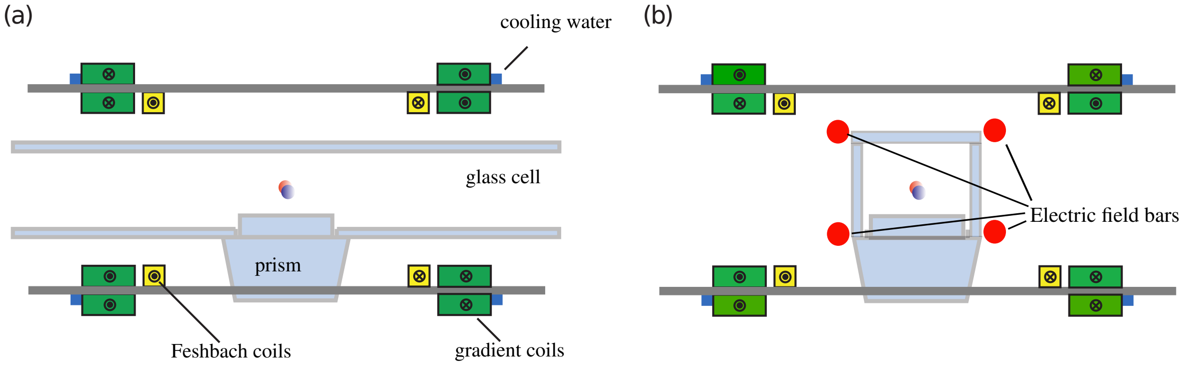

Figure 4.3: Schematic drawing of the setup. The left picture shows a view from the side. Three pairs of coils can be used in different configurations to generate homogeneous and quadrupole fields. The view along direction of the glass cell (b) indicates the position of field bars that can be supplied with up to ±7 kV in order to create electric fields. (figure adapted from [Ler10])

Four rods, made of polished steel, are mounted along the glass cell with a distance between the rods of approximately 6 cm in horizontal direction. These can be used to generate electric fields. The strongest electric fields can be created in horizontal direction and a creation of weak electric fields in vertical direction should be possible as well. Currently two high voltage power supplies from Iseg can supply the field bars with up to ±7 kV. The creation of electric fields could be improved if the rods were placed inside the vacuum. This however, would require major changes in the apparatus.

4.1.4 Simultaneous condensation of Rb and Cs

Cs demands for an optical approach in order to reach quantum degeneracy. An overview of the trapping beams used is shown in Fig. 4.4. The first trap used in the scheme is called reservoir trap. It is created by two trapping beams with a waist of 430 μm and a maximum power of 60 W each, which are switched on already at the end of the MOT phase. The reservoir trap is loaded with atoms that are pre-cooled by the Raman sideband cooling. Due to limited spacial overlap with the atomic cloud from the Raman cooling and evaporation effects we find $\approx 1 \times 10^6$ atoms in the reservoir trap after a 900 ms holding time.

At the time when the reservoir is switched on, 4 small trapping beams are added. Evaporative cooling of the mixture proves to be difficult due to the high 3-body loss the Rb-Cs mixture. To overcome this problem the Rb and the Cs are loaded into two separate dimple traps that are created within the big reservoir trap. As already described in Fig. 3.2 the trap depth for Cs is higher than for Rb. Therefore, Rb escapes from the Cs trap during evaporation leaving only Cs in the trap. For the trap where Rb is trapped, a second laser with a wavelength of 820 nm is overlapped with the trapping beam. This laser is blue detuned against the Cs D-lines and therefore creates a repulsive potential for Cs, which keeps the Cs atoms away from the Rb trap. The 820 nm laser is much closer to the Rb D-lines than the 1046 nm laser and hence the photon scattering rate is much

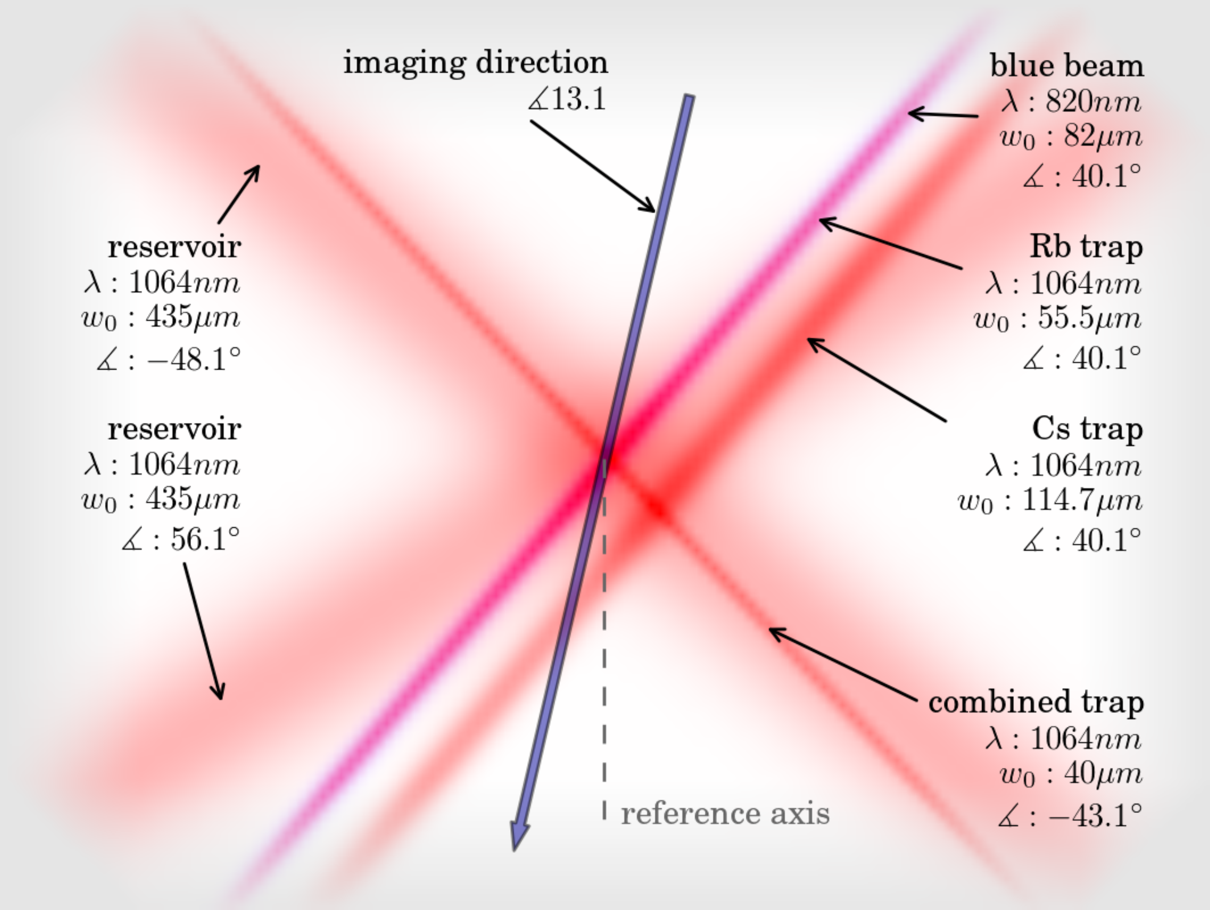

Figure 4.4: Schematic drawing of the dipole traps used in our experiment. In addition to 2 large dipolar traps labelled reservoir beams we use 3 other beams at 1064 nm wavelength labelled **Cs trap, combined trap** and **Rb trap**. The waists of 102 μm, 45 μm and 57 μm are chosen to give optimum conditions for condensation of each species. The Rb trap is overlapped with a 820 nm wavelength trapping beam just to keep the Cs atoms away from the Rb trap during the loading phase.

higher. As a consequence this laser is kept on just long enough to ensure that no Cs remains in the Rb trap. During the evaporation process it is ramped down to zero.

The dimple traps are loaded by slowly ramping down the reservoir. The evaporative cooling loads the atoms into the two dimple traps. Since the scattering cross section of Rb is much smaller then the scattering cross section of Cs, elastic inter species collisions enhance the thermalisation of Rb. After loading, the two clouds are separated from each other by moving the dimples further apart. If the two traps were too close particles evaporating from one trap could enter the other trap and cause undesired heating and losses. This heating and loss effects not only necessitate the separation of the traps but also have further implications on the evaporation scheme.

In single species Cs experiments it is favorable to lower the trap depth in the evaporation process by reducing the power of the trapping beams while the sample remains levitated. This is due to the fact that this way the trap depth is lowered more equally allowing the particles to escape over a larger solid angle. As in the vertical direction the trap is deeper evaporation mainly occurs sidewards. However, a considerable fraction of the hot particles leaving the trap are guided along the trapping beams.

If one of the trapping beams connects two traps, like the combined beam in our setup, the hot atoms from one trap are guided into the other trap. As this is a clearly undesirable situation a different evaporation scheme is followed in our Rb-Cs experiment. The lowering of the optical power is accompanied by a lowering of the levitating magnetic field gradient. This causes evaporation mainly to occur downwards, in the vertical direction.

The vertical evaporation scheme is likely to become a common approach in mixture experiments. Apart from NaK the differences in magnetic-moment-to-mass ratios lead to different effective vertical forces for the two species. Mostly the lighter species experiences a smaller trap depth. However, one could also envision evaporation schemes where the lighter species is levitated and the heavier species is evaporated due to under levitation. Certainly, the scheme chosen also depends on the relative abundance of species, as well as on their thermalisation properties.

The vertical evaporation has some further implications on the whole evaporation process. Similar to rf-evaporation in magnetic traps, the trap frequency barely changes if evaporation is achieved by lowering the levitation forces. This leads to higher densities in the atomic samples, and to a higher critical condensation temperature. The trap frequencies in the combined trap are therefore a compromise to allow sufficient fast thermalisation of the Rb cloud, while keeping the Cs density as low as possible in order to avoid three-body losses.

Depending on which further measurements are intended, the evaporation is continued until quantum degeneracy is reached. For creation of mixtures evaporation is stopped just before BECs are generated. For the creation of Feshbach molecules it is favorable to use cold thermal clouds because at low fields the BECs suffer from an immiscibility problem. The apparatus can create up to 150 k Rb and 100 k Cs atoms at temperatures close to condensation.

For the overlap of the clouds several factors have to be balanced. Firstly, the timespan between the beginning of the overlap of the clouds and the association of molecules has to be kept short since high three-body losses occur during this timespan. Secondly, if the two clouds are moved to fast onto each other the kinetic energy can lead to a heating of the clouds. Thirdly a strong confinement of the moving cloud allows for a faster movement without the excitation of oscillations, but leads to a higher density and hence to higher three-body losses. In the experiment the depths of the traps and the speed of the movement are balanced empirically to yield an optimum number of molecules.

We choose a strategy with a strong confinement in the two directions that are orthogonal to the direction of the movement and a weak confinement in the direction of movement. The overlap procedure takes 75 ms to 150 ms and the clouds mainly overlap during the last 20 ms. The kinetic energy released by the collision of the two clouds is less than 100 nK.

4.2 Laser setup for spectroscopy and ground-state transfer

For spectroscopy of RbCs Feshbach molecules and the creation of ground-state molecules two laser setups were created: a simple, inexpensive setup based on piezo cavities, and a more elaborate setup based on ultra-stable cavities. The light generated by the setups

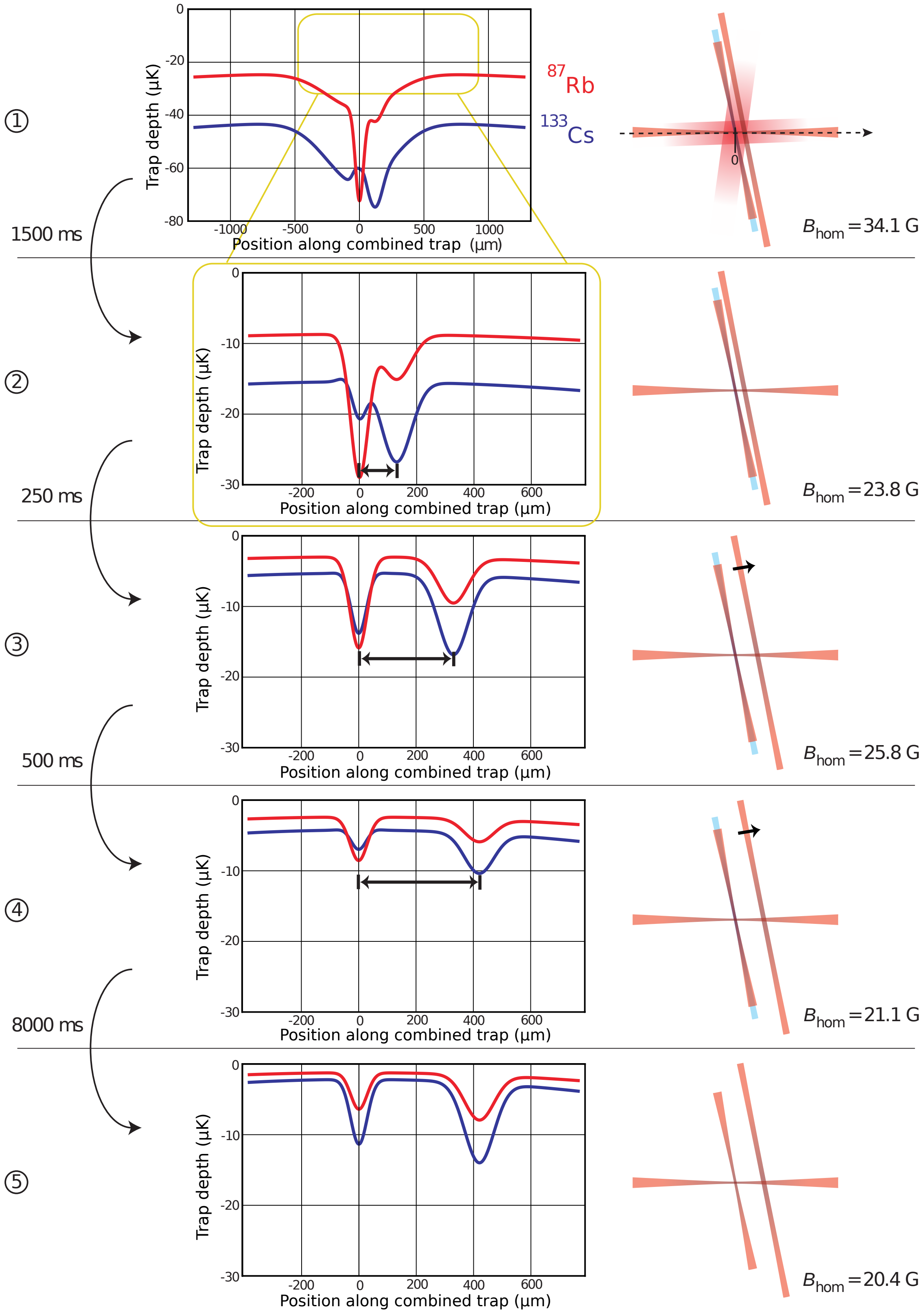

Figure 4.5: Trapping potentials and evaporation scheme in the Rb-Cs experiment. The graphs show the trap depths for Rb (red) and Cs (blue) created by the trapping beams sketched on the right. During the loading process the two traps reside close to each other. For evaporation the distance between the two traps is increased. (Figure adapted from [Ler10])

lies in the $1520 - 1580\,\mathrm{nm}$ and in the $950 - 1000\,\mathrm{nm}$ region and is sent to the experiment via optical fibers. At the experiment the two light beams have a $1/e^2$-intensity waist radii of $39\,\mu\mathrm{m}$ and $42\,\mu\mathrm{m}$ respectively. The waists are chosen such that drifts in the experiment lead to a tolerable amount of realignment while the intensity is high enough to drive the desired transitions. Further the waists have to be larger than the size of the cloud, which is $14\,\mu\mathrm{m}$. The power on the experimental table is around $P = 15\,\mathrm{mW}$, which yields an intensity of $650\,\mathrm{W/cm}^2$. The simple setup was generated to carry out the spectroscopy experiments (see chapter 6). After the spectroscopical data had been taken it became clear that the transition strengths are around $2\pi \times 0.3\,\mathrm{kHz}/\sqrt{\mathrm{mW\,cm}^{-2}}$. This is much weaker than initially expected and almost an order of magnitude weaker than the weakes transition in Cs_2 [Dan08b, Mar09]. The weak transitions leads to more stringent requirements on the linewidth of the lasers for efficient ground-state transfer than in other experiments like Rb_2 [Lan08]. For efficient ground-state transfer in RbCs the laser linewidth has to be reduced to values below $500\,\mathrm{Hz}$ (for details on the linewidth requirements see chapter 7). This led to a second improved setup with ultra-stable optical resonators [Lud07, Aln08b, Aln08a].

In both setups the two spectroscopy lasers are referenced to independent cavities. Two-photon coherence and a narrow two-photon linewidth is reached by narrowing the linewidth of each laser separately. Both setups use commercial diode lasers from Toptica to generate the light that is used in the experiment. Further lasers used in the setup are home-built diode lasers that are conceptually similar to typical diode laser designs such as the ones discussed in Ref. [Ric95]. Diode lasers are well known for their tunabiblity, their comparatively low cost and maintenance and have become the workhorse for quantum optics for decades [Cam85, Wie91, Ric95]. The spectral characteristics of the system is well understood [Fle81]. The width of the frequency spectrum of a free running laser has been predicted by Schawlow and Townes to be [Sch58]

$$\Delta\nu = \frac{h\nu c^2(1-R)^2\mu}{4\pi P L_{\mathrm{opt}}^2}(1+\alpha^2), \tag{4.1}$$

where ν is the frequency of the laser, c is the speed of light, R is the reflectivity of the resonator and $\mu = N_2/(N_1 + N_2)$ describes the inversion, which depends on the occupation of the excited state N_2 and the ground state N_1 of the gain material. Further parameters are the optical power P, the length of the resonator L_{opt} and α, which describes a broadening of the linewidth and has typical values between 3 and 7 for diode lasers and has been introduced by Henry [Hen82]. The resonator of a diode laser typically consists of the reflecting back end of the diode and a grating that reflects 10 to 30 % of the light back into the diode. This low reflectivity of the resonator and the typical short lengths of several cm lead to a comparatively broad Schawlow-Townes linewidth. Therefore the linewidth is usually narrowed by stabilizing the diode lasers via electrical feedback to a frequency reference.

For STIRAP ground-state transfer it is necessary that fluctuations of the laser phase remain small [Yat02]. The laser field can be typically written as

$$\mathbf{E} = \mathcal{E}(t)e^{-i\phi(t)}e^{i\omega t}, \tag{4.2}$$

where $\mathcal{E}$ describes the amplitude of the electric field, $\phi(t)$ describes the phase and ω describes the frequency of the light and is chosen such that the mean value of $\phi(t)$ is zero.

For STIRAP it is important that the fluctuations of $\phi(t)$ remain small. The description of light fields and noise has a long standing history and a standard approach to model noise is to describe the time derivative of the phase $\dot{\phi}$ by a zero-mean Markov process [Gla63, Aga78]. A detailed description of the connection between laser noise and STIRAP transfer efficiency can be found in [Yat02] and the consequences for STIRAP in RbCs are discussed in chapter 7. The analysis of the transfer efficiency treats the derivative of the phase $\dot{\phi}$ as a stochastic variable ξ that is modelled by a stochastic model that reads for null cross correlation as

$$\langle \xi_j(t) \rangle = 0, \quad \langle \xi_j(t), \xi_k(t') \rangle = \begin{cases} DGe^{-G|t-t'|}, & j = k \\ 0, & j \neq k. \end{cases} \tag{4.3}$$

The indices j, k denote the laser the parameter G is the inverse autocorrelation time of the noise and D is connected to the width of the fluctuations.

For the design of the laser system it is important to note that for fast fluctuations $G \to \infty$, the full width half maximum (FWHM) of the laser linewidth equals $2D$. The model in [Yat02] predicts different effects for fluctuations of the frequency offset that have a correlation time shorter than the timescale set by the Rabi frequency and fluctuations that have a longer correlation time. The 500 Hz mentioned above are derived for the worst case of uncorrelated noise.

4.2.1 Piezo cavity setup

Cavities with a finesse of 900 and 2000 respectively are used as a reference. The spectral width of the light is around 1 to 3 kHz. The drifts are on the order of 10 kHz per hour.

We have two identical setups, one for each of the spectroscopy lasers. With the term setup I will therefore refer to the setup for only one of the spectroscopy lasers. The few differences between the two setups will be pointed out where existent.

In order to achieve a narrow line width in a wavelength region where no atomic gas cell spectroscopy is available, lasers can be locked to optical resonators, also referred to as cavities. One of the most prominent locking schemes is the Pound-Drever-Hall (PDH) laser phase and frequency stabilization scheme [Dre83], in which light reflected from an optical resonator is used to generate a frequency dependent error signal. A servo loop controls keeps the frequency of the laser on the resonance of the cavity.

In a simple picture the resonance condition for light in cavities is $N\lambda = 2nl$ where λ is the wavelength of the light, l is the length of the cavity, n is the index of refraction of the medium, and N is an integer number. Hence, the frequency of the resonator and the light locked to the resonator is determined by the length of the resonator. As mechanical vibrations in the high frequency range are suppressed due to mechanical damping, cavities provide a frequency reference with a high short-term stability.

In the low frequency range and for long-term stability, acoustic vibrations and long-term drifts due to thermal expansions have to be avoided. Therefore, cavity mirrors are typically mounted onto a single block of material, called spacer, having a low thermal expansion coefficient. In the piezo cavity setup the spacer consists of a single round piece of quartz glass with a diameter of 3 cm and a central bore of 1 cm diameter. For the 1550 nm setup the length of the spacer is 10 cm, while for the 980 nm setup the length is 20 cm.

To keep the index of refraction n constant, the spacer is surrounded by an airtight housing to avoid large changes in the index of refraction by changes in the pressure or humidity of the air. In this low cost version the cavities are not under vacuum. The housing is temperature stabilized to keep the length of the spacer approximately constant.

In order to tune the resonance frequency of the cavity one of the mirrors is mounted on a piezo that can move the mirror by up to 1 μm. This is enough to tune the resonance frequency by one free spectral range (FSR), which is defined by $\Delta\nu_{\mathrm{fsr}} = c/(2nl)$ and corresponds to the frequency spacing of neighbouring resonances. The change of the length, necessary to change the frequency by a FSR, equals half the wavelength of the light.

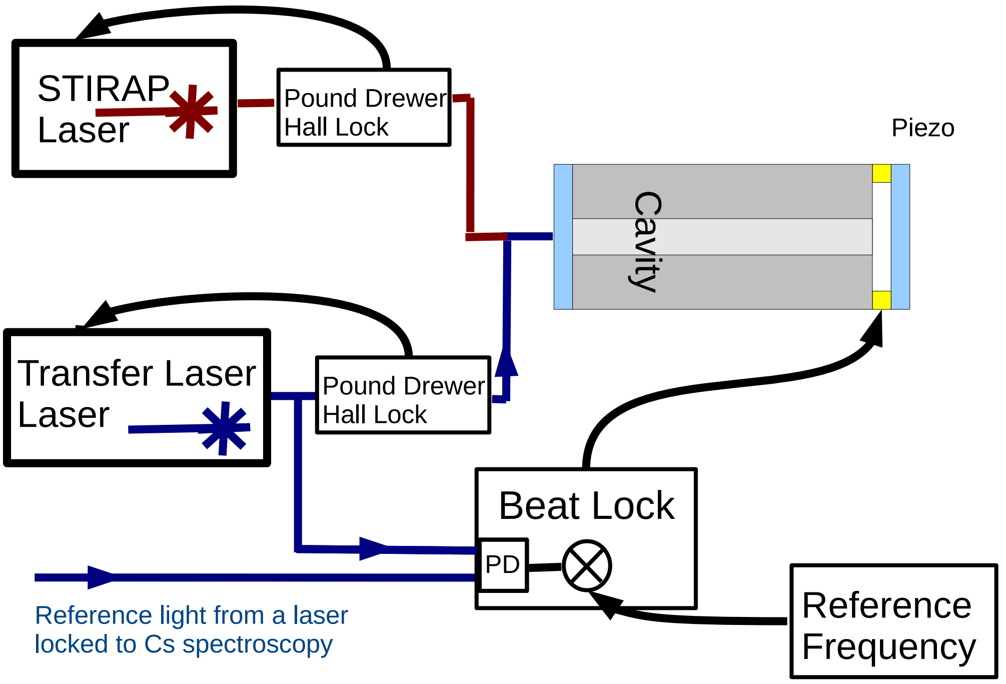

Figure 4.6: Locking scheme for the piezo cavity setup. The STIRAP laser is locked via a PDH lock to the cavity. In order to stabilize the length of the cavity a second laser called transfer laser is locked to the cavity. The cavity frequency is monitored by comparing this second laser to a stable reference. Drifts of the cavity can then be corrected via a feedback to the piezo of the cavity.

As shown in Fig. 4.6, a second laser called transfer laser is locked to the cavity. This laser runs at a wavelength where stable reference light is available. For practical reasons 852 nm is chosen and the reference light is taken from a modulation transfer spectroscopy setup [Shi82] of Cs, which is used to stabilize the light for the Cs MOT. The light of the 852 nm laser is overlapped with the reference light and a beat signal is detected with a photodiode. Changes in the length of the cavity result in a change in the frequency of the beat signal. This beat signal is mixed with a reference frequency and an error signal is generated by a simple method described in [Sch99]. This error signal is used in a servo loop to control the piezo of the cavity.

4.2.2 PDH error signals

In a more quantitative picture, cavities can be understood as Fabry-Pérot interferometers where light is reflected between two mirrors. The phase difference between each reflection δ is then given by:

$$\delta = \left(\frac{2\pi}{\lambda}\right) 2nl. \tag{4.4}$$

For a reflectance of the surfaces R, the transmittance function T is given by

$$T = \frac{(1-R)^2}{1+R^2-2R\cos\delta} = \frac{1}{1+F\sin^2(\delta/2)}, \tag{4.5}$$

where $F = \frac{\pi\sqrt{R}}{1-R}$ is the finesse.

For PDH-locking the light reflected from the cavity is used. A concise yet profound introduction can be found in [Bla01]. In his review, Black describes the reflection coefficient $F(\omega_\mathrm{l})$ as the ratio of the reflected beam E_ref and the incoming beam E_inc, where the two beams are denoted as

$$E_\mathrm{inc} = E_0 e^{i\omega_\mathrm{l} t}, \quad E_\mathrm{ref} = E_1 e^{i\omega_\mathrm{l} t}, \tag{4.6}$$

using complex values of E_0, E_1 to account for phase shifts.

For a symmetric cavity without losses $F(\omega_\mathrm{l})$ is given by

$$F(\omega_\mathrm{l}) = E_\mathrm{ref}/E_\mathrm{inc} = \frac{R\left[\exp\left(i\frac{\omega_\mathrm{l}}{\Delta\nu_\mathrm{fsr}}\right)-1\right]}{1-R^2\exp\left(i\frac{\omega_\mathrm{l}}{\Delta\nu_\mathrm{fsr}}\right)}, \tag{4.7}$$

where R is the amplitude reflection coefficient of the mirrors.

For PDH locking the phase of the incoming laser is modulated by a modulation frequency $\Omega_\mathrm{m} \approx 2\pi \times 50\,\mathrm{MHz}$. The incoming field then reads

$$E_{inc} = E_0 e^{i(\omega_\mathrm{l} t + \beta\sin\Omega_\mathrm{m} t)}, \tag{4.8}$$

where β is called the modulation index. This leads to the generation of sidebands in the frequency space, which are split by the modulation frequency Ω_m. The amplitudes of the carrier P_c and the sidebands P_s are described by Bessel functions as

$$P_\mathrm{c} = J_0^2(\beta)P_0, \quad P_\mathrm{s} = J_1^2(\beta)P_0, \tag{4.9}$$

where P_0 is the total power of the incident beam. Hereafter it will be assumed that β is small enough for higher order sidebands to be neglected. In this case the total power is expressible as $P_\mathrm{c} + 2P_\mathrm{s} \approx P_0$.

For a PDH frequency measurement the light reflected from the cavity is sent onto a photodiode. Given that the reflection coefficient $F(\omega_\mathrm{l})$ is different for the carrier and the sidebands, amplitude fluctuations can be observed at the photodiode with a frequency Ω_m. If the signal from the photodiode is mixed with the frequency sent to the phase modulator, an error signal ϵ can be obtained that is antisymmetric on the cavity resonance. For an appropriate phase shift of $\pi/2$ between the photodiode signal and the mixing frequency, the error signal is expressible as

$$\epsilon = -2\sqrt{P_\mathrm{c}P_\mathrm{s}}\mathrm{Im}\left\{F(\omega_\mathrm{l})F^*(\omega_\mathrm{l}+\Omega_\mathrm{m}) - F^*(\omega_\mathrm{l})F(\omega_\mathrm{l}-\Omega_\mathrm{m})\right\}. \tag{4.10}$$

The error signal becomes maximal for $P_\mathrm{c} = 2P_\mathrm{s}$. For low finesse cavities the error signal remains high for a frequency detuning smaller than the modulation frequency. For a high-finesse cavity the error signal approaches zero between the resonance and the sideband. Therefore, for PDH locking to a high-finesse cavity, careful offset adjustment of the locking circuit is necessary in order to maintain the full capture range spanned by the sidebands. The steepness of the error signal on resonance increases with the finesse and reaches $0.75\,\mathrm{V/kHz}$ for an error signal of $2\,\mathrm{V}$ peak to peak amplitude and a finesse of $400\,000$. This slope allows to evaluate the frequency fluctuations of a laser from the fluctuations of the PDH error signal.

4.2.3 High finesse cavity

A high STIRAP transfer efficiency necessitates narrow linewidth lasers. Hence, high-finesse cavities are used as a reference to stabilize the lasers. Such cavities are well known for atomic clocks and lasers stabilized onto the cavities can reach the sub-Hertz limit if stabilization is carried out with a low noise feedback circuit. Our setup follows the description in [Lud07, Aln08b, Aln08a] and is described in detail in [Ram11]. Therefore I will just mainly summarize the main characteristics. As shown below, for a STIRAP

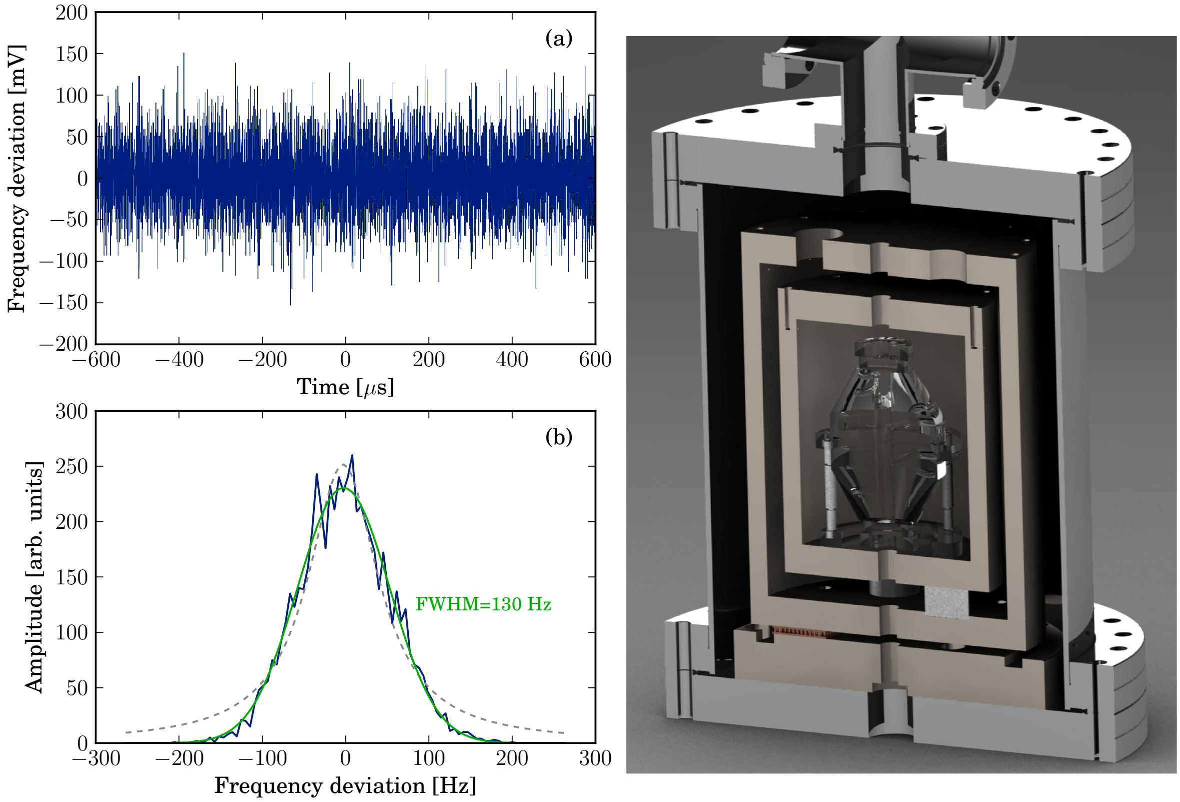

Figure 4.7: Graph (a) shows a noise trace of the PDH error signal of the laser that is limiting the two-photon linewidth of the setup. It has been recorded with a digital oscilloscope. The corresponding frequency distribution is shown in (b). The blue line is a histogram of (a), the green and gray lines show a Gaussian and a Lorentzian fit respectively. The graph on the right shows a drawing of the cavity including two thermal shields and a vacuum housing.

efficiency in RbCs above 90% the laser linewidth (FWHM) has to be below 500 Hz. This the linewidth does not need to be as narrow as it needs to be for high resolution spectroscopy [Par11]. Therefore, standard electronic components used in our group are used in the feedback circuit.

To avoid frequency drifts the temperature of the cavity has to be well stabilized. Therefore, the technical setup as shown in Fig. 4.7 features a thermal shield that can be temperature stabilized using Peltier elements and a second inner shield that acts as a low pass filter for temperature fluctuations. The temperature is stabilized via a high resolution digital PID circuit. The circuit is digital because, for long timescales, analog circuits tend to suffer from inaccurate integrators when timescales exceed several hours[2].

Changes in the frequency of the cavity can also occur due to changes in the index of refraction of the medium between the mirrors. Hence for high-finesse cavities a vacuum housing is mandatory. In this case high (but not ultra high) vacuum conditions below 10^{-8} mBar are sufficient as this reduces the effect of the air to a shift blow 1 Hz. The laser is locked to the cavity via the PDH locking technique described above. Approximately 300 μW are sent to the optical cavities. In the current setup two similar cavities are built, and each laser is locked to a separate cavity. This allows for a higher finesse as mirrors that are optimal for two different wavelengths are difficult to produce. The cavities are planned to have a finesse well above 200 000 and a finesse of 440 000 is measured using cavity ring down measurements.

To measure the linewidth of the lasers, the most reliable method is to compare two independent systems. However, currently there is only one laser system available (for each wavelength). Still some information on the linewidth can be gained from the error signal generated by the PDH method. For a finesse of 400 000 the calculated slope of the error signal is $s_{\mathrm{err}} = 0.75\,\mathrm{V/kHz}$ given a peak-to-peak amplitude of 2 V. The voltage noise of the error signal that is used to drive the feedback loop can be recorded with a digital oscilloscope. The slope s_{err} can be used to convert voltage into frequency fluctuations and thereby estimate the linewidth of the laser. A histogram of the frequency fluctuations can be plotted. The width of the distribution corresponds to the linewidth of the laser.

The estimation of linewidths from an error signal, that is used in a feedback loop does not qualify as a measurement of the linewidth, but rather is a quick and rough estimate. A setup of two identical lasers is currently created, which will allow to characterize the linewidth in a more clean and reliable way. In Fig. 4.7 a time trace of the error signal (a) and the corresponding frequency distribution is evaluated (b) using the slope of the error signal. The graph shows the linewidth of the laser creating the light in the 1550 nm range. This laser is a commercial laser that is not designed for high resolution spectroscopy and has a digital electronics for a stepper motor close to the circuits for the laser diode. This deteriorates the linewidth of the laser. This laser was chosen as an interims solution, when it turned out that a laser diode ordered for a home-built laser was not single mode. The laser has meanwhile been replaced. The linewidth data for this very laser is presented here because, firstly, it was used for the ground-state transfer measurements presented in this thesis and, secondly, it has the broadest linewidth and thus the two-photon linewidth of the setup is mainly determined by this laser. Since the spectrum of the laser is determined by technical noise, it is not surprising that it has a Gaussian line shape. The frequency

---

[2] On this long timescale even small input bias currents and offset drifts of operational amplifiers used in analog integrators can lead to significant errors

spectrum is fitted by a Gaussian and a FWHM of 130 Hz is obtained. This gives a rough estimate of the linewidth of the laser to be 130 Hz.

4.2.4 Frequency tuning

To ensure a wide-range tunability of the STIRAP laser system, the lasers stabilized on the cavities (reference lasers) are not used directly for STIRAP but a second set of lasers is used. These second lasers, which are used for STIRAP, are stabilized to the reference lasers via the so called phase-lock technique [Ric95]. The phase-locking technique is described in [Ric95] and our scheme is different only in the electronic components that are used. Two lasers are overlapped on a photodiode and a beat note is observed with its frequency corresponding to the frequency difference of the two lasers. The signal from the photodiode is mixed[3] with a reference signal from a Rohde & Schwarz frequency generator. If the two frequencies are equal the obtained DC signal corresponds to the phase difference between the two initial signals, which in turn depends on the phase difference between the two lasers. This phase signal is used as an error signal for a feedback loop to stabilize the STIRAP laser. The electronics for the servo loop is home-built and described in [Mar12].

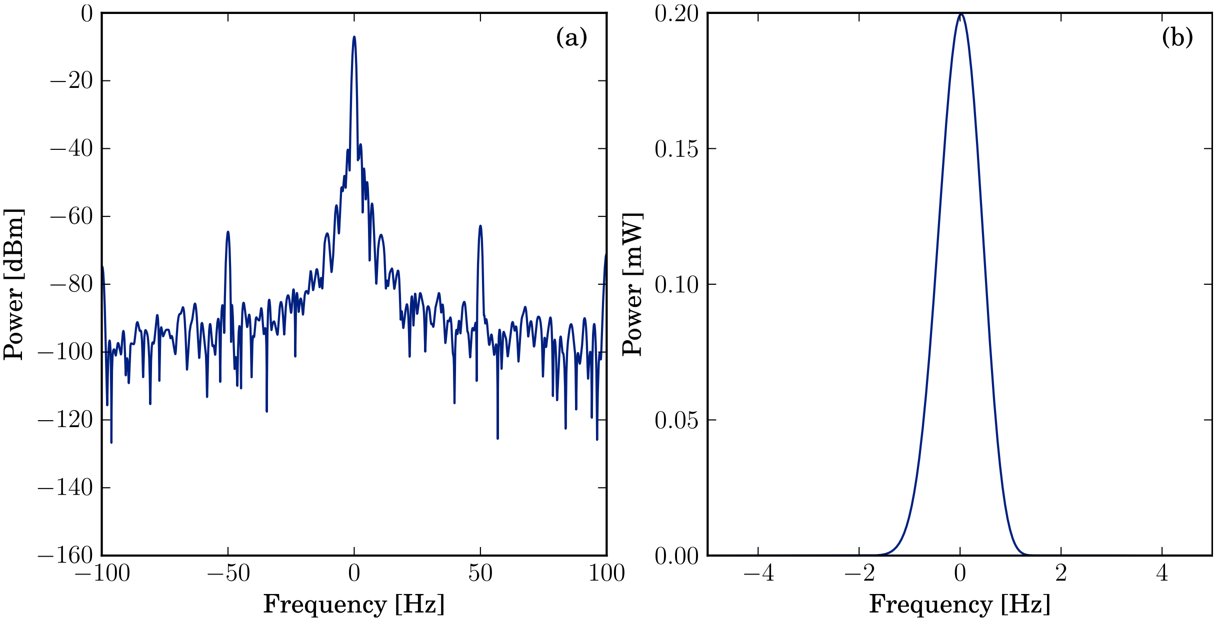

Figure 4.8: Beat signal of two lasers referenced to each other via a phase lock technique measured with a spectrum analyzer. Graph (a) shows a logarithmic scale while (b) shows a linear scale. The width of the peak in (b) is limited by the resolution bandwidth of the spectrum analyzer. In both graphs a frequency offset of ≈ 672 MHz has been subtracted.

The frequency difference of the two lasers can be tuned by tuning the reference frequency from the frequency generator. In our case the tuning range exceeds 1 GHz, which is half a FSR of the reference cavities. As the maximum frequency difference between any arbitrary frequency and a resonance line of the cavity is half a FSR, the locking scheme allows for stabilizing the light over the whole tuning range of the laser.

Another option to allow tunability would be to shift the frequency with an accusto-optic modulator (AOM). However, the tuning range of AOMs is limited and therefore

---

[3] The mixer used for mixing of the two frequencies is a ZFM-2-S$^+$ from Minicircuits.

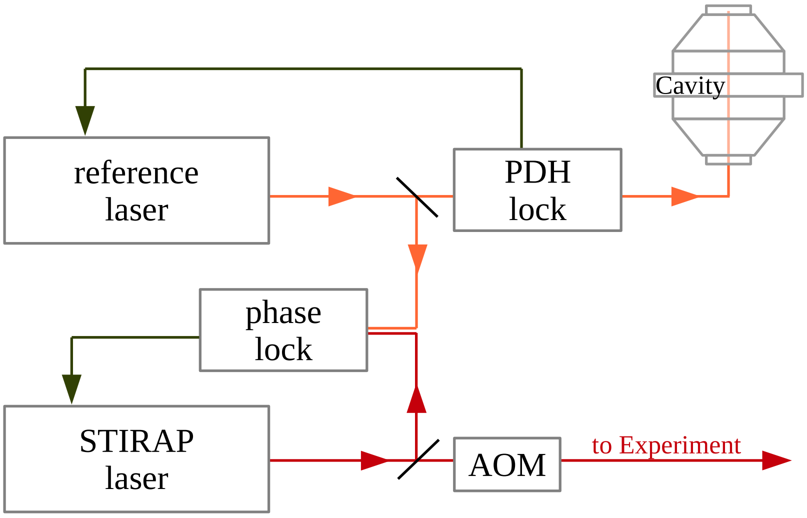

Figure 4.9: Block diagram of the locking scheme used for STIRAP. A reference laser (home-built) is locked to a high-finesse cavity via PDH locking technique. A second laser (Toptica DL-Pro) is referenced to the first laser via radio-frequency phase-locking technique [Ric95]. An AOM is used to control the intensity of the light that is sent to the experiment.

that solution would not be as flexible as a phase lock. By locking one laser to another via phase-lock technique, the linewidth of the system can be increased if the lock is not perfect. A spectrum of the beat note that is shown in Fig. 4.8 shows that the relative frequency fluctuations are less than 1 Hz. The second laser follows almost exactly the reference laser with the desired frequency offset. Therefore, the linewidth of the STIRAP system is increased by less than 1 Hz due to the use of the phase lock.

The intensity of the light sent to the experiment is regulated via an AOM, which allows for generation of controlled pulse shapes on a μs time scale. An overview block diagram of the whole scheme is shown in Fig. 4.9.

The high-finesse cavity setup combines a narrow laser linewidth with a highly flexible tuning range of several tens of nm. The laser power available at the experiment exceeds 10 mW.

4.2.5 Ambient magnetic field noise

Noise in the laser system is not the only effect that can limit the efficiency of STIRAP ground-state transfer. As explained later, fluctuations of the magnetic field can shift the different states of the molecules with respect to each other. This can lead to fluctuations in the detuning of the laser system from resonance. Therefore, the magnetic field noise is undesired component in the ground-state transfer. Its strong influence on the STIRAP ground-state transfer efficiency necessitates a measurement of the magnetic field noise in order to have a complete picture.

Ambient magnetic field noise is generated by various devices in the laboratory and its surroundings. Depending on the operation of the neighbouring experiments and machines it can vary considerably. However, the STIRAP data is taken almost exclusively at times when there was no operation of major devices nearby. Therefore, a measurement of the

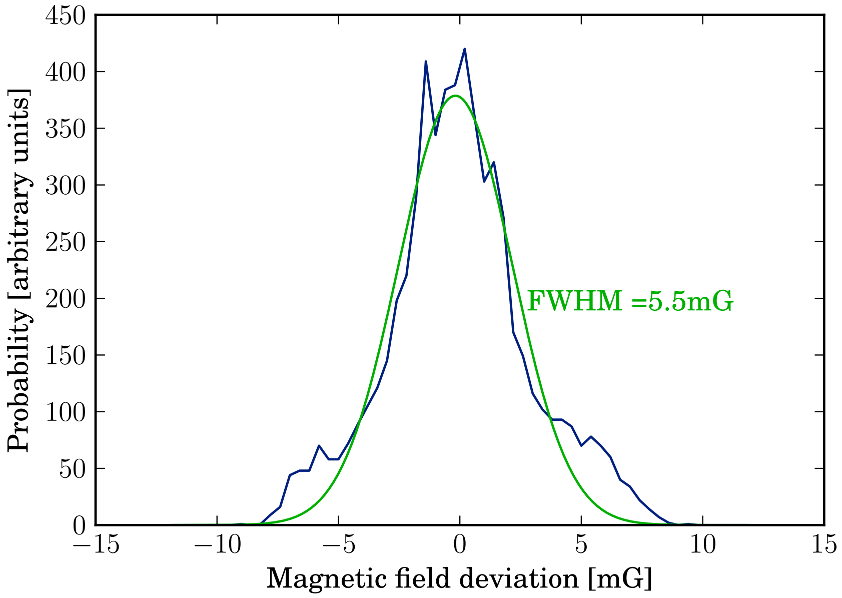

Figure 4.10: Histogram of the ambient magnetic field fluctuations close to the center of the experiment a measured via a “Stefan Mayer Fluxmaster”. The green line represents a Gaussian fit to the data.

noise on a “quiet” day should give the most accurate picture of the noise present in the setup. Since the measurement device, a “Stefan Mayer Fluxmaster”, does not allow to measure at high fields, only ambient magnetic field noise could be measured. Hence the measured noise rather gives a hint on the minimal magnetic noise present. Also high-frequency components that are generated by devices such as switching power supplies are not measured since “the Fluxmaster” has a limited bandwidth of 1 kHz.

In Fig. 4.10 a histogram shows the magnetic field fluctuations present in the system when the coils are switched of. The FWHM of 5.5 mG is a typical value for magnetic field noise in our laboratory environment.

Chapter 5

RbCs Feshbach molecules

The creation of Feshbach molecules is a comparatively simple but important step in our scheme to produce ultracold dipolar ground-state molecules. Feshbach association is a widely used technique [Dui04, Hut06, Köh06, Chi10]. Feshbach association is achieved by ramping the magnetic field over a Feshbach resonance [Reg03, Her03, Xu03, Dür04]. The creation of RbCs Feshbach molecules is discussed in detail in our publication [Tak12]. In this chapter first the model of the Feshbach structure of RbCs is presented. With this Feshbach structure the association into two different molecular states is described in the following sections and the chapter concludes with some characterization of the Feshbach molecule sample.

5.1 Feshbach structure of RbCs

The determination of the Feshbach structure and the assignment of quantum numbers to the observed Feshbach resonances involved a close collaboration between experiment and theory [Tak12]. Feshbach resonances had been observed in this experiment already by Pilch *et al.* [Pil09b, Pil09a]. With a perfect knowledge of the BO-potentials of the molecule it would be possible to predict the energy of the least bound vibrational levels and the magnetic field values at which Feshbach resonances occur. The energy of the least bound levels however depends critically on the fine details of the BO-potential and a determination of the positions of FRs is thus a priori not possible. Therefore, experiments were carried out to test the assignments and the models were adapted to the new data in an iterative process.

Prior to our measurements the precision to which the BO-potential of RbCs was known did not allow to predict the position of Feshbach resonances. BO-potential energy curves for were developed by Docenko *et al.* [Doc10] and are based on measurements using Fourier transform spectroscopy. By this method a broad range of vibrational and rotational levels can be addressed and the accuracy in the determination of the energies is the order of $h \times 1\,\mathrm{GHz}$. While this precision is high enough to estimate the number of bound states, the exact position of the Feshbach states can not be derived. For the initial modelling the short-range part is constrained to follow the potential curves while the long-range parameters are adjusted to produce the measured Feshbach resonances and weakly bound states.

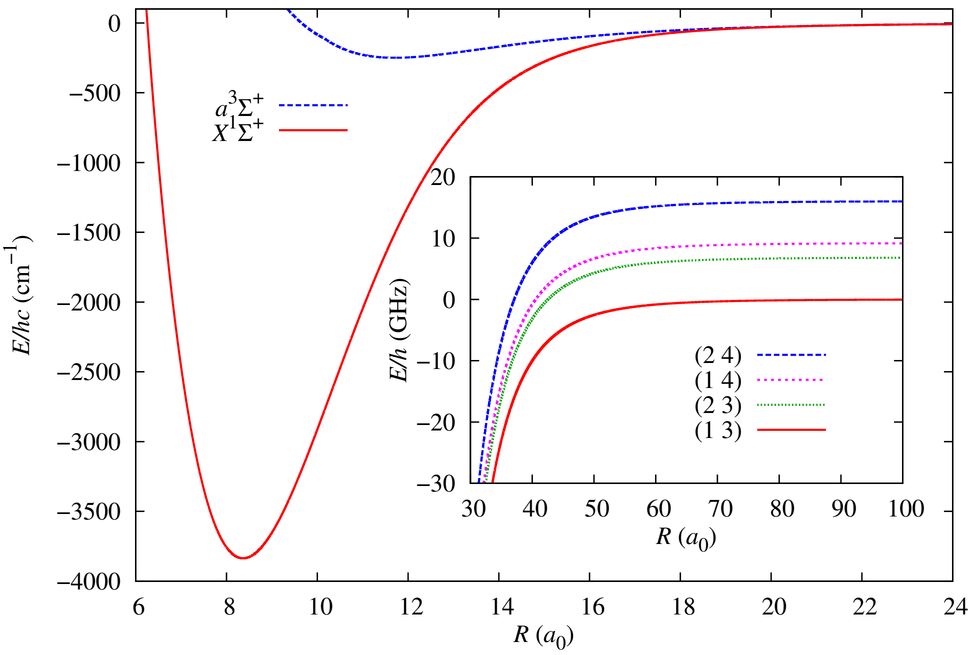

Figure 5.1: Born-Oppenheimer potentials for the electronic ground state of RbCs. The inset shows an expanded view of the long-range potentials separating to the four different hyperfine thresholds. Our atoms are initially in the (1 3) state, therefore the (2 3), (1 4) and (2 4) BO-potentials represent closed channels that can cause Feshbach resonances. (Figure taken from [Tak12].)

Quantum numbers describing Feshbach molecules

The quantum numbers used to describe Feshbach molecules differ from the quantum numbers used to describe deeply bound molecules. For RbCs in the electronic ground state there are 4 field-free atomic thresholds, which are labelled in increasing order of energy by $(f_{\mathrm{Rb}}, f_{\mathrm{Cs}}) = (1,3)$, $(2,3)$, $(1,4)$, and $(2,4)$. In a magnetic field each threshold splits into $(2f_{\mathrm{Rb}}+1)\cdot(2f_{\mathrm{Cs}}+1)$ sub levels labelled $|f_{\mathrm{Rb}}, m_{\mathrm{Rb}}\rangle + |f_{\mathrm{Cs}}, m\mathrm{Cs}\rangle$. Feshbach molecules at zero magnetic field can be described by a set of quantum numbers (f_{Rb}, f_{Cs}, F, M_F) where F is the resultant of f_{Rb} and f_{Cs} and $M_F = m_{\mathrm{Rb}} + m_{\mathrm{Cs}}$. In the non-rotating field-free case these quantum numbers are exact. An external field mixes states with different F values, destroying the exactness of F as a quantum number. It can also mix different f_{Rb} and f_{Cs} values. However, due to the large hyperfine splitting of Rb and Cs, f_{Rb} and f_{Cs} remain meaningful quantum numbers in the field region used in this experiment (see also Fig. 4.1). Therefore, the Feshbach molecules are best described by $(f_{\mathrm{Rb}}, m_{\mathrm{Rb}}, f_{\mathrm{Cs}}, m_{\mathrm{Cs}})$.

Further quantum numbers are needed for the molecules' end-over-end angular momentum L and the molecular vibration n. The former has values of $L = 0$, 1, 2, etc. designated by $s, p, d,$ etc. respectively. The latter is specified with respect to the asymptote of the atom pair ($n = 0$), so that the topmost bound level is $n = -1$, the next lower vibrational level is $n = -2$, and so on. The projection of L onto the field axis is M_L. The sum of all angular momenta projected onto the field axis $M = m_{\mathrm{Rb}} + m_{\mathrm{Cs}} + M_L$ is always a "good" quantum number. The total angular momentum M is conserved as long there are no external processes like collisions or interactions with photons involved. In the general case the weakly bound states are labelled by $|n(f_{\mathrm{Rb}}, f_{\mathrm{Cs}})L(m_{\mathrm{Rb}}, m_{\mathrm{Cs}}), M\rangle$. The free atom state we use $|f_{\mathrm{Rb}}, m_{\mathrm{Rb}}\rangle|f_{\mathrm{Cs}}, m_{\mathrm{Cs}}\rangle = |1,1\rangle|3,3\rangle$ has $M = 4$. Hence only Feshbach states with this value are considered and M is sometimes omitted in the notation.

Feshbach structure and experimental data

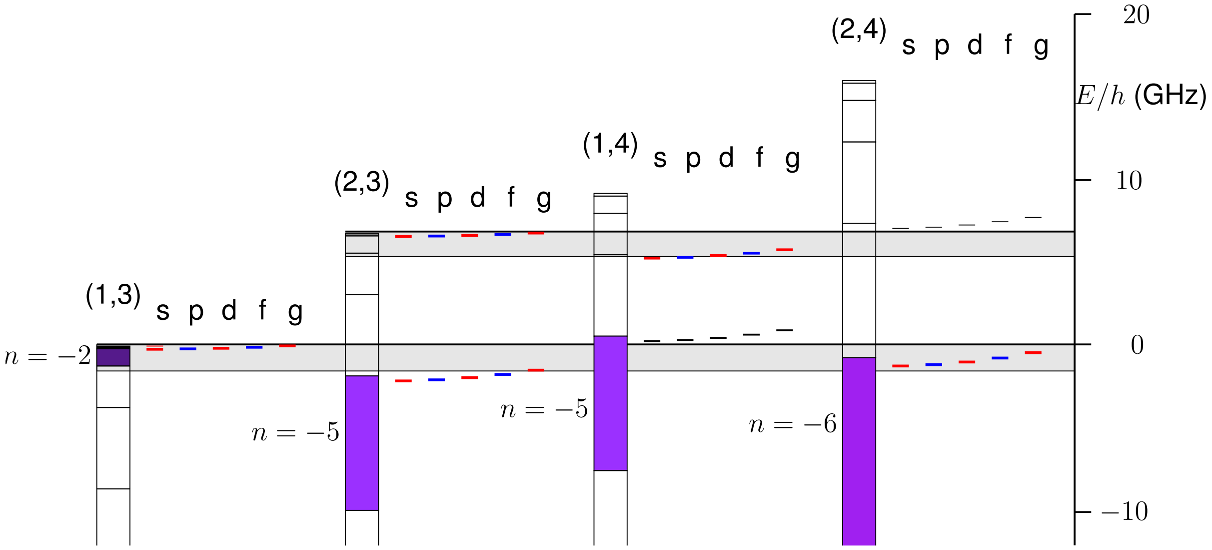

Figure 5.2: Thresholds for RbCs and the energy ranges within which each vibrational state must lie are indicated by gray boxes. The energy range of the vibrational states that can cause Feshbach resonances for atoms in the $(1,3)$ state is colored. The horizontal boxes indicate the range in which the energies of the states can be tuned with respect to each other by a magnetic field of up to 500 G. Selected levels are shown as a function of L(labelled $s, p, d, \cdots$) for a specific choice of binding energy of the least bound state. (Figure taken from [Tak12].)

The number of bound states that has to be considered for Feshbach resonances can be limited by some general considerations as illustrated in Fig. 5.2. The spacing of the highest vibrational levels depends on the long-range part of the molecular potential, namely the long-range dispersion coefficients [Der01, Por03]. This can be used to predict ranges of binding energy where the vibrational levels lie. Zero-energy Feshbach resonances are caused by molecular levels that cross atomic thresholds as a function of magnetic field. The level shifts due to the Zeeman effect at fields below 500 G can be estimated to be below 1.5 GHz. As illustrated in the figure by gray vertical boxes this energy range is smaller than the vibrational energy spacing of the lower vibrational levels. Therefore, only one vibrational level of each closed channel BO-potential can cause Feshbach resonances. Unlike lighter alkali molecules, in RbCs not only the $v=-1$ vibrational level contributes to Feshbach resonances but levels down to $v=-6$ can create Feshbach resonances even at low magnetic field. This is due to the large hyperfine splitting in Rb and Cs and a large van der Waals C_6 coefficient. A specific choice of the scattering length and thereby the binding energy of the least bound state for $L=0$ of 110 kHz below threshold limits the number of levels that can cause Feshbach resonances. This least bound state has been assumed by theorists and the experimental confirmation by free-bound magnetic-field modulation spectroscopy [Tak12] strenghthened the confidence in the model. In this case only the levels $|n(f_{\mathrm{Rb}}, f_{\mathrm{Cs}})\rangle = 2(1,3)\rangle$ and $|-6(2,4)\rangle$ can cause resonances at the $|1,1\rangle + |3,3\rangle$ threshold. As $M=4$ only states with $M_F=4$ can contribute for s-states

Field B (G)	Width Δ (G)
181.64(8)	0.27(10)
197.06(5)	0.09(1)
217.34(5)	0.06(1)
225.43(3)	0.16(1)
247.32(5)	0.09(3)
279.12(5)	0.09(3)
310.69(6)	0.60(4)
314.74(11)	0.18(10)
352.65(34)	2.70(47)

Figure 5.3: Observed Feshbach resonances. The list shows a selection of the broadest incoming s-wave resonances that are observed and could be used for Feshbach association. The magnetic field uncertainties result from a quadrature of resonance position uncertainty due to atom number noise and an estimated field calibration error of 0.03 G. The complete data set including narrower resonances and incoming p-wave resonances can be found in [Tak12].

and only states with $M_F = 2 \cdots 6$ for d-states. With the above considerations the degrees of freedom are sufficiently restricted to generate a model of the RbCs Feshbach structure.

In order to fit the Feshbach structure different sets of computer codes were used by the theoretical groups [Pas07, Tie98, Tak12] that gave results in agreement with each other. However, initially there was no assignment of quantum numbers and our older data contained resonances at positions where no (incoming s-wave) resonances were predicted by the models. Improvements of the experimental setup that led to colder atomic samples allowed to remeasure some of the Feshbach resonances in order to distinguish between incoming p-wave and incoming s-wave resonances. The set of observed Feshbach resonances was extended and magnetic field regions where resonances are predicted were remeasured. An iterative process involving calculations of the theory groups and measurement of Feshbach resonances at selected magnetic fields led to a refined model of Feshbach structure of RbCs. The result of the model is given in Fig. 5.4. A list of Feshbach resonances that could be used for association of molecules is shown in table 5.3.

In the figure the states that can cause resonances at the $|1,1\rangle + |3,3\rangle$ threshold are shown. The colors correspond to the M_F values as indicated in the graph.

The knowledge of the Feshbach structure allows to select the most suitable Feshbach states for creation of Feshbach molecules and ground-state transfer. For the creation of Feshbach molecules, the Feshbach resonances have to be sufficiently broad in order to allow for an adiabatic field ramp despite the magnetic field noise always present in experiments. Further, the resonances have to be sufficiently narrow in order to allow quick ramps over the regions of diverging scattering length. Since the wave function overlap between the Feshbach molecules and the deeply bound levels of the electronic excited states is better for more deeply bound Feshbach levels, it is desirable to create Feshbach molecules in one of the $n = -6$ levels. Lastly, the cooling of our magnetic field coils allows the creation of high magnetic fields only for a limited time. For the present experimental setup it therefore is desirable to associate Feshbach molecules at low magnetic fields. We therefore opt for states of the $n = -6$ vibrational level that cause Feshbach resonances at low magnetic fields.

5.2 Creation of Feshbach molecules

5.2.1 Association into the $|-6(2,4)d(2,2)\rangle$ state

Association of Feshbach molecules typically is achieved by an adiabatic magnetic field ramp over the Feshbach resonance from high to low magnetic field values.As shown in Fig. 5.5, the $v = -1$ least bound state in RbCs lies close to the atomic threshold and there are avoided crossings between this state and the $v = -6$ Feshbach states. Since these avoided crossings are very close to the Feshbach resonances, the Feshbach molecules automatically follow the adiabatic states and are turned into the $|-1(1,3)s(1,3)\rangle$ state. This state has the same magnetic moment as the free atom state and the molecules in this state cannot be separated from the atoms by Stern-Gerlach separation [Her03]. Therefore, the magnetic field is further lowered until the next avoided crossing is reached. An adiabatic ramp over this avoided crossing then leads to the creation of Feshbach

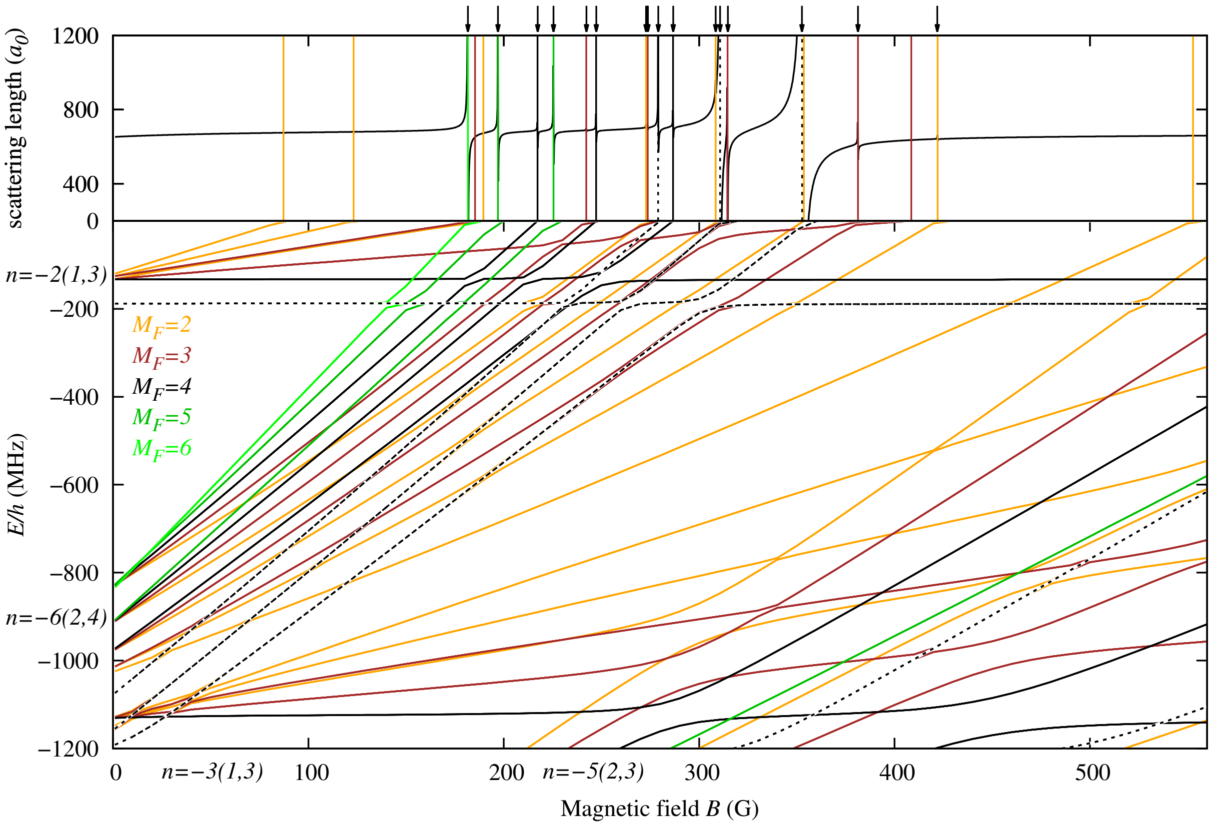

Figure 5.4: The upper graph shows the scattering length of RbCs for the $|1,1\rangle + |3,3\rangle$ threshold. The lower graph shows the weakly bound states for $M = 4$ calculated using fitted potentials. Bound states are plotted in a color corresponding to their value of M_F. States arising from $L = 2$ (d states) are shown as solid lines whereas states arising from $L = 0$ (s states) are shown as dashed lines. On the scattering length plot (upper part), the resonance positions are marked as vertical lines with the same color as the bound state that they arise from. The hyperfine manifolds of the $L = 2$ states are indicated by slanted text. The arrows above the plot indicate the measured positions of incoming s-wave resonances. (Graph taken from [Tak12].)

molecules in the desired $v = -6$ state. This leads to the fact that in order to reach a certain Feshbach state, the molecules are formed at the next higher Feshbach resonance. In Fig. 5.5 the Feshbach levels that are used in order to create the Feshbach molecules in the $|-6(2,4)d(2,2)\rangle$ and $|-6(2,4)d(2,4)\rangle$ final states are shown.

The Feshbach resonance at 225.4 G is the broadest Feshbach resonance below 300 G that can be used to create molecules with our scheme in a $v = -6$ Feshbach state. The resonance at 181G is broader but a $v = -6$ Feshbach state below the $v = -1$ state cannot be reached by adiabatic field ramps.

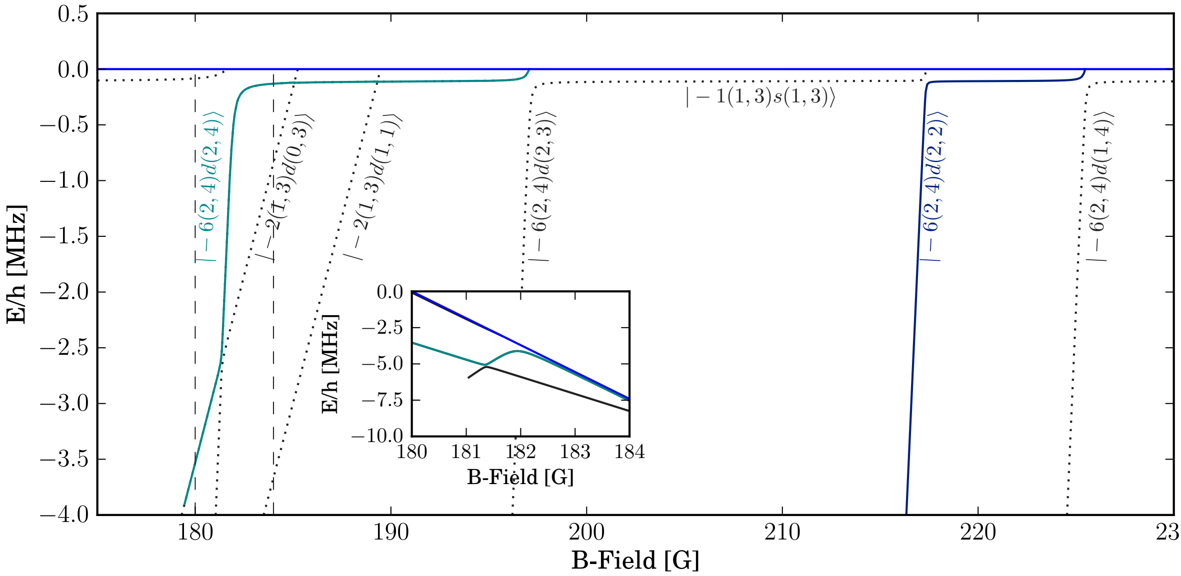

Figure 5.5: Expanded view of the Feshbach structure. In the large graph the energies are shown relative to the dissociation limit, which is marked by the blue line. The turquoise and dark blue lines indicate the paths used to create Feshbach molecules in our two target states. The dotted lines represent states that are not used for association. In the plot the energy of the dissociation limit is subtracted. The inset shows a fraction of the data with the energy of the dissociation limit not subtracted. In this view the magnetic moments can be directly derived from the slope of the states. (The plot is based on calculated data from R. Le Sueur.)

When the Feshbach molecules reach their target state Stern-Gerlach separation is performed in order to remove the atoms from the trap. The $v = -6$ Feshbach states in the considered field region have a magnetic moment with a sign different from the free atom state. Therefore, the magnetic field gradient used for levitation of the atoms has to be reversed for levitation of the molecules. If the Feshbach molecules are created from atoms in a levitated trap, the change of the magnetic moment when ramping from the $v = -1$ state to the $v = -6$ state leads to a change in the vertical forces the molecule experiences. When the magnetic moment changes from negative values to positive values, the gradient field necessary to levitate the molecules goes through a pole. Due to the limited speed of the magnetic field coils the gradient field is not kept at values to optimally levitate the molecules but rather switched as quickly as possible from one direction to the other. In the meantime the homogeneous field is ramped over the avoided crossing.

With this scheme we create around 2000 Feshbach molecules from a mixture of 150000 Rb and around 80000 Cs atoms. The Rb atoms are partly condensed before combination of the clouds while the Cs atoms are close to condensation. For determination of the number of Feshbach molecules the molecules are dissociated [Her03] by a quick magnetic field ramp and the number of atoms is recorded.

5.2.2 Association into the $|-6(2,4)d(2,4)\rangle$ state

The association into the $|-6(2,4)d(2,4)\rangle$ state allows for a more rapid application of the Stern-Gerlach separation technique. We associate the molecules on the 197 G resonance with a ramp speed of 270 G/s. After the association we quickly ramp the field to 180 G. When magnetic field is ramped down to 180G, the molecules are in the $|-2(1,3)d(0,3)\rangle$ state and Stern-Gerlach separation can simply be achieved by increasing the quadrupole field. This is possible because the magnetic moment of $\mu = -0.9\,\mu_{\mathrm{B}}$ of the $|-2(1,3)d(0,3)\rangle$ state has the same sign as the magnetic moment of the free atoms ($\mu = 1.3\,\mu_{\mathrm{B}}$), but a smaller value. This allows for a quicker application of the Stern-Gerlach separation technique.

After the molecules are separated from the atoms either the power of the trapping beams is increased or the molecules are loaded into an optical lattice to hold the molecules against gravity. The loading of molecules into the lattice is achieved by an exponential ramp from zero to 40 E_{r} with a duration of 5 ms. Since this loading is not adiabatic and we are loading thermal samples, we observe a loss of typically 30%. Since we operate with a thermal sample, a possible explanation could be that some of the molecules are loaded to higher Bloch bands and can tunnel out of the lattice. After the molecules are loaded into the dimple or into the lattice, the levitation field can then be ramped down to zero and the Feshbach molecules are transferred into the $|-6(2,4)d(2,4)\rangle$ target state. Evidence that the molecules are held by the lattice is given by the fact that the molecules do not fall down even without the additional traps.

Association in this state leads to the creation of around 3000 Feshbach molecules, which is more than in the $|-6(2,4)d(2,2)\rangle$ state. However, without the application of the lattice, the number of molecules and their position tend to fluctuate, since the second ramp from the $|-2(1,3)d(0,3)\rangle$ state into the final state induces additional motion of the cloud. Since the lattice was not implemented at earlier stages of the experiment, the formerly described state is used for spectroscopy. The $|-6(2,4)d(2,4)\rangle$ state is used as the starting state for STIRAP and spectroscopy on the $\Omega = 1$ electronic excited potential. The $|-6(2,4)d(2,2)\rangle$ state is used as the starting state for spectroscopy on the $A^1\Sigma^+{-}b^3\Pi_0$ electronic excited potential.

5.2.3 Lifetime of Feshbach molecules

We have measured the lifetime of the Fechbach molecules. The molecules are held in the lattice or dimple for a certain hold time, then the molecules are dissociated and the number of atoms is measured. For the measurement we record the number of Cs and Rb atoms and average the two numbers. The measurement presented in Fig. 5.6 (b) shows a drastic increase in the lifetime if the molecules are held in an optical lattice. For Feshbach molecules in the optical lattice lifetimes of 900 ms are found for the $|-2(1,3)d(0,3)\rangle$ state. Limitations of the lifetimes could be residual photon scattering by the trapping lasers. The shorter lifetimes in the $|-6(2,4)d(2,4)\rangle$ state are not yet conclusively explained. The lifetime of the Feshbach molecules is much shorter if they are kept in the dimple. For the spectroscopy measurements, which were taken at a time when the lattice was not yet implemented, this lifetime was limiting the observation time.

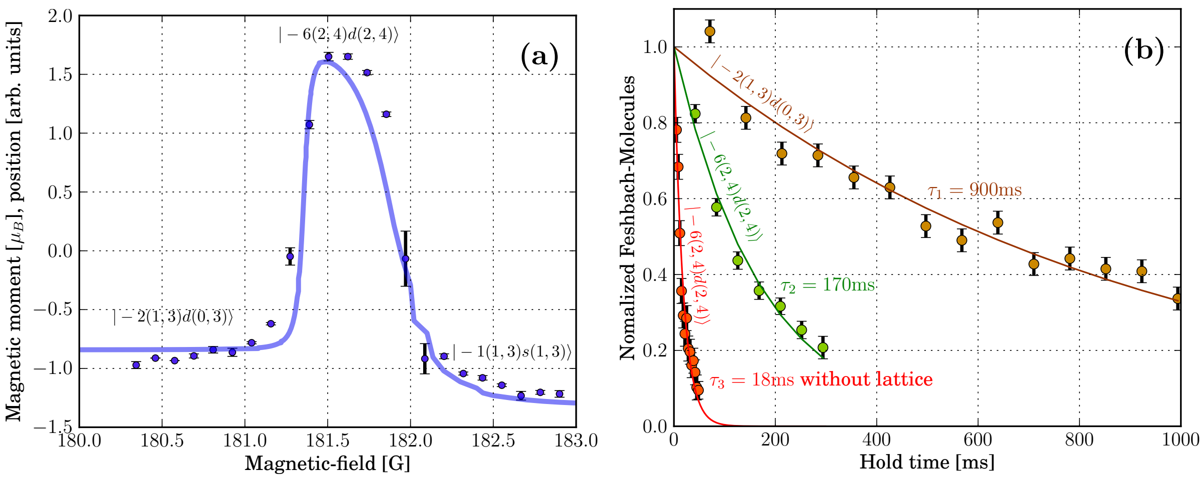

Figure 5.6: (a) Magnetic moment of the Feshbach state (line). The data points are showing the position of an untrapped cloud on the screen in arbitrary units. The position of the cloud follows the calculated magnetic moments. (Theoretical data from R. LeSueur [Tak12]) (b) Lifetime of Feshbach molecules. Lifetimes of Feshbach molecules are measured for different states. If the molecules are trapped in an optical lattice the lifetimes are much longer than for confinement in an optical trap without the lattice.

5.2.4 Magnetic moment spectroscopy

As the magnetic field range where the molecules are in the desired $|-6(2,4)d(2,4)\rangle$ state is rather small, magnetic moment spectroscopy [Dür04] can be used to determine the magnetic field values where the state has mostly the character of the target state. The $v = -6$ state has the highest magnetic moment and therefore the system can be optimized to this parameter. Nevertheless magnetic moment spectroscopy is a useful tool for analysing whether the Feshbach molecules have jumped over an avoided crossing or adiabatically followed the state.

A freely expanding cloud in a magnetic gradient field experiences a force based on its magnetic moment. This force leads to a shift of the position of the cloud corresponding to the magnetic moment. In a practical sense the expansion times should be selected such that the shift of the cloud position is clearly observable. The shift should not bee too large as a shift of position leads to a shift of the magnetic field and thereby the cloud can be ramped over a nearby resonance and thereby change its magnetic moment. This effect is illustrated in [Dür04].

In Fig. 5.6 the position of the cloud on the screen is plotted together with the corresponding magnetic moment. Before the Feshbach structure was reliably calculated these measurements were used to ensure that the Feshbach molecules are in the right state to achieve the best transition matrix elements for spectroscopy.

5.2.5 Characterization of Feshbach molecules

The Feshbach molecules form the starting point of all further experiments. If the temperature, the number of molecules, and the trapping frequencies ω_x, ω_y, ω_z are known, the other properties can be derived. The number of Feshbach molecules in our experiment is typically around $N = 2000$. The temperature of the Feshbach molecules is measured by expansion of a levitated molecular cloud in free space. The Feshbach molecules are transferred back to atoms just before imaging. For large expansion times ($t \gg \omega_x^{-1}, \omega_y^{-1}, \omega_z^{-1}$) the size of the cloud is given by

$$\sigma = t\sqrt{2k_\mathrm{B}T/m}, \tag{5.1}$$

where m is the mass of the molecule, T is the temperature [Ket99]. This relation can be used to evaluate the temperature by a fit to the data. The temperature measured after the molecules have been stored in and subsequently released from the lattice is $T = 240(30)\,\mathrm{nK}$. The temperature has been measured directly after the creation of the molecules and after the molecules have been loaded into an optical lattice. It is found that the (almost) adiabatic loading of the molecules into the lattice and subsequent adiabatic release does not lead to any heating within the sensitivity of our temperature measurements.

To give an overview of the properties of the ultracold gas of Feshbach molecules table 5.1 summarizes the main characteristic values. The peak density is derived from the

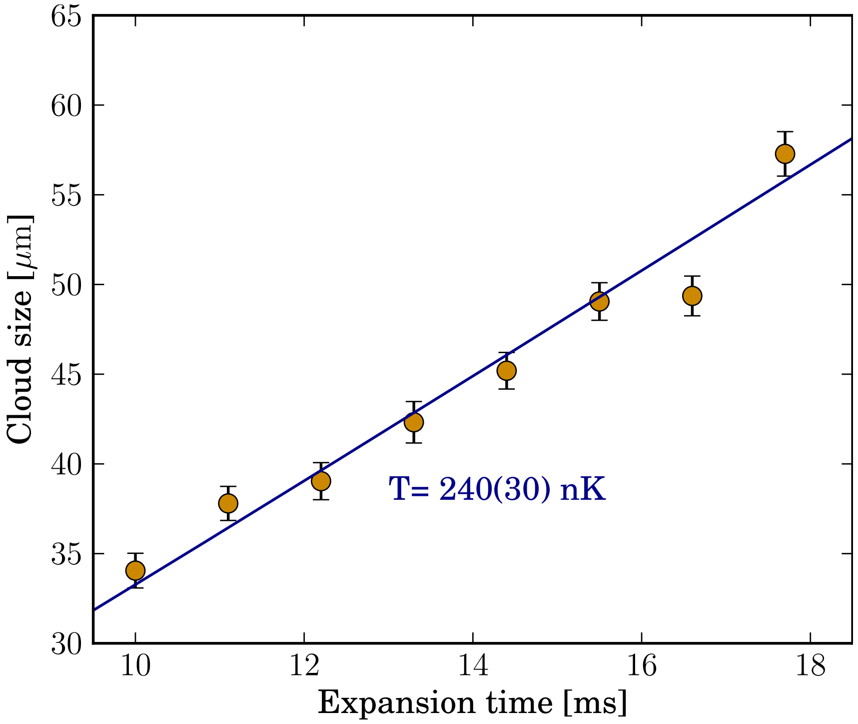

Figure 5.7: Temperature measurement: After the molecules are released from the lattice, the traps are switched off and the (levitated) cloud of molecules can freely expand. After a certain expansion time the molecules are dissociated and an image of the atoms is taken immediately. The size of the cloud is determined by a fit of a Gaussian. The graph shows the size of the cloud for different expansion times.

	symbol	**value**	**unit**
Temperature	T	240	nK
Number of molecules	N	2000	
Trap frequency x	$\omega_x/2\pi$	35	Hz
Trap frequency y	$\omega_y/2\pi$	82	Hz
Trap frequency z	$\omega_z/2\pi$	117	Hz
Peak density	n_0	$3.6 \cdot 10^{11}$	cm^{-3}
Cloud size	σ_x	14	μm
	σ_y	6.0	μm
	σ_z	4.2	μm
Lifetime	τ_1	900	ms
	τ_2	170	ms
Phase space density	$n\lambda_{\mathrm{dB}}^3$	0.005	

Table 5.1: Properties of the cloud of ultracold Feshbach molecules. The two different lifetimes are for the two different Feshbach states $-2|(1,3)d(0,3)\rangle$ and $-6(2,4)d(2,4)\rangle$ when stored in an optical lattice.

temperature, the number of molecules, and the parameters of the trap by:

$$n_0 = N\omega_{\mathrm{eff}}^3 (\frac{m}{2\pi k_{\mathrm{B}} T})^{3/2} \tag{5.2}$$

where N is the total number of particles $\omega_{\mathrm{eff}} = \sqrt[3]{\omega_x \omega_y \omega_z}$ is the effective trap frequency. The low phase-space density is due to the loss in density when twice 10^5 atoms are converted to 2×10^3 molecules. Further the increased mass of the molecules as compared to atoms leads to a smaller de Broglie wavelength λ_{dB}.

The creation of an ultracold sample of Feshbach molecules forms a starting point for the further spectroscopy measurements and creation of ground-state molecules. The molecules in the $|-6(2,4)d(2,2)\rangle$ are used for most of the spectroscopy measurements. In the $|-6(2,4)d(2,4)\rangle$ state all spins are pointing into the same direction. Hence, this state is a pure triplet state with well-defined $I = 5$. This state is used as the starting state for the STIRAP ground-state transfer.

The phase-space density of the sample is mainly limited by the low efficiency of the creation of Feshbach molecules, which in turn depends on the phase-space density of the atomic mixture. Since high three-body losses limit the phase-space density of the mixture these losses ultimately limit the phase-space density of the sample. If the atomic clouds could be mixed in a condensed phase the Feshbach molecules could be created more efficiently and a high phase-space density would be achieved. See e.g. Refs. [Her03, Mar05] for the homonuclear case. The lifetimes of the Feshbach molecules in the optical lattice are long enough for spectroscopy experiments and a detailed investigation of ground-state molecules.

Chapter 6

Spectroscopy

The identification of suitable excited-state levels as well as the detection of ground-state levels is a necessary step for STIRAP ground-state transfer. For SITRAP an electronically excited molecular level has to be identified that has a strong coupling to both the Feshbach molecules and the molecular ground state. Since selection rules prevent transitions from pure singlet to pure triplet states and excited state with well defined spin would either couple to the triplet Feshbach molecules or to the singlet ground state. Hence it is necessary to identify an excited state that has both singlet and triplet character. It has been predicted [Stw04] that the mixed $A^1\Sigma^+ - b^3\Pi_0$ potential should feature states that have mixed character and couple well to both the Feshbach molecules and the ground state. Apart from selection rules another main factor that influences the choice of the excited state is the Franck-Condon overlap between the Feshbach molecules and the excited state and between the excited state and the ground state. This overlap is difficult to predict a priori without a very precise knowledge of the molecular potential [Deb11]. Therefore high resolution spectroscopy has to be carried out to characterize the excited states. Prior to our measurements the energy of the excited states and ground state was only known with an uncertainty of a few GHz [Doc10, Fel99]. This uncertainty is much more than a typical linewidth of the transition to the excited states or the linewidth of the laser. Therefore, a broad scan has to be carried out to search for and detect the excited states and the ground state.

Molecules have a hyperfine structure in the ground state [Ald08] and in the excited states [Bai11]. For the ground state, it is necessary to detect this structure in order to assure that the molecules are transferred to a single hyperfine state. Preferentially the molecules should be transferred to the lowest hyperfine state in order to avoid spin-changing collisions. An excited state that couples directly to the lowest hyperfine state avoids the application of an additional transfer step [Osp10a] from a higher to a lower hyperfine state. Furthermore the excited state has some hyperfine structure. If the hyperfine structure splitting is smaller than the linewidth of the excited state, the laser simultaneously couples to multiple excited hyperfine levels. In this case an adiabatic path that allows for STIRAP transfer is not always guaranteed, but rather depends on the level structure and coupling scheme [Ber98]. In other words, for unresolved hyperfine structure it might or might not be possible to achieve a highly efficient ground-state transfer depending on how the individual levels couple to the initial an final state [Vit99, Cou92, Che07]. Therefore it is necessary that the excited state has a suitable hyperfine structure that allows for a coherent coupling of the three states. The mentioned requirements for the excited states ask for a study of various excited states in order to identify a state that fulfills all of these conditions. In this chapter a short introduction to the level structure of RbCs is followed by an analysis of the excited-state and ground-state spectroscopy.

6.1 Molecular structure

In RbCs there are eight electronic states that correlate with the excited $5S_{1/2} + 6P_{1/2}$ and $5S_{1/2} + 6P_{1/2}$ asymptotes respectively: two 0^+ states, two 0^- states, three $\Omega = 1$ states and one $\Omega = 2$ state [Kot05]. These correspond at short range with the $A^1\Sigma^+$, $b^3\Pi$, $B^1\Pi$ and $c^3\Sigma^+$ electronic case in Hund's case(a) labelling.

Prior to the measurements the information available on the RbCs molecular potential was based on theoretical ab initio calculations [Kot05] and Fourier transform spectroscopy [Doc10]. The known level structure and all the relevant potential energy curves for the experiment are shown in Fig. 6.1. The transitions from the Feshbach to the excited state and from the excited to the ground state are indicated by arrows. The inset shows an enlarged view of the potentials in the energy region that can be addressed by our laser system. The horizontal lines indicate the vibrational levels. The color coding indicates the BO-potential the states belong to.

The potential energy curves are used to select excited state levels for which a good Franck-Condon overlap with both the Feshbach states and the ground state is expected. For a strong transition dipole moment it is further important that selection rules are obeyed, which excludes some potentials as possible candidates. The starting Feshbach state belongs the $a^3\Sigma^+$ potential and the ground state belongs to the $X^1\Sigma^+$ state. There would be no way to perform an optical (dipole) transfer if all the states involved were exactly described by ideal Hund's cases a) or b). The selection rule $\Delta S = 0$ would prevent such transitions. However, in heavy alkali dimers the strong spin-orbit coupling mixes singlet and triplet potentials. In this case the selection rule does not apply since the state is not an eigenstate of the spin operator and has both singlet and triplet character. This allows to couple the state to both singlet and triplet potentials. For the $A^1\Sigma^+$ and the $b^3\Pi_0$ state the mixing is so strong that vibrational levels simultaneously belong to both of the BO-potentials. These states are treated as a belonging to a single mixed $A^1\Sigma^+ - b^3\Pi_0$ potential. The states are numbered without distinguishing whether the singlet or triplet character is predominant.

The $\Omega = 1$ states $b^3\Pi_1$ have mainly triplet character. In the energy range considered, there is no other $\Omega = 1$ BO-potential that could mix with this potential. A small singlet fraction comes from the admixture of higher lying potentials. Since the energy difference to the next higher lying $\Omega = 1$ potentials is large, even the strong spin orbit coupling of RbCs remains a perturbative effect. For few vibrational levels there is a singlet contribution from a nearby level of the $A^1\Sigma^+ - b^3\Pi_0$ potential. If the difference in energy between the two states is very small even a weak coupling can lead to a significant mixing. This applies for the $v' = 29$ state of the $b^3\Pi_1$ potential, which lies close to the $v' = 38$ state of the mixed $A^1\Sigma^+ - b^3\Pi_0$ potential. The v' is the vibrational quantum number and the prime indicates that it is an excited state. The quantum numbers of the initial state will be denoted without a prime and the quantum numbers of the electronic ground state will

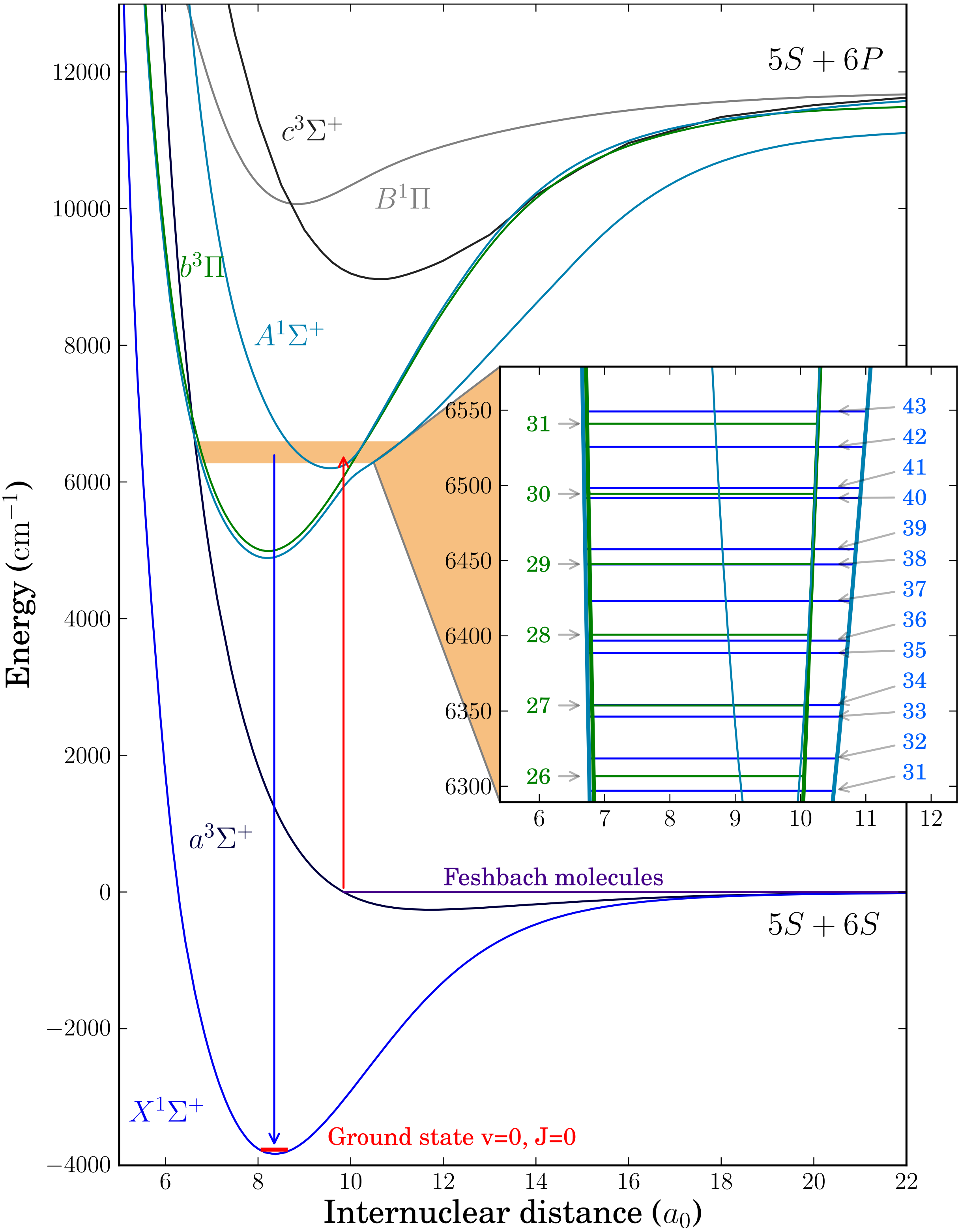

Figure 6.1: Potential energy curves of the electronic ground state and the lower electronic excited states. The inset shows an expanded view of the region that can be investigated by the spectroscopy lasers. The mixed A-b ($b^3\Pi_1$) vibrational levels are labeled in blue (green).(data from [Kot05, Doc10])

be denoted with double primes.

The states of the $b^3\Pi_2$ are of no interest for ground-state transfer as the selection rule $\Delta\Omega = 0, \pm 1$ prevents transitions to the ground state. Since there is no significant mixing between states of different Ω this selection rule applies.

The choice of vibrational levels investigated in this experiment is based on theoretical predictions of transition dipole moments for the two transitions from the Feshbach to the excited state and further, from the excited state to the ground state. Theoretical calculations [Kot05, Deb11] predicted reasonable transition dipole moments for vibrational states of the mixed $A^1\Sigma^+ - b^3\Pi_0$ potential in the range between $6300\,\mathrm{cm}^{-1}$ and $6600\,\mathrm{cm}^{-1}$. This range is illustrated in Fig. 6.1 together with the vibrational levels. Therefore excited state spectroscopy is carried out in this range, using a narrow line with diode laser[1] centered at 1550 nm.

6.2 Excited state spectroscopy

Molecular loss spectroscopy is carried out to search for and identify a suitable level $|2\rangle$ of the excited molecular potentials. Levels in the range from 6320 to $6450\,\mathrm{cm}^{-1}$ are investigated. As it turned out during the measurements, the partially unresolved hyperfine structure of the $A^1\Sigma^+ - b^3\Pi_0$ state hinders a successful application of a highly efficient STIRAP transfer. Hence states of the $b^3\Pi_1$ potential are also investigated.

The spectroscopy presented in this thesis uses the $|-6(2,4)d(2,2)\rangle$ state for the measurements of the states belonging to the $A^1\Sigma^+ - b^3\Pi_0$ potential. The spectroscopy on the levels of the $b^3\Pi_1$ potential uses the $|-6(2,4)d(2,4)\rangle$ Feshbach state.

In all one-photon spectroscopy measurements the Feshbach molecules are irradiated by a laser L_P for a certain irradiation time t_irr ranging from $10\,\mu$s to 10 ms and the number of remaining Feshbach molecules is recorded. This is done as before by dissociating the Feshbach molecules and recording the number of remaining atoms. For each resulting data point a new sample of Feshbach molecules is prepared and the laser frequency f_1 is stepped to a new value.

6.2.1 Spectroscopy of the $\mathrm{A}^1\Sigma^+ - \mathrm{b}^3\Pi_0$ potential

The $A^1\Sigma^+ - b^3\Pi_0$ potential was the primary candidate for STIRAP transfer as good Franck-Condon overlap was predicted and the states couple well to both, the Feshbach state and the ground state.

Since prior to our measurements the precise energy of the excited levels had been known only up to a precision in the GHz regime, first of all a search over a broad range of frequencies f_1 is performed using the maximum laser intensity ($P_\mathrm{max} = 20\,\mathrm{mW}$) possible in our setup. The choice of the irradiation time is restricted to 10 ms by the lifetime of the Feshbach molecules.[2]

At these values the absorption lines are broadened up to a few hundred MHz. Yet there remain still enough Feshbach molecules for clearly distinguishing molecules from

---

[1] The laser setup is described in chapter 4.

[2] In contrast to the lifetimes of Feshbach molecules shown above, at the time of the spectroscopy measurements the lifetime was only a few tens of ms because the lattice was not yet implemented.

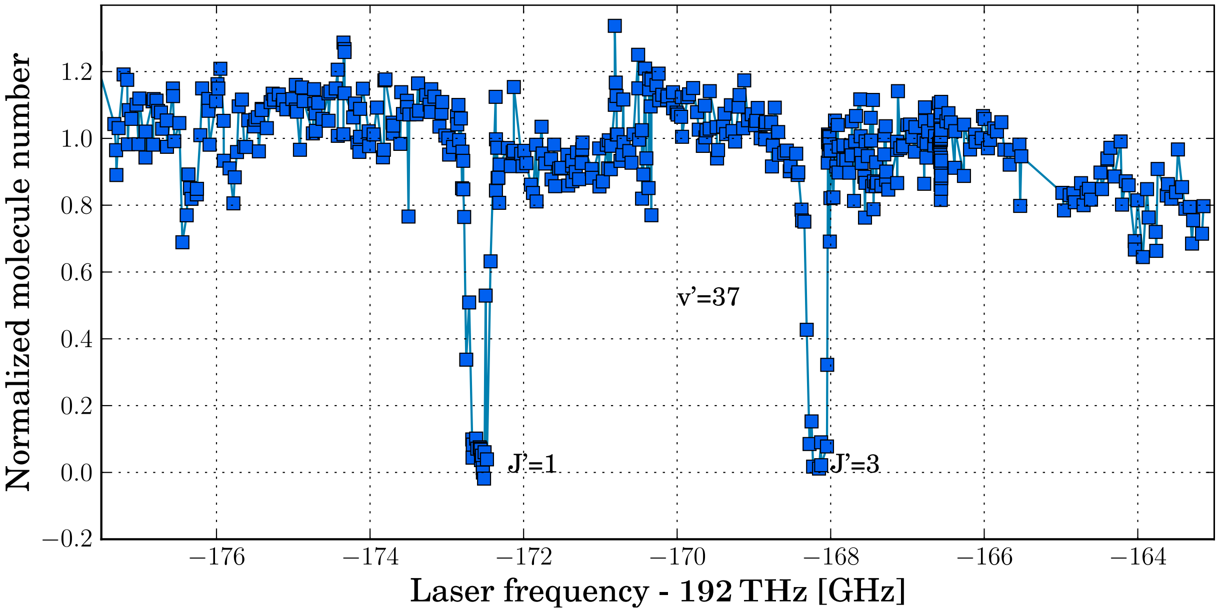

Figure 6.2: Overview scan of the $v' = 37$ spectroscopic measurements. The data points show the remaining fraction of Feshbach molecules. Two rotational lines $J' = 1$ and $J' = 3$ are detected. The transition to the $J' = 2$ rotational state is not allowed by a selection rule that forbids $\Delta J = 0$ for $\Omega = 0 \rightarrow \Omega = 0$ transitions.

the background noise. The short fluctuations in the number of molecules mainly stem from interferences in the imaging system. Further pointing instabilities of the dipole traps and fluctuations in the air can reduce the efficiencies for creation of the ultracold atomic clouds and the Feshbach molecules. Slow drifts in the number of molecules are mainly due to drifts in the alignment of some of the several dozen of laser beams in the experiment. These drifts are caused by a change of the temperature in the laboratory.

The initial choice of the step size in the first scan is based on the predicted transition strength [Kot05]. The step size of all further measurements is based on our experiences with the first peaks we identified. In the broad scan experiments a free running diode laser is stepped. Because this procedure does not result in equally spaced data points, the frequency is measured for each data point by a home built wavemeter. The data from such a measurement is shown in Fig. 6.2. Two well separated resonances are observed, which are interpreted as originating from two rotational states $J' = 1$ and $J' = 3$. In order to determine the rotational quantum numbers J' the splitting of the two resonances is compared to the rotational splittings expected from values measured by Docenko *et al.* [Doc10]. The measured splitting between the two lines matches the rotational splitting between the $J' = 1$ and the $J' = 3$ level from Docenko *et al.* with less than 1% error[3]. This leads to the conclusion that the initial Feshbach state is a d state ($J = 2$).[4]

In order to further characterize the excited state spectrum, high resolution laser scans and lifetime measurements are carried out. For the high resolution scans the laser is locked to a cavity as described in section 4.2. For each measurement the irradiation time and power is adjusted to prevent artificial broadening of the peak. The results of some of these measurements are shown in Fig. 6.3. The data points show the number of molecules as a function of the laser frequency detuning. The data is normalized to the number of molecules without any irradiation. The zero frequency points are the centers of the resonances. For each resonance the center frequency is also measured by a wavemeter in order to determine the absolute value.[5]

The absorption lines are modelled by the following function

$$N = N_0 \exp\left(-t_{\mathrm{irr}}\Omega_{\mathrm{P}}^2 \frac{\gamma}{\gamma^2 + 4\Delta_{\mathrm{P}}^2}\right), \tag{6.1}$$

where N_0 is the initial number of Feshbach molecules, γ is the excited state linewidth, t_{irr} is the irradiation time, Δ_{P} is the detuning of the laser from resonance, and Ω_{P} is the Rabi frequency of the transition. In this equation all frequencies are angular frequencies. The lifetime of the excited state is $\tau = 1/\gamma$. In the cases where multiple lines are present a sum of multiple Lorentzian functions in the exponent is used to describe the lines.

In some of the plots in Fig. 6.3 more than one line is present. This is due to the hyperfine structure of the excited state. In an excited state of the $A^1\Sigma^+ - b^3\Pi_0$ potential there is no large magnetic moment the nuclear spins can couple to. However some higher order coupling mechanisms like electron mediated spin-spin coupling or quadrupole coupling results in a small hyperfine structure splitting [Ald08, Ald09, Ran10]. For RbCs

---

[3] The precise determination of the position of the resonances is achieved by high resolution spectroscopy.

[4] At the time when these measurements were taken, the Feshbach structure of RbCs was not yet completely understood. The determination of the rotational quantum number of the Feshbach state did provide helpful information for the modelling of the Feshbach structure.

[5] The absolute frequency values are summarized in table 6.1.

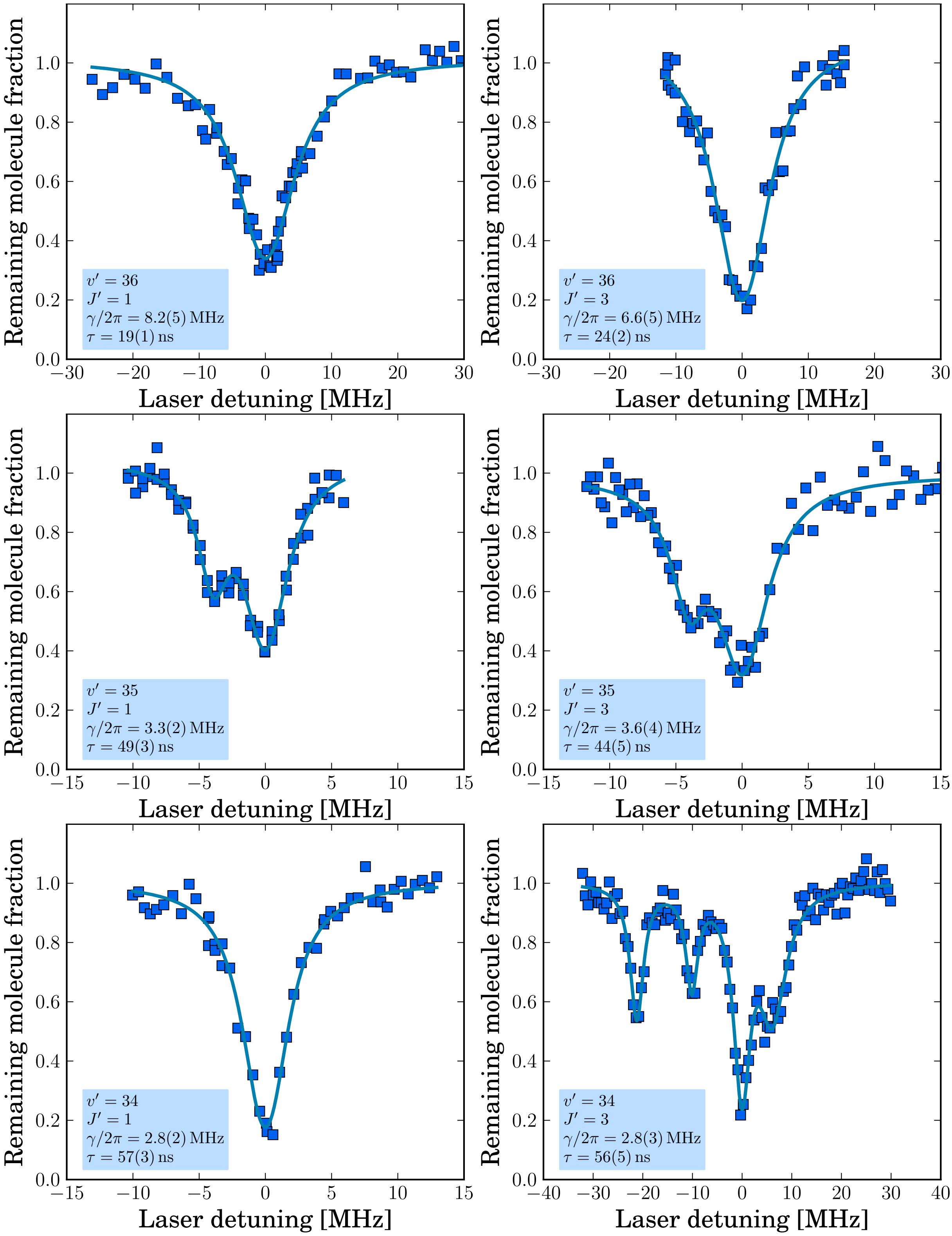

Figure 6.3: High resolution scan on the $J' = 1$ and $J' = 3$ rotational lines of the $v' = 36$, 35, 34 states. The data points indicate the fraction of molecules after irradiation as a function of frequency detuning from the center of the resonance.

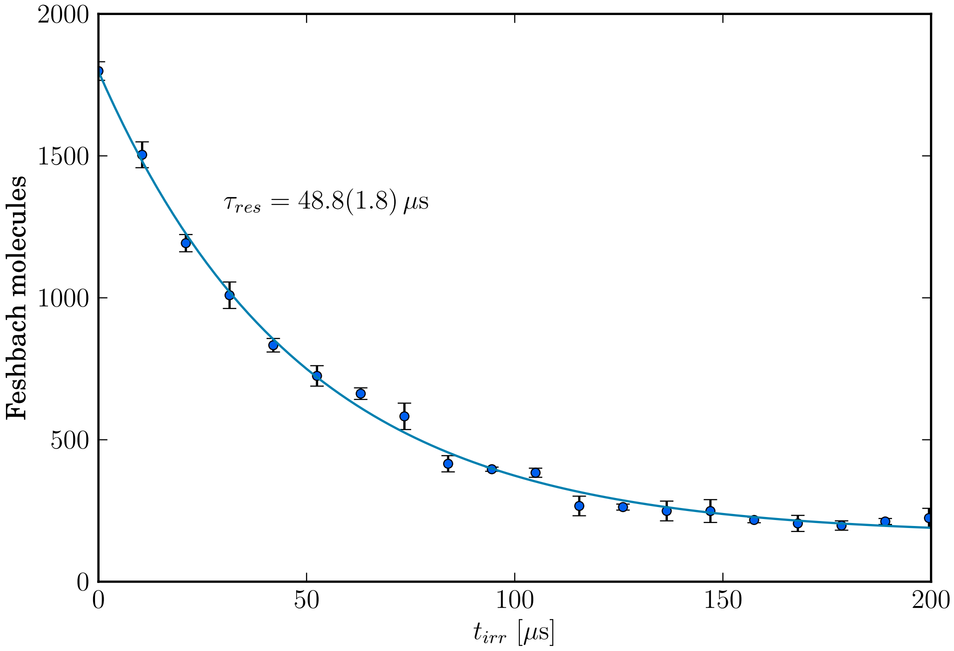

Figure 6.4: Lifetime of the Feshbach molecules when irradiated with resonant light. In this example the $v' = 34, J' = 1$ state is chosen. The laser power is 9 mW the intensity is 440 W/cm^2 and the polarization is horizontal or $\sigma^{\pm}$. The resulting Rabi frequency is $\Omega = 2\pi \times 96(8)$ kHz. The normalized Rabi frequency is $\Omega_{\text{norm}} = 144(12)\,\text{Hz}/\sqrt{\text{mW/cm}^2}$. The errors are statistical errors. The systematic errors can be as large as 15% and are mainly due to drifts of the alignment of the trapping lasers that can lead to a reduced spatial overlap of the molecular cloud with the spectroscopy beam.

in the $A^1\Sigma^+ - b^3\Pi_0$ state this hyperfine structure typically spreads over a region of few MHz. The spectrum of the $v' = 34, J' = 3$ state is an exception. By coincidence there is a state from another BO-potential next to this state. A coupling to this state increases the hyperfine splitting.[6]

The different widths of the lines are related to the singlet and triplet character of the excited state. Singlet states feature a stronger coupling to the ground-state potential and thereby an increased spontaneous decay rate. This corresponds to a decreased excited state lifetime τ and an increased linewidth γ for the states that feature more singlet character. Effects of the hyperfine structure are visible mostly in the narrower lines. However hyperfine structure is present in all the excited states even if it is obscured by a large natural linewidth.

The Rabi frequency could be determined from the fit function of the high resolution scan measurement. In this case the measured Rabi frequency is very sensitive to the noise of the few central data points. Therefore we determine the Rabi frequencies by a separate measurement keeping the laser on resonance while varying the irradiation time. In this case (6.1) simplifies to

$$N = N_0 \exp\left(-t_{\text{irr}} \frac{\Omega_{\text{P}}^2}{\gamma}\right), \tag{6.2}$$

which is a simple exponential decay. The equation is valid as long as the time constant of

---

[6] Coriolis coupling has been discussed as one of the possible causes. However, it is not determined which mechanism is predominantly inducing the coupling

the decay $\tau_{\mathrm{res}} = \gamma/\Omega_{\mathrm{P}}^2$ is much larger than the lifetime of the excited state $\tau_{\mathrm{res}} \gg \tau$. The coefficient Ω^2/γ appears frequently in the description of the STIRAP transfer efficiency as a figure of merit. Notably the decay measurements provide a means of directly measuring the coefficient. An example of such a measurement is shown in Fig. 6.4. For comparison of different transitions strengths typcally normalized Rabi frequencies $\Omega_{\mathrm{norm}} = \Omega/\sqrt{I}$ are given in experimental studies since these do not depend on the intensity I of the laser light and directly relects the strength of the transition. In our experiment the statistical errors for determination of the transition strength are smaller than the systematic errors that occur due to drifts in the overlap of the spectroscopy beam with the molecular cloud. When the same data is taken on different days, differences of up to 15% are observed. For the intensity waist radius of our spectroscopy beams being 39 μm, the 15% correspond to a displacement of 11 μm. It is worth noting that the systematic effects lead only to a reduction of the transition strength. Thereby it is safe to assume that the actual values are larger than our values by up to 15%. In the following data the errors indicate the statistical errors. For all of the spectroscopy data the statistical errors are much smaller than the systematic errors. Therefore, the explicit notation of the statistical errors is omitted for data describing transition strengths.

6.2.2 Spectroscopy of the $\mathrm{b}^3\Pi_1$ potential

The presence of unresolved excited hyperfine states in the $A^1\Sigma^+ - b^3\Pi_0$ potential tends to hinder highly efficient STIRAP[7] in RbCs. Therefore, states of the $b^3\Pi_1$ potential are investigated in order to identify a well isolated excited state. The investigation of $\Omega = 1$ states is inspired by the work of Grochola *et al.* [Gro09] on LiCs where a much larger hyperfine splitting is observed for $\Omega = 1$ states, which is explained by a simple equation (6.3) from Townes and Schawlow [Tow55]. If the hyperfine coupling constant a of one atom dominates the hyperfine structure, a molecule in a singlet state can be described by

$$W_{\mathrm{hfs}} = \frac{a\Omega}{J'(J'+1)} \frac{f(f+1) - J'(J'+1) - i(i+1)}{2}, \tag{6.3}$$

where i is the nuclear spin of the atom, J' is the total angular momentum of the excited state, and $\mathbf{f}$ is the combination of $\mathbf{i} + \mathbf{J}'$. The situation is more complicated for RbCs but our measurements show that some qualitative features remain valid. Similar to the case of LiCs the following general behaviour of the hyperfine structure is observed. Firstly the hyperfine structure is much larger than for the $\Omega = 0$ states. Secondly, the hyperfine structure is organized in three groups of peaks.

An overview scan of the $|\Omega = 1, v' = 29\rangle, (b^3\Pi_1)$ state, which lies comparatively close to the $|0, 38\rangle$, $(A^1\Sigma^- b^3\Pi_0)$, state is shown in Fig. 6.5. A coupling of these two states is causing the first state to have some singlet character, which turns out to be sufficient for a transition to the molecular ground state. The $v' = 29$ state shows three J' components in contrast to the $v' = 38$ state. This can be explained by selection rule 3.24, which states that $\Delta J = 0$ is forbidden for $\Omega = 0 \to \Omega = 0$. For STIRAP ground-state transfer our main interest is on the $J' = 1$ states, since a connection to the rotational ground state can only be made through these. Selection rules permit only transitions with $\Delta J = 0, \pm 1$. The aim is to identify a state that is well separated from the other states and has a strong

---

[7] See chapter 7.

transition dipole moment. Therefore we perform more scans with limited irradiation times and a higher frequency resolution as shown in the lower part of Fig. 6.5.

Due to the hyperfine structure, the $J' = 1$ line is split into three groups of lines. The left group features a very broad line. Therefore our further investigations mainly focus on this line for which sufficient Rabi frequencies for ground-state transfer can be expected. The broad leftmost state in Fig. 6.5 will be used for STIRAP and will further on be denoted by $|2\rangle$. It is analyzed further with reduced power as shown in Fig. 6.6. When the power is reduced the linewidth diminishes until it reaches the natural linewidth of 128(11) kHz, which is much smaller than the natural linewidths of all the $A^1\Sigma^+ - b^3\Pi_0$ states. This small linewidth can be explained by the small singlet character and thereby reduced coupling to the ground-state manifold.

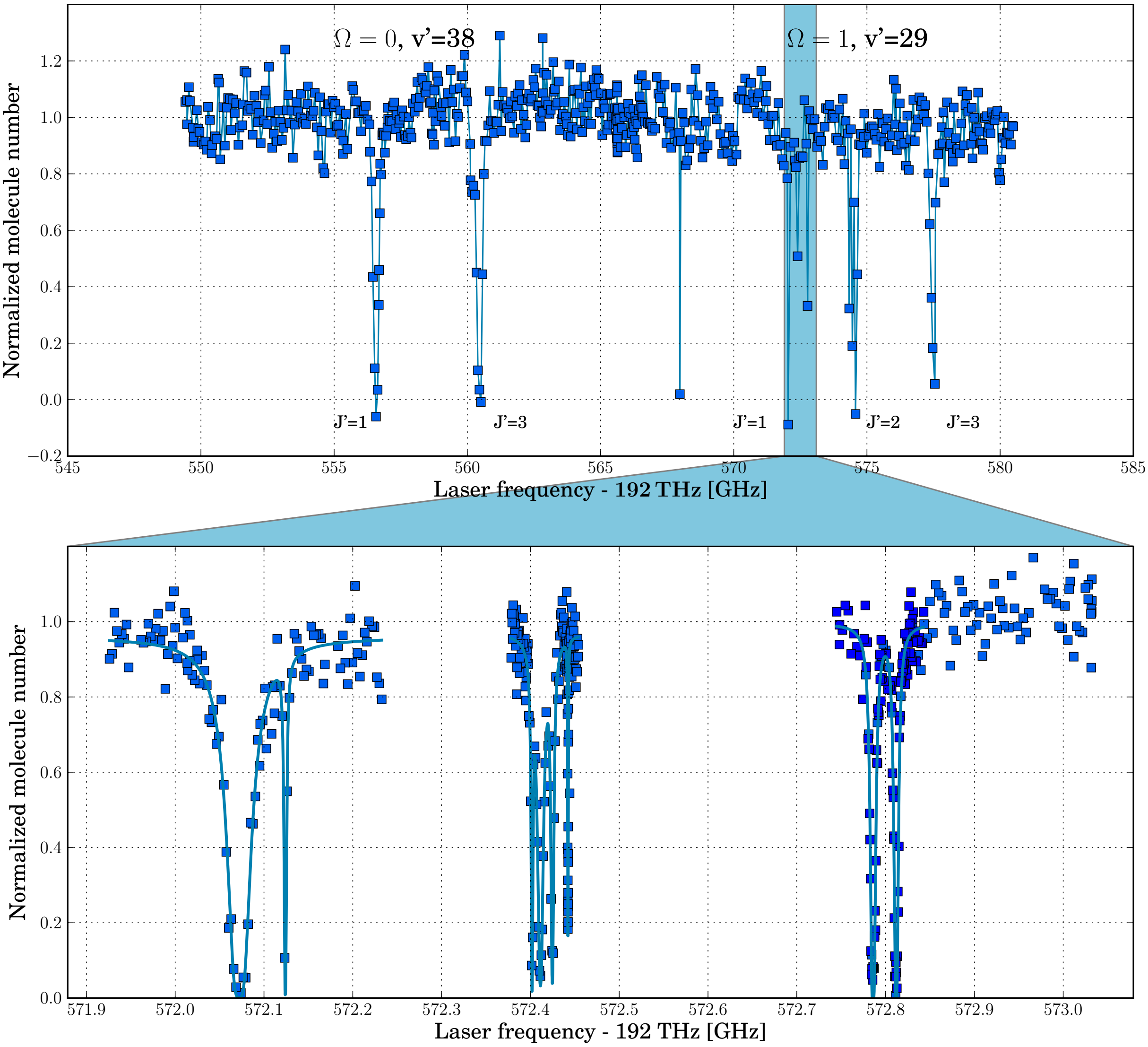

Figure 6.5: The upper part of the figure shows data from overview scans with limited resolution and 30 ms irradiation. The intensity is 450 W/cm^2. The peaks are labelled according to the vibrational and rotational state they belong to. The unlabelled peak is believed to be due to an error in the measurement. The lower part shows a scan on the marked region with higher resolution. All three peaks are measured with the same laser power. The time is 10ms for the first and last peak and 2ms for the middle peak.

In terms of this small linewidth the state can be regarded as well separated from its neighbouring state. As is shown in Fig. 6.5 the distance to the next state is on the order of 50 MHz, which is large compared to the natural linewidth. It is evident already from the fits in this graph that the weak second line has a negligible influence on the molecules at the center of the STIRAP state even for full power irradiation on a 10 ms time scale.

The Rabi frequency is determined from a lifetime measurement shown in 6.6 (b) with a reduced laser power of 0.12 mW and a waist of $w_0 = 38.7\,\mu$m. A frequency of $\Omega/2\pi = 24\,$kHz is obtained for an intensity $I = 2P/\pi w_0^2 = 5.1\,\mathrm{W/cm}^2$. This corresponds to a normalized Rabi frequency of $0.33\,\mathrm{kHz}/\sqrt{\mathrm{mW/cm}^2}$, which is equivalent to a maximum Rabi frequency of 250 kHz for a laser power of 13.5 mW.

The normalized Rabi frequency is lower than for some excited states of the $A^1\Sigma^+ - b^3\Pi_0$ potential. For STIRAP ground-state transfer however, the strongly reduced decay rate of the excited state γ overcompensates the fact that the Rabi frequency is lower than for some other states. Therefore the $|1, 29\rangle$ state has two features that make it the optimum state for STIRAP - it has the highest Ω^2/γ for a given laser power and it has well isolated hyperfine states.

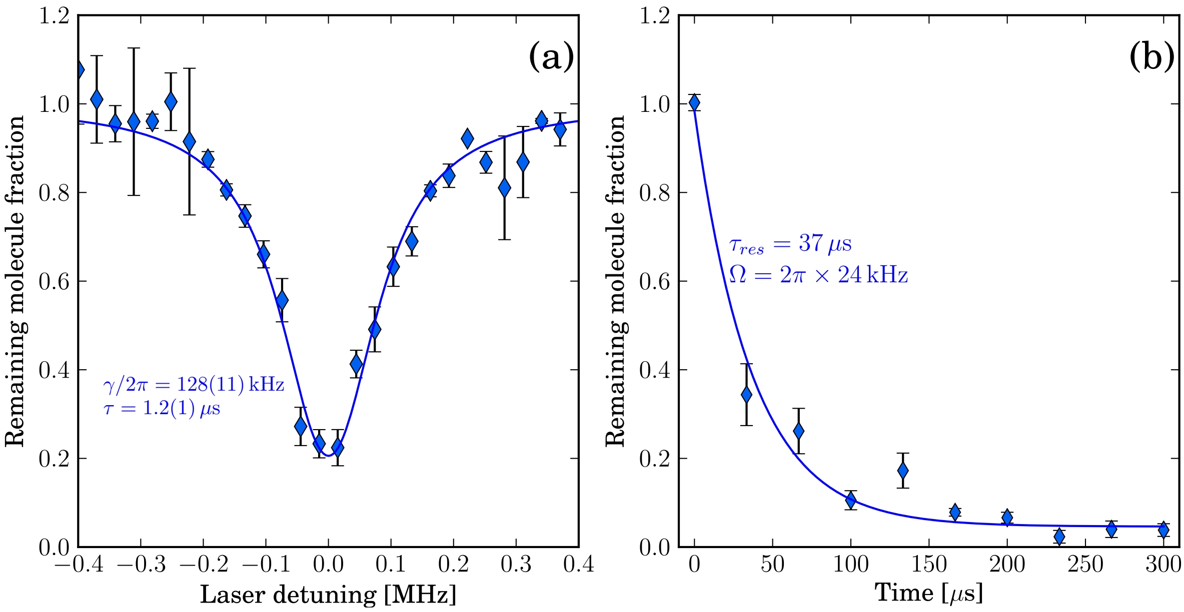

Figure 6.6: Line profile (a) and transition strength (b) of the hyperfine state used for the STIRAP and two-photon measurements. The laser power is in both cases $P = 0.12\,$mW with a beam waist of $w_0 = 38.7\,\mu$m. For plot (a) the irradiation time is $60\,\mu$s. The error bars represent statistical fluctuations and the larger error bars in (a) away from the center are due to the fact that less data is taken in this region. The normalized Rabi frequency is $\Omega_P = 2\pi \times 0.33\,\mathrm{kHz}\sqrt{I/(\mathrm{mW/cm}^2)}$.

6.2.3 Summary of the excited states

An overview of all the states that have been investigated with the above described methods is given in table 6.1. In order to compare the experimental data to theoretical predictions from the group of O. Dulieu the Rabi frequencies are expressed as transition dipole moments D. In general the transition dipole moment is determined by the matrix elements of a dipole operator $\hat{D}$ [Her50]

$$D = \langle \psi_f^* | \hat{D} | \psi_i \rangle, \tag{6.4}$$

where ψ_i and ψ_f denote the initial and final states. The large number of degrees of freedom in molecules makes the calculation of transition dipole moments a highly complex endeavour. However, two approximations allow to split the calculation of transition dipole moments between rovibronic levels of different electronic potentials in a stepwise process [Deb11]. Firstly, the Born-Oppenheimer approximation allows to split the calculation for an electronic transition between vibrational levels into two steps, an R-dependent electronic transition and the vibrational part. Secondly, the assumption that the radial wave functions are independent of the rotation J for a rovibrational level allows to further simplify the calculation. The transition dipole moments can hence be calculated in a three step process. First the R-dependent transition dipole moments $\mu^{a-\Pi}$ and $\mu^{X-\Sigma}$ are calculated following Ref. [Aym05]. The superscript denotes the electronic states between which the transition occurs. In a next step the vibrational wave functions $\Psi^{(X)}(R)$, $\Psi^{(a)}(R)$, and $\Psi^{(0^+)}(R)$ of the $X^1\Sigma^+$, $a^3\Sigma^+$, and 0^+ molecular states are used to calculate the transition dipole moments for a transition between specific vibrational levels. The TDMs read

$$\mu_{\nu\nu'}^{a-0^+} = \langle \Psi_\nu^a | \mu^{a-\Pi}(R) | \Psi_{\nu'}^{0^+(\Pi)} \rangle, \tag{6.5}$$

$$\mu_{\nu''\nu'}^{X-0^+} = \langle \Psi_{\nu''}^X | \mu^{X-\Sigma}(R) | \Psi_{\nu'}^{0^+(\Sigma)} \rangle, \tag{6.6}$$

where ν, ν', and ν'' denote the vibrational quantum numbers of the initial, intermediate and final levels respectively. In a last step the Hönl-London factors, which describe the influence rotational levels, are included. The transition dipole moment reads

$$D_{|i\rangle,|f\rangle}^{q,\pm\epsilon} = \sqrt{\frac{(2J_i+1)(2J_f+1)(1+q)}{1+|\epsilon|}} \times \begin{pmatrix} J_f & 1 & J_i \\ -M_f & \epsilon & M_i \end{pmatrix} \times \begin{pmatrix} J_f & 1 & J_i \\ -\Lambda_f & \epsilon & \Lambda_i \end{pmatrix} \times \mu_{\nu_i,\nu_f}^{\Gamma_i-\Gamma_f}, \tag{6.7}$$

where $|i\rangle$ and $|f\rangle$ denote initial and the final state, ν_i (ν_f) is the vibrational level, M_i (M_f) is the projection of the rotation J_i (J_f) onto the lab-frame quantization axis and Λ_i (Λ_f) is the projection onto the molecular axis. The electronic states are denoted by Γ_i (Γ_f). The index q labels $\Sigma-\Sigma(q=0)$ and $\Sigma-\Pi(q=\pm1)$ transitions, and $\epsilon = 0(=\pm1)$ defines the laser polarization along (perpendicular to) the polarization axis.

The described procedure allows the calculation of transition dipole matrix elements D. The TDMs can also be derived from the measured Rabi frequencies Ω by

$$\hbar\Omega = DE, \tag{6.8}$$

where E is the electrical field of the light. The electrical field can be calculated from the light intensity using the relation

$$I = \frac{c\epsilon_0}{2}E^2, \tag{6.9}$$

where c is the speed of light and ϵ_0 is the vacuum permeability. This allows for a comparison of experimental and theoretical transition strengths.

For comparison, both theoretical and experimental values are listed in table 6.1. The table shows a good agreement of the transition energies and rotational constants. The uncertainties of these measurements depend mainly on the accuracy of the wavemeter.

$v^{'}$	$B_{\mathrm{v}'}^{theo}$	$B_{\mathrm{v}'}^{exp}$	J'	$E_{\mathrm{f,i}}^{theo}$	$E_{\mathrm{f,i}}^{exp}$	$\mathcal{P}$	$D_{\mathrm{f,i}}^{theo}$	$D_{\mathrm{f,i}}^{exp}$	Ω kHz	τ^{cal}	τ^{exp}
	(10^{-3}cm^{-1})			(cm^{-1})			(10^{-4} a.u.)		$\sqrt{\mathrm{I}/\frac{\mathrm{mW}}{\mathrm{cm}^2}}$	(ns)	
$\Omega = 0^+$											
33	12.7		1	6321.84	6321.863	v	4.7	3.2	0.35	28	24
						h	3.3	4.6	0.51	28	24
34	14.9	15.0	1	6329.36	6329.357	v	0.7	0.8	0.09	84	55
						h	0.5	1.3	0.14	84	55
			3	6329.51	6329.507	v	1.3	2.1	0.24	84	
						h	1.2	2.1	0.23	84	
35	14.7	14.8	1	6364.04	6364.031	v	1.2	2.9	0.32	72	48
						h	0.8	5.0	0.55	72	48
			3	6364.18	6364.179	v	2.1	4.5	0.50	72	
						h	1.9	4.0	0.44	72	
36	13.0		1	6372.30	6372.314	v	4.7	3.9	0.44	30	24
						h	3.3	5.3	0.59	30	24
37	14.7	14.8	1	6398.67	6398.663	v	1.8	2.7	0.3	80	57
						h	1.3	4.6	0.51	80	57
			3	6398.82	6398.811	v	3.2	-		80	
						h	2.8	-		80	
38	13.0		1	6422.97	6422.986	v	3.3	0.95	0.11	30	27
				6422.97	6422.986	h	2.3	2.0	0.23	30	27
$\Omega = 1$											
27	16.5		1	6329.17		v	5.0				
28	16.4		1	6376.18		v	4.2				
29	16.4		1	6423.07	6423.501	v	2.9	2.7	0.33		1200

Table 6.1: Computed and experimental properties of the transitions from the Feshbach level $v = -6$ of $a^3\Sigma^+$ to the (v', J') levels of the $\Omega = 0^+$ coupled states and of the $\Omega = 1$ in the wavelength range from about 1581 nm to 1557 nm and for vertical (v, $\epsilon = 0$) and horizontal (h, $\epsilon = \pm 1$) polarizations $\mathcal{P}$. The rotational constants $B_{\mathrm{v}'}$, the transition energies $E_{\mathrm{f,i}}$, the transition dipole moments $D_{\mathrm{f,i}}$, the radiative lifetimes τ. The rotational factor used to give the transition strength (assuming $M_J = +1$, according to two-photon experiments) are respectively $\sqrt{\frac{1}{10}}$, $\sqrt{\frac{1}{20}}$, $\sqrt{\frac{32}{105}}$, $\sqrt{\frac{26}{105}}$ for $J = 1$ v, $J = 1$ h, $J = 3$ v, $J = 3$ h. This is under the assumption that different M_J' sublevels are not resolved. The errors are discussed in the text.

The transition dipole moments show larger deviations, which is due to the fact that the measured Rabi frequencies depend on the alignment of the laser system, which in turn can not be quantified easily. The normalized Rabi frequencies have been varying throughout the measurements by up to 15% due to drifts of the cloud position. The calculated transition dipole moments have much larger errors and the accuracy of the theoretical values is less than the number of digits given. Therefore the differences between experimental and theoretical values can be attributed to the theoretical uncertainties.

Prior to the measurements of the transition dipole moments only the order of magnitude was estimated. Therefore quantifying the transition strength with an error of even 15% is a major improvement of the situation. The precision clearly suffices to determine suitable states for STIRAP ground-state transfer.

With the $\Omega = 1, v' = 29$ state a state is identified that has a sufficiently large hyperfine splitting in order to resolve single states. Further, the transition dipole moment for the transition from the Feshbach state to the $|1, 29\rangle$ state allows for a Rabi frequency of 250 kHz, which is large enough for STIRAP ground-state transfer.

6.3 Two-photon dark-state resonance spectroscopy

Two-photon dark-state resonance spectroscopy is a common way to detect properties of low lying levels in ultracold molecules [Str10, Lan09a, Mar09] and has been a spectroscopic tool for decades [COX65, Wod71]. Two-photon spectroscopy played an important role in the early days of BEC when it was used to determine a negative scattering length for ^{7}Li [Abr95]. First observations of a coherent coupling of states have been made by Autler and Towns [Aut55]. It is well known that an essential property of a lambda-type three-level system is the existence of a dark state as an eigenstate of the system [Ber98]. The physics underlying the dark-state spectroscopy is identical to that involved in related phenomena such as electromagnetically induced transparency [Fle05] and has been investigated extensively during the past.

In our experiment two-photon spectroscopy is used for three purposes. Firstly, to determine the energy of the ground state with respect to the free atom asymptote. Secondly, to determine the transition strength of the second transition. Thirdly, to resolve the hyperfine structure of the ground state. The next two sections describe a stepwise development of the corresponding theory accompanied with experimental results.[8] The different measurements are structured according to the complexity of the description, starting with a simple model of a three-level system coupled by two lasers on resonance.

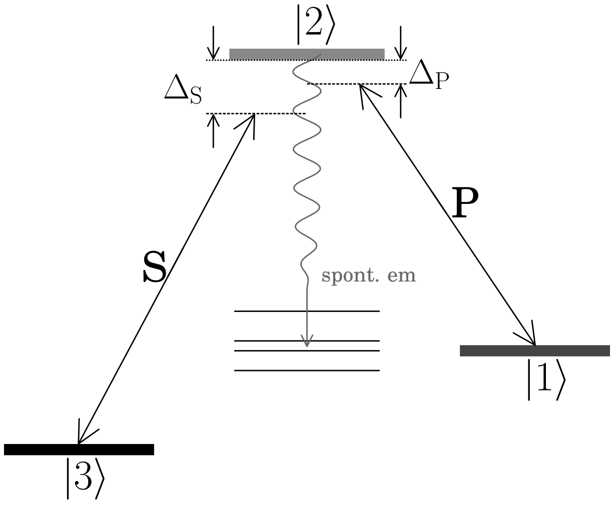

Figure 6.7: Three-level scheme. The pump laser P and the Stokes laser S couple state $|1\rangle$ to state $|3\rangle$ via an intermediate excited state $|2\rangle$. The latter has a limited lifetime due to spontaneous decay.

In a three-level system in Λ-type configuration, three atomic states are coupled via an electric field

$$\mathbf{E}(t) = \mathbf{E}_\mathrm{P}(t)\cos(\omega_\mathrm{P} t + \phi_\mathrm{P}) + \mathbf{E}_\mathrm{S}(t)\cos(\omega_\mathrm{S} t + \phi_\mathrm{S}), \tag{6.10}$$

where ω_P and ω_S are the carrier frequencies of the light field, and ϕ_P, ϕ_S are the respective phases. The amplitudes $\mathbf{E}_\mathrm{P}$ and $\mathbf{E}_\mathrm{S}$ are functions of time and change either smoothly as

---

[8] While chronologically a two-photon resonance has to be detected first before measurements at resonance can be made, the description of measurements on resonance is much simpler. Therefore, the following sections are not structured in chronological order of the taken measurements.

in the case of STIRAP or be switched suddenly (but still much slower than the optical frequency) if a projection of one state onto another is desired. The detunings of the carrier frequencies from the respective Bohr transition frequencies are denoted by

$$\Delta_S = \omega_S + E_3/\hbar - E_2/\hbar, \quad \Delta_P = \omega_P + E_1/\hbar - E_2/\hbar, \tag{6.11}$$

where Δ_S and Δ_P denote the detunings of the carrier frequencies from resonance and E_1, E_2 and E_3 are the energies of the uncoupled states $|1\rangle$, $|2\rangle$ and $|3\rangle$. An alternative way, more suitable for the discussion of STIRAP, is to describe the detunings in terms of single-photon and two-photon detuning.

$$\hbar\delta \equiv \hbar(\omega_\mathrm{S} - \omega_\mathrm{P}) - E_1 + E_3, \tag{6.12}$$

$$\hbar\Delta \equiv \frac{\hbar}{2}(\omega_\mathrm{P} + \omega_\mathrm{S}) + \frac{1}{2}(E_1 + E_3) - E_2 \tag{6.13}$$

The two-photon detuning is named δ, the one-photon detuning is Δ.

The near resonant light fields E_P and E_S respectively couple the states $|1\rangle \leftrightarrow |2\rangle$ and $|2\rangle \leftrightarrow |3\rangle$ with coupling strengths that are described by the Rabi frequencies

$$\begin{aligned}\Omega_\mathrm{P}(t) &= -\langle 1|\mathbf{d}\cdot\mathbf{E}_\mathrm{P}(t)|2\rangle,\\ \Omega_\mathrm{S}(t) &= -\langle 2|\mathbf{d}\cdot\mathbf{E}_\mathrm{S}(t)|3\rangle.\end{aligned} \tag{6.14}$$

The Hamiltonian describing the coupling of the three states by two coherent radiation fields is a 3 × 3 matrix. If the decay of the excited state is neglected and the rotating-wave approximation (RWA) is used, the Hamiltonian (in a suitable rotating frame) reads [Fle05]

$$H(t) = \frac{\hbar}{2}\begin{bmatrix} 0 & \Omega_\mathrm{P}(t) & 0 \\ \Omega_\mathrm{P}(t) & 2\Delta_\mathrm{P} & \Omega_\mathrm{S}(t) \\ 0 & \Omega_\mathrm{S}(t) & 2(\Delta_\mathrm{P} - \Delta_\mathrm{S}) \end{bmatrix}. \tag{6.15}$$

For zero two-photon detuning $\delta = 0$, the Hamiltonian can be diagonalized analytically and the following eigenstates of the system are found:

$$\begin{aligned}|a^+\rangle &= \sin\theta\sin\Phi|1\rangle + \cos\Phi|2\rangle + \cos\theta\sin\Phi|3\rangle,\\ |a^0\rangle &= \cos\theta|1\rangle - \sin\theta|3\rangle,\\ |a^-\rangle &= \sin\theta\cos\Phi|1\rangle - \sin\Phi|2\rangle + \cos\theta\cos\Phi|3\rangle,\end{aligned} \tag{6.16}$$

where the angle Φ is defined by

$$\tan 2\Phi = \frac{\sqrt{\Omega_\mathrm{P}^2 + \Omega_\mathrm{S}^2}}{\Delta_\mathrm{P}}. \tag{6.17}$$

The mixing angle θ is defined by the relationship

$$\tan\theta = \frac{\Omega_\mathrm{P}(t)}{\Omega_\mathrm{S}(t)}. \tag{6.18}$$

The state $|a^0\rangle$ does not contain any fraction of the excited state $|2\rangle$. If the states $|1\rangle$ and $|3\rangle$ are stable, particles in the $|a^0\rangle$ state do not decay and therefore this state is called dark state. Molecules in the excited state quickly decay to states that cannot be observed and are hence lost from our system on a timescale given by the lifetime of the excited state, which is $\tau = 1.2\,\mu$s. Therefore, molecules in states $|a^+\rangle$ and $|a^-\rangle$ quickly get lost from the system and only population in the $|a^0\rangle$ state is stable.

6.3.1 Resonant spectroscopy

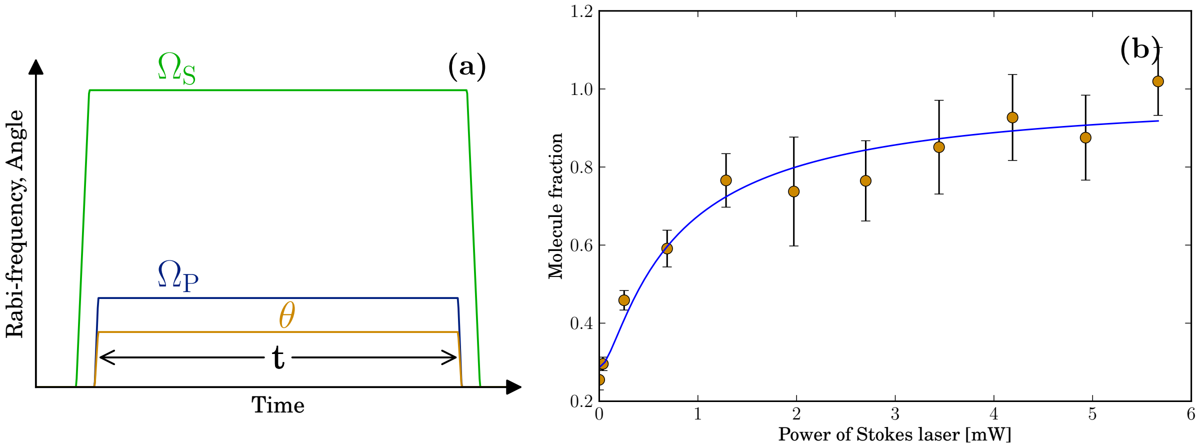

Figure 6.8: Timing scheme of the two-photon spectroscopy (a): First the Stokes laser is switched on, coupling states $|2\rangle$ and $|3\rangle$, then the pump laser is switched on. After a hold time t both lasers are switched off in reverse order. In (b) a two-photon projection measurement of the $|\Omega = 1, v' = 29, J' = 1\rangle$ state is shown. The laser power $P_\mathrm{P} = 0.70\,\mathrm{mW}$ leads to a Rabi frequency of $\Omega_\mathrm{P} = 57\,\mathrm{kHz}$. The power of the Stokes laser is varied. The points show the experimental data, the line is a fit to the data, which yields Rabi frequency of $\Omega_S = 96\,\mathrm{kHz}/\sqrt{\mathrm{mW}}$. The Rabi frequency normalized to the laser power is $510\,\mathrm{Hz}/\sqrt{\mathrm{mW/cm}^2}$.

If both the pump and the stokes laser are on resonance, the transition strength of the Stokes transition can be determined by projection of the initial $|1\rangle$ state onto the dark state $|a^0\rangle$.

By rapidly changing laser intensities and thereby changing the Rabi frequencies Ω_P and Ω_S, a set of states $|a_1^+\rangle$, $|a_1^0\rangle$, $|a_1^-\rangle$ is projected onto another set of states $|a_2^+\rangle$, $|a_2^0\rangle$, $|a_2^-\rangle$. For our projection measurements the molecules are initially in state $|1\rangle$ and both spectroscopy lasers are off. Then the Stokes laser is switched on and couples the unpopulated states $|2\rangle$ and $|3\rangle$. This defines the mixing angle $\theta = 0$. By rapidly switching on the pump laser the mixing angle θ changes, and the initial state $|1\rangle$ is projected onto the new set of eigenstates. State $|1\rangle$ in this new basis reads

$$|1\rangle = \alpha^+|a^+\rangle + \alpha^0|a^0\rangle + \alpha^-|a^-\rangle. \tag{6.19}$$

Since the states $|a^+\rangle$ and $|a^-\rangle$ contain some fraction of the unstable $|2\rangle$ state, molecules in these states will decay out of the system. After a hold time t much larger than the lifetime τ of the excited state, only molecules in the $|a^0\rangle$ state are left. This can be described as a projection $|a^0\rangle\langle a^0|$ onto the $|a^0\rangle$ state. For detection of the molecules, first the pump laser is switched off and then the Stokes laser is switched off. Since only molecules in the $|1\rangle$ state can be detected, this corresponds to a projection $|1\rangle\langle 1|$ onto the initial state. The final state therefore reads

$$|final\rangle = |1\rangle\langle 1||a^0\rangle\langle a^0|1\rangle = \cos^2\theta|1\rangle. \tag{6.20}$$

The fraction of molecules remaining after the measurement is

$$N/N_0 = ||\langle final|final\rangle||^2 = \cos^4\theta = \frac{\Omega_\mathrm{S}^4}{(\Omega_\mathrm{P}^2 + \Omega_\mathrm{S}^2)^2}. \tag{6.21}$$

Relation (6.21) is used to determine the Rabi frequency Ω_S. Thereby the transition strength and dipole moment of the second transition are determined.

In Fig. 6.8 a measurement is shown for which both lasers are kept on resonance and the power of the Stokes laser is varied. The power of the probe laser is 0.7 mW, which results in a Rabi frequency of $\Omega_\mathrm{P} = 2\pi \times 57\,\mathrm{kHz}$. For determination of the transition strength of the Stokes transition Ω_S is varied by changing the power of the Stokes laser. The Rabi frequency $\Omega_\mathrm{S}^2 = \Omega_{\mathrm{norm,S}}^2 \times P_\mathrm{S}$ is expressed in terms of the power of the Stokes laser P_S and the normalized Rabi frequency $\Omega_{\mathrm{norm,S}}$, which is to be determined by a fit using (6.21). Further fit parameters are the total number of molecules N_0, and an offset. The latter is typically due to some Cs atoms that remain in the trap after the Stern-Gerlach separation. We measure a normalized Rabi frequency of $510\,\mathrm{Hz}/\sqrt{\mathrm{mW/cm^2}}$. For the two-photon spectroscopy the same systematic errors occur as for the one photon spectroscopy. Since the two-photon data is based on the one-photon data the systematic errors of the measurements increase, which leads to an estimated error of 20%.

6.3.2 Three-level systems with off-resonant coupling

In order to find the exact binding energy and thereby the frequency ω_{23} of the transition from state $|2\rangle$ to state $|3\rangle$ we scan the frequency of the Stokes laser until the two-photon resonance occurs, while the pump laser is kept on resonance. The pulse sequence is the same as in the measurements described above (see Fig. 6.8). The Rabi frequencies of the two lasers are chosen in such a way that $\Omega_\mathrm{S} \gg \Omega_\mathrm{P}$. In this case the pump laser is probing a system of two states coupled by the Stokes laser. If the Stokes laser resonantly couples states $|2\rangle$ and $|3\rangle$, the laser induced coherence leads to quantum interference between the two excitation pathways. This way the absorption at the resonant frequency ω_{12} is eliminated, preventing the loss of Feshbach molecules.

The elimination of absorption by resonant coupling of an excited target state to a third state has been known for more than 20 years under the term electromagnetically induced transparency (EIT) [Har90]. In the past EIT gained a lot of attention due to the fact that it gives rise to a steep dispersion leading to novel phenomena such as slow light [VH99]. A review covering the theoretical basis can be found in [Fle05] and the equations derived there can also be used to describe our two-photon spectroscopy.

Since in the following measurements the frequency of either the pump or the Stokes laser is varied the respective detunings Δ_P and Δ_S have to be taken into account. If the two-photon detuning $\delta = (\Delta_\mathrm{P} - \Delta_\mathrm{S})$ is not zero a fraction of the $|2\rangle$ state is mixed into the $|a^0\rangle$ state. In the limit $\Omega_\mathrm{P} \ll \Omega_\mathrm{S}$ the pump laser can be treated as a perturbation, which simplifies the diagonalisation of the Hamiltonian. Analogously to the discussion in [Fle05] an equation describing our measurements can be derived.

$$N = N_0 \exp\left(-t_\mathrm{irr}\Omega_\mathrm{P}^2 \frac{4\gamma\delta^2 + \Gamma_\mathrm{eff}(\Omega_\mathrm{S}^2 + \Gamma_\mathrm{eff}\gamma)}{|\Omega_\mathrm{S}^2 + (\gamma + 2i\Delta_\mathrm{P})(\Gamma_\mathrm{eff} + 2i\delta)|^2}\right). \tag{6.22}$$

Here t_irr is the irradiation time and Γ_eff accounts phenomenologically for loss and decoherence between levels $|1\rangle$ and $|3\rangle$. This equation describes all the following spectroscopy measurements and explains the different line shapes.

For detection of the molecular ground state the probe laser is kept on resonance

$\Delta_\mathrm{P} = 0$, which leads to

$$N = N_0 \exp\left(-t_\mathrm{irr}\Omega_\mathrm{P}^2 \frac{4\gamma\Delta_\mathrm{S}^2 + \Gamma_\mathrm{eff}(\Omega_\mathrm{S}^2 + \Gamma_\mathrm{eff}\gamma)}{(\Omega_\mathrm{S}^2 + \gamma\Gamma_\mathrm{eff})^2 + 4\gamma^2\Delta_\mathrm{S}^2}\right). \tag{6.23}$$

From this follows that Γ_eff can be neglected in cases where $\gamma\Gamma_\mathrm{eff} \ll \Omega_\mathrm{S}^2$. If this condition can be fulfilled, the equation simplifies to

$$N = N_0 \exp\left(-t_\mathrm{irr}\frac{\Omega_\mathrm{P}^2}{\gamma}\frac{4\gamma^2\Delta_\mathrm{S}^2}{\Omega_\mathrm{S}^4 + 4\gamma^2\Delta_\mathrm{S}^2}\right). \tag{6.24}$$

In cases when the fraction of lost Feshbach molecules $1-N/N_0$ is small, meaning $t_\mathrm{irr}\Omega_\mathrm{P}^2/\gamma \ll 1$, the exponent always remains small. In this case $\exp(-x) \approx 1 - x$ and a Lorentzian profile with an offset is expected. The width of this Lorentzian is independent of $\Omega_\mathrm{P}^2/\gamma$. Therefore measurements of this kind can be used to determine Ω_S independently of Ω_P. Due to the fact that only a small fraction of the Feshbach molecules should be lost the baseline of the signal lies close to the full molecule signal. If the signal-to-noise ratio is unfavorable the measurements become unreliable.

The measurements presented here are therefore set up in a way that almost all Feshbach molecules are lost if the Stokes laser is far from resonance. In this case the condition $t_\mathrm{irr}\Omega_\mathrm{P}^2/\gamma \gg 1$ is valid. For this condition, it has to be assumed that $4\gamma^2\Delta_\mathrm{S}^2 \ll \Omega_\mathrm{S}^4$ in order to observe a signal that is distinguishable from background noise ($N \gg 0$). Hence equations (6.23) and (6.24) transform into Gaussian functions

$$N = N_0 \exp\left(-\tau_i\frac{4\gamma^2\Delta_\mathrm{S}^2}{(\Omega_\mathrm{S}^2 + \gamma\Gamma_\mathrm{eff})^2}\right)\exp\left(-\tau_i\frac{\gamma\Gamma_\mathrm{eff}}{(\Omega_\mathrm{S}^2 + \gamma\Gamma_\mathrm{eff})}\right). \tag{6.25}$$

$$N = N_0 \exp\left(-\tau_i\frac{4\gamma^2\Delta_\mathrm{S}^2}{\Omega_\mathrm{S}^4}\right). \tag{6.26}$$

At this point, for simplicity, the dimensionless irradiation time $\tau_i = t_\mathrm{irr}\Omega_\mathrm{P}^2/\gamma$ has been introduced. In the case that includes decoherence (6.25) one can clearly see that $\Gamma_\mathrm{eff} \neq 0$ reduces the amplitude and induced a (small) broadening of the linewidth. If τ_i is chosen to be ($\tau_i \gg 1$), $\gamma\Gamma_\mathrm{eff}$ has to be much smaller than Ω_S^2 in order to observe a peak. Hence eq. (6.25) can be simplified to

$$N = N_0 \exp\left(-\tau_i\frac{4\gamma^2\Delta_\mathrm{S}^2}{\Omega_\mathrm{S}^4}\right)\exp\left(-\tau_i\frac{\gamma\Gamma_\mathrm{eff}}{\Omega_\mathrm{S}^2}\right). \tag{6.27}$$

Dark state resonances can be detected by scanning the detuning of the Stokes laser Δ_S until the resonance ($\Delta_\mathrm{S} = 0$) is observed. For large detunings the molecules decay. On resonance the first exponential function becomes zero and some molecules should be observed. Equation (6.27) provides a simple way of determining the decoherence parameter Γ_eff by variation of the irradiation time keeping both lasers on resonance. If the lasers are on resonance eq. (6.27) reads

$$N = N_0 \exp\left(-\tau_i\frac{\gamma\Gamma_\mathrm{eff}}{\Omega_\mathrm{S}^2}\right). \tag{6.28}$$

Equation (6.28) can also be directly derived from (6.23) and holds for all values of τ_i. A more detailed description on laser noise and coherence is given in chapter 7.

6.3.3 Measurement of the decoherence

A measurement of the decoherence rate Γ_{eff} is shown in Fig. 6.9. The states involved are the $|6(2,4)d(2,4)\rangle$ Feshbach state, the $|\Omega' = 0, v' = 35, J' = 1\rangle$ excited state and the $|v'' = 0, J'' = 2\rangle$ ground state. The lifetime of the molecules is measured to be $\tau = 0.75\,\text{ms}$. In the measurement presented above, τ is much smaller than the lifetime of the Feshbach molecules. Hence the decay due to decoherence can be clearly distinguished from the decay of Feshbach molecules due to other effects.[9]

A large decoherence rate of 30 kHz is derived. This rate is much larger than any decay rate that could be caused by decoherence of the laser (See section 7.2). The large decoherence rate might be connected to the existence of multiple hyperfine levels in the excited state that are addressed simultaneously. In Ref. [Vit99] it is shown that for multiple intermediate levels a dark state exists only when the ratio between each pump coupling and the respective Stokes coupling is the same for all intermediate states. The influence of multiple intermediate magnetic sublevels has been studied in Refs. [Mar95, Mar96, Sho95]. The collapse of adiabatic passage due to multiple nearly degenerate intermediate levels is analyzed in Ref. [Sol03]. It has been found that the formation of a dark state depends on a favorable ratio of the transition dipole matrix elements of the individual levels. Since we observe strong losses from our alleged dark state, it may be assumed that for this intermediate state the ratio of the coupling of the different hyperfine states is not favorable and does not lead to the formation of a dark state.

The measurement of the effective decoherence rate allows for a qualitative estimation of

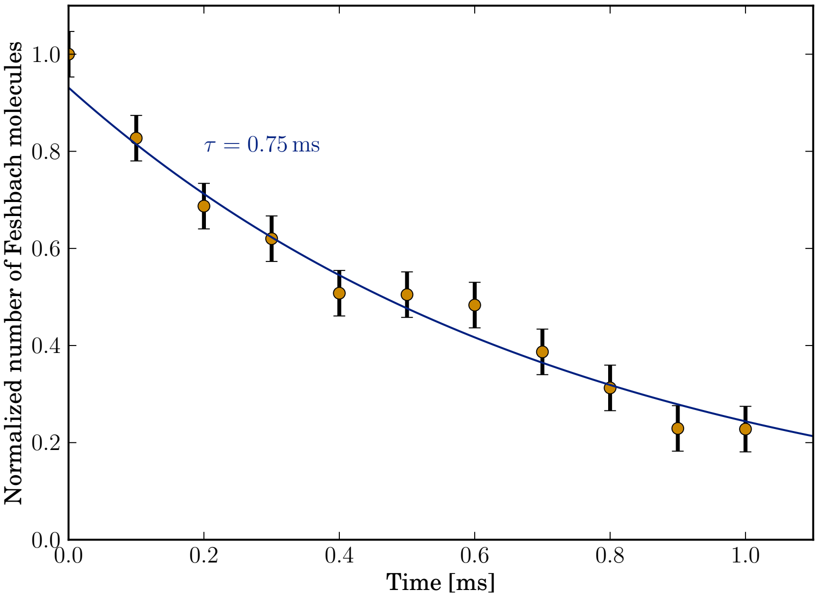

Figure 6.9: Measurement of the decoherence rate on the $|6(2,4)d(2,4)\rangle \leftrightarrow |\Omega' = 0, v' = 35, J' = 1\rangle \leftrightarrow |v'' = 0, J'' = 2\rangle$ transition. The Rabi frequencies are $\Omega_P = 2\pi \times 280\,\text{kHz}$ and $\Omega_S = 2\pi \times 1.3\,\text{MHz}$. A lifetime of $\tau = 0.75\,\text{ms}$ is measured, which yields a decoherence rate of $\Gamma_{\text{eff}} = \Omega_{\text{S}}^2/\Omega_{\text{P}}^2\tau = 30\,\text{kHz}$.

---

[9] Similar measurements have been carried out for the $\Omega = 1$ excited states. For these the effect of decoherence is so small that it can not be distinguished from the decay of Feshbach molecules due to their limited lifetime.

a STIRAP transfer efficiency. For STIRAP, the timescale is set by the Rabi frequency and an adiabatic passage is only possible for transition times much longer than the inverse Rabi frequency (For details see chapter 7). For a successful STIRAP the dark state should have a lifetime much longer than the transfer time since during the transfer the molecules are in this dark state and any loss from this state reduces the efficiency. Hence the decoherence rate Γ_{eff} should be much smaller than the Rabi frequencies. While a quantitative estimation of STIRAP efficiency based on this kind of measurement is not reliable, the measurement provides an easy way to classify the investigated transitions qualitatively.[10] In order to expect a high efficient STIRAP transfer the decoherence rate Γ_{eff} should be at least a factor of ten smaller than the Rabi frequencies. We find large decoherence rates for the $\Omega = 0$ excited states[11]. For the $\Omega = 1$ excited state, the decay due to decoherence is much smaller and could not be distinguished from the lifetime of the Feshbach molecules in the trap.

6.3.4 Detection of two-photon resonance

For the detection of two-photon resonance the Stokes laser is scanned, while the pump laser is kept on resonance. In order to find a suitable route for ground-state transfer the excited levels $|\Omega = 0, v' = 35, J' = 1\rangle$, $|0, 36, 1\rangle$, $|0, 37, 1\rangle$ and the $|1, 29, 1\rangle$ have been investigated using two-photon spectroscopy on the $J'' = 0$ and $J'' = 2$ ground-state levels. The following measurements show dark-state resonances involving the $|v'' = 0, J'' = 0\rangle$ ground state.

Figure 6.10 shows measurements of two-photon dark-state resonances involving the excited states $|1, 29, 1\rangle$ (a) and $|0, 35, 1\rangle$ (b). The laser detuning is the detuning from resonance. In addition we measure the absolute frequency of the laser with a wavemeter. For the $|0, 35, 1\rangle$ excited state we measures the wavelengths of the pump and Stokes laser to be $L_{\text{P}} = 6364.0439\,\text{cm}^{-1}$ and $L_{\text{S}} = 10175.2913\,\text{cm}^{-1}$ respectively. These values are used to determine the binding energy of the lowest rovibronic level of the ground state as follows. The difference of the laser frequencies at 217 G measured with respect to the $\text{Rb}(5^2S_{1/2}, f_{\text{Rb}} = 1) + \text{Cs}(6^2S_{1/2}, f_{\text{Cs}} = 3)$ asymptote yields $3811.2477\,\text{cm}^{-1}$. The binding energy at zero field, with respect to the center of gravity of the hyperfine manifold $3811.5755(16)\,\text{cm}^{-1}$, is obtained by adding the Zeeman shift ($0.0131\,\text{cm}^{-1}$, or 0.349 GHz) and the relevant energy spacing ($0.3150\,\text{cm}^{-1}$). The error estimates our wavemeter precision.

A fit of the measured data yields information on the Rabi frequency of the Stokes transition. As is shown in Fig. 6.10 for the $v' = 29$ level the measurement follows the theory of the ideal case, whereas for the $v' = 35$ level the phenomenological decoherence parameter Γ_{eff} has to be used in order to fit the data. Furthermore in the latter case a signal could only be obtained for very short measurement times.

Since the ground state has a hyperfine structure, this leads to an artificial broadening of the line. Depending on the system parameters there are two ways to solve the problem. Firstly, if the single hyperfine lines are sufficiently separated from each other, the hyperfine structure can be resolved by choosing appropriate values of Ω_{S} and thereby narrowing the

---

[10] This includes also other decoherence effects, which can arise for example from the laser system.

[11] In fact, the measurement presented above shows one of the lowest decoherence rates that we have measured for $\Omega = 0$ states.

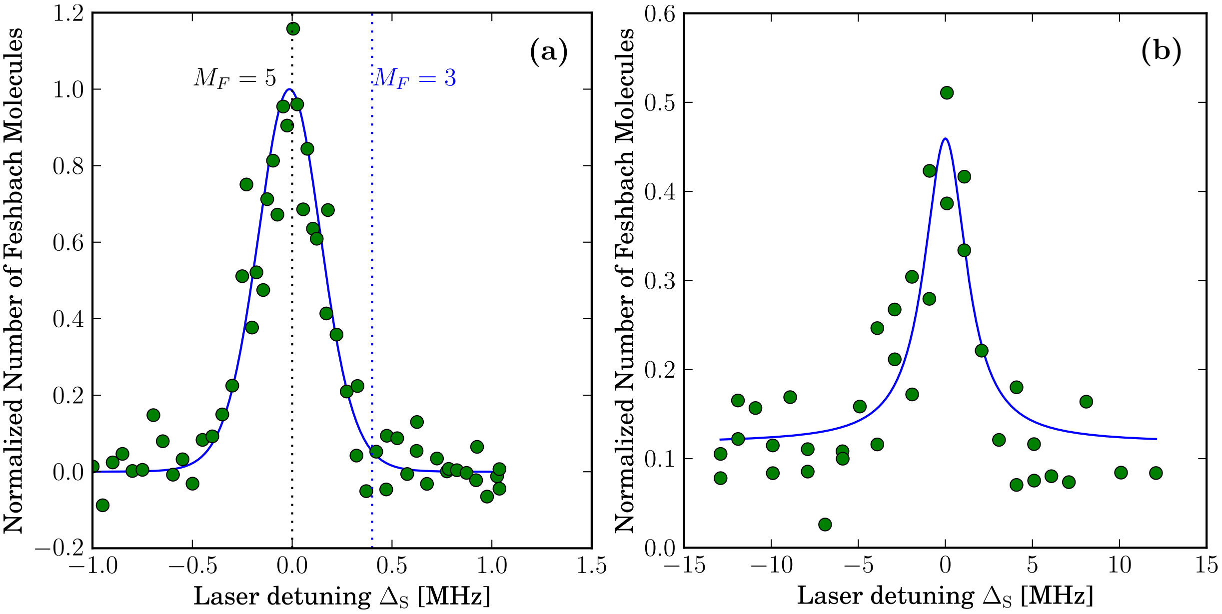

Figure 6.10: Two-photon ground-state spectroscopy involving the $v' = 29$ (a) and the $v' = 37$ (b) excited state level. The data is normalized to the number of Feshbach molecules initially present. The polarizations of the light of the pump and Stokes laser are π and $\sigma^{\pm}$ respectively. In (a) the Rabi frequency $\Omega_P = 2\pi \times 19\,\text{kHz}$ is known from previous measurements.The irradiation time is $1000\,\mu\text{s}$ and the excited state line width is $\gamma_{29} = 2\pi \times 130\,\text{kHz}$. The fitted Rabi frequency is $\Omega_S = 2\pi \times 202(5)\,\text{kHz}$, which corresponds to a normalized Rabi frequency of $2\pi \times 0.74\,\text{kHz}/\sqrt{\text{mW/cm}^2}$. The dashed lines indicate positions of the two hyperfine lines that are observed in our further measurements (see section 7.3) for this combination of polarizations. For (b) the Rabi frequencies are $\Omega_P = 2\pi \times 325\,\text{kHz}$ and $\Omega_S = 2\pi \times 1130(60)\,\text{kHz}$, which corresponds to a normalized Rabi frequency of $2\pi \times 2.4\,\text{kHz}/\sqrt{\text{mW/cm}^2}$. The irradiation time is $10\,\mu\text{s}$ and the excited state line width is $\gamma_{37} = 2\pi \times 3.1\,\text{MHz}$. In (b) a decoherence rate of $\Gamma_{\text{eff}} = 2\pi \times 230\,\text{kHz}$ is fitted.

line (figure 6.13). The choice of Ω_s in turn is limited by decoherence. Hence the spacing Δ_{HFS} has to fulfill the following inequality

$$\Delta_{\text{HFS}} \gg \frac{\Omega_S^2}{\gamma} \gg \Gamma_{\text{eff}} \tag{6.29}$$

in order to allow for a suitable choice of Ω_S. For the $|\Omega = 1, v' = 29\rangle$ state small decoherence rates permit an appropriate choice of Ω_S. Secondly, if resolution of the hyperfine states is not possible ($\Omega = 0$ states), the peak can be broadened. Hence we choose large values of Ω_S in order to broaden the peak such that it becomes much broader than the hyperfine structure splitting. However this strategy requires a sufficiently strong transition and sufficient laser power.

In the experiment both strategies are applied. The $\Omega = 0$ excited state has large loss and decoherence rates that prevent the choice of low values of Ω_S. Hence the measurements are taken with large values of Ω_S, which is possible because of the large transition strength due to the large singlet character of the excited states. In the spectroscopy involving the $\Omega = 1$ excited state, the excited states features only a small amount of singlet character leading to small dipole matrix elements and limiting the maximum Ω_S. In this case however the excited state hyperfine structure is well resolved leading to a single excited state and therefore much lower decoherence. The observed peak is smaller than the splitting of the hyperfine structure. In later measurements that are presented in section 7.3 we detect two hyperfine states for this very combination of polarization. For comparison these two hyperfine states are drawn in graph Fig. 6.10 (a). [12]

6.3.5 Observation of Autler-Townes splitting

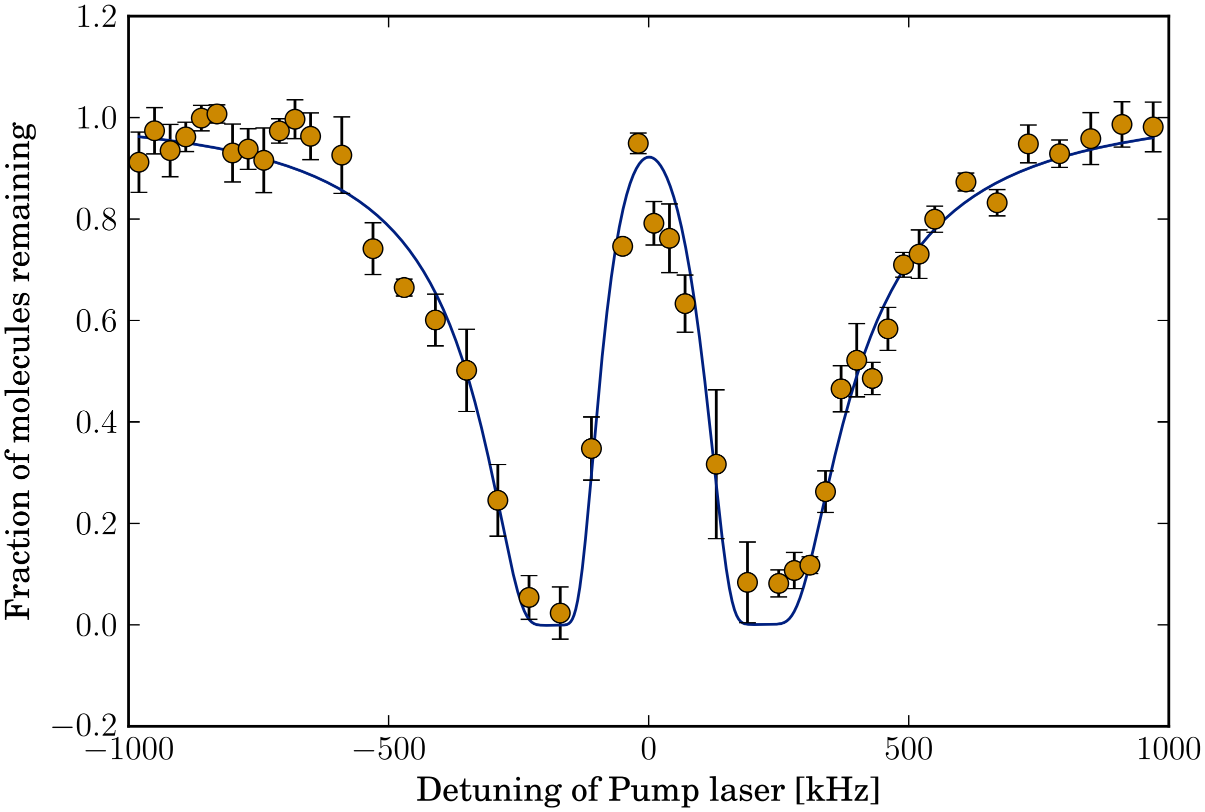

Figure 6.11: Autler-Townes splitting on the transition $|6(2,4)d(2,4)\rangle \leftrightarrow |\Omega' = 1, v' = 29, J' = 1\rangle \leftrightarrow |v'' = 0, J'' = 0\rangle$. The observation time is 2 ms and laser powers are $P_\mathrm{P} = 0.05\,\mathrm{mW}$ and $P_\mathrm{S} = 14.2\,\mathrm{mW}$. The Rabi frequencies from the fit are $\Omega_\mathrm{P} = 12\,\mathrm{kHz}$ and $\Omega_\mathrm{S} = 290\,\mathrm{kHz}$. The normalized Rabi frequency for the second transition is $\Omega_\mathrm{S} = 540\,\mathrm{Hz}/\sqrt{\mathrm{mW}/\mathrm{cm}^2}$.

If the pump laser is scanned, while the Stokes laser is kept on resonance the absorption line shows a double peak structure. This appearance has been first observed by Autler and Townes [Aut55]. Our measurement is shown in Fig. 6.11. The double peak line shape is characteristic for an Autler-Towns splitting and is a clear sign of two-photon coherence. The shape of the line can be modelled by Eq. (6.22). Compared to the measurement shown in Fig. 6.9 the states used in this measurement remain coherently coupled for at least 2 ms. This can be seen from the fact that the central peak still reaches its maximum. This kind of measurement nicely shows the effects of coherent coupling of states. However, the fit that is based on Eq. (6.22) involves many degrees of freedom. Apart from the irradiation time t_irr and the excited state linewidth γ all parameters in the equation are free. N_0 is used to normalize the data. The large number of degrees of freedom leads to a mutual

---

[12] In later measurements it has been observed that the $M_F = 5$ state couples stronger to the excited state than the $M_F = 3$ states. Therefore the most likely interpretation is that the former is represented by the peak, while the latter is not observed.

influence of the parameters. Therefore the parameters of the system are more reliably determined by the measurements described earlier.

6.3.6 Hyperfine structure measured by two-photon spectroscopy

Basic information on ground-state properties of alkali-dimers has been available for several decades [IM86]. However the detailed structure of the different vibrational, rotational, and hyperfine levels and molecular electronic potentials is still a challenge in ongoing research and the hyperfine structure of groundr-state RbCs has not been observed prior to our measurements.

Theoretical calculations of the hyperfine structure have been carried out by Aldegunde *et al.* [Ald08]. The Hamiltonian for $^1\Sigma$ molecules in the ground electronic states and in a fixed vibrational level can be written as

$$H = H_{\mathrm{el}} + H_{\mathrm{vib}} + H_{\mathrm{rot}} + H_{\mathrm{hf}} + H_{\mathrm{S}} + H_Z, \tag{6.30}$$

where H_{el}, H_{vib}, H_{rot}, H_{hf}, H_{S}, and H_Z describe the electronic, vibrational, rotational, hyperfine, Stark, and Zeeman parts. The first two parts take a constant value and at zero electric field H_{S} is zero. The hyperfine part is given by

$$H_{\mathrm{hf}} = \sum_{\mathrm{i}=1}^{2} \mathbf{V}_i \cdot \mathbf{Q}_i + \sum_{\mathrm{i}=1}^{2} c_i \mathbf{N} \cdot \mathbf{I}_i + c_3 \mathbf{I}_1 \cdot \mathbf{T} \cdot \mathbf{I}_2 + c_4 \mathbf{I}_1 \cdot \mathbf{I}_2, \tag{6.31}$$

where the first two terms describe the electric quadrupole interaction, and the interaction between the nuclear magnetic moments and the magnetic field generated by the rotation of the molecule. The last two terms represent the tensor and scalar interactions between the nuclear dipole moments, with spin-spin coupling constants c_3 and c_4 respectively. The nuclear spins are denoted by $\mathbf{I}_1$, $\mathbf{I}_2$ and $\mathbf{N}$ denotes the rotational angular momentum. In the ground state N is identical with J.

The Zeeman Hamiltonian for an external magnetic field $\mathbf{B}$ is given by

$$H_Z = -g_r \mu_N \mathbf{N} \cdot \mathbf{B} - \sum_{\mathrm{i}=1}^{2} g_i \mu_N \mathbf{I}_i \cdot \mathbf{B}(1 - \sigma_i), \tag{6.32}$$

where g_r is the rotational g factor of the molecule, g_i are the nuclear g factors of the atoms, and σ_i is called the isotropic part of the nuclear shielding tensor. Data for these constants are summarized in Ref. [Ald08].

According to [Ald08] for $N = 0$ the splittings are dominated by the scalar spin-spin interaction and the nuclear Zeeman effect. Further the terms that lead to a coupling of different rotational levels have an influence of less than 1%. Therefore for a simple version, the calculations can be restricted to terms diagonal in $\mathbf{N}$. In this case the rotational Hamiltonian is zero and the Hamiltonian of the system can be written as

$$H = c_4 \mathbf{I}_1 \cdot \mathbf{I}_2 - \sum_{\mathrm{i}=1}^{2} g_i \mu_N \mathbf{I}_i \cdot \mathbf{B}(1 - \sigma_i). \tag{6.33}$$

The eigenstates of this Hamiltonian can be calculated with little numerical effort using Clebsh-Gordan coefficients. The atomic constants are well known and the molecular constant c_4 has been calculated with ab initio methods in Ref. [Ald08]. An overview of the hyperfine structure that can be reached by two-photon transitions starting from our $M_F = +4$ Feshbach state is given in Fig. 6.12.

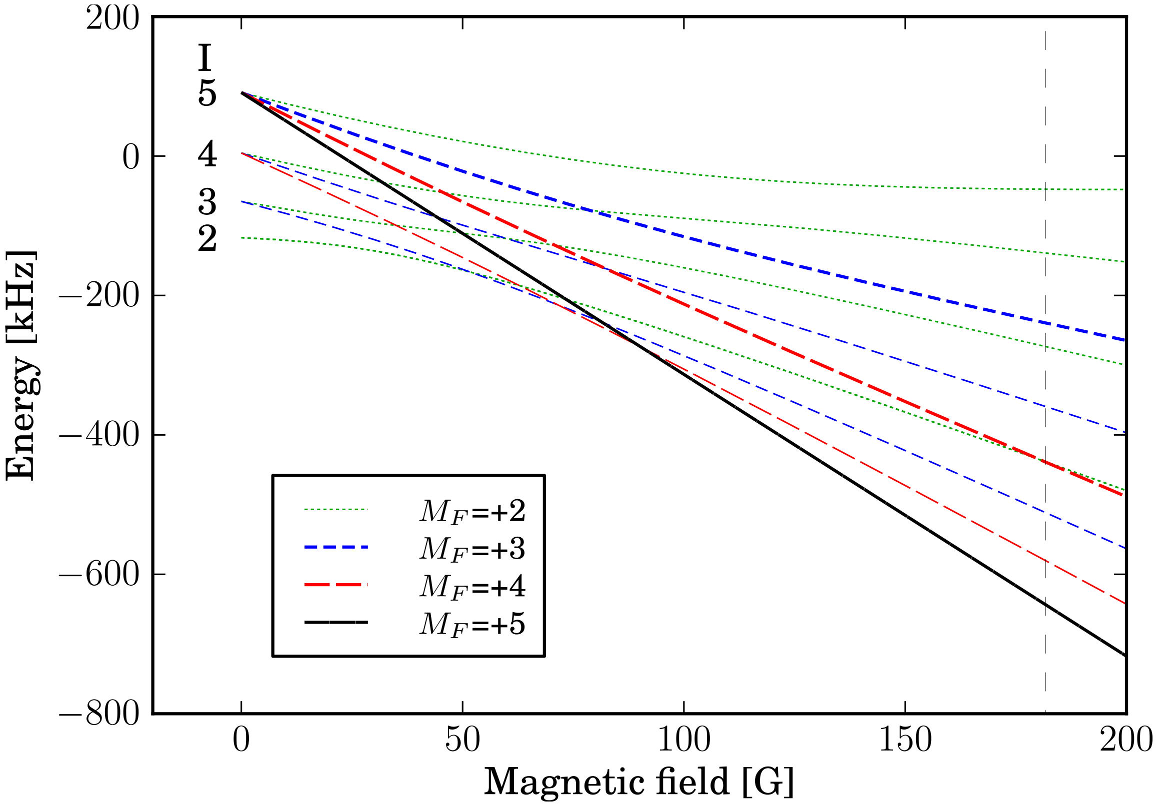

Figure 6.12: Hyperfine structure of the RbCs ground state. The graph shows the relevant states that can be addressed by a two-photon process starting from an initial state with $M_F = +4$. In our further measurements only the states with $M_F = +3, +4, +5$ are relevant. The states that are observed in the measurements are represented by strong lines. The vertical line indicates the magnetic field of the Feshbach resonance at 181.5 G at which the experiments are carried out. (Graph based on Ref. [Ald08])

Measurements

In our measurements the starting Feshbach state is $|-6(2,4)d(2,4)\rangle$ with $M_F = 4$. Vertical polarization of the light is parallel to the quantization axis and therefore results in π polarization. In this case transitions with $\Delta M_F = 0$ can be driven. A horizontal polarization of the light yields mixture of $k = 1/\sqrt{2}(\sigma^+ + \sigma^-)$ polarization. This allows for transitions with $\Delta M_F = \pm 1$ according to selection rule 3.27. Hence, with two photons transitions with $\Delta M_F = -2 \cdots + 2$ can be driven. Starting from an $M_F = +4$ state, ground state levels with $M_F = +5, +4, +3, +2$ can be reached as shown in Fig. 6.12.

For the STIRAP measurements the first laser always has π polarization, while the second laser can be changed between $\sigma^\pm$ and π polarization. In this case either states with $M_F = +5, +3$ or states with $M_F = +4$ can be reached. This greatly reduces the number of observable hyperfine levels. The number of actually observed hyperfine levels is smaller. Apparently with the currently used intermediate state only hyperfine levels belonging to the $I = +5$ manifold could be measured. This could be due to some additional selection rules involving the excited level.

If the Rabi frequencies are sufficiently low, the two-photon linewidth is narrow enough to observe the ground-state hyperfine structure by use of projection measurements. Figure 6.13 shows such a measurement with low Rabi frequencies. The polarization is predominantly π for both lasers with a small admixture of $\sigma^\pm$ for the Stokes laser. In this case

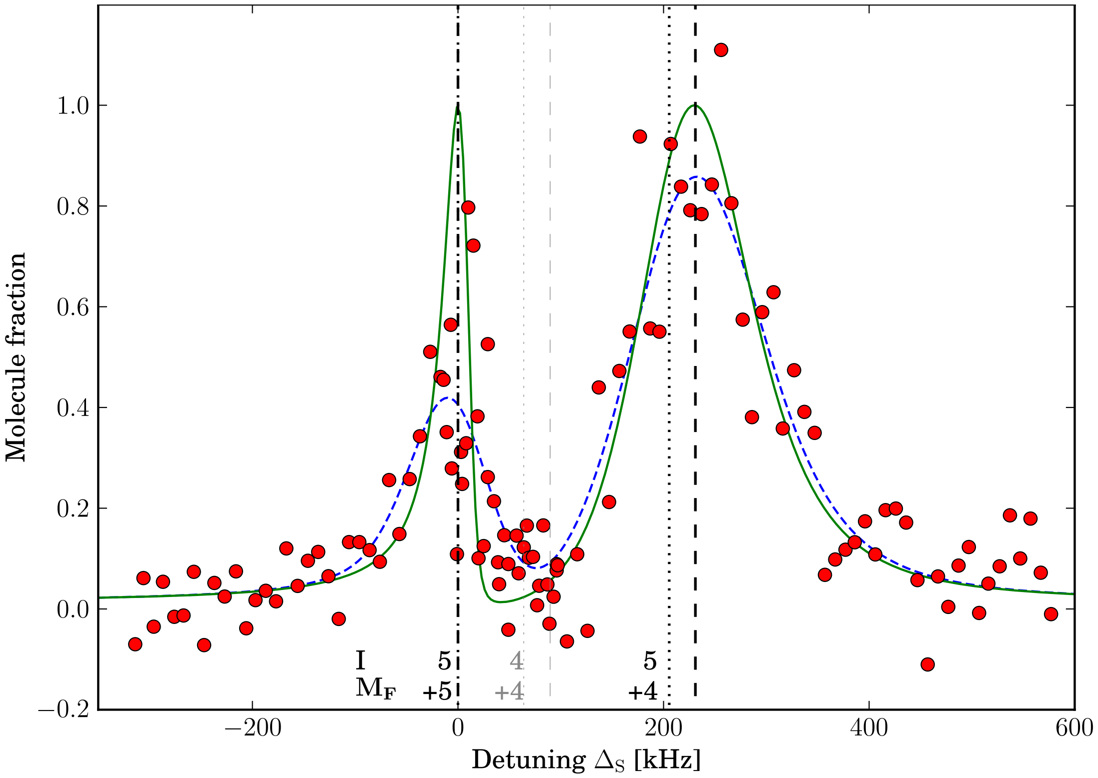

Figure 6.13: Two-photon spectroscopy of the RbCs ground state at 181.5 G. The pump laser is kept on resonance $\Delta_P = 0$ with the transition between the $|-6(2,4)d(2,4)\rangle$ Feshbach state and the $|\Omega = 1, v' = 29\rangle(b^3\Pi_1)$ excited state. The Stokes-laser detuning Δ_S is scanned. The dashed curve shows a numeric model including a statistical averaging over an ensemble of Gaussian-distributed two-photon detunings. The solid line is the same numeric model without noise. The dots represent the individual data points. The Rabi frequencies are $\Omega_p = 2\pi \times 27\,\text{kHz}$, $\Omega_S = 2\pi \times 150\,\text{kHz}$. The vertical lines indicate the positions of the hyperfine levels. The dotted lines are for a c_4 coefficient of 17 kHz. For the dashed lines a numeric solution of Eq. (6.33) is fitted to the data leaving c_4 as a free fit parameter. The fit results in a value of $c_4 = 7(3)\,\text{kHz}$, where the error represents the statistical error due to the fluctuation of the data points.

two distinguishable peaks are observed. For pure polarization only $M_F = +4$ levels could be observed. The splitting of the two levels however does not match to the splittings of the corresponding levels. Therefore another interpretation taking into account a small admixture of $\sigma^\pm$ polarization is more reasonable.

As shown later using STIRAP, the coupling to the $M_F = +5$ level is much stronger than the coupling to the $M_F = +3$ level. Any admixture of $\sigma^\pm$ polarization should mainly show the $M_F = +5$ state. In the STIRAP measurements below, only the $I = 5$ levels could be observed. Hence the two most visible levels should be the $I = 5, M_F = +4$ level and the $I = 5, M_F = +5$ level. For this interpretation the splitting of the observed peaks fits with the calculated hyperfine splitting at 181 G.

Analysis of the data

For the fits shown in Fig. 6.13 the Hamiltonian of Eq. 6.15 has to be extended to at least four states. It then reads

$$H(t) = \frac{\hbar}{2}\begin{bmatrix} 0 & \Omega_\mathrm{P}(t) & 0 & 0 \\ \Omega_\mathrm{P}(t) & -2\Delta_\mathrm{P} - i\gamma & \Omega_\mathrm{S}(t) & \alpha_1\Omega_\mathrm{S}(t) \\ 0 & \Omega_\mathrm{S}(t) & -2(\Delta_\mathrm{P} - \Delta_\mathrm{S}) & 0 \\ 0 & \alpha_1\Omega_\mathrm{S}(t) & 0 & -2(\Delta_\mathrm{P} - \Delta_\mathrm{S} - \delta_1) \end{bmatrix}, \tag{6.34}$$

where α_1 describes the coupling strength of the additional hyperfine state relative to first hyperfine state. The detuning δ_1 describes energy splitting between the two hyperfine states in units of $\hbar$. The Hamiltonian can easily be extended for more hyperfine levels.

As analytical diagonalization is cumbersome for this 4×4 matrix, numerical diagonalization is used to obtain the eigenvectors. The complex part of the corresponding eigenvalues describes the decay rate. The resulting numerical data for different detunings Δ_S are fitted to the measured data. Since the data shows a high fluctuation for detunings at which the model predicts a steep slope, we assume that there are fluctuations in the two-photon detuning. In order to account for such fluctuations we assume that the fluctuations can be modelled by a Gaussian distribution and include and average over a Gaussian distribution in the model. Slow fluctuations can result from shifts in the molecular levels due to magnetic field fluctuations or fluctuations in the vertical position of the cloud. Since the initial Feshbach state has a magnetic moment of $\approx 1.6\mu_\mathrm{B}$ and the magnetic moment of the ground state is much smaller, a fluctuations in the magnetic field can lead to a shift of the energies. Since the molecules for this measurement are levitated by an inhomogeneous magnetic field fluctuations in the position can also lead to a shift in the two-photon detuning. Fluctuations of the size of $\sigma_\Delta = 45\,\mathrm{kHz}$ have been determined by the fit. This corresponds to 20 mG. For levitated molecules the energy shift between a levitated and an unlevitated state is $E = mg\Delta_z$, where g is the gravity, m is the mass and Δ_z is the change in altitude. The determined fluctuations correspond to fluctuations of $\Delta_z = 8\,\mu\mathrm{m}$. Since the fluctuations of the magnetic field at high values have not yet been measured. Throughout the measurements fluctuations of the cloud position have also been observed. The exact cause of the fluctuations can not be clearly determined from available data. However in order to overcome fluctuations associated with fluctuations of the position, the measurements presented in the next chapter are carried out with molecules in an optical lattice without levitation.

The observed peaks can be compared to the calculated hyperfine structure. The splitting at 181 G depends on the value of c_4. This allows to determine c_4 to be $c_4 = 7(3)\,\mathrm{kHz}$. The large error is due to the fact that the influence of c_4 on the hyperfine splitting is rather weak at 181 G. A larger amount of data would be necessary for a reliable measurement. Therefore systematic effects like drifts of magnetic field have not been investigated. However, this measurement shows that hyperfine structure can be detected and investigated with this type of measurement.

Summary

Two photon measurements are carried out identification of the ground-state levels and a measurement of the absolute binding energy, which we determine to be $3811.5755(16)\,\mathrm{cm}^{-1}$. For a well isolated intermediate level and a single ground state the two-photon measurements are described analytically. The information gained by the projection measurements including the Rabi frequencies sets the base for successful application of STIRAP. For suitably chosen parameters the sensitivity of projection measurements is high enough to observe the hyperfine splitting of RbCs ground-state molecules. The two-photon measurement can be used to determine the c_4 coefficient.

Chapter 7

Coherent ground-state transfer

The Stimulated Raman Adiabatic Passage technique has been known for more than two decades [Ber98, Vit01] as a robust method for coherently transferring population between two quantum states. It has first been proposed and used in molecular beam experiments [Gau88, Gau90] for transferring molecules between different vibrational states. In the group of K. Bergmann a large variety of aspects of STIRAP has been investigated [Sho91, Cou92, Kuh92, Mar95, Sho95, Mar96]. A detailed analysis of the influences of noise on the transfer efficiency of STIRAP can be found in Ref. [Vit98b] and provides the basis for understanding of STIRAP in RbCs. In the RbCs experiment the Rabi frequency of the weaker transition is ($\Omega = 2\pi \times 250\,\mathrm{kHz}$), which is much weaker than in other similar experiments [Dan08b, Lan08, Ni08]. One condition for adiabatic transfer derived in Ref. [Ber98] is $\Omega_{\mathrm{eff}}\Delta\tau > 10$, where $\Omega_{\mathrm{eff}} = \sqrt{\Omega_{\mathrm{P}}^2 + \Omega_{\mathrm{S}}^2}$ and $\Delta\tau$ is the transfer time. Lower Rabi frequencies thus require a longer transfer time. It is shown in Ref. [Vit98b] that the impact of noise is proportional to the transfer time. Therefore, in RbCs the influence of noise is more critical than in comparable experiments. Hence a detailed analysis of the possible factors that influence the transfer efficiency is included. In the last section the experimental data is analyzed and the ground-state hyperfine level is identified.

7.1 Introduction to stimulated Raman adiabatic passage (STIRAP)

With STIRAP an almost complete transfer between states that otherwise can not directly be coupled can be achieved, by coupling two stable states via an intermediate state (which does not need to be stable). Compared to other schemes involving three levels, one major benefit of STIRAP is that the intermediate level does not get populated. This allows for high efficient transfer even in cases when the intermediate state has a short lifetime.

At least three quantum states are involved in STIRAP. The labelling of the states and most of the algebra can be adapted directly from the description of the two-photon measurements in the last chapter. In contrast to the two-photon spectroscopy measurements the set of eigenstates is changed slow enough, so that the system always remains in the

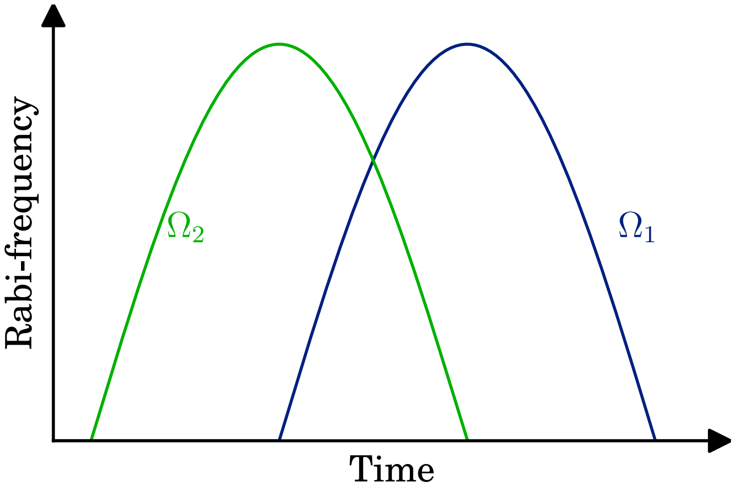

Figure 7.1: Typical STIRAP timing sequence. In a typical STIRAP sequence the Stokes laser first couples the states $|2\rangle$ and $|3\rangle$. As the Rabi frequency of the Stokes coupling is reduced, the power of the pump laser is increased and thereby the Rabi frequency on the pump transition. The mixing angle θ changes smoothly from 0 to $\pi/2$.

same eigenstate[1]

$$|a^0\rangle = \cos\theta|1\rangle - \sin\theta|3\rangle, \quad \tan\theta = \frac{\Omega_P(t)}{\Omega_S(t)} \tag{7.1}$$

and adiabatically follows the transition from $|1\rangle$ to $|3\rangle$.

As long as the pump laser is off ($\Omega_P = 0$) the eigenstate $|a^0\rangle$ is identical to $|1\rangle$. The procedure of setting up the Stokes coupling does not affect the system in this picture. The adiabatic passage from $|1\rangle$ to $|3\rangle$ only occurs when the ratio of Ω_P/Ω_S is changed smoothly, changing θ from 0 to $\pi/2$. The system adiabatically follows this change until it finally resides in state $|3\rangle$. Ideally 100% of the population in $|1\rangle$ can be transferred to $|3\rangle$.

The theoretical basis of STIRAP has been laid out by Vitanov *et al.* in a series of publications. On resonance and for large intermediate level detunings Δ the three-level system can be reduced to an effective two level problem [Vit97a] and various properties can be deduced analytically. Vitanov has further shown [Vit97c] that for fixed pulse areas the transfer efficiency is adversely affected by the intermediate level detuning Δ as it deteriorates the adiabaticity of the process. Therefore, we carry out STIRAP on resonance. The effect of irreversible dissipation from a decaying intermediate state is analyzed in [Vit97b].

Situations where multiple intermediate states are involved are treated in [Sho91, Vit98b, Vit98a, Sol03, Sho95, Kar03, Mar95, Vit99]. If the intermediate state consists of multiple levels that are coupled simultaneously to the states $|1\rangle$ and $|3\rangle$ a dark state does not necessarily exist, but rather depends on the details of the various couplings involved. In Cs_2 the excited state hyperfine structure is small and not resolved [Bai11]. The high efficiencies observed [Dan08b] are a clear proof that situations that fulfill the requirements for STIRAP given in Ref. [Vit99] can exist. However, there is no evidence that this is always the case for hyperfine structure - especially in heteronuclear molecules, which are less symmetric. The two-photon line shape and its dependency on the detuning

---

[1] see equations (6.16,6.18)

from resonance and the intermediate level decay rate is analyzed in [Rom97]. A Gaussian line shape is found for decay rates γ that are large compared to the inverse transfer time $\gamma \gg 1/\tau$. A nonzero intermediate level detuning Δ can further narrow the two-photon linewidth.

7.2 Transfer efficiency in the presence of noise

In real experimental systems there are always (small) fluctuations of the laser frequencies and two-photon coherence is not perfect. It turns out that STIRAP can be very sensitive to fluctuations in the laser frequencies and two-photon detuning. Therefore the effect of laser line width on STIRAP efficiency has been a key issue since the first molecular beam experiments [Kuh92]. Analysis of coupled multilevel systems in the presence of laser noise date back to the 70's [Ebe76, Aga78, Dix80, Has88]. The effect of detunings and decoherence on STIRAP has been discussed in depth in [Yat02] where an analytic solution is derived based on a stochastic model of the laser noise. The outcomes will be summarized here followed by a discussion of the consequences for the experimental application.

7.2.1 Modelling noise

Phase noise of the light field can be modelled by describing the fluctuating part of the derivative of the laser phase[2] as a stochastic variable $\xi(t)$ [Yat02]. For practical purposes a constant detuning is treated separately from the stochastic process, which therefore is assumed to have a zero mean value $\langle \xi(t) \rangle = 0$, where $\langle . \rangle$ denotes the statistical average over the ensemble.

Frequently for the stochastic distribution a Wiener-Levy process is assumed, which represents δ-function correlated white noise. The stochastic variables are defined by

$$\langle \xi_j(t) \rangle = 0, \quad \langle \xi_j(t) \xi_k(t') \rangle = 2D_{\mathrm{jk}} \delta(t - t'), \tag{7.2}$$

where the indices $j, k \in \{P, S\}$ denote the laser, D_{jj} is the bandwidth of the laser j and D_{PS} is the cross correlation of the two lasers. This model characterizes the noise by a single parameter, the laser bandwidth. Due to its simplicity it is frequently used.

Many experimental sources of noise especially in the acoustic range create fluctuations in the laser field that have a correlation time that is large compared to the timescales set by the STIRAP and therefore cannot simply be modelled by a Wiener-Levy process. Therefore the experimental situation is more accurately described by an Ornstein-Uhlenbeck (OU) process [Uhl30], which takes a finite correlation time into account.

In the OU model assuming null cross correlation the two stochastic variables are defined by

$$\langle \xi_j(t) \rangle = 0, \quad \langle \xi_j(t) \xi_k(t') \rangle = \begin{cases} D_j G_j exp(-G_j |t - t'|), & j = k \\ 0, & j \neq k. \end{cases} \tag{7.3}$$

---

[2] This corresponds to an instantaneous frequency offset.

In Ref. [Yat02] it is assumed that the two lasers follow the same statistics ($G_P = G_S = G$, $D_P = D_S = D$) but may be offset by a time T. Specifically it is assumed that

$$\xi_S(t) = \xi_P(t + T). \tag{7.4}$$

For $T = 0$ the lasers are perfectly correlated, while for $T \to \infty$ the fluctuations become independent. The latter assumption is applicable in the case of our experiment as the light of the to beams comes from two completely independent setups. For our setup it is safe to assume zero cross correlation as the two light beams come from two lasers locked two to separate cavities. Even for two lasers locked to the same cavity zero cross correlation can be assumed if the major source of noise is electronic noise and shot noise. Referencing two lasers to the same cavity only leads to strongly correlated fluctuations if fluctuations of the cavity are the dominating effect. Be cause of the relation (7.4) the problem is reduced from to stochastic variables to one that is defined by

$$\langle \xi(t) \rangle = 0, \quad \langle \xi(t)\xi(t') \rangle = DGe^{-G|t-t'|}. \tag{7.5}$$

To get a more intuitive understanding of the parameters G, D it is helpful to point out how they are related to what is commonly referred to as *linewidth*. In two limiting cases $G \to \infty$ and $G \to 0$ there is a direct relation.

For $G \to \infty$ the OU process turn into a Wiener-Levy process as the autocorrelation becomes

$$\langle \xi(t)\xi(t') \rangle = 2D\delta(t - t'). \tag{7.6}$$

In the case $G \gg D$ the spectrum of the intensity has a Lorentzian profile and D is the intensity half-width at half maximum (HWHM).

For $G \to 0$ the distribution is close to the extreme case of an ensemble of fields with constant frequencies that obey Gaussian statistics. If $G \ll D$ the product DG is the variance σ_{G}^2 of a Gaussian distribution and the HWHM is $\sqrt{2\ln 2}\sqrt{DG}$.

7.2.2 STIRAP in the presence of noise

The fluctuations in the laser frequency add to the detunings of the coupling lasers. The Hamiltonian of the system than reads as [Yat02]

$$H(t) = \frac{\hbar}{2} \begin{bmatrix} -\delta + 2\xi_P & \Omega_P(t) & 0 \\ \Omega_P(t) & -2\Delta - i\gamma & \Omega_S(t) \\ 0 & \Omega_S(t) & +\delta + 2\xi_S \end{bmatrix}. \tag{7.7}$$

For this Hamiltonian in the case of zero one-photon detuning the efficiency of the STIRAP process $P = P^{(0)} \times P^{(\xi)}$ can be expressed in an analytical form, where $P^{(0)}$ represent the noise-free contribution and is given by[3] [Yat02]

$$\begin{aligned} P^{(0)} \quad & = exp\Big[- \textstyle\int_{\infty}^{+\infty} \Big(4\gamma \frac{\dot{\theta}^2}{\Omega_{\mathrm{rms}}^2} + \gamma\delta^2 \frac{1-\cos(4\theta)}{2\Omega_{\mathrm{rms}}^2} \\ & +\delta^2 \dot{\Omega}_{\mathrm{rms}} \frac{1-\cos 4\theta}{\Omega_{\mathrm{rms}}^5}(2\gamma^2 - \Omega_{\mathrm{rms}}^2) + 2\delta^2\dot{\theta}\frac{sin 4\theta}{\Omega_{\mathrm{rms}}^4}(-\gamma^2 + \Omega_{\mathrm{rms}}^2)\Big)\, dt\Big]. \end{aligned} \tag{7.8}$$

---

[3] For better readability the time dependencies of θ and Ω_{rms} are not written out explicitly.

The contribution from the noise of two uncorrelated laser fields is expressible as

$$P^{(\xi)} = \exp\left(-DG(2G+\gamma)\int_{\infty}^{+\infty} \frac{1+\cos 4\theta}{\Omega_{\mathrm{rms}}^2 + 4G^2 + 2\gamma G} dt\right). \tag{7.9}$$

The above equations are valid for any kind of pulse shapes. The pulse shapes are expressed by the time dependent mixing angle θ and the mean Rabi frequency $\Omega_{\mathrm{rms}} = \sqrt{\Omega_P^2 + \Omega_S^2}$. As can be seen from the above equations, no losses occur as long as $\theta = 0$ or $\theta = \pi/2$. Therefore the integrals can be restricted to the time interval where both lasers are involved. The two equations above allow to model any pulse shape and are used for modelling our data.

7.2.3 Cosine shaped pulses

If pulses are used that result in a cosine shaped time dependency of the Rabi frequencies equations (7.8) and (7.9) can be simplified. In this case the Rabi frequencies are given by

$$\Omega_S(t) = \Omega_0 f(t), \Omega_P = \Omega_0 f(t - t_d), \tag{7.10}$$

where Ω_0 is the maximum Rabi frequency and t_d is a shift between the two pulses. The pulse shape function $f(t)$ is given by

$$f(t) = \begin{cases} \cos\left[\frac{\pi}{2}\frac{t}{\tau}\right], & -\tau < t < \tau, \\ 0 & \text{otherwise.} \end{cases} \tag{7.11}$$

For $t_d = \tau$ the Rabi frequency $\Omega_{\mathrm{rms}} = \Omega_0$ and $\dot{\theta} = \frac{\pi}{2\tau}$ remain constant throughout the transfer. The integrals in equations (7.8,7.9) can be solved and the resulting loss contributions are expressible as [Yat02]

$$P^{(0)} = \exp\left(-\frac{\gamma\pi^2}{\Omega_0^2\tau} - \frac{\delta^2\gamma\tau}{2\Omega_0^2}\right). \tag{7.12}$$

The first term in the exponent describes losses due to inadiabaticity. For high efficient STIRAP ($P^0 \ll 1$) the first term leads to an adiabaticity criterion

$$\Omega^2\tau \gg \gamma\pi^2. \tag{7.13}$$

Another adiabaticity criterion is mentioned in Ref. [Kuh92] and reads

$$\Omega_0\tau \gg 2\sqrt{1+\tau\Delta}. \tag{7.14}$$

This criterion mainly takes into account that a system of states coupled by radiation can follow a change in the radiation intensity by a timescale that is set by the Rabi frequency. Both adiabaticity criteria have to be fulfilled.

The second term of Eq. (7.12) describes the detuning. The transfer efficiency with respect to the detuning δ has a Gaussian shape and a $1/e$ two-photon linewidth of [Yat02]

$$\Delta\omega = \sqrt{2}\Omega_0/\sqrt{\gamma\tau}. \tag{7.15}$$

The parameter describing the noise reads for cosine shaped pulses

$$P^{(\xi)} = \exp\left(-\frac{DG\tau(2G+\gamma)}{4G^2 + 2G\gamma + \Omega_0^2}\right). \tag{7.16}$$

This parameter can be simplified for two limits, fast noise and slow noise.

7.2.4 Slow and fast noise

From (7.16) a clear difference between slow frequency fluctuations and white noise can be evaluated. In the case of the white noise limit when $G \to \infty$ the equation reads

$$P^{(\xi)} = \exp\left(-\frac{1}{2}D\tau\right) \quad (G \to \infty). \tag{7.17}$$

As mentioned before D is the HWHM of the frequency distribution of the laser, which is also called bandwidth. In the opposite case of slow fluctuations (7.16) becomes

$$P^{(\xi)} = \exp\left(-\frac{DG\gamma\tau}{\Omega_0^2}\right) \quad (G \to 0). \tag{7.18}$$

To be more precise, the fast limit is valid for $G \gg \Omega_0, \gamma$, and the slow limit is valid for $G \ll \Omega_0, \gamma$. It has been noted in Ref. [Yat02] that the last expression can also be obtained if Eq. (7.12) is averaged over a statistical distribution of different two-photon detunings taking into account $\langle \delta^2 \rangle = 2N\sigma_{\mathrm{G}}^2$. The factor 2 results from the assumption of two uncorrelated sources of noise. An averaging over different constant detunings occurs not only within a single transfer but also, when the detuning varies from measurement to measurement. Hence the statistical averaging has to be carried out over the whole time in which experimental data is acquired. This is typically several hours. Therefore also very slow fluctuations contribute to the slow noise.

The effects of white noise and correlated noise on the transfer efficiency can be directly compared if the efficiency is expressed in terms of the full width at half maximum (FWHM) of the frequency power spectrum, which is also called laser *linewidth*. In terms of the *linewidth*, which is denoted as $2w$, $P^{(\xi)}$ can be written

$$P^{(\xi)} = \exp\left(-\frac{1}{2}w\tau\right) \quad (G \to \infty). \tag{7.19}$$

$$P^{(\xi)} = \exp\left(-\frac{w^2\gamma\tau}{2\ln 2 \cdot \Omega_0^2}\right) = \exp\left(-\frac{w\gamma}{\Omega_0^2 \ln 2}\frac{1}{2}w\tau\right) \quad (G \to 0). \tag{7.20}$$

As can be easily seen the effect of slow frequency fluctuations is reduced by a factor of $\frac{w\gamma}{\Omega_0^2 \ln 2}$ as compared to white noise. For our system the Rabi frequencies are on the same order of magnitude as the excited state decay rate. The linewidth of the noise w is typically much smaller. Therefore slow noise affects the transfer efficiency much less than fast noise. This severe difference in the influences of different kinds of frequency fluctuations necessitates a clear distinction of the sources generating the noise. As a consequence fluctuations of the laser frequency that stem from slow vibrations have much less consequences than the same linewidth generated by fast electronic noise in the locking circuit.

In a noisy system equations (7.12), (7.18) and (7.17) are useful for distinguishing between different the kinds of noise. Losses due to inadiabaticity and slow noise depend on $1/\Omega_0^2$ while fast noise is independent of Ω_0. A measurement of the transfer efficiency P for different values of the Rabi frequencies Ω_0 should result in a linear dependence of $\ln(P)$ on $1/\Omega_0^2$. An extrapolation for $1/\Omega_0^2 \to 0$ should give the fraction of fast noise. It is important to note that the theoretical framework is valid for small losses only. Therefore these measurements should not be carried out at too low efficiencies. However, due to fluctuations in the number of initial Feshbach molecules and low signal to noise ratios such measurements have not been carried out yet for RbCs. In a similar way a variation of τ allows to distinguish losses due to inadiabaticity from losses due to noise since for the former the exponent scales with $1/\tau$ while for the latter the exponent scales with τ.

7.2.5 Maximum allowed noise

A direct analytic connection between the linewidth and the maximum achievable transfer efficiency can be derived from the above equations. In the limits of white noise ($G \to \infty$) or very slow fluctuations ($G \to 0$) the optimum transfer time τ_{opt} and the resulting transfer efficiency can be evaluated by determination of the maximum of $P(\tau)$:

$$\tau_{\text{opt}} = \sqrt{\frac{2\gamma\pi^2}{\Omega_0^2 D}}, \quad P = \exp\left(-\sqrt{2\gamma D}\frac{\pi}{\Omega_0}\right), \quad (G \to \infty), \tag{7.21}$$

$$\tau_{\text{opt}} = \sqrt{2\ln 2}\frac{\pi}{w}, \quad P = \exp\left(-\sqrt{\frac{2}{\ln 2}\frac{w\gamma\pi}{\Omega_0^2}}\right), \quad (G \to 0). \tag{7.22}$$

This further allows the estimation of maximum allowed linewidths for a desired efficiency P_{min} in the two cases. For simplicity a loss term $\alpha = -\ln(P_{\text{min}}) \approx 1 - P_{\text{min}}$ can be introduced. The maximum linewidths allowed for a given desired maximal loss α are then given by

$$w = \alpha^2\Omega_0^2/(2\pi^2\gamma), \quad (G \to \infty) \tag{7.23}$$

$$w = \sqrt{\frac{\ln 2}{2}}\alpha\Omega_0^2/(\gamma\pi), \quad (G \to 0) \tag{7.24}$$

If the excited state decay rate γ and the Rabi-frequencies are known, the relations above allow for a priori estimation of the necessary linewidths.

7.2.6 Requirements for the linewidths in the RbCs experiment

In the RbCs experiment the excited state decay rate is $\gamma = 2\pi \times 130\,\text{kHz}$, and the maximum Rabi frequency[4] is $\Omega_0 = 2\pi \times 250\,\text{kHz}$. If a transfer efficiency of 90% is to be achieved for fast noise the linewidth should be below

$$2w = 2\alpha^2\Omega_0^2/2\pi^2\gamma = 2\pi \times 560\,\text{Hz}. \tag{7.25}$$

For slow noise the FWHM of the noise spectrum should be below

$$2w = 2\sqrt{\frac{\ln 2}{2}}\alpha\Omega_0^2/\gamma\pi = 2\pi \times 19\,\text{kHz}. \tag{7.26}$$

It is worth to note that these limits are for two independent sources of noise. If the noise stems predominantly from one source these limits have to be multiplied by $\sqrt{2}$. For one source of noise, the slow noise should be well below $2w = 27\,\text{kHz}$. For the fast noise, white noise with a Lorentzian distribution has to be assumed. If the distribution deviates from

---

[4] Typical value for every-day operation.

Lorentzian, it might be reasonable not to use the FWHM of the spectrum but to use the FWHM of the envelope Lorentzian.

The obtained values ask for a discussion of the influences of various sources of noise and their effects on the STIRAP transfer efficiency. The fast noise mainly stems from the lasers. As shown in section 4.2.3 the FWHM of the laser is 130 Hz. This is well below the 560 Hz required. Furthermore the noise is dominated by one laser. However the method used for characterisation only gives a very rough estimate on the noise since measuring a signal that is used in a servo loop is not an independent method.

The slow noise can add up from different sources. As already mentioned in the context of the two-photon spectroscopy one of the sources of slow noise stems from the fluctuations of the molecular states. These fluctuations are generated by fluctuations of the magnetic field, which shifts the energy difference of the levels due to a difference of the magnetic moments. Since for RbCs the magnetic moments of the initial and final states differ by $\Delta\mu = 1.6\mu_B$ the FWHM of 27 kHz correspond to magnetic field fluctuations with a FWHM of 11 mG or a standard deviation of $\sigma_B = 3\,\text{mG}$. In the experiment magnetic field fluctuations with a FWHM of 5.5 mG have been observed[5]. Since the experiment was not synchronized to the power line frequency for technical reasons, fluctuations in the background mangetic field lead to fluctuations in the two photon detnuning from shot to shot. Furthermore additional noise from the switching power supplies can result in fast fluctuating noise components. These fluctuations, which correspond to 12 kHz, are closer to the maximum allowed limit of 27 kHz than the noise from the laser system. Based on these fluctuations the transfer efficiency should be limited at 96%. However due to the lack of suitable sensors only contributions from the background are measured. The contributions that arise from the switching power supply are neglected. Hence it can be assumed that the effect of magnetic field fluctuations is larger at 181 G. The noise from the powersupplies can be avoided if batteries are used instead.

Further sources of slow frequency fluctuations are for example the noise generated by the fibers used to transferring the STIRAP light beams from the laser setup to the experiment. A FWHM of 800 Hz has been measured for a single fiber. As the two lasers are transferred through distinct fibers the resulting noise adds up to a FWHM of 1.1 kHz. Given the large fluctuations of 12 kHz originating from the magnetic field, the contribution fiber noise is less than 1% and hence can be neglected. Frequency fluctuations generated by vibrations of the resonators to which the lasers are referenced[6] typically are well below 100 Hz. Therefore these fluctuations can safely be neglected.

7.2.7 STIRAP for levitated molecules

To compensate the effect of gravity ultracold Feshbach molecules can be levitated by a magnetic field gradient as is described above. The magnetic field gradient generates an external potential compensating the potential energy in the field of gravity. Since the ground state has only a very small magnetic moment gravity is only compensated for the Feshbach molecules. While the Feshbach molecules are hindered from falling out of a

---

[5] Measurements of the background magnetic noise next to the cell. These measurement do not include noise and fluctuations by the coils when the experiment is running.

[6] In the experiment highly stable resonators are used which were developed for atomic clocks and allow for the construction of lasers with sub Hz linewidth.

weakly confining optical trap, levitation leads to a position dependent shift between the initial state and the final state. Thereby a position dependent two-photon detuning is created.

For heavy molecules with small Rabi frequencies this effect can be detrimental for STIRAP. The gravitational energy for RbCs expressed in units of the Planck constant is $E_{\mathrm{grav}} = 5.4\,\mathrm{kHz}/\mu\mathrm{m}$. A cloud size of $\sigma_{\mathrm{z}} = 4.2\,\mu\mathrm{m}$ leads to a two photon linewidth of $2w = 2\pi \times 53\,\mathrm{kHz}$. At best a maximum transfer efficiency of 75 % can be achieved for the parameters given in RbCs. This example however is idealized since the size of the two cloud in z-direction depends critically on the alignment of the trapping beams. A slight misalignment of the beams can lead to a larger cloud size of up to $6\,\mu\mathrm{m}$, which further decreases the efficiency to 65 %. Shifts of the cloud position due to vibrations and movements of the trapping beams or due to oscillations of the cloud can further deteriorate the efficiency. In fact our first attempts of STIRAP measurements were carried out with levitated molecules, but at best an efficiency of 50% has been achieved. Hence for RbCs it is essential to use non levitated Feshbach molecules for STIRAP. In order to prevent the Feshbach molecules from falling down they can either be kept in a strong dipole trap or be loaded into a lattice. Loading the molecules into a lattice has three benefits. Firstly, it can be turned on in 5 ms without exciting oscillation modes. Secondly, the lattice prevents collisions of the Feshbach molecules and leads to much longer lifetimes of the molecules. Thirdly, with our enhanced strategy to form Feshbach molecules in an optical lattice, the molecules will be created in the lattice.

For other molecular transfer experiments the effect of levitation might be less severe. Since the loss term decreases with $1/\Omega^2$ for STIRAP with larger Rabi frequencies for Refs. [Lan08, Ni08] this effect should be negligible.[7] The early experiments with Cs_2, which is the only other molecule experiment with comparably low Rabi frequencies, were carried out in free flight [Dan08b]. However even for Cs_2 the peak Rabi frequencies are a factor of ten higher and hence this effect should be suppressed by a factor of a hundred.

To conclude, the formalism reported in [Yat02] has been used to derive limits on the amount of noise allowed at short and long timescales. The requirements on the linewidth of the noise scale with Ω_0^2. For RbCs due to its low Rabi frequencies and a large magnetic moment of the Feshbach molecules not only the laser linewidth has to be narrow, but also magnetic field fluctuations have to be well controlled. The requirements on the stability of the magnetic fields and the linewidth of the lasers are much more stringent than for any other experiment that has reported the creation of ground-state molecules using STIRAP.

7.3 Experimental results

7.3.1 Ground-state transfer

Ground-state transfer measurements have been carried out on the $|0, 35, 1\rangle$ and the $|1, 29, 1\rangle$ levels. While for the latter an efficiency of 89% is achieved, for the former only efficiencies below 20% could be measured, resulting in a low round trip efficiency of 4%, which even after some statistics could not be distinguished from noise threshold by more than two standard deviations. The differences of the two excited state levels are

---

[7] It is not stated in the references whether the molecules were levitated.

manifold. Notably the requirements on the fluctuations resulting from (7.22) and (7.21) mainly depend on Ω_0^2/γ. For the $|1, 29, 1\rangle$ state the maximum Rabi frequency of the pump transition that limits Ω_0 is $\Omega_\mathrm{P} = 250\,\mathrm{kHz}$ for an intensity of $580\,\mathrm{W/cm^2}$ and the decay rate of the excited state is $\gamma = 2\pi \times 128(11)\,\mathrm{kHz}$. This leads to $\Omega_0^2/\gamma = 2\pi \times 490\,\mathrm{kHz}$. The coupling strength on the Stokes transition is higher than the coupling strength of the pump transition for both of the states and therefore does not limit STIRAP. For the $|0, 35, 1\rangle$ state the maximum Rabi frequency of the pump transition for the same laser intensity is $\Omega_\mathrm{P} = 380\,\mathrm{kHz}$ and the decay rate of the excited state is $\gamma = 2\pi \times 3.3(2)\,\mathrm{MHz}$. This leads to $\Omega_0^2/\gamma = 2\pi \times 44\,\mathrm{kHz}$. Since for a given level of noise the transfer efficiency for optimized transfer times depends on Ω_0^2/γ, for the $|1, 29, 1\rangle$ excited state a higher STIRAP efficiency should be expected. Hence this excited state is chosen for the STIRAP measurements.

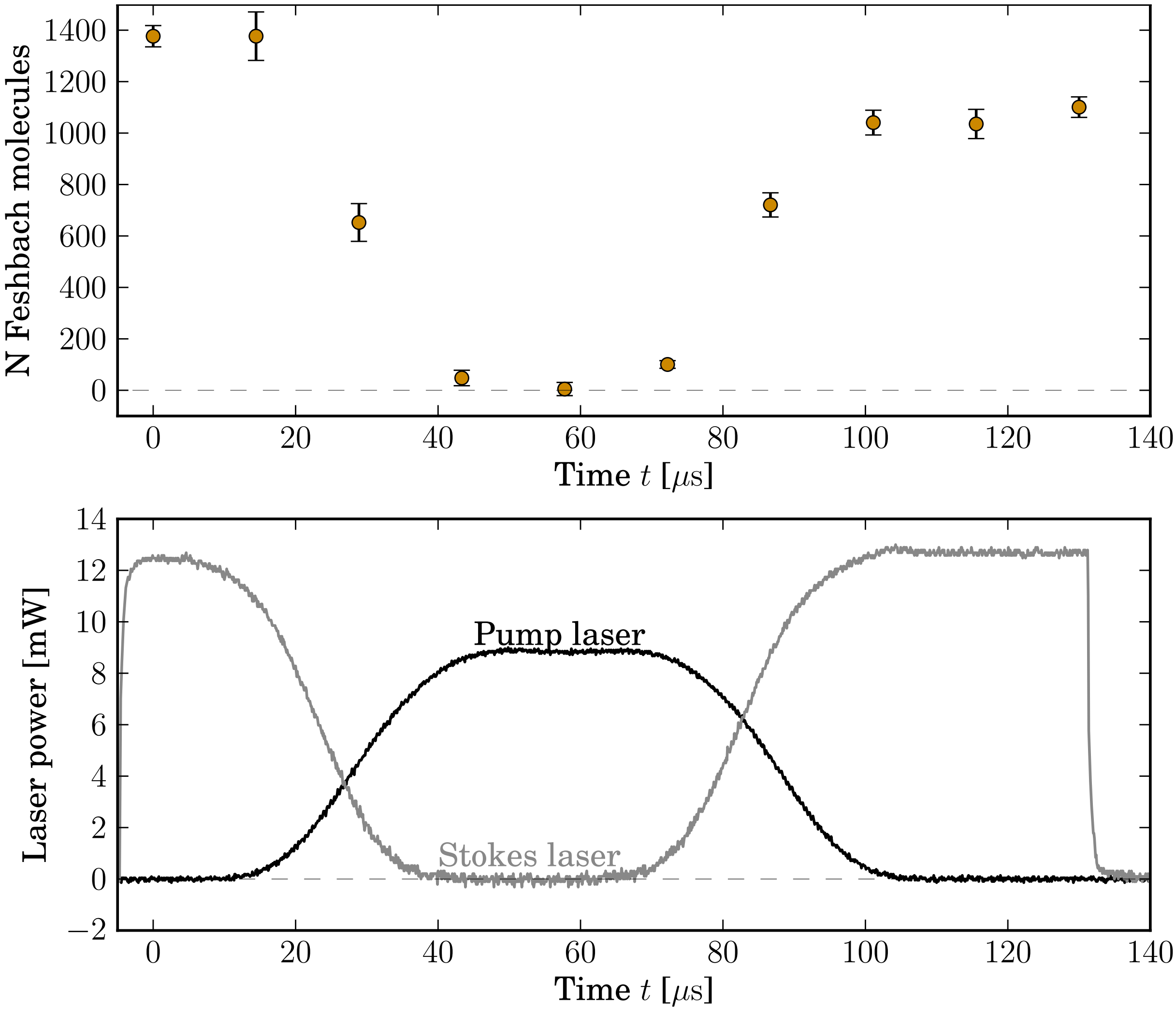

Figure 7.2: STIRAP ground-state transfer. The upper graph shows the number of Feshbach molecules. The error bars show statistical fluctuations. The lower graph shows the laser power. The noise in the curves is generated by the oscilloscope and the photodiode used to record the data.

A ground-state transfer with 89% efficiency is measured as shown in Fig. 7.2. The data points on the upper graph show the number of Feshbach molecules; the error bars represent statistical fluctuations. The round trip efficiency is 79%. This corresponds to a single pass efficiency of 89%. The lines on the lower graph show the intensities of the lasers and have been recorded with a digital oscilloscope. For the pulse shape a rather simple procedure is chosen using a linear voltage ramp on an RF-attenuator. The latter controls the AOM's that regulate the intensity of the light. The nonlinearities of the attenuator and the AOM lead to an initially quadratic increase in laser power, which eventually reaches saturation. This leads to the pulse shapes shown in the lower part of the figure. The curve of the pump laser is shifted with respect to the Stokes laser due to a delay created by the AOM.

In a further measurement we have corrected this delay and acquired some more data in the transition region. Furthermore the efficiency is determined by measuring the number

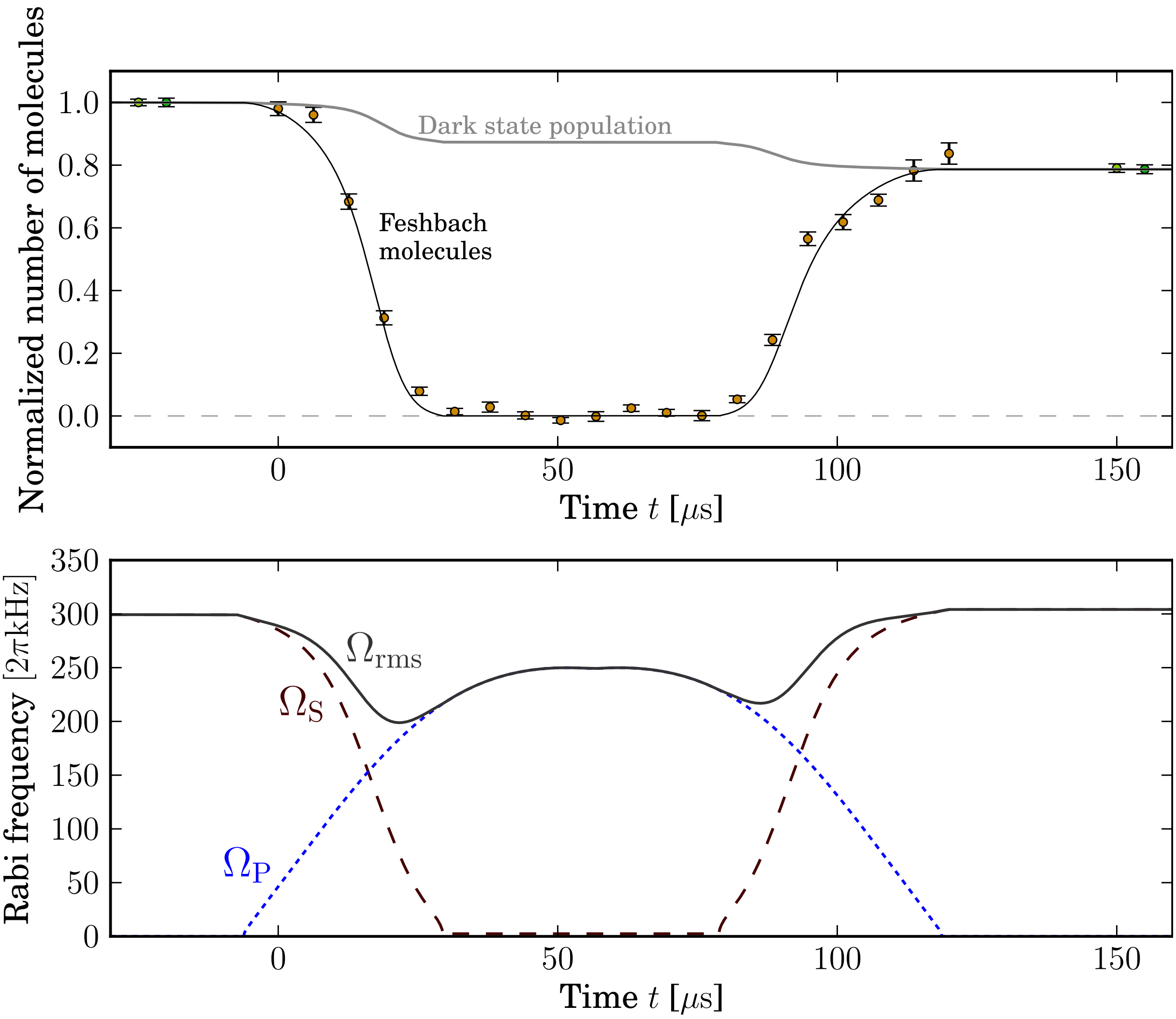

Figure 7.3: STIRAP ground-state transfer of RbCs molecules. RbCs Feshbach molecules are transferred to the ro-vibrational ground state during the first 50 μs. The ground-state molecules are transferred back to Feshbach molecules from $t = 70\,\mu$s onwards. The points with error bars show the number of Feshbach molecules measured, when the lasers are suddenly switched off at the time denoted. The lines show the number of Feshbach molecules and the number of molecules in the dark state based on Eqs. (7.8) and (7.9). The lower graph shows the Rabi frequencies Ω_{P}, Ω_{S} and Ω_{rms}, which are obtained from measured laser intensities and used for modelling the data. The measured laser intensities have been approximated by analytic functions.

of molecules before and after the STIRAP round trip with an increased amount of data points. These measurements are shown in Fig. 7.3. For the (orange) marker showing the transition region statistical averaging has been performed for 12 data points, while for the (green) markers before and after the STIRAP 45 data points were taken each. The different colors indicate that the data points have been taken on different experimental runs using the same settings. The lines in the lower part of the figure show the Rabi frequencies and are generated by measuring the laser intensity with an oscilloscope. The measured laser power is fitted using polynomials in order to get analytic functions. The Rabi frequencies have been calculated using the normalized Rabi frequencies, which are $\Omega_\mathrm{P} = 2\pi \times 0.33\,\mathrm{kHz}\sqrt{\mathrm{I(mW/cm^2)}}$ and $\Omega_\mathrm{P} = 2\pi \times 0.51\,\mathrm{kHz}\sqrt{\mathrm{I(mW/cm^2)}}$. Based on (7.8), (7.9) and the Rabi frequencies, the number of molecules in the dark state and in the Feshbach state is evaluated. Thereby it is assumed that the noise has a long correlation time and can be described by the slow noise limit ($G \to 0$). The width of the fluctuations is left as a free parameter and a FWHM of 11.8 kHz is obtained. For magnetic fluctuations this corresponds to 7.4 mG. However, the main part of the losses is due to inadiabaticity. For the given pulse shape completely noise-free model would lead only to a minor increase in the transfer efficiency. Taking into account the 20% error in the determination of the transition strength it is not possible to draw any conclusion on the amount of noise present in the system.

Our transfer efficiency is comparable to or higher than the transfer efficiencies reported for similar molecular experiments [Ni08, Lan08, Dan08b]. Over time the transfer efficiencies of these experiments have improved. Improvements of the transfer efficiencies are also possible for RbCs and several aspects could be further analyzed.

Firstly, the shape of the pulses can be improved. The analysis above was carried out on the pulses actually used and a deviation from perfect cosine shaped pulses with the optimum transfer time leads to a somewhat lower efficiency. In the optimized case, as described in the theory above, a transfer efficiency of 91% could be expected for the same amount of noise.

Secondly, the fluctuations of the magnetic field can be analyzed in detail. The obtained fluctuations coincide with the magnetic field noise measured at the cell of 5.5 mG. These values do not include noise generated by the (switching) power supplies. The noise generated from the power supplies can be omitted if batteries are used instead. Furthermore the fluctuations of the magnetic field from data point to data point can be reduced if the transfer is synchronized with the power line frequency. An easy and reliable way to investigate magnetic field noise are coherent transitions that are not driven by laser light but by microwave frequencies. Magnetic field noise has been investigated on a similar setup in a neighbouring laboratory and it was found that the coherence of microwave transitions increases if batteries are used and the system is synchronized with the mains frequency (Manfred Mark, priv comm.). Hence batteries and synchronization, both of which are currently installed, should increase the transfer efficiency.

Thirdly, the laser system can be improved. Currently the most noisy laser has been replaced by a new home built version[8] that features much less technical noise and a high optical power of 60 mW. Two identical lasers are currently being set up in order to be able to carry out a detailed characterization.

The improvements in the magnetic field, the pulse shapes, and the laser system cer-

---

[8] The setup and characterization of two new lasers is the topic of the Master thesis of Verena Pramhaas.

tainly should lead to an increased efficiency for STIRAP. However, STIRAP efficiency is currently not limiting the phase-space density of our sample. Major improvements in the phase-space density can mainly be expected from an advanced strategy to create a high PSD sample of Feshbach molecules.

7.3.2 Identification of the hyperfine state

In order to identify the hyperfine level of the ground state that is reached by the STIRAP transfer, the Stokes laser is scanned while the Pump laser is kept on resonance. As shown in Fig. 7.4, two ground-state hyperfine levels can be detected. While the polarization of the first laser is parallel to the magnetic field $k_\mathrm{P} = \pi$, the polarization of the second laser is orthogonal $k_\mathrm{S} = 1/\sqrt{2}(\sigma^+ + \sigma^-)$. Starting from $M_F = 4$ ground-state levels with $M_F = 3, 5$ can be reached. The data points show the normalized number of Feshbach molecules after a STIRAP round trip. This corresponds to the STIRAP round-trip efficiency.

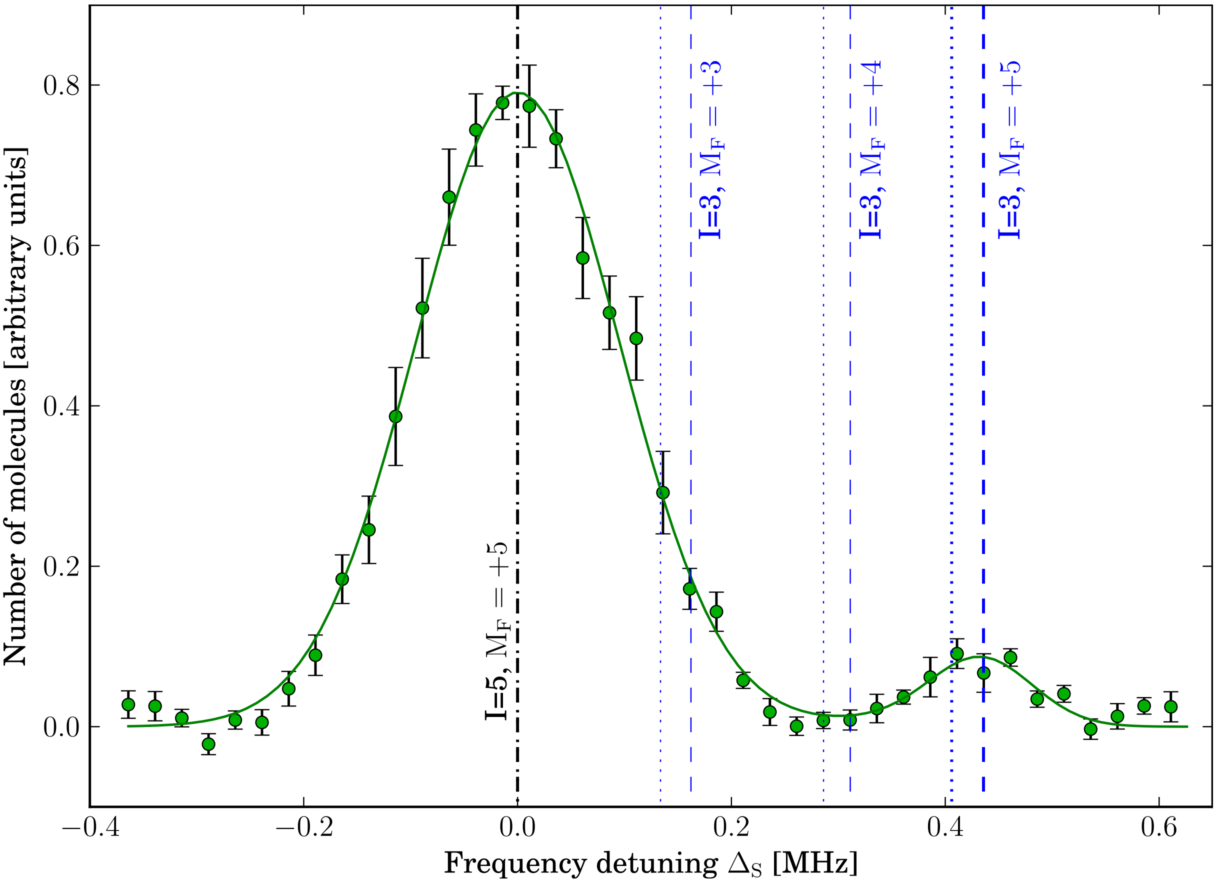

Figure 7.4: Round-trip STIRAP efficiency plotted against frequency detuning of the Stokes laser. The solid line is a fit of two Gaussian functions with the second peak shifted by 430 kHz. The dotted lines show the position of the hyperfine states as expected from the calculations of Aldegunde *et al.* [Ald08]. The dashed lines show the states when the value of c_4 is fitted to the data. From the fits a value of $c_4 = 12(2)$ kHz is obtained.

From Eq. (7.8) follows a Gaussian shape of the two-photon line independent of the shape of the STIRAP pulses. Since the two states are well separated it is safe to neglect the coupling to neighbouring hyperfine levels to first order. The obtained splitting between the two observed levels of 430 kHz is compared to theoretical calculations of the hyperfine structure. The large splitting leaves the interpretation of the lower peak belonging to the $M_F = 5$ state and the higher one belonging to the uppermost $M_F = 3$ state as the only possibility. Hence the ground-state hyperfine level that can be reached with a high efficiency is the lowest hyperfine level. Further the fact that the two-photon linewidth is much narrower than the splitting between the levels allows for the conclusion that the Feshbach molecules are almost entirely transferred to a single hyperfine ground-state level.

Compared to the STIRAP transfer measurements, for the scan the laser powers have been increased. The Rabi frequency Ω_P is increased by 20% while Ω_S is increased by a factor of 2.2. In contrast to the STIRAP measurement where a balanced situation is desired, for the scan measurements an increased Stokes laser power is desirable in order to reach sufficient coupling to ground-state hyperfine levels that have a weaker transition strength.

A two-photon linewidth of 135 kHz and 77 kHz for a STIRAP round trip can be deduced from the fits. This linewidth is somewhat larger than expected for cosine shaped pulses of equal size. In the measurement however the maximum Rabi frequencies are not balanced as $\Omega_{\mathrm{S,max}} \gg \Omega_{\mathrm{P,max}}$ for the first peak while $\Omega_{\mathrm{S,max}} \ll \Omega_{\mathrm{P,max}}$ for the second. In this imbalanced situation a large fraction of the transfer is achieved in a fraction of the total time, reducing the effective transfer time. This leads to an effective broadening of the two-photon linewidth.

Similar to the measurement presented in Fig. 6.12 the value of the c_4 constant can be determined by fitting the hyperfine splitting to the data. For the measurement presented above a value of $c_4 = 12(2)$ kHz is obtained. This value is larger than the value obtained in the spectroscopy measurement of $c_4 = 7(3)$ kHz obtained from the spectroscopy measurements. However both values are smaller than the theoretical value of $c_4 = 17$ kHz.

Certainly for a precise determination of the c_4 constant the systematic errors would have to be thoroughly investigated and more date would have to be acquired to rule out possible errors. Drifts of the magnetic field on the mG level, which can be induced by drifts of the coil position or the current, can have a serious influence since the data is just taken from one scan. However the precise determination of c_4 was not the aim of this measurement.

To conclude, the measurements show that RbCs Feshbach molecules can be transferred to the lowest hyperfine state of the ro-vibrational ground state with an efficiency close to 90%. This transfer efficiency is comparable to the transfer efficiencies in Refs. [Ni08, Dan08b, Dan10]. Further improvements on the pulse shape and the magnetic field noise as well as increased laser power will lead to a transfer efficiency above 90 %. For RbCs it is possible to directly reach the lowest hyperfine level of the ro-vibrational ground state. This is important since only in the lowest hyperfine state inelastic collisions are prevented.

Chapter 8

Outlook

The findings in this thesis clearly show the successful creation of ultracold RbCs ground-state molecules using highly efficient coherent transfer schemes. This opens the path to experimental exploration of a variety of novel phenomena in the regime of strongly interacting dipolar quantum gases. With the identification of suitable states and the demonstration of efficient STIRAP ground-state transfer it is clearly demonstrated that the efficient creation of molecules that are chemically stable is possible and that the creation of a chemically stable dipolar quantum gas is in reach. These achievements provide support for theoretical investigations on stable strongly interacting dipolar quantum gases.

The binding energy of the lowest rovibrational level $|V''=0, J''=0\rangle$ of the $X^1\Sigma^+$ ground state is determined to be $D_0^X = 3811.5755(16)\,\mathrm{cm}^{-1}$, which is a 300-fold improvement in accuracy with respect to previous data. In combination which the Feshbach spectroscopy and the determination of the d-wave character of two Feshbach states by single photon spectroscopy, these measurements lead to a profound understanding of the RbCs ground-state potential. The observation of hyperfine structure experimentally confirms earlier theoretical calculations and proves that selective population of a single hyperfine ground-state level is possible. The selective population of the lowest hyperfine level prevents exothermic reactions and should lead to a stable gas of ultracold RbCs molecules.

Up to now RbCs still suffers from the high three-body losses, which prevent the achievement of high phase-space densities necessary for a more efficient creation of Feshbach molecules. The challenge of a more efficient creation of Feshbach molecules will be faced with the strategy described in section 3.3.4. When Cs is frozen out in a Mott-insulator state the magnetic field can freely be tuned to a RbCs Feshbach resonance and the three-body losses should be strongly suppressed. The simultaneous creation of Mott insulator states of two clouds close to each other is a first step for highly efficient merging of two strongly interacting quantum gases.

STIRAP in RbCs can further be improved by a control of the magnetic field fluctuations and a reduction of the laser noise. In contrast to Cs_2 molecular experiments [Dan08b, Mar07], the magnetic moment of the Feshbach state is much higher. Hence magnetic field fluctuations have a larger impact on the two photon detuning and thereby can reduce the STIRAP efficiency. The low transition strength of $\Omega_\mathrm{P} = 0.33\,\mathrm{kHz}\sqrt{\mathrm{I}/(\mathrm{mW/cm}^2)}$ makes ground state transfer a much more challenging endeavour than in KRb [Ni08]. The high transfer efficiencies of 89 % show that even for low Rabi frequencies the transfer can be well controlled.

The scattering properties of stable ultracold molecules remain widely unexplored. For KRb chemical reactions have been observed [Ni10] and means to control these interactions have been developed [Mic10a, Osp10b]. Also for chemically stable molecules non-trivial scattering namely the existence of metastable dimer-dimer complexes has been predicted [May13]. Compared to purely atomic collisions, ultracold collisions involving molecules have the potential to support a much larger numbers of Fano-Feshbach resonances due to the huge amount of ro-vibrational state available [May13]. The density of Fano-Feshbach resonance can be too high to resolve individual resonances and can lead to a scattering behaviour differing from atomic scattering [May12]. Furthermore stable molecules can temporarily transform into meta-stable four-body complexes with lifetimes that can exceed typical experimental timescales [May13]. Chemically stable ground-state molecules are an ideal system to explore this effect. Ongoing experiments on Cs_2 are currently measuring two-body rates of atom-dimer collisions.

The significance of the creation of dipolar ground state molecules can mainly be understood in the context of the wide variety of phenomena predicted for ultracold quantum gases [Bar12, Mic06, Büc07a, Bre07, Pup08, Pup09, CS10]. Due to the forward-looking orientation of the experiment the amount of predicted phenomena exceeds the amount of observed effects. Novel quantum effects like super-solid phases [Bat00, Sen05, Pol10, Bar12], dipolar crystalline phases [Pup08, Rab07, Mic07] or a Luttinger liquid behaviour in one-dimensional dipolar quantum gases [Cit07] remain yet to be explored. Also the super-Tonks-Girardeau regime for dipolar gases [Ast08a] and supersolid phases in 1D [Bur09] are further interesting perspectives for experiments with strongly interacting dipolar quantum gases. The possibility to tailor three-body interactions for dipoles in an optical lattice [Büc07b] allows for the realization of model systems with more complex Hamiltonians that lead to novel exotic quantum phases such as a resonating valence bond phase [Moe01]. Self assembled crystalline phases due to Wigner localization [Cre10] are not only interesting as such but also allow for the construction of a quantum simulator [Pup08].

Appendix A

Publications

The work presented in this thesis led to following publications.

Production of a dual-species Bose-Einstein condensate of Rb and Cs atoms

Lercher, A.; Takekoshi, T.; Debatin, M.; Schuster, B.; Rameshan, R.; Ferlaino, F.; Grimm, R. & Nägerl, H.-C.
The European Physical Journal D, Springer-Verlag, **65**, 3-9, (2011)

Molecular spectroscopy for ground-state transfer of ultracold RbCs molecules

Debatin, M.; Takekoshi, T.; Rameshan, R.; ReichsÃűllner, L.; Ferlaino, F.; Grimm, R.; Vexiau, R.; Bouloufa, N.; Dulieu, O. & Nägerl, H.-C.
Phys. Chem. Chem. Phys., **13**, 18926, (2011)

Towards the production of ultracold ground-state RbCs molecules: Feshbach resonances, weakly bound states, and the coupled-channel model

Takekoshi, T.; Debatin, M.; Rameshan, R.; Ferlaino, F.; Grimm, R. & Nagerl, H.-C. Phys. Rev. A, **85**, 032506, (2012)

Appendix B

References

Bibliography

[Abr95] E. Abraham, W. McAlexander, C. Sackett, and R. Hulet, *Spectroscopic Determination Of the S-Wave Scattering Length Of Lithium*, Physical Review Letters **74**, 1315 (1995).

[Aga78] G. S. Agarwal, *Quantum statistical theory of optical-resonance phenomena in fluctuating laser fields*, Phys. Rev. A **18**, 1490 (1978).

[Aik10] K. Aikawa, D. Akamatsu, M. Hayashi, K. Oasa, J. Kobayashi, P. Naidon, T. Kishimoto, M. Ueda, and S. Inouye, *Coherent Transfer of Photoassociated Molecules into the Rovibrational Ground State*, Phys. Rev. Lett. **105**, 203001 (2010).

[Aik12] K. Aikawa, A. Frisch, M. Mark, S. Baier, A. Rietzler, R. Grimm, and F. Ferlaino, *Bose-Einstein Condensation of Erbium*, Phys. Rev. Lett. **108**, 210401 (2012).

[Ald08] J. Aldegunde, B. A. Rivington, P. S. Żuchowski, and J. M. Hutson, *Hyperfine energy levels of alkali-metal dimers: Ground-state polar molecules in electric and magnetic fields*, Phys. Rev. A **78**, 033434 (2008).

[Ald09] J. Aldegunde, H. Ran, and J. M. Hutson, *Manipulating ultracold polar molecules with microwave radiation: The influence of hyperfine structure*, Phys. Rev. A **80**, 043410 (2009).

[Aln08a] J. Alnis, A. Matveev, N. Kolachevsky, T. Udem, and T. W. Hänsch, *Subhertz linewidth diode lasers by stabilization to vibrationally and thermally compensated ultralow-expansion glass Fabry-Pérot cavities*, Phys. Rev. A **77**, 053809 (2008).

[Aln08b] J. Alnis, A. Matveev, N. Kolachevsky, T. Wilken, R. Holzwarth, and T. W. Haensch, *Stable diode lasers for hydrogen precision spectroscopy*, European Physical Journal-Special Topics **163**, 89 (2008).

[And81] S. V. Andreev, V. I. Balykin, V. S. Letokhov, and V. G. Minogin, *Radiative slowing and reduction of the energy spread of a beam of sodium atoms to 1.5K in an oppositely directed laser beam*, Pis'ma Zh. Eksp. Teor. Fiz. **34**, 463 (1981).

[And95] M. H. Anderson, J. R. Ensher, M. R. Matthews, C. E. Wieman, and E. A. Cornell, *Observation of Bose-Einstein condensation in dilute atomic vapor*, Science **269**, 198 (1995).

[And05] M. Anderlini, E. Courtade, M. Cristiani, D. Cossart, D. Ciampini, C. Sias, O. Morsch, and E. Arimondo, *Sympathetic cooling and collisional properties of a Rb- Cs mixture*, Phys. Rev. A **71**, 061401 (2005).

[And06] A. André, D. DeMille, J. M. Doyle, M. D. Lukin, S. E. Maxwell, P. Rabl, R. J. Schoelkopf, and P. Zoller, *A coherent all-electrical interface between polar molecules and mesoscopic superconducting resonators*, Nature Phys. **2**, 636 (2006).

[Ast08a] G. E. Astrakharchik and Y. E. Lozovik, *Super-Tonks-Girardeau regime in trapped one-dimensional dipolar gases*, Phys. Rev. A **77**, 013404 (2008).

[Ast08b] G. E. Astrakharchik, G. Morigi, G. De Chiara, and J. Boronat, *Ground state of low-dimensional dipolar gases: Linear and zigzag chains*, Phys. Rev. A **78**, 063622 (2008).

[Aub06] S. Aubin, S. Myrskog, M. H. T. Extavour, L. J. Leblanc, D. Mckay, A. Stummer, and J. H. Thywissen, *Rapid sympathetic cooling to Fermi degeneracy on a chip*, Nature Phys. **2**, 384 (2006).

[Aut55] S. Autler and C. Townes, *Stark Effect In Rapidly Varying Fields*, Physical Review **100**, 703 (1955).

[Aym05] M. Aymar and O. Dulieu, *Calculation of accurate permanent dipole moments of the lowest (1,3)Sigma(+) states of heteronuclear alkali dimers using extended basis sets*, Journal Of Chemical Physics **122** (2005).

[Bah96] J. T. Bahns, W. C. Stwalley, and P. L. Gould, *Laser cooling of molecules: A sequential scheme for rotation, translation, and vibration*, J. Chem. Phys. **104**, 9689 (1996).

[Bah00] J. Bahns, P. Gould, and W. Stwalley, *Formation of Cold ($T < 1$ K) Molecules*, Adv. At. Mol. Opt. Phys. **42**, 171 (2000).

[Bai11] J. Bai, E. H. Ahmed, B. Beser, Y. Guan, S. Kotochigova, A. M. Lyyra, S. Ashman, C. M. Wolfe, J. Huennekens, F. Xie, D. Li, L. Li, M. Tamanis, R. Ferber, A. Drozdova, E. Pazyuk, A. V. Stolyarov, J. G. Danzl, H.-C. Naegerl, N. Bouloufa, O. Dulieu, C. Amiot, H. Salami, and T. Bergeman, *Global analysis of data on the spin-orbit-coupled A (1)Sigma(+)(u) and b (3)Pi(u) states of Cs-2*, Physical Review A **83** (2011).

[Bak09] W. S. Bakr, J. I. Gillen, A. Peng, S. Fölling, and M. Greiner, *A quantum gas microscope for detecting single atoms in a Hubbard-regime optical lattice*, Nature **462**, 74 (2009).

[Bak10] W. S. Bakr, A. Peng, M. E. Tai, R. Ma, J. Simon, J. I. Gillen, S. Folling, L. Pollet, and M. Greiner, *Probing the Superfluid-to-Mott Insulator Transition at the Single-Atom Level*, Science **329**, 547 (2010).

[Bar02] M. Baranov, L. Dobrek, K. Góral, L. Santos, and M. Lewenstein, *Ultracold Dipolar Gases - a Challenge for Experiments and Theory*, Physica Scripta **T102**, 74 (2002).

[Bar05] M. Bartenstein, A. Altmeyer, S. Riedl, R. Geursen, S. Jochim, C. Chin, J. Hecker Denschlag, R. Grimm, A. Simoni, E. Tiesinga, C. J. Williams, and P. S. Julienne, *Precise determination of ^{6}Li cold collision parameters by radio-frequency spectroscopy on weakly bound molecules*, Phys. Rev. Lett. **94**, 103201 (2005).

[Bar06] R. Barnett, D. Petrov, M. Lukin, and E. Demler, *Quantum magnetism with multicomponent dipolar molecules in an optical lattice*, Phys. Rev. Lett. **96**, 190401 (2006).

[Bar08] M. A. Baranov, *Theoretical progress in many-body physics with ultracold dipolar gases*, Physics Reports **464**, 71 (2008).

[Bar12] M. Baranov, M. Dalmonte, G. Pupillo, and P. Zoller, *Condensed Matter Theory of Dipolar Quantum Gases*, Chem. Rev. **112**, 5012 (2012).

[Bat95] G. G. Batrouni, R. T. Scalettar, G. T. Zimanyi, and A. P. Kampf, *Supersolids in the Bose-Hubbard Hamiltonian*, Phys. Rev. Lett. **74**, 2527 (1995).

[Bat00] G. G. Batrouni and R. T. Scalettar, *Phase Separation in Supersolids*, Phys. Rev. Lett. **84**, 1599 (2000).

[Bea10] Q. Beaufils, A. Crubellier, T. Zanon, B. Laburthe-Tolra, E. Marèchal, L. Vernac, and O. Gorceix, *Radio-frequency association of molecules: an assisted Feshbach resonance*, Eur. Phys. J. D **56**, 99 (2010).

[Ber98] K. Bergmann, H. Theuer, and B. W. Shore, *Coherent population transfer among quantum states of atoms and molecules*, Rev. Mod. Phys. **70**, 1003 (1998).

[Bet99] H. L. Bethlem, G. Berden, and G. Meijer, *Decelerating neutral dipolar molecules*, Phys. Rev. Lett. **83**, 1558 (1999).

[Bet00] H. L. Bethlem, G. Berden, F. M. H. Crompvoets, R. T. Jongma, A. J. A. van Roij, and G. Meijer, *Electrostatic trapping of ammonia molecules*, Nature **406**, 491 (2000).

[Bla01] E. D. Black, *An introduction to Pound-Drever-Hall laser frequency stabilization*, Am. J. Phys. **69**, 79 (2001).

[Blo29] F. Bloch, *Über die Quantenmechanik der Elektronen in Kristallgittern*, Zeitschrift für Physik **52**, 555 (1929).

[Blo08] I. Bloch, J. Dalibard, and W. Zwerger, *Many-body physics with ultracold gases*, Rev. Mod. Phys. **80**, 885 (2008).

[Boh09] J. L. Bohn, M. Cavagnero, and C. Ticknor, *Quasi-universal dipolar scattering in cold and ultracold gases*, New J. Phys. **11**, 055039 (2009).

[Bra95] C. C. Bradley, C. A. Sackett, J. J. Tollett, and R. G. Hulet, *Evidence of Bose-Einstein condensation in an atomic gas with attractive interactions*, Phys. Rev. Lett. **75**, 1687 (1995).

[Bra03] E. Braaten and H.-W. Hammer, *Efimov States in a Bose-Einstein Condensate near a Feshbach Resonance*, Phys. Rev. Lett. **90**, 170402 (2003).

[Bra06] E. Braaten and H.-W. Hammer, *Universality in few-body systems with large scattering length*, Phys. Rep. **428**, 259 (2006).

[Bra07] E. Braaten and H. Hammer, *Efimov physics in cold atoms*, Annals of Physics **322**, 120 (2007).

[Bre07] G. K. Brennen, A. Micheli, and P. Zoller, *Designing spin-1 lattice models using polar molecules*, New J. Phys. **9**, 138 (2007).

[Bru93] C. Bruder, R. Fazio, and G. Schön, *Superconductor-Mott-insulator transition in Bose systems with finite-range interactions*, Phys. Rev. B **47**, 342 (1993).

[Bru12] D. A. Brue and J. M. Hutson, *Magnetically Tunable Feshbach Resonances in Ultracold Li-Yb Mixtures*, Physical Review Letters **108**, 043201 (2012).

[Büc07a] H. P. Büchler, E. Demler, M. Lukin, A. Micheli, N. Prokof'ev, G. Pupillo, and P. Zoller, *Strongly correlated 2D quantum phases with cold polar molecules: controlling the shape of the interaction potential*, Phys. Rev. Lett. **98**, 060404 (2007).

[Büc07b] H. P. Büchler, A. Micheli, and P. Zoller, *Three-body interactions with cold polar molecules*, Nature Phys. **3**, 726 (2007).

[Bur09] F. J. Burnell, M. M. Parish, N. R. Cooper, and S. L. Sondhi, *Devil's staircases and supersolids in a one-dimensional dipolar Bose gas*, Physical Review B **80** (2009).

[Cam85] J. C. Camparo, *The diode laser in atomic physics*, Contemp. Phys. **26**, 443 (1985).

[Car09] L. D. Carr, D. DeMille, R. V. Krems, and J. Ye, *Cold and ultracold molecules: Science, technology and applications*, New J. Phys. **11**, 055049 (2009).

[Che07] T. Cheng, H. Darmawan, and A. Brown, *Stimulated Raman adiabatic passage in molecules: The effects of background states*, Physical Review A **75** (2007).

[Chi04] C. Chin and R. Grimm, *Thermal equilibrium and efficient evaporation of an ultracold atom-molecule mixture*, Phys. Rev. A **69** (2004).

[Chi05] C. Chin and P. S. Julienne, *Radio-frequency transitions on weakly bound ultracold molecules*, Phys. Rev. A **71** (2005).

[Chi09] C. Chin, V. V. Flambaum, and M. G. Kozlov, *Ultracold molecules: new probes on the variation of fundamental constants*, New J. Phys. **11**, 055048 (2009).

[Chi10] C. Chin, R. Grimm, P. S. Julienne, and E. Tiesinga, *Feshbach resonances in ultracold gases*, Rev. Mod. Phys. **82**, 1225 (2010).

[Cit07] R. Citro, E. Orignac, S. De Palo, and M. L. Chiofalo, *Evidence of Luttinger-liquid behavior in one-dimensional dipolar quantum gases*, Physical Review A **75** (2007).

[Cor00] S. L. Cornish, N. R. Claussen, J. L. Roberts, E. A. Cornell, and C. E. Wieman, *Stable* ^{85}Rb *Bose-Einstein Condensates with Widely Tunable Interactions*, Phys. Rev. Lett. **85**, 1795 (2000).

[Cou92] G. W. Coulston and K. Bergmann, *Population transfer by stimulated Raman scattering with delayed pulses: Analytical results for multilevel systems*, J. chem. Phys. **96**, 3467 (1992).

[Cou98] P. Courteille, R. S. Freeland, D. J. Heinzen, F. A. van Abeelen, and B. J. Verhaar, *Observation of a Feshbach Resonance in Cold Atom Scattering*, Phys. Rev. Lett. **81**, 69 (1998).

[COX65] A. COX, G. Flynn, and E. Wilson, *Microwave Double-Resonance Experiments*, Journal Of Chemical Physics **42**, 3094 (1965).

[Cre10] J. C. Cremon, G. M. Bruun, and S. M. Reimann, *Tunable Wigner States with Dipolar Atoms and Molecules*, Phys. Rev. Lett. **105**, 255301 (2010).

[CS07] B. Capogrosso-Sansone, N. V. Prokof'ev, and B. V. Svistunov, *Phase diagram and thermodynamics of the three-dimensional Bose-Hubbard model*, Physical Review B **75** (2007).

[CS10] B. Capogrosso-Sansone, C. Trefzger, M. Lewenstein, P. Zoller, and G. Pupillo, *Quantum phases of cold polar molecules in 2D optical lattices*, Phys. Rev. Lett. **104**, 125301 (2010).

[Dam03] B. Damski, L. Santos, E. Tiemann, M. Lewenstein, S. Kotochigova, P. Julienne, and P. Zoller, *Creation of a Dipolar Superfluid in Optical Lattices*, Phys. Rev. Lett. **90**, 110401 (2003).

[Dan08a] L. Dang, M. Boninsegni, and L. Pollet, *Vacancy supersolid of hard-core bosons on the square lattice*, Physical Review B **78** (2008).

[Dan08b] J. G. Danzl, E. Haller, M. Gustavsson, M. J. Mark, R. Hart, N. Bouloufa, O. Dulieu, H. Ritsch, and H.-C. Nägerl, *Quantum Gas of Deeply Bound Ground State Molecules*, Science **321**, 1062 (2008).

[Dan09a] I. Danshita and C. A. R. S. de Melo, *Stability of Superfluid and Supersolid Phases of Dipolar Bosons in Optical Lattices*, Physical Review Letters **103** (2009).

[Dan09b] J. G. Danzl, M. J. Mark, E. Haller, M. Gustavsson, R. Hart, A. Liem, H. Zellmer, and H.-C. Nägerl, *Deeply bound ultracold molecules in an optical lattice*, New J. Phys. **11**, 055036 (2009).

[Dan09c] J. G. Danzl, M. J. Mark, E. Haller, M. Gustavsson, R. Hart, and H.-C. Nägerl, *Production of a quantum gas of rovibronic ground-state molecules in an optical lattice*, Icols Proceedings (2009).

[Dan10] J. G. Danzl, M. J. Mark, E. Haller, M. Gustavsson, R. Hart, J. Aldegunde, J. M. Hutson, and H.-C. Nägerl, *An ultracold high-density sample of rovibronic ground-state molecules in an optical lattice*, Nature Phys. **6**, 265 (2010).

[Dav95] K. B. Davis, M. O. Mewes, M. R. Andrews, N. J. van Druten, D. S. Durfee, D. M. Kurn, and W. Ketterle, *Bose-Einstein condensation in a gas of sodium atoms*, Phys. Rev. Lett. **75**, 3969 (1995).

[Deb11] M. Debatin, T. Takekoshi, R. Rameshan, L. Reichsöllner, F. Ferlaino, R. Grimm, R. Vexiau, N. Bouloufa, O. Dulieu, and H.-C. Nägerl, *Molecular spectroscopy for ground-state transfer of ultracold RbCs molecules*, Phys. Chem. Chem. Phys. **13**, 18926 (2011).

[deC99] R. deCarvalho, J. M. Doyle, B. Friedrich, T. Guillet, J. Kim, D. Patterson, and J. D. Weinstein, *Buffer-gas loaded magnetic traps for atoms and molecules: A primer*, Eur. Phys. J. D **7**, 289 (1999).

[Deh08] B. Deh, C. Marzok, C. Zimmermann, and P. W. Courteille, *Feshbach resonances in mixtures of ultracold (6)Li and (87)Rb gases*, Physical Review A **77** (2008).

[Dei08a] J. Deiglmayr, M. Aymar, R. Wester, M. Weidemüller, and O. Dulieu, *Calculations of static dipole polarizabilities of alkali dimers: Prospects for alignment of ultracold molecules*, J. Chem. Phys. **129**, 064309 (2008).

[Dei08b] J. Deiglmayr, A. Grochola, M. Repp, K. Mörtlbauer, C. Glück, J. Lange, O. Dulieu, R. Wester, and M. Weidemüller, *Formation of Ultracold Polar Molecules in the Rovibrational Ground State*, Physical Review Letters **101**, 133004 (2008).

[Dei10] J. Deiglmayr, A. Grochola, M. Repp, O. Dulieu, R. Wester, and M. Weidemüller, *Permanent dipole moment of LiCs in the ground state*, Phys. Rev. A **82**, 032503 (2010).

[DeM02] D. DeMille, *Quantum Computation with Trapped Polar Molecules*, Phys. Rev. Lett. **88**, 067901 (2002).

[DeM08] D. DeMille, S. Sainis, J. Sage, T. Bergeman, S. Kotochigova, and E. Tiesinga, *Enhanced sensitivity to variation of m_e/m_p in molecular spectra*, Phys. Rev. Lett. **100**, 043202 (2008).

[Der01] A. Derevianko, J. F. Babb, and A. Dalgarno, *High-precision calculations of van der Waals coefficients for heteronuclear alkali-metal dimers*, Phys. Rev. A **63**, 052704 (2001).

[Di 04] M. Di Rosa, *Laser-cooling molecules*, Eur. Phys. J. D **31**, 395 (2004).

[Dix80] S. N. Dixit, P. Zoller, and P. Lambropulous, *Non-Lorentzian laser line shapes and the reversed peak asymmetry in double optical resonances*, Phys. Rev. A **21**, 1289 (1980).

[Doc10] O. Docenko, M. Tamanis, R. Ferber, T. Bergeman, S. Kotochigova, A. V. Stolyarov, A. de Faria Nogueira, and C. E. Fellows, *Spectroscopic data, spin-orbit functions, and revised analysis of strong perturbative interactions for the* $A^1\Sigma^+$ *and* $b^3\Pi$ *states of RbCs*, Phys. Rev. A **81**, 042511 (2010).

[Don02] E. A. Donley, N. R. Clausen, S. T. Thompson, and C. E. Wieman, *Atom-molecule coherence in a Bose-Einstein condensate*, Nature **417**, 529 (2002).

[Doy04] J. Doyle, B. Friedrich, R. Krems, and F. Masnou-Seeuws, *Editorial: Quo vadis, cold molecules?*, Eur. Phys. J. D **31**, 149 (2004).

[Dre83] R. W. P. Drever, J. L. Hall, F. V. Kowalski, J. Hough, G. M. Ford, A. J. Munley, and H. Ward, *Laser phase and frequency stabilization using an optical resonator*, Appl. Phys. B **31**, 97 (1983).

[Dui04] R. Duine and H. Stoof, *Atom-molecule coherence in Bose gases*, Physics Reports-Review Section Of Physics Letters **396**, 115 (2004).

[Dul06] O. Dulieu, M. Raoult, and E. Tiemann, *Cold molecules: a chemistry kitchen for physicists?*, J. Phys. B **39** (2006).

[Dul09] O. Dulieu and C. Gabbanini, *The formation and interactions of cold and ultracold molecules: new challenges for interdisciplinary physics*, Rep. Prog. Phys. **72**, 086401 (2009).

[Dür04] S. Dürr, T. Volz, A. Marte, and G. Rempe, *Observation of Molecules Produced from a Bose-Einstein Condensate*, Phys. Rev. Lett. **92**, 020406 (2004).

[Ebe76] J. H. Eberly, *Atomic Relaxation in the Presence of Intense Partially Coherent Radiation Fields*, Phys. Rev. Lett. **37**, 1387 (1976).

[Efi79] V. Efimov, *Low-energy properties of three resonantly interacting particles*, Sov. J. Nuc. Phys. **29**, 546 (1979).

[Eli03] M. S. Elioff, J. J. Valentini, and D. W. Chandler, *Subkelvin Cooling NO Molecules via "Billiard-like" Collisions with Argon*, Science **302**, 1940 (2003).

[Fan35] U. Fano, *Sullo spettro di assorbimento dei gas nobili presso il limite dello spettro d'arco*, Nuovo Cimento **12**, 154 (1935).

[Fan61] U. Fano, *Effects of configuration interaction on intensities and phase shifts*, Phys. Rev. **124**, 1866 (1961).

[Fed96] P. O. Fedichev, Y. Kagan, G. V. Shlyapnikov, and J. T. M. Walraven, *Influence of nearly resonant light on the scattering length in low-temperature atomic gases*, Phys. Rev. Lett. **77**, 2913 (1996).

[Fel99] C. E. Fellows, R. F. Gutterres, A. P. C. Campos, J. Vergès, and C. Amiot, *The RbCs $X^1\Sigma^+$ ground electronic state: new spectroscopic study*, J. Mol. Spect. **197**, 19 (1999).

[Fer06] G. Ferrari, R. E. Drullinger, N. Poli, F. Sorrentino, and G. M. Tino, *Cooling of Sr to high phase-space density by laser and sympathetic cooling in isotopic mixtures*, Phys. Rev. A **73**, 023408 (2006).

[Fer08] F. Ferlaino, S. Knoop, and R. Grimm, *Ultracold Feshbach molecules*, in: R. V. Krems, B. Friedrich, and W. C. Stwalley (Eds.), *Cold Molecules: Theory, Experiment, Applications*, arXiv:0809.3920, 2008.

[Fer09] F. Ferlaino, S. Knoop, and R. Grimm, *Cold Molecules: Theory, Experiment, Applications*, chap. Ultracold Feshbach molecules, Taylor & Francis, 2009.

[Fes58] H. Feshbach, *Unified theory of nuclear reactions*, Annals of Physics **5**, 357 (1958).

[Fes62] H. Feshbach, *A Unified Theory of Nuclear Reactions.*, Annals of Physics **19**, 287 (1962).

[Fio98] A. Fioretti, D. Comparat, A. Crubellier, O. Dulieu, F. Masnou-Seeuws, and P. Pillet, *Formation of cold Cs_2 molecules through photoassociation*, Phys. Rev. Lett. **80**, 4402 (1998).

[Fis89] M. P. A. Fisher, P. B. Weichman, G. Grinstein, and D. S. Fisher, *Boson localization and the superfluid-insulator transition*, Phys. Rev. B **40**, 546 (1989).

[Fle81] M. Fleming and A. Mooradian, *Spectral Characteristics Of External-Cavity Controlled Semiconductor-Lasers*, IEEE Journal Of Quantum Electronics **17**, 44 (1981).

[Fle05] M. Fleischhauer, A. Imamoglu, and J. P. Marangos, *Electromagnetically induced transparency: Optics in coherent media*, Rev. Mod. Phys. **77**, 633 (2005).

[Fre10] J. K. Freericks, M. M. Maśka, A. Hu, T. M. Hanna, C. J. Williams, P. S. Julienne, and R. Lemański, *Improving the efficiency of ultracold dipolar molecule formation by first loading onto an optical lattice*, Phys. Rev. A **81**, 011605 (2010).

[Fri09] B. Friedrich and J. M. Doyle, *Why are cold molecules so hot?*, ChemPhysChem **10**, 604 (2009).

[Fri12] A. Frisch, K. Aikawa, M. Mark, A. Rietzler, J. Schindler, E. Zupanic, R. Grimm, and F. Ferlaino, *Narrow-line magneto-optical trap for erbium: Simple approach for a complex atom*, arXiv:1203.1460 (2012).

[Gau88] U. Gaubatz, P. Rudecki, M. Becker, S. Schiemann, M. Külz, and K. Bergmann, *Population switching between vibrational levels in molecular beams*, Chem. Phys. Lett. **149**, 463 (1988).

[Gau90] U. Gaubatz, P. Rudecki, S. Schiemann, and K. Bergmann, *Population transfer between molecular vibrational levels by stimulated Raman scattering with partially overlapping laser fields. A new concept and experimental results*, J. Chem. Phys. **92**, 5363 (1990).

[Geh03] M. E. Gehm, *Properties of* ^{6}Li (2003), 2003.

[Gla63] R. Glauber, *Coherent and Incoherent States Of Radiation Field*, Physical Review **131**, 2766 (1963).

[Gre02] M. Greiner, O. Mandel, T. Esslinger, T. W. Hänsch, and I. Bloch, *Quantum phase transition from a superfluid to a Mott insulator in a gas of ultracold atoms*, Nature **415**, 39 (2002).

[Gre03] M. Greiner, C. A. Regal, and D. S. Jin, *Emergence of a Molecular Bose-Einstein Condensate from a Fermi Gas*, Nature **426**, 537 (2003).

[Gri00] R. Grimm, M. Weidemüller, and Y. B. Ovchinnikov, *Optical dipole traps for neutral atoms*, Adv. At. Mol. Opt. Phys. **42**, 95 (2000).

[Gri05] A. Griesmaier, J. Werner, S. Hensler, J. Stuhler, and T. Pfau, *Bose-Einstein condensation of chromium*, Phys. Rev. Lett. **94**, 160401 (2005).

[Gro61] E. Gross, *Structure of a quantized vortex in boson systems*, Il Nuovo Cimento Series 10 **20**, 454 (1961).

[Gro09] A. Grochola, A. Pashov, J. Deiglmayr, M. Repp, E. Tiemann, R. Wester, and M. Weidemüller, *Photoassociation spectroscopy of the* $B^1\Pi$ *state of LiCs*, J. Chem. Phys. **131**, 054304 (2009).

[Gut99] G. L. Gutsev, P. Jena, and R. J. Bartlett, *Structure and stability of the AlX and* AlX$^-$ *species*, J. chem. Phys. **110**, 2928 (1999).

[Had02] Z. Hadzibabic, C. Stan, K. Dieckmann, S. Gupta, M. Zwierlein, A. Gorlitz, and W. Ketterle, *Two-species mixture of quantum degenerate Bose and Fermi gases*, Physical Review Letters **88** (2002).

[Had06] Z. Hadzibabic, P. Krÿger, M. Cheneau, B. Battelier, and J. Dalibard, *Berezinskii-Kosterlitz-Thouless crossover in a trapped atomic gas*, Nature **441**, 1118 (2006).

[Hai04] C. Haimberger, J. Kleinert, M. Bhattacharya, and N. P. Bigelow, *Formation and detection of ultracold ground-state polar molecules*, Phys. Rev. A **70**, 021402(R) (2004).

[Hai09] C. Haimberger, J. Kleinert, P. Zabawa, A. Wakim, and N. P. Bigelow, *Formation of ultracold, highly polar* $X^1\Sigma^+$ *NaCs molecules*, New J. Phys. **11**, 055042 (2009).

[Hal09] E. Haller, M. Gustavsson, M. J. Mark, J. G. Danzl, R. Hart, G. Pupillo, and H. C. Nägerl, *Realization of an excited, strongly correlated quantum gas phase*, Science **325**, 1224 (2009).

[Hal10] E. Haller, R. Hart, M. J. Mark, J. G. Danzl, L. Reichsöllner, M. Gustavsson, M. Dalmonte, G. Pupillo, and H.-C. Nägerl, *Pinning quantum phase transition for a Luttinger liquid of strongly interacting bosons*, Nature **466**, 597 (2010).

[Ham03] M. Hammes, D. Rychtarik, B. Engeser, H.-C. Nägerl, and R. Grimm, *Evanescent-Wave Trapping and Evaporative Cooling of an Atomic Gas at the Crossover to Two Dimensions*, Phys. Rev. Lett. **90**, 173001 (2003).

[Han07] T. M. Hanna, T. Köhler, and K. Burnett, *Association of molecules using a resonantly modulated magnetic field*, Phys. Rev. A **75**, 013606 (2007).

[Han10] T. M. Hanna, E. Tiesinga, and P. S. Julienne, *Creation and manipulation of Feshbach resonances with radiofrequency radiation*, New J. Phys. **12**, 083031 (2010).

[Han11] A. H. Hansen, A. Khramov, W. H. Dowd, A. O. Jamison, V. V. Ivanov, and S. Gupta, *Quantum degenerate mixture of ytterbium and lithium atoms*, Physical Review A **84** (2011).

[Har90] S. E. Harris, J. E. Field, and Imamoglu, *Nonlinear Optical Processes Using Electromagnetically Induced Transparency*, Phys. Rev. Lett. **64**, 1107 (1990).

[Har08] M. L. Harris, P. Tierney, and S. L. Cornish, *Magnetic trapping of a cold Rb-Cs atomic mixture*, Journal of Physics B: Atomic, Molecular and Optical Physics **41**, 035303 (2008).

[Has88] T. Haslwanter, H. Ritsch, J. Cooper, and P. Zoller, *Laser-Noise-Induced Population Fluctuations In 2-Level And 3-Level Systems*, Physical Review A **38**, 5652 (1988).

[Héb01] F. Hébert, G. G. Batrouni, R. T. Scalettar, G. Schmid, M. Troyer, and A. Dornreich, *Quantum phase transitions in the two-dimensional hardcore boson model*, Phys. Rev. B **65**, 014513 (2001).

[Hen82] C. Henry, *Theory Of the Linewidth Of Semiconductor-Lasers*, IEEE Journal Of Quantum Electronics **18**, 259 (1982).

[Heo12] M.-S. Heo, T. T. Wang, C. A. Christensen, T. M. Rvachov, D. A. Cotta, J.-H. Choi, Y. S. Lee, and W. Ketterle, *Formation of ultracold fermionic NaLi Feshbach molecules*, Phys. Rev. A **86**, 021602(R) (2012).

[Her50] G. Herzberg, *Molecular Spectra and molecular structure - Vol I*, D. Van Nostrand, Princeton, 1950.

[Her03] J. Herbig, T. Kraemer, M. Mark, T. Weber, C. Chin, H.-C. Nägerl, and R. Grimm, *Preparation of a pure molecular quantum gas*, Science **301**, 1510 (2003).

[Hes87] H. Hess, G. Kochanski, J. Doyle, N. Masuhara, D. Kleppner, and T. Greytak, *Magnetic Trapping Of Spin-Polarized Atomic-Hydrogen*, Physical Review Letters **59**, 672 (1987).

[Hod05] E. Hodby, S. T. Thompson, C. A. Regal, M. Greiner, A. C. Wilson, D. S. Jin, E. A. Cornell, and C. E. Wieman, *Production efficiency of ultracold Feshbach molecules in bosonic and fermionic systems*, Phys. Rev. Lett. **94**, 120402 (2005).

[Hog11] S. D. Hogan, M. Motsch, and F. Merkt, *Deceleration of supersonic beams using inhomogeneous electric and magnetic fields*, Phys. Chem. Chem. Phys. **13**, 18705 (2011).

[Hub63] J. Hubbard, *Electron Correlations In Narrow Energy Bands*, Proceedings Of The Royal Society Of London Series A-Mathematical And Physical Sciences **276**, 238+ (1963).

[Hum13] M. T. Hummon, M. Yeo, B. K. Stuhl, A. L. Collopy, Y. Xia, and J. Ye, *2D Magneto-Optical Trapping of Diatomic Molecules*, Phys. Rev. Lett. **110**, 143001 (2013).

[Hun12] L. R. Hunter, S. K. Peck, A. S. Greenspon, S. S. Alam, and D. DeMille, *Prospects for laser cooling TlF*, Phys. Rev. A **85**, 012522 (2012).

[Hut06] J. Hutson and P. Soldán, *Molecule formation in ultracold atomic gases*, International Reviews in Physical Chemistry **25**, 497 (2006).

[Hut12] N. R. Hutzler, H.-I. Lu, and J. Doyle, *The Buffer Gas Beam: An Intense, Cold, and Slow Source for Atoms and Molecules*, Chem. Rev. **112**, 4803 (2012).

[IM86] G. Igel-Mann, U. Wedig, P. Fuentealba, and H. Stoll, *Ground-state properties of alkali dimers XY (X, Y=Li to Cs)*, J. Chem. Phys. **84**, 5007 (1986).

[Ino98] S. Inouye, M. R. Andrews, J. Stenger, H.-J. Miesner, D. M. Stamper-Kurn, and W. Ketterle, *Observation of Feshbach resonances in a Bose-Einstein condensate*, Nature **392**, 151 (1998).

[Jak02] D. Jaksch, V. Venturi, J. I. Cirac, C. J. Williams, and P. Zoller, *Creation of a Molecular Condensate by Dynamically Melting a Mott Insulator*, Phys. Rev. Lett. **89**, 040402 (2002).

[Jak05] D. Jaksch and P. Zoller, *The cold atom Hubbard toolbox*, Annals of Physics **315**, 52 (2005), ¡ce:title¿Special Issue¡/ce:title¿.

[Jan11] L. M. C. Janssen, P. S. Zuchowski, A. van der Avoird, G. C. Groenenboom, and J. M. Hutson, *Cold and ultracold NH-NH collisions in magnetic fields*, Phys. Rev. A **83**, 022713 (2011).

[Jin12] D. S. Jin and J. Ye, *Introduction to Ultracold Molecules: New Frontiers in Quantum and Chemical Physics*, Chem. Rev. **112**, 4801 (2012).

[Joc02] S. Jochim, M. Bartenstein, G. Hendl, J. Hecker Denschlag, R. Grimm, A. Mosk, and W. Weidemüller, *Magnetic Field Control of Elastic Scattering in a Cold Gas of Fermionic Lithium Atoms*, Phys. Rev. Lett **89**, 273202 (2002).

[Joc03a] S. Jochim, M. Bartenstein, A. Altmeyer, G. Hendl, S. Riedl, C. Chin, J. Hecker Denschlag, and R. Grimm, *Bose-Einstein Condensation of Molecules*, Science **302**, 2101 (2003).

[Joc03b] S. Jochim, M. Bartenstein, A. Altmeyer, G. Hendl, C. Chin, J. Hecker Denschlag, and R. Grimm, *Pure Gas of Optically Trapped Molecules Created from Fermionic Atoms*, Phys. Rev. Lett **91**, 240402 (2003).

[Jon06] K. M. Jones, E. Tiesinga, P. D. Lett, and P. S. Julienne, *Ultracold photoassociation spectroscopy: Long-range molecules and atomic scattering*, Rev. Mod. Phys. **78**, 483 (2006).

[Jör08] R. Jördens, N. Strohmaier, K. Günter, H. Moritz, and T. Esslinger, *A Mott insulator of fermionic atoms in an optical lattice*, Nature **455**, 204 (2008).

[Jun04a] T. Junglen, T. Rieger, S. Rangwala, P. Pinkse, and G. Rempe, *Slow ammonia molecules in an electrostatic quadrupole guide*, Eur. Phys. J. D **31**, 365 (2004).

[Jun04b] T. Junglen, T. Rieger, S. A. Rangwala, P. W. H. Pinkse, and G. Rempe, *Two-dimensional trapping of dipolar molecules in time-varying electric fields*, Phys. Rev. Lett. **92**, 223001 (2004).

[Jun08] M. Junker, D. Dries, C. Welford, J. Hitchcock, Y. P. Chen, and R. G. Hulet, *Photoassociation of a Bose-Einstein condensate near a Feshbach resonance*, Phys. Rev. Lett. **101**, 060406 (2008).

[Kar03] A. Karpati and Z. Kis, *Adiabatic creation of coherent superposition states via multiple intermediate states*, J. Phys. B **36**, 905 (2003).

[Kau09] A. M. Kaufman, R. P. Anderson, T. M. H., E. Tiesinga, P. S. Julienne, and H. D. S., *Radio-frequency dressing of multiple Feshbach resonances*, Phys. Rev. A **80**, 050701 (2009).

[Ker00] A. J. Kerman, V. Vuletić, C. Chin, and S. Chu, *Beyond Optical Molasses: 3D Raman Sideband Cooling of Atomic Cesium to High Phase-Space Density*, Phys. Rev. Lett. **84**, 439 (2000).

[Ket99] W. Ketterle, W. Durfee, and D. M. Stamper-Kurn, *Making, probing and understanding Bose-Einstein condensates*, in: M. Inguscio, S. Stringari, and C. E. Wieman (Eds.), *Bose-Einstein Condensation In Atomic Gases*, vol. 140 of *PROCEEDINGS OF THE INTERNATIONAL SCHOOL OF PHYSICS ENRICO FERMI*, 67, I O S PRESS, NIEUWE HEMWEG 6B, 1013 BG AMSTERDAM, NETHERLANDS, 1. MIT, Dept Phys, Cambridge, MA 02139 USA, 1999.

[Ket08] W. Ketterle and M. W. Zwierlein, *Making, probing and understanding ultracold Fermi gases*, Rivista del Nuovo Cimento **31**, 247 (2008).

[Kim04] E. Kim and M. H. W. Chan, *Probable observation of a supersolid helium phase*, Nature **427**, 225 (2004).

[Kin04] T. Kinoshita, T. Wenger, and D. S. Weiss, *Observation of a One-Dimensional Tonks-Girardeau Gas*, Science **305**, 1125 (2004).

[Koc12] C. P. Koch and M. Shapiro, *Coherent Control of Ultracold Photoassociation*, Chem. Rev. **112**, 4928 (2012).

[Köh06] T. Köhler, K. Góral, and P. S. Julienne, *Production of cold molecules via magnetically tunable Feshbach resonances*, Rev. Mod. Phys. **78**, 1311 (2006).

[Kot05] S. Kotochigova and E. Tiesinga, *Ab initio relativistic calculation of the RbCs molecule*, J. Chem. Phys. **123**, 174304 (2005).

[Kot10] S. Kotochigova, *Dispersion interactions and reactive collisions of ultracold polar molecules*, New J. Phys. **12**, 073041 (2010).

[Kra04] T. Kraemer, J. Herbig, M. Mark, T. Weber, C. Chin, H.-C. Nägerl, and R. Grimm, *Optimized production of a cesium Bose-Einstein condensate*, Appl. Phys. B **79**, 1013 (2004).

[Kra06a] T. Kraemer, *Few-body interactions in an ultracold gas of cesium atoms*, Ph.D. thesis, University of Innsbruck (2006).

[Kra06b] T. Kraemer, M. Mark, P. Waldburger, J. G. Danzl, C. Chin, B. Engeser, A. D. Lange, K. Pilch, A. Jaakkola, H.-C. Nägerl, and R. Grimm, *Evidence for Efimov quantum states in an ultracold gas of caesium atoms*, Nature **440**, 315 (2006).

[Kra06c] S. D. Kraft, P. Staanum, L. Lange, J. andVogel, R. Wester, and M. Weidemüller, *Formation of ultracold LiCs molecules*, J. Phys. B. **39**, 993 (2006).

[Kuh92] A. Kuhn, G. W. Coulston, S. S., K. Bergmann, and W. S. Warren, *Population transfer by stimulated Raman scattering with delayed pulses using spectrally broad light*, J. Chem. Phys. **96**, 4215 (1992).

[Lah07] T. Lahaye, T. Koch, B. Fröhlich, M. Fattori, J. Metz, A. Griesmaier, S. Giovanazzi, and T. Pfau, *Strong dipolar effects in a quantum ferrofluid*, Nature **448**, 672 (2007).

[Lah08] T. Lahaye, J. Metz, B. Fröhlich, T. Koch, M. Meister, A. Griesmaier, T. Pfau, H. Saito, Y. Kawaguchi, and M. Ueda, *d-wave collapse and explosion of a dipolar Bose-Einstein condensate*, Phys. Rev. Lett. **101**, 080401 (2008).

[Lah09] T. Lahaye, C. Menotti, L. Santos, M. Lewenstein, and T. Pfau, *The physics of dipolar bosonic quantum gases*, Rep. Prog. Phys. **72**, 126401 (2009).

[Lan08] F. Lang, K. Winkler, C. Strauss, R. Grimm, and J. Hecker Denschlag, *Ultracold Triplet Molecules in the Rovibrational Ground State*, Phys. Rev. Lett. **101**, 133005 (2008).

[Lan09a] F. Lang, C. Strauss, K. Winkler, T. Takekoshi, R. Grimm, and J. H. Denschlag, *Dark state experiments with ultracold, deeply-bound triplet molecules*, Faraday Discuss. **142**, 271 (2009).

[Lan09b] A. D. Lange, K. Pilch, A. Prantner, F. Ferlaino, B. Engeser, H.-C. Nägerl, R. Grimm, and C. Chin, *Determination of atomic scattering lengths from measurements of molecular binding energies near Feshbach resonances*, Phys. Rev. A **79**, 013622 (2009).

[Leg70] A. J. Leggett, *Can a Solid Be "Superfluid"?*, Phys. Rev. Lett. **25**, 1543 (1970).

[Leo98] P. J. Leo, E. Tiesinga, P. S. Julienne, D. K. Walter, S. Kadlecek, and T. G. Walker, *Elastic and Inelastic Collisions of Cold Spin-Polarized* ^{133}Cs *Atoms*, Phys. Rev.Lett. **81**, 1389 (1998).

[Ler10] A. Lercher, *Doppel-Spezies Bose-Einstein-Kondensat von Rubidium und Cäsium Atomen in räumlich getrennten optischen Fallen*, Ph.D. thesis, U. of Innsbruck (2010).

[Ler11] A. Lercher, T. Takekoshi, M. Debatin, B. Schuster, R. Rameshan, F. Ferlaino, R. Grimm, and H.-C. Nägerl, *Production of a dual-species Bose-Einstein condensate of Rb and Cs atoms*, The European Physical Journal D **65**, 3 (2011).

[Let88] P. D. Lett, R. N. Watts, C. I. Westbrook, and W. D. Phillips, *Observation of Atoms Laser Cooled below the Doppler Limit*, Phys. Rev. Lett. **61**, 169 (1988).

[Lew07] M. Lewenstein, A. Sanpera, V. Ahufinger, B. Damski, A. Sen, and U. Sen, *Ultracold atomic gases in optical lattices: mimicking condensed matter physics and beyond*, Adv. Phys. **56**, 243 (2007).

[Li10] Q. Li, E. H. Hwang, and S. Das Sarma, *Collective modes of monolayer, bilayer, and multilayer fermionic dipolar liquid*, Phys. Rev. B **82**, 235126 (2010).

[Lim10] A. R. P. Lima, *Hydrodynamic Studies of Dipolar Quantum Gases*, Ph.D. thesis, Freien Universität Berlin (2010).

[LO11] E. Lavert-Ofir, S. Gersten, A. B. Henson, I. Shani, L. David, J. Narevicius, and E. Narevicius, *A moving magnetic trap decelerator: a new source of cold atoms and molecules*, New J. Phys. **13**, 103030 (2011).

[Lu11] M. Lu, N. Q. Burdick, S. H. Youn, and B. L. Lev, *Strongly Dipolar Bose-Einstein Condensate of Dysprosium*, Phys. Rev. Lett. **107**, 190401 (2011).

[Lu12] M. Lu, N. Q. Burdick, and B. L. Lev, *Quantum degenerate dipolar Fermi gas*, Phys. Rev. Lett. **108**, 215301 (2012).

[Lud07] A. D. Ludlow, X. Huang, M. Notcutt, T. Zanon-Willette, S. M. Foreman, M. M. Boyd, S. Blatt, and J. Ye, *Compact, thermal-noise-limited optical cavity for diode laser stabilization at 1 X 10(-15)*, Optics Letters **32**, 641 (2007).

[Mac12] A. Macia, D. Hufnagl, F. Mazzanti, J. Boronat, and R. E. Zillich, *Excitations and Stripe Phase Formation in a Two-Dimensional Dipolar Bose Gas with Tilted Polarization*, Phys. Rev. Lett. **109**, 235307 (2012).

[Mar95] J. Martin, B. W. Shore, and K. Bergmann, *Coherent population transfer in multilevel systems with magnetic sublevels. II. Algebraic analysis*, Phys. Rev. A **52**, 583 (1995).

[Mar96] J. Martin, B. W. Shore, and K. Bergmann, *Coherent population transfer in multilevel systems with magnetic sublevels. III. Experimental results*, Phys. Rev. A **54**, 1556 (1996).

[Mar05] M. Mark, T. Kraemer, J. Herbig, C. Chin, H.-C. Nägerl, and R. Grimm, *Efficient creation of molecules from a cesium Bose-Einstein condensate*, Europhys. Lett. **69**, 706 (2005).

[Mar07] M. Mark, F. Ferlaino, S. Knoop, J. G. Danzl, T. Kraemer, C. Chin, H.-C. Nägerl, and R. Grimm, *Spectroscopy of ultracold trapped cesium Feshbach molecules*, Phys. Rev. A **76**, 042514 (2007).

[Mar09] M. J. Mark, J. G. Danzl, E. Haller, M. Gustavsson, N. Bouloufa, O. Dulieu, H. Salami, T. Bergeman, H. Ritsch, R. Hart, and H.-C. Nägerl, *Dark resonances for ground-state transfer of molecular quantum gases*, Appl. Phys. B **95**, 219 (2009).

[Mar12] M. Mark, *Experiments with tunable quantum gases in optical lattices*, Ph.D. thesis, University of Innsbruck (2012).

[May12] M. Mayle, P. R. Brandon, and J. L. Bohn, *Statistical aspects of ultracold resonant scattering*, Phys. Rev. A **85**, 062712 (2012).

[May13] M. Mayle, G. Quéméner, B. P. Ruzic, and J. Bohn, *Scattering of ultracold molecules in the highly resonant regime*, Phys. Rev. A **87**, 012709 (2013).

[McC11] D. J. McCarron, H. W. Cho, D. L. Jenkin, M. P. Köppinger, and S. L. Cornish, *Dual-species Bose-Einstein condensate of* ^{87}Rb *and* ^{133}Cs, Phys. Rev. A **84**, 011603 (2011).

[Mee05] S. Y. T. van de Meerakker, P. H. M. Smeets, N. Vanhaecke, R. T. Jongma, and G. Meijer, *Deceleration and electrostatic trapping of OH radicals*, Phys. Rev. Lett. **94**, 023004 (2005).

[Mee12] S. Y. T. van de Meerakker, H. L. Bethlem, N. Vanhaecke, and G. Meijer, *Manipulation and Control of Molecular Beams*, Chem. Rev. **112**, 4828 (2012).

[Mer12] S. Merz, N. Vanhaecke, W. Jäger, M. Schnell, and G. Meijer, *Decelerating molecules with microwave fields*, Phys. Rev. A **85**, 063411 (2012).

[Met03] H. J. Metcalf and P. van der Straten, *Laser cooling and trapping of atoms*, J. Opt. Soc. Am. B **20**, 887 (2003).

[Mic06] A. Micheli, G. K. Brennen, and P. Zoller, *A toolbox for lattice-spin models with polar molecules*, Nature Phys. **2**, 341 (2006).

[Mic07] A. Micheli, G. Pupillo, H. P. Büchler, and P. Zoller, *Cold polar molecules in two-dimensional traps: Tailoring interactions with external fields for novel quantum phases*, Phys. Rev. A **76**, 043604 (2007).

[Mic10a] A. Micheli, Z. Idziaszek, G. Pupillo, M. A. Baranov, P. Zoller, and P. S. Julienne, *Universal rates for reactive ultracold polar molecules in reduced dimensions*, Phys. Rev. Lett. **105**, 073202 (2010).

[Mic10b] P. G. Mickelson, Y. N. Martinez de Escobar, M. Yan, B. J. DeSalvo, and T. C. Killian, *Bose-Einstein condensation of ^{88}Sr through sympathetic cooling with ^{87}Sr*, Phys. Rev. A **81**, 051601 (2010).

[Mig85] A. L. Migdall, J. V. Prodan, W. D. Phillips, T. Bergeman, and H. J. Metcalf, *First Observation of Magnetically Trapped Neutral Atoms*, Phys. Rev. Lett. **54**, 2596 (1985).

[Mir11] M. H. G. Miranda, A. Chotia, B. Neyenhuis, D. Wang, G. Quéméner, S. Ospelkaus, J. Bohn, J. Ye, and D. S. Jin, *Controlling the quantum stereodynamics of ultracold bimolecular reactions*, Nature Phys. **7**, 502 (2011).

[Moe01] R. Moessner and S. Sondhi, *Resonating valence bond phase in the triangular lattice quantum dimer model*, Physical Review Letters **86**, 1881 (2001).

[Moo03] M. G. Moore and H. R. Sadeghpour, *Controlling two-species Mott-insulator phases in an optical lattice to form an array of dipolar molecules*, Phys. Rev. A **67**, 041603 (2003).

[Mor06] O. Morsch and M. Oberthaler, *Dynamics of Bose-Einstein condensates in optical lattices*, Rev. Mod. Phys. **78**, 179 (2006).

[Mos01] A. Mosk, S. Kraft, M. Mudrich, K. Singer, W. Wohlleben, R. Grimm, and M. Weidemüller, *Mixture of ultracold lithium and cesium atoms in an optical dipole trap*, Appl. Phys. B **73**, 791 (2001).

[Mud02] M. Mudrich, S. Kraft, K. Singer, R. Grimm, A. Mosk, and M. Weidemüller, *Sympathetic Cooling with Two Atomic Species in an Optical Trap*, Phys. Rev. Lett. **88**, 253001 (2002).

[Mün11] F. Münchow, C. Bruni, M. Madalinski, and A. Görlitz, *Two-photon photoassociation spectroscopy of heteronuclear YbRb*, Phys. Chem. Chem. Phys. **13**, 18734 (2011).

[Mya97] C. J. Myatt, E. A. Burt, R. W. Ghrist, E. A. Cornell, and C. E. Wieman, *Production of Two Overlapping Bose-Einstein Condensates by Sympathetic Cooling*, Phys. Rev. Lett. **78**, 586 (1997).

[N06] H.-C. Nägerl, T. Kraemer, M. Mark, P. Waldburger, J. G. Danzl, C. Chin, B. Engeser, A. D. Lange, K. Pilch, A. Jaakkola, and R. Grimm, *Experimental evidence for Efimov quantum states*, Atomic Physics 20 AIP Conf. Proc. **869**, 269 (2006).

[Nar08] E. Narevicius, A. Libson, C. G. Parthey, I. Chavez, J. Narevicius, U. Even, and M. G. Raizen, *Stopping Supersonic Beams with a Series of Pulsed Electromagnetic Coils: An Atomic Coilgun*, Physical Review Letters **100**, 093003 (2008).

[Nar12] E. Narevicius and M. G. Raizen, *Toward Cold Chemistry with Magnetically Decelerated Supersonic Beams*, Chem. Rev. **112**, 4879 (2012).

[Nem09] N. Nemitz, F. Baumer, F. Muenchow, S. Tassy, and A. Goerlitz, *Production of heteronuclear molecules in an electronically excited state by photoassociation in a mixture of ultracold Yb and Rb*, Physical Review A **79** (2009).

[Nes12] D. J. Nesbitt, *Toward State-to-State Dynamics in Ultracold Collisions: Lessons from High-Resolution Spectroscopy of Weakly Bound Molecular Complexes*, Chem. Rev. **112**, 5062 (2012).

[Neu78] W. Neuhauser, M. Hohenstatt, P. Toschek, and H. Dehmelt, *Optical-Sideband Cooling of Visible Atom Cloud Confined in Parabolic Well*, Phys. Rev. Lett. **41**, 233 (1978).

[Ni08] K.-K. Ni, S. Ospelkaus, M. H. G. de Miranda, A. Pe'er, B. Neyenhuis, J. J. Zirbel, S. Kotochigova, P. S. Julienne, D. S. Jin, and J. Ye, *A High Phase-Space-Density Gas of Polar Molecules*, Science **322**, 231 (2008).

[Ni09] K.-K. Ni, S. Ospelkaus, D. J. Nesbitt, J. Ye, and D. S. Jin, *A dipolar gas of ultracold molecules*, Phys. Chem. Chem. Phys. **11**, 9626 (2009).

[Ni10] K. K. Ni, S. Ospelkaus, D. Wang, G. Quemener, B. Neyenhuis, M. H. G. de Miranda, J. L. Bohn, J. Ye, and D. S. Jin, *Dipolar collisions of polar molecules in the quantum regime*, Nature **464**, 1324 (2010).

[Oka10] M. Okano, H. Hara, M. Muramatsu, K. Doi, S. Uetake, Y. Takasu, and Y. Takahashi, *Simultaneous magneto-optical trapping of lithium and ytterbium atoms towards production of ultracold polar molecules*, Appl. Phys. B **98**, 691 (2010).

[Orz01] C. Orzel, A. K. Tuchman, M. L. Fenselau, M. Yasuda, and M. A. Kasevich, *Squeezed States in a Bose-Einstein Condensate*, Science **291**, 2386 (2001).

[Osp06] C. Ospelkaus, S. Ospelkaus, L. Humbert, P. Ernst, K. Sengstock, and K. Bongs, *Ultracold Heteronuclear Molecules in a 3D Optical Lattice*, Phys. Rev. Lett. **97** (2006).

[Osp10a] S. Ospelkaus, K.-K. Ni, G. Quéméner, B. Neyenhuis, D. Wang, M. H. G. de Miranda, J. L. Bohn, J. Ye, and D. S. Jin, *Controlling the hyperfine state of rovibronic ground-state polar molecules*, Phys. Rev. Lett. **104**, 030402 (2010).

[Osp10b] S. Ospelkaus, K.-K. Ni, D. Wang, M. H. G. de Miranda, B. Neyenhuis, G. Quemener, P. S. Julienne, J. L. Bohn, D. S. Jin, and J. Ye, *Quantum-state controlled chemical reactions of ultracold potassium-rubidium molecules*, Science **327**, 853 (2010).

[Par04] B. Paredes, A. Widera, V. Murg, O. Mandel, S. Folling, I. Cirac, G. V. Shlyapnikov, T. W. Hansch, and I. Bloch, *Tonks-Girardeau gas of ultracold atoms in an optical lattice*, Nature **429**, 277 (2004), 10.1038/nature02530.

[Par11] C. G. Parthey, A. Matveev, J. Alnis, B. Bernhardt, A. Beyer, R. Holzwarth, A. Maistrou, R. Pohl, K. Predehl, T. Udem, T. Wilken, N. Kolachevsky, M. Abgrall, D. Rovera, C. Salomon, P. Laurent, and T. W. Hänsch, *Improved Measurement of the Hydrogen $1S$˘$2S$ Transition Frequency*, Phys. Rev. Lett. **107**, 203001 (2011).

[Par12] J. W. Park, C.-H. Wu, I. Santiago, T. G. Tiecke, S. Will, P. Ahmadi, and M. W. Zwierlein, *Quantum degenerate Bose-Fermi mixture of chemically different atomic species with widely tunable interactions*, Phys. Rev. A **85**, 051602(R) (2012).

[Pas07] A. Pashov, O. Docenko, M. Tamanis, R. Ferber, H. Knoeckel, and E. Tiemann, *Coupling of the X (1)Sigma(+) and a (3)Sigma(+) states of KRb*, Physical Review A **76** (2007).

[Pat13] R. W. Pattinson, T. P. Billam, S. A. Gardiner, D. J. McCarron, H. W. Cho, S. L. Cornish, N. G. Parker, and N. P. Proukakis, *Equilibrium solutions for immiscible two-species Bose-Einstein condensates in perturbed harmonic traps*, Phys. Rev. A **87**, 013625 (2013).

[Pel08] P. Pellegrini, M. Gacesa, and R. Côté, *Giant formation rates of ultracold molecules via Feshbach-optimized photoassociation*, Phys. Rev. Lett. **101**, 053201 (2008).

[Pen56] O. Penrose and L. Onsager, *Bose-Einstein Condensation and Liquid Helium*, Phys. Rev. **104**, 576 (1956).

[Phi82] W. D. Phillips and H. Metcalf, *Laser deceleration of an atomic beam*, Phys. Rev. Lett. **48**, 596 (1982).

[Pik10] A. Pikovski, M. Klawunn, G. V. Shlyapnikov, and L. Santos, *Interlayer superfluidity in bilayer systems of fermionic polar molecules*, Phys. Rev. Lett. **105**, 215302 (2010).

[Pil09a] K. Pilch, *Optical trapping and Feshbach spectroscopy of an ultracold Rb-Cs mixture*, Ph.D. thesis, U. of Innsbruck (2009).

[Pil09b] K. Pilch, A. D. Lange, A. Prantner, G. Kerner, F. Ferlaino, H.-C. Nägerl, and R. Grimm, *Observation of interspecies Feshbach resonances in an ultracold Rb-Cs mixture*, Phys. Rev. A **79**, 042718 (2009).

[Pit61] L. Pitaevskii, *Vortex Lines In An Imperfect Bose gas*, Soviet Physics Jetp-USSR **13**, 451 (1961).

[Pit03] L. Pitaevskii and S. Stringari, *Bose-Einstein condensation*, Oxford University Press, 2003.

[Pol10] L. Pollet, J. D. Picon, H. P. Büchler, and M. Troyer, *Supersolid phase with cold polar molecules on a triangular lattices*, Phys. Rev. Lett. **104**, 125302 (2010).

[Por03] S. Porsev and A. Derevianko, *Accurate relativistic many-body calculations of van der Waals coefficients C-8 and C-10 for alkali-metal dimers*, Journal Of Chemical Physics **119**, 844 (2003).

[Pot10] A. C. Potter, E. Berg, D.-W. Wang, B. I. Halperin, and E. Demler, *Superfluidity and dimerization in a multilayered system of fermionic polar molecules*, Phys. Rev. Lett. **105**, 220406 (2010).

[Pup08] G. Pupillo, A. Griessner, A. Micheli, M. Ortner, D.-W. Wang, and P. Zoller, *Cold atoms and molecules in self-assembled dipolar lattices*, Phys. Rev. Lett. **100**, 050402 (2008).

[Pup09] G. Pupillo, A. Micheli, H. P. Büchler, and P. Zoller, *Condensed matter physics with cold polar molecules*, in: R. V. Krems, W. C. Stwalley, and B. Friedrich (Eds.), chap. 12 in *Cold molecules: Theory, experiment, applications*, CRC Press, Boca Raton, 2009.

[Qu11] Qu and J. Bohn, *Dynamics of ultracold molecules in confined geometry and electric field*, Phys. Rev. A **83**, 012705 (2011).

[Que11] G. Quemener, J. Bohn, A. Petrov, and S. Kotochigova, *Universalities in ultracold reactions of alkali-metal polar molecules*, Phys. Rev. A **84**, 062703 (2011).

[Qué12] G. Quéméner and P. S. Julienne, *Ultracold Molecules under Control!*, Chem. Rev. **112**, 4949 (2012).

[R.06] F. R., A. I. Bishop, M. N. Shneider, and P. F. Barker, *Controlling the motion of cold molecules with deep periodic optical potentials*, Nature Phys. **2**, 465 (2006).

[Raa87] E. L. Raab, M. Prentiss, A. Cable, S. Chu, and D. E. Pritchard, *Trapping of Neutral Sodium Atoms with Radiation Pressure*, Phys. Rev. Lett. **59**, 2631 (1987).

[Rab06] P. Rabl, D. DeMille, J. M. Doyle, M. D. Lukin, R. J. Schoelkopf, and P. Zoller, *Hybrid Quantum Processors: Molecular Ensembles as Quantum Memory for Solid State Circuits*, Phys. Rev. Lett. **97**, 033003 (2006).

[Rab07] P. Rabl and P. Zoller, *Molecular dipolar crystals as high-fidelity quantum memory for hybrid quantum computing*, Phys. Rev. A **76**, 042308 (2007).

[Ram11] R. Rameshan, *Aufbau einer High-Finesse-Cavity zur Stabilisierung eines Diodenlasers*, Master's thesis, U. of Innsbruck (2011).

[Ran10] H. Ran, J. Aldegunde, and J. M. Hutson, *Hyperfine structure in the microwave spectra of ultracold polar molecules*, New Journal of Physics **12**, 043015 (2010).

[Reg03] C. A. Regal, C. Ticknor, J. L. Bohn, and D. S. Jin, *Creation of Ultracold Molecules from a Fermi Gas of Atoms*, Nature **424**, 47 (2003).

[Rib02] F. Riboli and M. Modugno, *Topology of the ground state of two interacting Bose-Einstein condensates*, Physical Review A **65** (2002).

[Ric95] L. Ricci, M. WeidemÃijller, T. Esslinger, A. Hemmerich, C. Zimmermann, V. Vuletic, W. KÃűnig, and T. HÃďnsch, *A compact grating-stabilized diode laser system for atomic physics*, Optics Communications **117**, 541 (1995).

[Rid11] A. Ridinger, S. Chaudhuri, T. Salez, D. R. Fernandes, N. Bouloufa, O. Dulieu, C. Salomon, and F. Chevy, *Photoassociative creation of ultracold heteronuclear* ^{6}Li^{40}K *molecules*, Europhys. Lett. **96**, 33001 (2011).

[Rie05] T. Rieger, T. Junglen, S. A. Rangwala, P. W. H. Pinkse, and G. Rempe, *Continuous loading of an electrostatic trap for polar molecules*, Phys. Rev. Lett. **95**, 173002 (2005).

[Rie11] S. Riedl, S. Hoekstra, W. Jäger, J. J. Gilijamse, S. Y. T. van de Meerakker, and G. Meijer, *Accumulation of Stark-decelerated NH molecules in a magnetic trap*, Eur. Phys. J. D **65**, 161 (2011).

[Roa02] G. Roati, F. Riboli, G. Modugno, and M. Inguscio, *Fermi-Bose Quantum Degenerate K-Rb Mixture with Attractive Interaction*, Phys. Rev. Lett. **89**, 150403 (2002).

[Rom97] V. I. Romanenko and L. P. Yatsenko, *Adiabatic population transfer in the three-level* Λ*-system: two-photon lineshape*, Opt. Comm. **140**, 231 (1997).

[Ryc04] D. Rychtarik, B. Engeser, H.-C. Nägerl, and R. Grimm, *Two-Dimensional Bose-Einstein Condensate in an Optical Surface Trap*, Phys. Rev. Lett. **92** (2004).

[Sag05] J. M. Sage, S. Sainis, T. Bergeman, and D. DeMille, *Optical production of ultracold polar molecules*, Phys. Rev. Lett. **94**, 203001 (2005).

[Sch58] A. L. Schawlow and C. H. Townes, *Infrared and Optical Masers*, Phys. Rev. **112**, 1940 (1958).

[Sch99] U. Schünemann, H. Engler, R. Grimm, M. Weidemüller, and M. Zielonkowski, *Simple scheme for tunable frequency offset locking of two lasers*, Rev. Sci. Instrum. **70**, 242 (1999).

[Sch08] U. Schneider, L. Hackermÿller, S. Will, T. Best, I. Bloch, T. A. Costi, R. W. Helmes, D. Rasch, and A. Rosch, *Metallic and Insulating Phases of Repulsively Interacting Fermions in a 3D Optical Lattice*, Science **322**, 204 (2008).

[Sch09] M. Schnell and G. Meijer, *Cold Molecules: Preparation, Applications, and Challenges*, Angew. Chem. Int. Ed. **48**, 6010 (2009).

[Sen05] P. Sengupta, L. P. Pryadko, F. Alet, M. Troyer, and G. Schmid, *Supersolids versus Phase Separation in Two-Dimensional Lattice Bosons*, Phys. Rev. Lett. **94**, 207202 (2005).

[Shi82] J. H. Shirley, *Modulation transfer processes in optical heterodyne saturation spectroscopy*, Opt. Lett. **7**, 537 (1982).

[Sho91] B. W. Shore, K. Bergmann, J. Oreg, and S. Rosenwaks, *Multilevel adiabatic population transfer*, Phys. Rev. A **44**, 7442 (1991).

[Sho95] B. W. Shore, J. Martin, M. P. Fewell, and K. Bergmann, *Coherent population transfer in multilevel systems with magnetic sublevels. I. Numerical studies*, Phys. Rev. A **52**, 566 (1995).

[Shu09] E. S. Shuman, J. F. Barry, D. R. Glenn, and D. DeMille, *Radiative force from optical cycling on a diatomic molecule*, Phys. Rev. Lett. **103**, 223001 (2009).

[Shu10] E. S. Shuman, J. F. Barry, and D. DeMille, *Laser cooling of a diatomic molecule*, Nature **467**, 820 (2010).

[Sil05] C. Silber, S. Gunther, C. Marzok, B. Deh, P. Courteille, and C. Zimmermann, *Quantum-degenerate mixture of fermionic lithium and bosonic rubidium gases*, Physical Review Letters **95** (2005).

[Sim03] A. Simoni, F. Ferlaino, G. Roati, G. Modugno, and M. Inguscio, *Magnetic Control of the Interaction in Ultracold K-Rb Mixtures*, Phys. Rev. Lett. **90**, 163202 (2003).

[Smi07] G. Smirne, R. M. Godun, D. Cassettari, V. Boyer, C. J. Foot, T. Volz, N. Syassen, S. Dürr, G. Rempe, M. D. Lee, K. Góral, and T. Köhler, *Collisional relaxation of Feshbach molecules and three-body recombination in* ^{87}Rb *Bose-Einstein condensates*, Phys. Rev. A **75**, 020702 (2007).

[Sol03] I. Sola and V. Malinovsky, *Collapse of the stimulated Raman adiabatic passage due to geometrical factors and how to overcome it*, Physical Review A **68** (2003).

[Spi07] I. B. Spielman, W. D. Phillips, and J. V. Porto, *Mott-Insulator Transition in a Two-Dimensional Atomic Bose Gas*, Phys. Rev. Lett. **98**, 080404 (2007).

[Spi10] F. M. Spiegelhalder, A. Trenkwalder, D. Naik, G. Kerner, E. Wille, G. Hendl, F. Schreck, and R. Grimm, *All-optical production of a degenerate mixture of* ^{6}*Li and* ^{40}*K and creation of heteronuclear molecules*, Phys. Rev. A **81**, 043637 (2010).

[Ste08a] D. A. Steck, *Rubidium 87 D Line Data* (2008), oregon Center for Optics and Department of Physics, University of Oregon.

[Ste08b] D. A. Steck, *Rubidium Cs 133 D Line Data* (2008), oregon Center for Optics and Department of Physics, University of Oregon.

[Ste10] D. A. Steck, *Sodium D Line Data* (2010), oregon Center for Optics and Department of Physics, University of Oreg.

[Stö04] T. Stöferle, H. Moritz, C. Schori, M. Köhl, and T. Esslinger, *Transition from a Strongly Interacting 1D Superfluid to a Mott Insulator*, Phys. Rev. Lett. **92**, 130403 (2004).

[Str10] C. Strauss, T. Takekoshi, F. Lang, K. Winkler, R. Grimm, J. Hecker Denschlag, and E. Tiemann, *Hyperfine, rotational, and vibrational structure of the* $a^3\Sigma_u^+$ *state of* $^{87}Rb_2$, Phys. Rev. A **82**, 052514 (2010).

[Stu05] J. Stuhler, A. Griesmaier, T. Koch, M. Fattori, T. Pfau, S. Giovanazzi, P. Pedri, and L. Santos, *Observation of dipole-dipole interaction in a degenerate quantum gas*, Phys. Rev. Lett. **95**, 150406 (2005).

[Stu08] B. K. Stuhl, B. C. Sawyer, D. Wang, and J. Ye, *Magneto-optical trap for polar molecules*, Phys. Rev. Lett. **101**, 243002 (2008).

[Stw04] W. C. Stwalley, *Efficient conversion of ultracold Feshbach-resonance-related polar molecules into ultracold ground state* ($X\,^1\Sigma^+ v = 0, J = 0$) *molecules*, Eur. Phys. J. D **31**, 221 (2004).

[Tak12] T. Takekoshi, M. Debatin, R. Rameshan, F. Ferlaino, R. Grimm, and H.-C. Nägerl, *Towards the production of ultracold ground-state RbCs molecules: Feshbach resonances, weakly bound states, and coupled-channel model*, Phys. Rev. A **85**, 032506 (2012).

[Tal05] G. Talhammer, M. Theis, K. Winkler, R. Grimm, and J. Hecker Denschlag, *Inducing an optical Feshbach resonance via stimulated Raman coupling*, Phys. Rev. A **71**, 033403 (2005).

[Tar09] M. R. Tarbutt, J. J. Hudson, B. E. Sauer, and E. A. Hinds, *Preparation and manipulation of molecules for fundamental physics tests*, in: R. V. Krems, W. C. Stwalley, and B. Friedrich (Eds.), *Cold molecules: Theory, expriment, applications*, CRC Press, Boca Raton, 2009, preprint available at arXiv:0803.0967.

[Tas10] S. Tassy, N. Nemitz, F. Baumer, C. Hoehl, A. Bataer, and A. Goerlitz, *Sympathetic cooling in a mixture of diamagnetic and paramagnetic atoms*, Journal Of Physics B-Atomic Molecular And Optical Physics **43** (2010).

[The04] M. Theis, G. Thalhammer, K. Winkler, M. Hellwig, G. Ruff, R. Grimm, and J. H. Denschlag, *Tuning the Scattering Length with an Optically Induced Feshbach Resonance*, Phys. Rev. Lett. **93**, 123001 (2004).

[Tho87] H. R. Thorsheim, J. Weiner, and P. S. Julienne, *Laser-Induced Photoassociation of Ultracold Sodium Atoms*, Phys. Rev. Lett. **58**, 2420 (1987).

[Tho02] A. M. Thomas, S. Hopkins, S. L. Cornish, and C. J. Foot, *Strong evaporative cooling towards Bose-Einstein condensation of a magnetically trapped caesium gas*, J. Opt. B. **5**, 107 (2002).

[Tho05] S. T. Thompson, E. Hodby, and C. E. Wieman, *Ultracold molecule production via a resonant oscillating magnetic field*, Physical Review Letters **95**, 190404 (2005).

[Tic07] C. Ticknor, *Energy dependence of scattering ground-state polar molecules*, Phys. Rev. A **76**, 052703 (2007).

[Tic08] C. Ticknor, *Collisional control of ground state polar molecules and universal dipolar scattering*, Phys. Rev. Lett. **100**, 133202 (2008).

[Tic11] C. Ticknor, *Two-dimensional dipolar scattering with a tilt*, Phys. Rev. A **84**, 032702 (2011).

[Tie93] E. Tiesinga, B. J. Verhaar, and H. T. C. Stoof, *Threshold and resonance phenomena in ultracold ground-state collisions*, Phys. Rev. A **47**, 4114 (1993).

[Tie98] E. Tiesinga, C. J. Williams, and P. S. Julienne, *Photoassociative spectroscopy of highly excited vibrational levels of alkali-metal dimers: Green-function approach for eigenvalue solvers*, Phys. Rev. A **57**, 4257 (1998).

[Tie10] T. Tiecke, *Properties of Potassium* (2010), van der Waals-Zeeman institute University of Amsterdam The Netherlands v1.0 (February, 2010).

[Tim99] E. Timmermanns, P. Tommasini, M. Hussein, and A. Kerman, *Feshbach resonances in atomic Bose-Einstein condensates*, Phys. Rep. **315**, 199 (1999).

[Tow55] C. H. Townes and A. L. Schawlow, *Microwave Spectroscopy*, Dover Publications Inc., 1955.

[Tre01] P. Treutlein, K. Y. Chung, and S. Chu, *High-brightness atom source for atomic fountains*, Phys. Rev. A **63**, 051401(R) (2001).

[Uhl30] G. E. Uhlenbeck and L. S. Ornstein, *On the Theory of the Brownian Motion*, Phys. Rev. **36**, 823 (1930).

[Ulm12] J. Ulmanis, J. Deiglmayr, M. Repp, R. Wester, and M. Weidemüller, *Ultracold Molecules Formed by Photoassociation: Heteronuclear Dimers, Inelastic Collisions, and Interactions with Ultrashort Laser Pulses*, Chem. Rev. **112**, 4890 (2012).

[Val00] J. Vala, O. Dulieu, F. Masnou-Seeuws, P. Pillet, and R. Kosloff, *Coherent control of cold-molecule formation through photoassociation using a chirped-pulsed-laser field*, Phys. Rev. A **63**, 013412 (2000).

[van08] S. van de Meerakker, T. Bethlem, and G. Meijer, *Taming molecular beams*, Nature Physics **4**, 595 (2008).

[VH99] L. Vestergaard Hau, S. E. Harris, Z. Dutton, and H. B. Cyrus, *Light speed reduction to 17 metres per second in an ultracold atomic gas*, Nature **397**, 594 (1999).

[Vit97a] N. V. Vitanov and S. Stenholm, *Analytic properties and effective two-level problems in stimulated Raman adiabatic passage*, Phys. Rev. A **55**, 648 (1997).

[Vit97b] N. V. Vitanov and S. Stenholm, *Population transfer via a decaying state*, Phys. Rev. A **56**, 1463 (1997).

[Vit97c] N. V. Vitanov and S. Stenholm, *Properties of stimulated Raman adiabatic passage with intermediate-level detuning*, Opt. Comm. **135**, 394 (1997).

[Vit98a] N. Vitanov, B. Shore, and K. Bergmann, *Adiabatic population transfer in multistate chains via dressed intermediate states*, Eur. Phys. J. D **4**, 15 (1998).

[Vit98b] N. V. Vitanov, *Adiabatic population transfer by delayed laser pulses in multistate systems*, Phys. Rev. A **58**, 2295 (1998).

[Vit99] N. V. Vitanov and S. Stenholm, *Adiabatic population transfer via multiple intermediate states*, Phys. Rev. A **60**, 3820 (1999).

[Vit01] N. V. Vitanov, T. Halfmann, B. W. Shore, and K. Bergmann, *Laser-Iinduced Population Transfer by Adiabatic Passage Techniques*, Annu. Rev. Phys. Chem **52**, 763 (2001).

[Vit08] M. Viteau, A. Chotia, M. Allegrini, N. Bouloufa, O. Dulieu, D. Comparat, and P. Pillet, *Optical Pumping and Vibrational Cooling of Molecules*, Science **321**, 232 (2008).

[Voi09] A.-C. Voigt, M. Taglieber, L. Costa, T. Aoki, W. Wieser, T. W. Hänsch, and K. Dieckmann, *Ultracold heteronuclear Fermi-Fermi molecules*, Phys. Rev. Lett. **102**, 020405 (2009), *ibid.* **105**, 269904(E) (2010).

[Vol06] T. Volz, N. Syassen, D. Bauer, E. Hansis, S. Dürr, and G. Rempe, *Preparation of a quantum state with one molecule at each site of an optical lattice*, Nature Phys. **2**, 692 (2006).

[Vul98] V. Vuletić, C. Chin, A. J. Kerman, and S. Chu, *Degenerate Raman Sideband Cooling of Trapped Cesium Atoms at Very High Atomic Densities*, Phys. Rev. Lett. **81**, 5768 (1998).

[Wal90] T. Walker, D. Sesko, and C. Wieman, *Collective behavior of optically trapped neutral atoms*, Phys. Rev. Lett. **64**, 408 (1990).

[Wal94] T. Walker and P. Feng, *Measurements of Collisions Between Laser-Cooled Atoms*, vol. 34 of *Advances In Atomic, Molecular, and Optical Physics*, 125 – 170, Academic Press, 1994.

[Web03a] T. Weber, J. Herbig, M. Mark, H.-C. Nägerl, and R. Grimm, *Bose-Einstein condensation of cesium*, Science **299**, 232 (2003).

[Web03b] T. Weber, J. Herbig, M. Mark, H.-C. Nägerl, and R. Grimm, *Three-body recombination at large scattering lengths in an ultracold atomic gas*, Phys. Rev. Lett. **91**, 123201 (2003).

[Wei98] J. D. Weinstein, R. deCarvalho, T. Guillet, B. Friedrich, and J. M. Doyle, *Magnetic trapping of calcium monohydride molecules at millikelvin temperatures*, Nature **395**, 148 (1998).

[Wei99] J. Weiner, V. S. Bagnato, S. Zilio, and P. S. Julienne, *Experiments and theory in cold and ultracold collisions*, Rev. Mod. Phys. **71**, 1 (1999).

[Wel11] N. Wells and I. C. Lane, *Electronic states and spin-forbidden cooling transitions of AlH and AlF*†, Phys. Chem. Chem. Phys. **13**, 19018 (2011).

[Wie91] C. Wieman and L. Hollberg, *Using Diode-Lasers for Atomic Physics*, Review Of Scientific Instruments **62**, 1 (1991).

[Wil08] E. Wille, F. M. Spiegelhalder, G. Kerner, D. Naik, A. Trenkwalder, G. Hendl, F. Schreck, R. Grimm, T. G. Tiecke, J. T. M. Walraven, S. J. J. M. F. Kokkelmans, E. Tiesinga, and P. S. Julienne, *Exploring an ultracold Fermi-Fermi mixture: Interspecies Feshbach resonances and scattering properties of* ^{6}Li *and* ^{40}K, Phys. Rev. Lett. **100**, 053201 (2008).

[Win78] D. J. Wineland, R. E. Drullinger, and F. L. Walls, *Radiation-Pressure Cooling of Bound Resonant Absorbers*, Phys. Rev. Lett. **40**, 1639 (1978).

[Win80] W. Wing, *Electrostatic Trapping Of Neutral Atomic Particles*, Physical Review Letters **45**, 631 (1980).

[Wod71] F. Wodarczyk and E. Wilson, *Radio Frequency-Microwave Double Resonance As A Tool In Analysis Of Microwave Spectra*, Journal Of Molecular Spectroscopy **37**, 445 (1971).

[Wu12] C.-H. Wu, J. W. Park, P. Ahmadi, S. Will, and M. W. Zwierlein, *Ultracold Fermionic Feshbach Molecules of* $^{23}\mathrm{Na}^{40}\mathrm{K}$, Phys. Rev. Lett. **109**, 085301 (2012).

[Wyn00] R. Wynar, R. S. Freeland, D. J. Han, C. Ryu, and D. J. Heinzen, *Molecules in a Bose-Einstein Condensate*, Science **287**, 1016 (2000).

[Xu03] K. Xu, T. Mukaiyama, J. R. Abo-Shaeer, J. K. Chin, D. E. Miller, and W. Ketterle, *Formation of Quantum-Degenerate Sodium Molecules*, Phys. Rev. Lett. **91**, 210402 (2003).

[Yat02] L. P. Yatsenko, V. I. Romaneno, B. W. Shore, and K. Bergmann, *Stimulated Raman adiabatic passage with partially coherent laser fields*, Phys. Rev. A **65**, 043409 (2002).

[Yel06] S. F. Yelin, K. Kirby, and R. Côté, *Schemes for robust quantum computation with polar molecules*, Phys. Rev. A **74**, 050301 (2006).

[Yi00] S. Yi and L. You, *Trapped atomic condensates with anisotropic interactions*, Phys. Rev. A **61**, 041604 (2000).

[Yi01] S. Yi and L. You, *Trapped condensates of atoms with dipole interactions*, Phys. Rev. A **63**, 053607 (2001).

[Yi07] S. Yi, T. Li, and C. P. Sun, *Novel quantum phases of dipolar Bose gases in optical lattices*, Phys. Rev. Lett. **98**, 260405 (2007).

[You10] S. H. Youn, M. Lu, U. Ray, and B. L. Lev, *Dysprosium magneto-optical traps*, Phys. Rev. A **82**, 043425 (2010).

[Zha09] P. Zhang, P. Naidon, and U. Masahito, *Independent Control of Scattering Lengths in Multicomponent Quantum Gases*, Phys. Rev. Lett. **103**, 133202 (2009).

[Zuc10a] P. Zuchowski, J. Aldegunde, and J. Hutson, *Ultracold RbSr Molecules Can Be Formed by Magnetoassociation*, Phys. Rev. Lett. **105**, 153201 (2010).

[Żuc10b] P. S. Żuchowski and J. M. Hutson, *Reactions of ultracold alkali-metal dimers*, Phys. Rev. A **81**, 060703(R) (2010).

[Zwi03] M. W. Zwierlein, C. A. Stan, C. H. Schunck, S. M. F. Raupach, S. Gupta, Z. Hadzibabic, and W. Ketterle, *Observation of Bose-Einstein Condensation of Molecules*, Phys. Rev. Lett. **91**, 250401 (2003).

Appendix C

Acknowledgments / Danksagung

Diese Arbeit wäre nicht möglich gewesen ohne das Mitwirken vieler, die mich während meiner Promotion unterstützt haben und bei denen ich mich bedanke.

In erster Linie möchte ich Hanns-Christoph Nägerl dafür danken, daß er mir die Möglichkeit gegeben hat meine Promotion am RbCs Experiment durchzuführen sowie für die langjährige Betreuung und Unterstützung. In diesem Rahmen danke ich auch Rudolf Grimm, der als Leiter der Gruppe den Rahmen für fruchtbare wissenschaftliche Arbeit geschaffen hat und nie um einen guten Rat verlegen war.

Bei den zahlreichen Kollegen, die am RbCs Experiment die Arbeit unterstützt haben, möchte ich mich recht herzlich bedanken. Karl Pilch hat mich in die Arbeit am RbCs experiment eingeführt und mir die Funktionsweise des Experiments erklärt. Dafür und für seine Gesprächsbereitschaft möchte ich mich recht herzlich bedanken. Mein herzlicher Dank gilt auch Bastian Schuster, der stets mit guter Laune bereit war die unbeliebten Aufgaben im Labor zu übernehmen und stets für Ordnung und ein gutes Klima im Labor gesorgt hat. Raffael Rameshan, der maßgeblich am Aufbau der Cavities beteiligt war sowie Lukas Reichsöllner und Michael Kugler gilt mein Dank für die vielfältige Unterstützung und auch die Unternehmungen jenseits der Arbeit.

Bei allen in der Gruppe, die meine Arbeit auf die ein oder andere Weise unterstützt haben und mein Leben in Innsbruck bereichert haben möchte ich mich herzlich bedanken. Insbesondere Manfred Mark und Gerhard Hendl danke ich recht herzlich für die zahlreichen Gespräche über Elektronik und die gute Zusammenarbeit. Mein Dank gilt auch den zahlreichen Mitarbeitern in den Werkstätten und Sekrtariaten die mit offenem Ohr und tatkräftiger Unterstützung die Arbeit begleitet haben. Ich möchte ich auch bei allen bedanken die die Zeit in Innsbruck zu einer guten Zeit gemacht haben. Insbesonder danke ich Martin Berninger herzlich für die zahlreichen anregenden Diskussionen.

Abschließend möchte ich mich noch bei meiner Mutter sowie bei Liviu und Ursula Cioflec bedanken, die mich in den vergangenen Jahren unterstützt haben. Mein herzlichster Dank gilt Eveline Cioflec für die stilistischen Anmerkungen und Korrekturen die vielfältige Unterstützung sowie für die zahlreichen tiefgründigen und ermunternden Gespräche.